

The Pennsylvania State University
The Graduate School
Department of Materials Science and Engineering

LOCAL ORIGIN OF MACROSCOPIC PROPERTIES AND PATTERNING IN

PbZr_{1-x}Ti_xO₃ FILMS

A Dissertation in
Materials Science and Engineering

by

Patamas Bintachitt

© 2009 Patamas Bintachitt

Submitted in Partial Fulfillment
of the Requirements
for the Degree of

Doctor of Philosophy

August 2009

The dissertation of Patamas Bintachitt was reviewed and approved* by the following:

Susan Troler-McKinstry
Professor of Ceramic Science and Engineering
Dissertation Advisor
Chair of Committee

Thomas R. Shrout
Senior Scientist and Professor of Materials Science and Engineering

Christopher Muhlstein
Associate Professor of Materials Science and Engineering

Thomas N. Jackson
Robert E. Kirby Chair Professor of Electrical Engineering

Gary L. Messing
Distinguished Professor of Ceramic Science and Engineering
Head of the Department of Materials Science and Engineering

*Signatures are on file in the Graduate School

ABSTRACT

The lead zirconate titanate (PZT) films that are most widely utilized in microelectromechanical systems (MEMS) are polycrystalline, with random orientation of the grains. The resulting transverse piezoelectric coefficient, $e_{31,f}$, is approximately -6 to -7 C/m² for PbZr_{0.52}Ti_{0.48}O₃. This thesis describes the preparation of high quality PZT films, the nonlinearity in their dielectric and piezoelectric responses, as well as their patterning by reactive ion etching.

Two types of PZT films were prepared: PZT films with mixed {001} and {111} orientation and those with strong levels of {001} orientation. Dense polycrystalline PZT films on (111)Pt/Ti/SiO₂/(001)Si substrates (with thicknesses from 0.28 to 4.40 μm) were obtained by optimizing the chemical solution deposition process. Higher piezoelectric coefficients (about -12 C/m²) can be obtained if significant {001} orientation is achieved. Thus, one goal of the research was to obtain {001} oriented PZT films on Pt-coated Si substrates. In this work, PbTiO₃ buffer layers were chosen due to good lattice matching with PZT films, and the strong propensity for development of {001} orientation. The pyrolysis, crystallization steps, and lead excess addition of PbTiO₃ buffer layers deposition were investigated. Using a thin PbTiO₃ buffer layer and controlled pyrolysis conditions allowed {100} oriented PZT films to be prepared. The PbTiO₃ buffer layer can be used over a full wafer to provide orientation. Higher piezoelectric coefficients, $e_{31,f}$ of -14 and -10 C/m² were achieved for {001} PZT thin films of 1.0 μm and 0.24 μm thickness, respectively using appropriate poling conditions.

The local and global domain wall contributions were studied by piezoelectric nonlinearity and dielectric nonlinearity in both {001}-textured PZT films and PZT films with mixed {001} and {111} orientation. Band Excitation Piezoelectric Force Microscopy (BE-PFM) was shown to enable quantitative measurements of the local piezoelectric nonlinearity. It was found that films over the thickness range probed showed Rayleigh-like behavior. 4 μm thick films were nearly

uniform in their Rayleigh coefficient, suggesting that any heterogeneities in the response developed at lateral length scales below the resolution of the PFM measurement. In contrast, thinner films showed significantly more patchiness in their response, so that fluctuations in behavior developed at a lateral length scale on the order of 0.6 to 2.5 micron. These variations did not appear to be correlated directly with the surface topology. The ability to detect lateral inhomogeneity in the nonlinearity of thinner films is likely to be a function of the volume probed in the measurement. Finally, it is hypothesized that the same population of domain wall contributes to the local and global nonlinearity.

Nanoindentation measurements were conducted in an attempt to distinguish 180° and non- 180° domain wall motion in these films. Non- 180° domain walls can be moved by both electrical and mechanical fields. In contrast, 180° domain walls can be moved by electric fields, but not by uniform stresses. In PZT films with mixed $\{111\}$ and $\{001\}$ orientation, some ferroelastic wall motion took place during loading, at stress levels on the order of GPa. The reduced elastic modulus is much higher on the unloading curve. Thus, on unloading, it is believed that there is no contribution from mechanical softening associated with ferroelasticity.

The global polarization switching in polycrystalline, $\{001\}$ -textured films on Si, and $\{001\}$ -films on $\text{SrRuO}_3 / \text{SrTiO}_3$ was studied through first order reversal curves (FORC) in order to assess the Preisach distribution governing the switching behavior. Then, the local polarization switching in polycrystalline PZT films was studied by using Switching Spectroscopy Piezoresponse Force Microscopy (SS-PFM). Acquisition of multiple hysteresis loops allows polarization switching parameters including nucleation biases, coercive biases, and the amount of switchable response to be mapped in real space. SS-PFM was studied on both bare PZT film surfaces and in capacitor structures (metal/ PZT film/ metal). The capacitor structure shows the evolution of correlated switching of $10^2 - 10^3$ grain clusters with well-defined imprint and nucleation biases. A transition from a regime where the domain wall motion is over a short range

to the formation of clusters to complete switching is observed. The switchable polarization as a function of bias window allows the voltage dependence and spatial distribution of regions with reversible and irreversible wall motions to be mapped.

The final chapter of experimental work describes the patterning of PZT films for MEMS. The ability to dry etch large depths of ferroelectric materials such as lead zirconate titanate is important in both microelectromechanical systems and in high frequency medical ultrasound transducers. Dense $\text{Pb}(\text{Zr}_{0.52}\text{Ti}_{0.48})\text{O}_3$ films ($\geq 1 \mu\text{m}$) were used to study the etching characteristics. The films were etched using an Inductively Coupled Plasma Reactive Ion Etcher (ICP-RIE) with a mixture of Ar and SF_6 gas. The variation of the etch rate with gas flow rate, source power, substrate holder power, and operation pressure and the uniformity of etching were investigated. The maximum etch rate achieved was $0.31 \mu\text{m}/\text{min}$. The electrical properties of PZT films directly exposed to the plasma after etching ($\epsilon_r = 1300$, $\tan\delta = 3.29\%$, $P_r = 29.8 \mu\text{C}/\text{cm}^2$, $E_c = 39 \text{ kV}/\text{cm}$) are similar to the electrical properties of PZT before etching ($\epsilon_r = 1400$, $\tan\delta = 4.35\%$, $P_r = 27.1 \mu\text{C}/\text{cm}^2$, $E_c = 32 \text{ kV}/\text{cm}$). Small changes in the minor hysteresis loops were found, suggesting that there may be a small change in the internal field induced by the patterning process. In addition, sidewall angles of $> 80^\circ$ have been achieved using a non-contact method (laser writer) for the lithography step.

2.10 Nanoindentation Measurements on PZT Films.....	58
2.11 Dielectric Nonlinearity.....	58
2.12 Dry Etching of PZT Films.....	59
2.12.1 Mask Design and Feature Sizes for Dry Etching.....	63
Chapter 3 Processing Control and Characterization of PZT Films with Mixed {001} and {111} Orientation and {001}-Textured PZT Films	65
3.1 Processing of PZT films with Mixed {001} and {111} Orientation.....	65
3.1.1 Processing Parameters, Crystallography, and Electrical Properties of PZT Films with Mixed {001} and {111} Orientation.....	65
3.1.2 Transverse Piezoelectric Coefficient ($e_{31,t}$) of PZT Films with Mixed {001} and {111} Orientation	77
3.2 {001}-Textured Orientation Control Processing	80
3.2.1 PbTiO ₃ Buffer Layer Study.....	80
3.2.2 PZT Films on PbTiO ₃ Buffer Layers	82
3.2.3 Increased %Pb Content in PbTiO ₃ Orienting Layer.....	87
3.2.4 {001}-Textured Orientation Control Processing of Thin PZT Films (~0.24 μm)	91
3.2.5 Optimized Poling for {001}-Textured PZT Films	94
3.2.6 Transverse Piezoelectric Coefficient of {001}-Textured PZT Films.....	95
3.3 {001} PZT Thin Films on SrRuO ₃ /(100) SrTiO ₃	97
3.4 Summary of Properties of PZT Films	98
3.5 Grain Sizes of PZT Films.....	101
Chapter 4 Dielectric Nonlinearity	104
4.1 Thickness and Orientation Dependence of the Dielectric Nonlinearity.....	105
4.2 Effects of External Bias Fields on the Dielectric Nonlinearity.....	109
4.2.1 PZT Films with Mixed {001} and {111} Orientation	109
4.2.2 {001}-Textured PZT Films on Pt-Coated Si Substrates	111
4.3 Summary of Dielectric Nonlinearity.....	113
Chapter 5 Piezoelectric Nonlinearity and Switching Spectroscopy Piezoelectric Force Microscopy.....	115
5.1 Piezoelectric Nonlinearity.....	115
5.1.1 Piezoelectric Nonlinearity by PFM with Single Frequency.....	116
5.1.1.1 Piezoelectric Nonlinearity of “Mixed {001} and {111} orientation” PZT Films	117
5.1.2 Piezoelectric Nonlinearity by Band Excitation SS-PFM	122
5.1.2.1 Piezoelectric Nonlinearity of Mixed Orientation PZT Films by BE-PFM	125
5.1.2.2 Piezoelectric Nonlinearity of Textured PZT Film by BE-PFM	138
5.1.3 Summary of Dielectric Nonlinearity and Piezoelectric Nonlinearity Comparison	139
5.2 Global Switching Measurements	140
5.3 Switching Spectroscopy Piezoelectric Force Microscopy (SS-PFM).....	145
5.3.1 Spatially Resolved Spectroscopic Mapping of Polarization Reversal	145

5.3.2 SS-PFM On and Off the Top Electrode	151
Chapter 6 Nanoindentation Studies of PZT Films	163
6.1 Loading and Unloading Elastic Curves	164
6.2 Pile-Up	166
6.3 Residual Stresses	168
6.4 Nanoindentation Tests on PZT Films with Mixed {111} and {100} Orientation	169
6.4.1 The Indentation Depth Set Up	169
6.4.2 Reduced Modulus and Hardness of PZT Films	171
Chapter 7 Dry Etching of PZT Films	180
7.1 The Mechanism of PZT Etching	184
7.2 Etching Effect of Substrate Holder Power	185
7.3 Effect of Operating Pressure on Etching	186
7.4 Effect of Gas Chemistry on DRIE of PZT Films	187
7.5 Etch Rate as a Function of Feature Spacing	190
7.6 The Repeatability of Dry Etching	191
7.7 Etch Uniformity over 4 inch Wafer	192
7.8 Influence of Substrate Holder Voltage	193
7.9 Etch Rate of SiO ₂ and Pt	195
7.10 Electrical Properties of PZT Films after Etching	196
7.10.1 Impact of Etching Induced Point Defects of PZT Films	198
Chapter 8 Conclusions and Future Work	207
8.1 Conclusions	207
8.1.1 Processing Control and Characterization of Mixed {001} and {111} Orientation and {001}-Textured PZT films	207
8.1.2 Dielectric Nonlinearity	208
8.1.3 Piezoelectric Nonlinearity and Switching Spectroscopy Piezoelectric Force Microscopy	208
8.1.3.1 Piezoelectric Nonlinearity	209
8.1.3.2 Switching Spectroscopy PFM	210
8.1.4 Nanoindentation of PZT films	210
8.1.5 Dry Etching of PZT Films	210
8.2 Future Work	211
8.2.1 180° and non-180° Domain Wall Contribution	212
8.2.2 The Origin of the Domain Wall Pinning	212
8.2.3 SS-PFM	213
8.2.4 Study Effect on e _{31,f} After Dry Etching in Term of Aging Effect	214
References	215
Appendix A Electrical Properties of PZT Films	224
A.1 Dielectric and Hysteresis Loops	224
A.1.1 {001} Textured PZT Films	224

Appendix B Piezoelectric Nonlinearity of PZT Films.....	231
B.1 Bias Evolution of Switchable Polarization and Piezoelectric Response.....	231
Appendix C Nanoindentation of PZT Films with Mixed {001} and {111} Orientation.....	235

LIST OF FIGURES

Figure 1- 1: A polarization – electric field hysteresis loop for a ferroelectric showing the coercive field (E_c), remanent polarization (P_r), and saturation polarization (P_{sat}) (a) Ideal single crystal case and (b) Polycrystalline case ^[6]	5
Figure 1- 2: A schematic showing the available polarization directions in two poled rhombohedral crystals of different orientations. ^[6]	6
Figure 1- 3: Schematic showing domain walls in ferroelectric materials (a) 180° domain walls, (b) non-180° domain walls, and (c) a mixture of 180° domain walls and non-180° domain walls. ^[6]	7
Figure 1- 4: The domain states in an ideal ferroelectric crystal at different electric fields in a polarization – electric field hysteresis loop. O = unpoled sample, A = perfectly poled sample in a single domain state, B and C = nucleation and growth of domains with opposite polarization direction, D = reverse oriented domains, E = perfectly single domain state with opposite polarization direction, and F = nucleation of reverse polarized domains. ^[6]	8
Figure 1- 5: PZT perovskite distortions and domains (a) cubic, above T_c no domains, (b) tetragonal, below T_c : 90° and 180° domain walls, and (c) rhombohedral below T_c 71°, 109°, and 180° domain walls, (Pm3m, P4mm, R3m, and R3c are the symmetry abbreviations. P = primitive lattice, R = rhombohedral lattice type, m = mirror plane, 3 and 4 = 3-fold and 4-fold rotations, c= glide plane parallel to 3. ^[15]	9
Figure 1- 6: (a) PZT phase diagram (Pm, R3m, P4mm, etc. are the symmetry abbreviations. Pm is a subgroup of R3m and Pbam, while Pc is a subgroup of Pm, Pbam, and R3c), (b and a = glide plane perpendicular to z axis, c= glide plane parallel to 3. ^[15] , (b) Composition dependence of the relative piezoelectric response in PZT thin films ^[11]	10
Figure 1- 7: (a) Intrinsic contribution from a single domain, (b) Extrinsic contribution from 180° domain wall motion, and (c) Extrinsic contribution from non-180° domain wall motion. The dashed lines represent the configuration before the application of the external electric fields. ^[6]	15
Figure 1- 8: Schematic of the electrode size effects to the amplitude of d_{33} in a system with only up and down polarization states. V_f is the volume fraction.	16
Figure 1- 9: (a) Schematic piezoelectric response of a poled ferroelectric crystal made of 2 domains with one 180° domain wall excited by ac voltage. (b) The piezoelectric response with higher amplitude excitation voltage. ^[6]	17
Figure 1- 10: (a) Piezoelectric coefficients as a function of temperature in all three ferroelectric phases of BaTiO ₃ predicted by LGD theory. (b) Orientation dependence	

of $d_{33}^{r*}(\theta)$ in the rhombohedral phase of BaTiO_3 at 180K. The $\langle 001 \rangle$ direction shows a higher d_{33} . ^[40]	20
Figure 1- 11: Piezoelectric coefficient dependence of composition and orientation (a) Piezoelectric coefficient and dielectric susceptibilities in PZT crystals, (b) Orientation dependence of piezoelectric coefficient for PZT at room temperature as a function of PbTiO_3 concentration, (c) Orientation dependence of piezoelectric coefficient for rhombohedral PZT, and (d) A cross section of orientation dependence of piezoelectric coefficient for rhombohedral PZT from (c). ^[40]	21
Figure 1- 12: A schematic showing the potential energy landscape for a moving domain wall as a function of position. For an ac electric field, there are the two possible types of domain wall motions: reversible and irreversible domain wall motions ^[6]	23
Figure 2- 1: Flow chart for preparation of 10% - 20 % Pb-excess PZT solution or 30 - 40% Pb-excess PbTiO_3 solutions	30
Figure 2- 2: (a) PZT film deposition used by Wolf and Trolier-McKinstry ^[18] which was found to produce a layer of porosity for each RTA step, (b) Modified process for dense PZT films without strong levels of texture	32
Figure 2- 3: Rapid Thermal Annealing (RTA) profile (a) previous condition ^[18] (b) modified condition for dense PZT films	32
Figure 2- 4: (a) PbTiO_3 buffer layer deposition (b) The modified process for $\{001\}$ -textured PZT film deposition ^[25]	35
Figure 2- 5: PZT deposition process for $\{001\}$ oriented films on single crystal SrTiO_3 coated with SrRuO_3	36
Figure 2- 6: Schematic of a grazing angle XRD ^[72]	38
Figure 2- 7: Experimental set up for e_{31f} measurement (a) equipment set up and (b) sample with attached strain gauge ^[6, 73]	42
Figure 2- 8: Schematic of the quarter-bridge assembly used for strain measurement.	43
Figure 2- 9: A Schematic of wedge bonder for wire-bonding (a) wire and needle setting, (b) sample holder setting, and (c) bonding parameter control panel.....	45
Figure 2- 10: Wire bonding technique	46
Figure 2- 11: Schematic of Piezoresponse Force Microscopy experimental set up for piezoelectric nonlinearity ^[66]	47
Figure 2- 12: The principle of band excitation SS-PFM: A = resonance amplitude, Ψ = phase, ω = resonance frequency, and Q = quality factor ^[74]	49

Figure 2- 13: Switching spectroscopy piezoresponse force microscopy measurements on a 1 μm thick, mixed {001} and {111} oriented PZT film (a) on electrode (b) on the PZT film directly.....	53
Figure 2- 14: A schematic of PFM hysteresis loop ^[52]	53
Figure 2- 15: The voltage waveform used for local hysteresis measurements ^[52, 62]	54
Figure 2- 16: The first order reversal curves method modeled by Ichiro Fujii.....	57
Figure 2- 17: Schematic illustration of the experiment setup for nanoindentation studies ^[75, 76]	58
Figure 2- 18: Sample preparation and dry etching process steps (a) Sputter Cr/Au on PZT film (b) Lithographically pattern the resist on Cr/Au (c) Electroplate Ni (d) Remove photoresist (e) Dry etch PZT (f) Remove Ni	61
Figure 2- 19: Inductively Coupled Plasma Reactive Ion Etcher (ICP-RIE), Alcatel AMS-100 Dielectric Etching I-Speeder ^[78]	62
Figure 2- 20: Feature size and mask detail used in the etching process of variations in the gas flow rate, substrate holder power, operation pressure, and repeatability	63
Figure 2- 21: Mask design for dry etching study of spacing variations of 50 μm , 30 μm , 20 μm , 10 μm , 5 μm , and 3 μm	64
Figure 2- 22: Mask pattern for uniformity study	64
Figure 3- 1: 5.79 μm 20% Pb-excess $\text{Pb}(\text{Zr}_{0.52}\text{Ti}_{0.48})\text{O}_3$ films with pyrolysis at 300°C, 1 min and 550°C, 2 min and RTA 700°C, 1 min, heating rate 7°C/s	67
Figure 3- 2: Surface morphology showing grain sizes ranging from 50 nm to 205 nm for a 5.79 μm thick $\text{Pb}(\text{Zr}_{0.52}\text{Ti}_{0.48})\text{O}_3$ film prepared with pyrolysis at 300°C, 1 min and 550°C, 2 min and RTA 700°C, 1 min, heating rate 7°C/s	68
Figure 3- 3: Electrical properties of 5.79 μm $\text{Pb}(\text{Zr}_{0.52}\text{Ti}_{0.48})\text{O}_3$ films prepared using pyrolysis at 300°C, 1 min and 550°C, 2 min and RTA 700°C, 1 min, heating rate 7°C/s (a) dielectric constant vs. frequency and (b) polarization-electric field loop.....	69
Figure 3- 4: Cross-sectional micrograph of ~ 1 μm thick $\text{Pb}(\text{Zr}_{0.52}\text{Ti}_{0.48})\text{O}_3$ films prepared using the following pyrolysis steps: (a) 200°C, 1 min + 350°C, 2 min, (b) 235°C, 1 min + 400°C, 2 min, (c) 260°C, 1 min + 450°C, 2 min, (d) 275°C, 1 min + 500°C, 2 min, (e) 200°C, 2 min + 350°C, 2 min, and (f) 235°C, 2 min + 400°C, 2 min.....	70
Figure 3- 5: $\text{Pb}(\text{Zr}_{0.52}\text{Ti}_{0.48})\text{O}_3$ films with optimized condition, 250°C, 1 min and 400°C, 1 min and RTA 700°C, 1 min, heating rate 4°C/s.....	73

Figure 3- 6: Electrical properties of 4.36 μm thick, dense $\text{Pb}(\text{Zr}_{0.52}\text{Ti}_{0.48})\text{O}_3$ films (a) dielectric constant vs. frequency (b) polarization-electric field loop.....	74
Figure 3- 7: 20% Pb-excess $\text{Pb}(\text{Zr}_{0.30}\text{Ti}_{0.70})\text{O}_3$ films (a) 2.17 μm thick film (b) 3.30 μm thick film.....	75
Figure 3- 8: XRD of $\text{Pb}(\text{Zr}_{0.52}\text{Ti}_{0.48})\text{O}_3$ films of various thickness deposited using a 0.75 M, 10% Pb-excess PZT solution.....	76
Figure 3- 9: The general curve of remanent polarization vs. log time. ^[82]	78
Figure 3- 10: Aging of the dielectric permittivity (ϵ_r) of 1.09 μm thick mixed {001} and {111} orientation PZT (52/48) film following poling.....	79
Figure 3- 11: XRD of 30% Pb-excess PbTiO_3 buffer layers for different pyrolysis and crystallization conditions.....	81
Figure 3- 12: XRD patterns of (a) PZT on a PbTiO_3 buffer layer (b) PZT film without PbTiO_3 buffer layer, with pyrolysis 250°C, 1 min and 400°C, 1 min and RTA 700°C, 1 min, heating rate 4°C/s.....	82
Figure 3- 13: XRD patterns of PZT films prepared with different heating rates on a PbTiO_3 layer on (a) Nova substrates (b) Ramtron substrates.....	84
Figure 3- 14: Cross section of {100} oriented PZT films on (a) a Nova substrate (b) a Ramtron substrate.....	85
Figure 3- 15: Hysteresis loops of PZT films on PbTiO_3 buffer layer (a) Nova substrate (b) Ramtron substrate.....	86
Figure 3- 16: X-ray diffraction scans of 40% Pb-excess PbTiO_3 buffer layers.....	87
Figure 3- 17: PZT films on (a) 30% Pb-excess buffer layer (b) 40% Pb-excess buffer layer, Nova substrates.....	88
Figure 3- 18: X-Ray diffraction scans of 40% Pb-excess PbTiO_3 layers on Ramtron compared to Nova substrates.....	89
Figure 3- 19: PZT films on 40% Pb-excess buffer layer with Ramtron substrates. The second pyrolysis temperature was 350°C for 20 s and the crystallization was done using a heating rate of 10°C/s. The 40% Pb-excess PbTiO_3 layers were prepared with pyrolysis temperatures of 250°C and 400°C for 1 min on Ramtron substrates.....	90
Figure 3- 20: PZT on 40% Pb-excess buffer layer with Ramtron substrates with different conditions: hold longer time was to hold at 520°C for 60 s and regular hold time was to hold at 520°C for 30 s.....	91
Figure 3- 21: X-Ray diffraction scans of thin PZT films (a) and (b) RTA every layer, and (c) RTA every 3 layers.....	92

Figure 3- 22: Comparison of the dielectric constants and losses for PZT films on 40% Pb-excess buffer layer with RTA every layer, RTA ever 3 layers, and anneal at 600°C for 30 s after a single RTA step	93
Figure 3- 23: P-E loops for thin PZT films on 40% Pb-excess buffer layer at different heat treatment (a) RTA every layer, (b) RTA every 3 layers, and (c) annealed after RTA step in (b).....	94
Figure 3- 24: $\epsilon_{31,f}$ poling study of PZT films (a) Nova substrates with Lotgering factor = 0.79 (b) Ramtron substrates with Lotgering factor = 1	95
Figure 3- 25: (a) $\epsilon_{31,f}$ of PZT films with mixed {001} and {111} orientation and (b) $\epsilon_{31,f}$ of PZT films on 30% and 40% Pb excess PbTiO ₃ layers on both Nova and Ramtron substrates as a function of PZT thickness	96
Figure 3- 26: X-Ray diffraction scans of PZT film on an SRO/STO substrate and SRO/STO substrate	97
Figure 3- 27: P-E loops for PZT film on SRO/STO	98
Figure 3- 28: Grain size observation by FE-SEM (a) 0.28 μm mixed {001} and {111} orientation PZT film, (b) 2.06 μm mixed {001} and {111} orientation PZT film, (c) 0.27 μm textured PZT film, and (d) 0.92 μm textured PZT film.....	102
Figure 4- 1: The field dependence of the dielectric permittivity for films of different thickness (a) PZT films with mixed {001} and {111} orientation (b) textured PZT films and (c) {001} PZT film on SrRuO ₃ /SrTiO ₃	106
Figure 4- 2: (a) ϵ_{init} , reversible Rayleigh parameter, (b) α , irreversible Rayleigh parameter and (c) ratio of irreversible to reversible Rayleigh parameters as a function of PZT film thickness and orientation. The previous report is the data from Gharb et al. ^[30]	108
Figure 4- 3: The field dependence of the dielectric permittivity for different thicknesses of PZT films with mixed {001} and {111} orientation measured at 1 kHz with different dc bias fields. (a) 0.28 μm , (b) 0.53 μm , (c) 1.09 μm , (d) 2.06 μm , (e) 4.04 μm , and (f) 4.40 μm	110
Figure 4- 4: The ratio of irreversible to reversible Rayleigh constants of PZT films with mixed {001} and {111} orientation as a function of applied dc bias fields at different film thicknesses.....	111
Figure 4- 5: The DC field dependence of the dielectric permittivity for different thicknesses of {001}- textured PZT films on Pt-coated Si substrates at 1 kHz (a) 0.27 μm , (b) 0.48 μm , and (c) 0.92 μm	111
Figure 4- 6: The external dc bias fields dependence of irreversible to reversible Rayleigh ratio for 0.27 μm , 0.48 μm , and 0.92 μm thick {001}-textured PZT films on Pt-coated Si.....	112

- Figure 5- 1: The ratio of irreversible to reversible piezoelectric response of PZT films with mixed $\{001\}$ and $\{111\}$ orientation at 1 kHz (a) as a function of bias field (b) data from (a) plotted as a function of normalized field (bias field/coercive field) 118
- Figure 5- 2: Measurement of apparent piezoelectric coefficients ($d_{33,f}$) across an electrode and on bare PZT film at two different E_{ac} amplitudes. The points from A to O were measured on the top electrode. “Off electrode” means the measurement was made on bare PZT films when only the electrode (rather than the tip) was driven..... 120
- Figure 5- 3: Schematic of the experimental PFM set up and bowing due to use of a large top electrode. The piezoelectric strains results in local surface motion due to local piezoelectric response and bending due to a bimorph effect.^[55, 56] 121
- Figure 5- 4: (a) Schematic of the effect of substrate bending on the measured displacements by a single beam interferometer (b) Schematic behavior of the displacement vs. substrate clamping (c) Deformation of the PZT/Si induced by piezoelectric effect across electrode, and (d) Displacement for a PZT film on a partially clamped Si substrate^[83] 122
- Figure 5- 5: A set of resonant characteristics, where different curves show different amplitudes for the driving field. In this case, the resonant frequency increased with drive amplitude.^[90] 126
- Figure 5- 6: Amplitude signal as a function of frequency over the frequency band employed in the band excitation measurement. Data where there was little drive amplitude dependence of the resonant frequency were chosen for quantitative measurements..... 128
- Figure 5- 7: The piezoelectric nonlinearity of 4.04 μm PZT films with mixed $\{001\}$ and $\{111\}$ orientation measured at a single point with the first 10 and last 4 measurements out of 100 times shown (a) Displacement (arbitrary units) as a function of ac voltage, (b) Initial piezoelectric coefficient ($d_{33, \text{init}}$), (c) Rayleigh coefficient (α_d), and (d) Irreversible to reversible ratio ($d_{33, \text{init}}/\alpha_d$)..... 130
- Figure 5- 8: Irreversible to reversible ratio, topology, and resonance frequency maps of 4.04 μm PZT films with mixed $\{001\}$ and $\{111\}$ orientation (a) 2 μm x 2 μm area with 50 nm pitch (b) 5 μm x 5 μm with 100 nm pitch, and (c) 10 μm x 10 μm with 400 nm pitch. The maximum ac field was 20 kV/cm (0.58 E_c). 132
- Figure 5- 9: Irreversible to reversible ratio, topology, and resonance frequency maps for the 1.09 μm thick PZT films with mixed $\{001\}$ and $\{111\}$ orientation (a) 5 μm x 5 μm area with 200 nm pitch (b) 10 μm x 10 μm with 200 nm pitch, and (c) 10 μm x 10 μm with 200 nm pitch. The maximum ac field was 13 kV/cm (0.3 E_c). 134
- Figure 5- 10: Irreversible to reversible ratio, topology, and resonance frequency map of 1.09 μm PZT films with mixed $\{001\}$ and $\{111\}$ orientation (a) 6 μm x 6 μm area

with 100 nm pitch (b) 9.6 μm x 9.6 μm with 160 nm pitch, and (c) 9 μm x 9 μm with 150 nm pitch. The maximum ac field was 20 kV/cm (0.47 E_c).	135
Figure 5- 11: Irreversible to reversible ratio, topology, and resonance frequency map of 2.06 μm PZT films with mixed {001} and {111} orientation (a) 5 μm x 5 μm area with 160 nm pitch and (b) 9.6 μm x 9.6 μm with 160 nm pitch. The maximum ac field was 8 kV/cm (0.22 E_c).	137
Figure 5- 12: Irreversible to reversible ratio, topology, and resonance frequency map of 0.53 μm PZT films with mixed {001} and {111} orientation, 5 μm (83 nm pitch) x 5 μm (250 nm pitch). The maximum ac field was 29 kV/cm (0.41 E_c).	138
Figure 5- 13: Irreversible to reversible ratio, topology, and resonance frequency map of 0.92 μm textured PZT films (a) 1 μm x 1 μm with 50 nm pitch and (b) 9.6 μm x 9.6 μm with 160 nm pitch. The maximum ac field was 27.8 kV/cm (0.46 E_c).	139
Figure 5- 14: (a) Polarization-electric field hysteresis loop measurement and (b) Rayleigh-like dielectric response of 1.09 mixed {001} and {111} orientation PZT thin film.	141
Figure 5- 15: (a) First order polarization reversal curves measured using large area electrodes and (b) Preisach density measured using large capacitor structures.	142
Figure 5- 16: Preisach distribution density of PZT films with mixed {001} and {111} orientation in thickness series (a) 0.28 μm , (b) 0.53 μm , (c) 1.09 μm , (d) 2.06 μm , (e) 4.04 μm , and (f) 4.40 μm .	143
Figure 5- 17: Preisach distribution density of {001}-textured PZT films in thickness series (a) 0.27 μm , (b) 0.48 μm , and (c) 0.92 μm .	144
Figure 5- 18: Preisach distribution density of 1 μm thick PZT film on SrRuO ₃ coated SrTiO ₃ .	144
Figure 5- 19: (a-b) Single point hysteresis loops from areas with maximum and medium piezoresponse and (c- g) Positive <i>remanent</i> piezoresponse maps with increasing excitation bias window ^[56] .	147
Figure 5- 20: <i>Switchable</i> response maps with increasing excitation bias window ^[56] .	148
Figure 5- 21: Spatial maps of ferroelectric switching parameters SS-PFM from the electrode area (a) initial piezoresponse, (b) imprint, (c) work of switching, (d-f) Schematic of the hysteresis loop switching parameters of switchable response, positive and negative nucleation bias, (g) topography of PZT films, (h) statistical distributions of PFM signal and switchable response, and (i) statistical distribution of positive and negative nucleation biases. ^[55]	150
Figure 5- 22: An example of transgranular coupling in a PZT ceramic. DW denotes domain wall ^[49] .	151

Figure 5- 23: Positive nucleation bias maps and hysteresis loops from several location acquired from (a) a bare PZT film sample surface and (b) the electroded surface ^[55]	153
Figure 5- 24: Piezoelectric hysteresis loops obtain from SS-PFM averaged over an 8 x 8 μm area for bare PZT films (tip as top electrode) (b) comparison of normalized hysteresis loop of global, and local (on and off electrode) measurements	154
Figure 5- 25: (a) Distribution of remanent piezoelectric response for different excitation windows showing similarity of behavior, (b) Distribution of switchable response showing Gaussian profiles, (c) Evolution of average switchable response, and (d) Evolution of deviation width of switchable response ^[56]	156
Figure 5- 26: (a) The comparison of global and local switching vs. excitation bias window, (b) A series of minor and major hysteresis loops calculated from the irreversible part of the Preisach density assuming the sample was depoled prior to the field excitation, and (c) Averaged local SS-PFM loops for similar excitation bias window ^[56]	158
Figure 5- 27: (a) Topography of bare PZT films, (b) Topography of electrode film, (c) Positive nucleation bias map at an excitation window of 7 V, (d) Correlation function of bare PZT films, electrode, and switchable polarization, (e) Correlation function at different bias voltages, (f) Fractal analysis of switchable polarization images for different excitation bias window, and (g) Excitation bias window dependence of fractal dimensionality ^[56]	160
Figure 6- 1: Typical strain and depolarization behavior for a uniaxial stress applied parallel to the poling direction in PZT ceramics, A-B linear behavior before domain switching, B-D, domain switching, D-E, linear behavior after all domains have been switched perpendicular to stress. E-A is the case of reversible domain switching, and E-F is the case of irreversible domain switching. After reference ^[101]	164
Figure 6- 2: Schematic loading and unloading curves measured using nanoindtation. ^[100]	166
Figure 6- 3: Schematic of material response during indentation test (a) image depicting a material that shows pile-up and (b) material that sinks in. ^[100]	167
Figure 6- 4: A scanning probe microscope image of Pile-up results for a PZT film.....	168
Figure 6- 5: (a) The strain rates with reduced modulus and (b) The strain rates with hardness as a function of plastic indentation depth of 0.28 μm mixed {001} and {111} orientation PZT film.....	170
Figure 6- 6: Force as a function of displacement showing loading and unloading curves, as well as the reproducibility of the measurements	171
Figure 6- 7: The elastic modulus as a function of percent indentation depth normalized by film thickness calculated from unloading curves and loading curves for each mixed {001} and {111} orientation PZT film thickness.	173

Figure 6- 8: The Elastic modulus for PZT 50/50 and PZT 52/48 ceramics. M_1 and M_2 represent Elastic modulus. P_1 and P_2 represent mechanical losses ^[105]	174
Figure 6- 9: Biaxial elastic modulus vs. maximum applied force on the tip. ^[97]	175
Figure 6- 10: (a) Elastic modulus as a function of load and (b) Elastic modulus as a function of grain size diameter, h = indentation depth and ef = film thickness ^[98]	176
Figure 6- 11: Nanoindentation of 200 nm PZT (52/48) films by Wu et al. (a) Indentation modulus vs. indentation depth and (b) Hardness vs. indentation depth. A = <111> with 32 nm grain size, B = <111> with 49 nm grain size, C = <111> with 58 nm grain size, D= random, E = <100> ^[108]	177
Figure 6- 12 (a) The hardness as a function of plastic indentation depth of different mixed {001} and {111} orientation PZT film thickness (b) The hardness as a function of percent indentation depth normalized by the film thickness of different mixed {001} and {111} orientation PZT film thickness.	178
Figure 6- 13: (a) The hardness as a function of grain size diameter and (b) the hardness as a function of reduced penetration depth of PZT and PMNT films ^[98]	179
Figure 7- 1: A schematic of isotropic etching. The arrows show the etching time dependence. ^[110]	181
Figure 7- 2: A schematic of anisotropic etching by a dry etching process ^[110]	181
Figure 7- 3: (a) PZT etch rate vs. substrate holder power variation at source power = 2000 W, Ar flow rate = 42.5 sccm, SF ₆ flow rate = 5 sccm (b) SEM of PZT cross section after etching at source power = 400 W	186
Figure 7- 4: (a) PZT etch rate vs. operating pressure at a source power = 2000 W, substrate holder power = 400 W, Ar = 42.5 sccm, SF ₆ = 5 sccm (b) SEM of PZT cross section after etching at pressure of 2.7 mTorr	187
Figure 7- 5: (a) PZT etch rate vs. Ar gas flow rate at a substrate holder power = 400 W, source power = 2000 W, SF ₆ = 5 sccm (b) SEM of PZT cross section after etching at Ar = 42.5 sccm	188
Figure 7- 6: (a) PZT etch rate vs. SF ₆ variation at source power = 2000 W, substrate holder power = 400 W, Ar = 42.5 sccm (b) SEM of PZT cross section after etching at SF ₆ = 20 sccm. The solid curves are for the etch rate, while the dashed lines are for the selectivity.....	189
Figure 7- 7: PZT etch rate vs. spacing (a) Spacing from 3 μ m to 50 μ m (b) Spacing from 20 μ m to 150 μ m. The selectivity is given in the dashed lines.	190
Figure 7- 8: (a) SEM of PZT film after etching with 3 μ m spacing (b) XRD pattern of PZT films after etching of different feature sizes	191

Figure 7- 9: Repeatability of PZT film etch rate.....	191
Figure 7- 10: Schematic overview of plasma sheet thickness and the resulting angular deviation including substrate holder voltage ^[137]	193
Figure 7- 11: (a) PZT etch rate and substrate holder voltage (self-bias) vs. substrate holder power variation at source power = 2000 W, Ar flow rate = 42.5 sccm, SF ₆ flow rate = 5 sccm (b) PZT etch rate and substrate holder voltage (self-bias) vs. Ar gas flow variation at a substrate holder power = 400 W, source power = 2000 W, SF ₆ flow rate = 5 sccm, and (c) PZT etch rate and substrate holder voltage (self-bias) vs. SF ₆ gas flow variation at source power = 2000 W, substrate holder power = 400 W, Ar = 42.5 sccm	195
Figure 7- 12: Cross section of Pt and SiO ₂ etching.....	196
Figure 7- 13: The hysteresis of PZT film after etching without annealing.....	197
Figure 7- 14: The P-E loops of PZT films before etching	199
Figure 7- 15: Major hysteresis loops after dry etching PZT films with three different masks and two etch rates. Low etch rate refers to $0.188 \pm 0.001 \mu\text{m}/\text{min}$ and the high etch rate refers to $0.283 \pm 0.005 \mu\text{m}/\text{min}$ (a) Low etch rate with Ni mask, (b) High etch rate with Ni mask, (c) Low etch rate with negative resist KMR 1100, (d) High etch rate with negative resist KMR 1100, (e) Low etch rate with positive resist Shipley 1827, and (f) High etch rate with positive resist Shipley 1827.....	198
Figure 7- 16: Minor loops of PZT after etching with Ni mask (a) and (b) Minor loops measured after exposing to a low etch rate ($0.188 \pm 0.001 \mu\text{m}/\text{min}$) (c) and (d) Minor loops measured after using a high etch rate ($0.283 \pm 0.005 \mu\text{m}/\text{min}$).....	202
Figure 7- 17: Minor loops of PZT after etching using a negative photoresist KMR 1100 mask (a) and (b) low etch rate ($0.188 \pm 0.001 \mu\text{m}/\text{min}$) (c) and (d) high etch rate ($0.283 \pm 0.005 \mu\text{m}/\text{min}$)	203
Figure 7- 18: Minor loops of PZT after etching with positive photoresist Shipley 1827 (a) and (b) Minor loops with low etch rate ($0.188 \pm 0.001 \mu\text{m}/\text{min}$) (c) and (d) Minor loops with high etch rate ($0.283 \pm 0.005 \mu\text{m}/\text{min}$).....	204
Figure 7- 19: Defects in a ferroelectric crystals (a) Imprinted P-E loop and (b) strongly pinched P-E loop	206
Figure A- 1: Dielectric constant and losses for PZT film on (a) 30% Pb-excess buffer layers, Nova substrates (b) 40% Pb-excess buffer layers, Nova substrates. The details of the process condition were described in Chapter 2 and Chapter 3.....	224
Figure A- 2: P-E loops for {100} textured PZT films of different thickness on 30% Pb-excess buffer layers (a) $0.94 \mu\text{m}$, (b) $0.65 \mu\text{m}$, (c) $0.25 \mu\text{m}$, Nova substrates. The details of the process condition were described in Chapter 2 and Chapter 3.....	225

Figure A- 3: P-E loops for PZT films of different thickness on 40% Pb-excess buffer layers (a) 0.88 μm , (b) 0.48 μm , and (c) 0.31 μm , Nova substrates. The details of the process condition were described in Chapter 2 and Chapter 3.	226
Figure A- 4: Dielectric constant and losses for {100} PZT films of different thickness on 40%excess buffer layers, Ramtron substrates. The details of the process condition were described in Chapter 2 and Chapter 3.	227
Figure A- 5: P-E loops for PZT films of different thickness on 40% Pb-excess buffer layers (a) 0.95 μm , (b) 0.48 μm , and (c) 0.25 μm , Ramtron substrates. The details of the process condition were described in Chapter 2 and Chapter 3.	228
Figure A- 6: Dielectric constant and losses for PZT films on 40% Pb-excess PbTiO_3 buffer layers (a) 0.92 μm , RTA with heating rate 3 $^\circ\text{s}$ (hold 30 s), (b) 0.71 μm , RTA with holding longer (hold 60 s) with heating rate 3 $^\circ\text{C/s}$, and (c) 0.72 μm , RTA with holding longer (hold 60 s) with heating rate 10 $^\circ\text{s}$	229
Figure A- 7: P-E loops for PZT films of different thickness on 40% Pb-excess buffer layers (a) 0.92 μm , RTA with heating rate 3 $^\circ\text{s}$ (hold 30 s), (b) 0.71 μm , RTA with holding longer (hold 60 s) with heating rate 3 $^\circ\text{C/s}$, and (c) 0.72 μm , RTA with holding longer (hold 30 s) with heating rate 10 $^\circ\text{s}$	230
Figure B- 1: Maps of switching parameters at different bias windows from 3 to 16 V for 50 by 50 pixel images.	232
Figure B- 2: Maps of switching parameters at different excitation bias windows from 4 to 16 V for 144 by 144 pixel images.....	234
Figure B- 3: Fractal dimension vs. excitation window for 6 μm data set.....	234
Figure C- 1: Loading and unloading curve of 0.28 μm PZT films	235
Figure C- 2: Loading and unloading curve of 0.53 μm mixed {001} and {111} orientation PZT film.....	236
Figure C- 3: Loading and unloading curve of 1.09 μm mixed {001} and {111} orientation PZT film.....	236
Figure C- 4: Loading and unloading curve of 2.06 mixed {001} and {111} orientation PZT film	237
Figure C- 5: loading and unloading curve of 4.40 μm mixed {001} and {111} orientation PZT film	237
Figure C- 6: Elastic modulus of film with the correction of substrate modeling by King method.....	238

LIST OF TABLES

Table 1- 1: Advantages and disadvantages of PFM measurement without and with a top electrode ^[65, 66]	27
Table 2- 1: Experimental plan of PbTiO ₃ buffer layer condition study	34
Table 2- 2: Powder diffraction file numbers used for XRD scan (from ICDD PDF-4 2007)	37
Table 2- 3: Wire-bonding parameters	46
Table 2- 4: PZT volume sampled in global and local measurements	52
Table 2- 5: Parameters of sample preparation for DRIE	60
Table 3- 1: Heat treatment condition of each experiment to obtain denser PZT films.....	71
Table 3- 2: $\epsilon_{31,f}$ of 20% Pb excess Pb(Zr _{0.52} Ti _{0.48})O ₃ , 5.79 μm and 10% Pb excess Pb(Zr _{0.52} Ti _{0.48})O ₃ , 4.36 μm	74
Table 3- 3: Electrical properties of 2.17 μm and 3.30 μm 20% Pb-excess Pb(Zr _{0.30} Ti _{0.70})O ₃ films.....	75
Table 3- 4: Remanent polarization and coercive field from hysteresis loops as a function of thickness.....	77
Table 3- 5: Summary of $\epsilon_{31,f}$ and electrical properties of PZT films	99
Table 3- 6: Grain sizes for PZT films of mixed {001} and {111} orientation and {001} texture.....	103
Table 4- 1: Summary of dielectric nonlinearity of mixed {001} and {111} orientation, {001}-textured PZT films	114
Table 5- 1: Setting resonance frequency and excitation ac field in BE-PFM experiment.....	124
Table 5- 2: Comparison between average local piezoelectric nonlinearity and global dielectric nonlinearity.....	140

Table 6- 1: Nanoindentation loading parameters tests for PZT films with mixed {001} and {111} orientation.....	170
Table 7- 1: Previous work in Reactive Ion Etching (RIE) and Deep RIE (DRIE) of PZT.....	183
Table 7- 2: Etch uniformity over 2 inch and 3.5 inch areas.....	192
Table 7- 3: The electrical properties of PZT films before and after etching	197

ACKNOWLEDGEMENTS

First of all, I would like to express my deepest gratitude to my advisor, Prof. Susan Trolier-McKinstry, for her support not only academically but also personally. I could never have succeeded in my Ph.D. program without her guidance. In all my years at Penn State, while working under Prof. Trolier-McKinstry, she was always available whenever I needed her advice. She always reaches out to help and makes sure that I understand the questions before guiding me to get the answers by myself. Whenever I encountered any problems in research, she would guide me to learn and overcome the problem. She is my role model. I have learned a lot and improved many scientific skills from her. She is one of the best teachers, researchers, and advisors at the same time. She has inspired me in all every aspect of life and makes me want to do the same to my students one day. Thank you for everything that you teach to make me have such a confidence in myself for giving a presentation in public, which I have never had before.

Also, thank you to all my committee members, Professors Thomas ShROUT, Christopher Muhlstein, and Thomas Jackson, for giving me good suggestions as well as asking all the difficult questions that helped guide my thinking about the scientific approach to my thesis research.

Very special thanks to my mentor in Thailand, Dr. Pavadee Aungkavattana. She suggested that I attend Penn State University and highly recommended Prof. Susan Trolier-McKinstry as an advisor.

My appreciation also extends to the Royal Thai Government scholarship for full financial support throughout the Ph.D. Program and to the Center of Dielectric Studies and the National Security Science and Engineering Faculty Fellowship program for research funding.

Thank you to Dr. Sergei Kalinin, Steven Jesse, Katya Katayani, Maxim Nikiforov, and Art Baddorf at Oak Ridge National Laboratory for their help in the Piezoelectric Force

Microscopy measurements and interpretation of SSPFM. Thank you to Amber Romasco and Dr. Christopher Muhlstein for measurements and discussions about the nanoindentation experiments.

Thank you to the past and present STM group: Cheng, Mustafa, Han, Eunki, Raja, Ichiro, Tana, Dan, Nazanin, Hajime, Raegan, Flavio, Heidi, Hideki, Song Won, Mike, Barb, and Susie. For all your friendships, I am grateful beyond expression.

Many thanks also go to my best friends: Akamol Shavalikul and Pattamaporn Timakul, that they have encouraged me during all my difficult times when I am depressed or encountered problems and for being true friends.

Last but not least, I would like to dedicate this thesis to my father, Dr. Prachuab Bintachitt, who had no opportunity to see this success by himself, but I could always feel that he is still alive vividly in my memory. For all my family members, I also thank my mother, Vattanee, my sister Primast, and my brother Piyawat for their love and all-times support.

Chapter 1

Introduction and Literature Review

1.1 Introduction

Lead zirconate titanate (PZT) films are used as piezoelectric layers in microelectromechanical systems (MEMS) because of their superior properties (large displacements, fast response, and high sensitivity). In making PZT MEMS devices, it is important to achieve dense and crack free thick films so that the device performance is enhanced. This chapter will describe some of the important features of these films, as well as review the literature in the field.

In this work, $\text{Pb}(\text{Zr}_{0.52}\text{Ti}_{0.48})\text{O}_3$ films ($\leq 5 \mu\text{m}$ in thickness) were processed on (111)Pt/Ti/SiO₂/(001) Si substrates by a chemical solution deposition technique, involving synthesis of a chemical solution, deposition of the solution by spinning, and heat treatment. The first goal of this thesis was to optimize the pyrolysis and crystallization steps to achieve dense PZT films. This work will be described in Chapters 2 and 3 of the thesis.

The PZT films that are most widely utilized in MEMS are polycrystalline, with random orientation of the grains. The resulting transverse piezoelectric coefficient, $e_{31,f}$ is approximately -6 to -7 C/m² for a PZT 52/48. Higher piezoelectric coefficients (about -12 C/m²) can be obtained if significant {001} orientation is achieved. Consequently, a second goal of the thesis is to be able to obtain {001} oriented PZT films on Pt-coated Si substrates. There are many parameters that will influence texture in PZT films: pyrolysis temperature, post pyrolysis oxygen treatment, RTA cycle, excess lead addition in the films, the presence of microcrystallization of the PbO (100) seed layer formed during pyrolysis in sol-gel films, Ti content and excess Pb in the films, as

well as the orientation of substrates. In this work, PbTiO_3 buffer layers were chosen due to good lattice matching with PZT films, and the strong propensity for development of $\{001\}$ orientation. PbTiO_3 was prepared by a chemical solution deposition technique. The pyrolysis and crystallization steps of PbTiO_3 buffer layers deposition were investigated. Afterwards, PZT films were deposited on top of the PbTiO_3 buffer layers. The pyrolysis steps and the heating rate of crystallization by RTA were studied to obtain $\{001\}$ oriented films. The optimization of these films is described in Chapter 3.

The third goal of this research is to understand the ac field amplitude dependence of the dielectric constant and the piezoelectric coefficient. In particular, the dielectric and piezoelectric nonlinearities were studied to quantify the extrinsic and intrinsic contributions as a function of grain size, thickness, and film orientation. Of particular interest was developing methodologies to understand the spatial distribution of nonlinearities. This work is described in chapters 4 and 5.

The fourth goal of this work is to study the mechanical properties of PZT films by nanoindentation testing, as described in Chapter 6. Nanoindentation has high potential to measure the mechanical properties of films because this method provides high resolution, high sensitivity, and simplicity. Using nanoindentation, the reduced elastic modulus and the hardness were acquired to study the role of ferroelastic domain wall motion at high stress levels.

Finally, in order to pattern these films, dry etching was studied. For this purpose, a photoresist layer on the PZT thick films was patterned by photolithography and Ni was electroplated as a hard mask. Then the films were etched using an Inductively Coupled Plasma Reactive Ion Etcher (ICP-RIE) with a mixture of Ar and SF_6 gas. The variation of the etch rate with gas flow rate, source power, substrate holder power, operation pressure and the uniformity of etching were investigated, as described in Chapter 7.

1.2 Piezoelectricity

There are a variety of applications in which it is useful to be able to generate motion in miniaturized mechanical systems. While several approaches can be used to accomplish this, this thesis will concentrate on the use of piezoelectric actuation.^[1] Piezoelectrics are used in many different types of applications. For example, AlN piezoelectric films are now used in high frequency resonant structures (in the range of MHz to GHz) with good temperature stability for thin film bulk acoustic resonators (FBAR). Piezoelectric sensors do not require power to operate, although the associated electronics do. Therefore, piezoelectric MEMs are attractive for low power sensors. Energy harvesting has been implemented in thick films and bulk piezoelectric ceramics. Finally, the piezoelectric effect can provide large displacement with low drive voltages, low powers, and with low hysteresis. In many cases, flexural structures are used to provide the large amplitude actuation. Piezoelectric scale well as device size is reduced. The energy density is still high, even as sizes drop. Piezoelectric are compatible to CMOS and can potentially be processed on chip.^[1]

In piezoelectric MEMS, both the direct and converse piezoelectric effects are utilized. The significant parameters for the piezoelectric effect are the strain tensor x_i ($i = 1$ to 6), the stress tensor σ_i ($i = 1$ to 6), the electric field E_i ($i = 1$ to 3), and the electric displacement field D_i ($i = 1$ to 3). The direct piezoelectric effect (Equation 1-1) describes the fact that some materials develop a dielectric displacement that is linearly proportional to an applied mechanical stress.

$$D_i = \sum_k d_{ik} \sigma_k \quad \text{or} \quad D_i = \sum_k e_{ik} x_k \quad \text{Equation 1- 1}^{[1]}$$

$$x_i = \sum_k d_{ki} E_k \quad \text{or} \quad \sigma_i = -\sum_k e_{ki} E_k \quad \text{Equation 1- 2}[1]$$

In contrast, the converse piezoelectric (Equation 1-2) is the mechanical strain which is linearly proportional to an applied electric field. The direct piezoelectric effect is generally

employed in sensor applications while the converse piezoelectric effect is used in actuator applications.^[1, 2]

For most piezoelectric MEMS devices, $e_{31,f}$ provides the in-plane piezoelectric stress used to bend the structure under an applied electric field (the converse piezoelectric effect) or polarization as a function of bending strain (the direct effect). There is also a dilation of the film thickness that occurs simultaneously; that is described using the $d_{33,f}$ coefficient. Equations 1-3 to 1-5 show the $d_{33,f}$ and $e_{31,f}$ responses.^[3-6] Einstein notation is used, as is contracted matrix notation (where the third rank tensor d_{ijk} or e_{ijk} is shown with only two indices).^[1]

$$d_{33,f} = d_{33} - \frac{2s_{13}^E}{s_{11}^E + s_{12}^E} d_{31} \quad \text{Equation 1- 3}^{[1]}$$

$$\frac{Q_i}{A} = e_{ij} x_j \quad \text{Equation 1- 4}^{[1]}$$

$$e_{31,f} = \frac{d_{31}}{s_{11}^E + s_{12}^E} = e_{31} - \frac{c_{13}^E}{c_{33}^E} e_{33} \quad \text{Equation 1- 5}^{[1]}$$

Here, x is the strain, d and e are piezoelectric coefficients, E is the applied electric field, s and c are the compliance and stiffness elastic moduli, Q is charge, and A is area. There is also a higher order electromechanical coupling, electrostriction, that appears in all crystals, in which the mechanical deformation is proportional to the square of the applied electric field.^[6] Equation 1-6 and Equation 1-7 show the electrostrictive coefficient tensor.^[6, 7]

$$x_{ij} = M_{ijkl} E_k E_l \quad \text{Equation 1- 6}^{[6, 7]}$$

$$x_{ij} = Q_{ijkl} D_k D_l \quad \text{Equation 1- 7}^{[6, 7]}$$

1.2.1 Ferroelectric Materials

Large $e_{31,f}$ constants are desirable in both piezoelectric MEMS sensors and actuators. As has been described elsewhere, the largest $e_{31,f}$ constants known develop in ferroelectric films.^[8] Ferroelectrics have a *spontaneous polarization* that can be reoriented with an electric field as shown in Figure 1- 1. All poled ferroelectric materials are piezoelectric because they all have polar crystal structures. Many ferroelectric materials become paraelectric at high temperature as they transform to a higher symmetry crystal structure. The transition point from ferroelectric phase to paraelectric phase is defined as the Curie temperature (T_c).^[9, 10] Figure 1- 1 shows the characteristic hysteresis loop of ferroelectric materials.

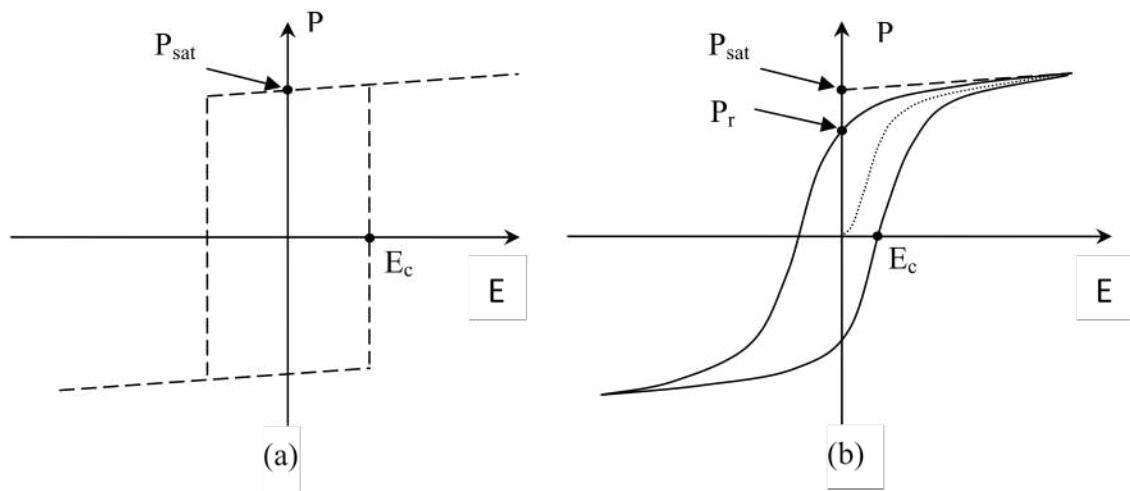


Figure 1- 1: A polarization – electric field hysteresis loop for a ferroelectric showing the coercive field (E_c), remanent polarization (P_r), and saturation polarization (P_{sat}) (a) Ideal single crystal case and (b) Polycrystalline case^[6]

1.2.1.1 Domain Structures

When a ferroelectric crystal is cooled, different regions will adopt different possible directions for the polarization in order to minimize the free energy. Each *domain* is a volume of

uniform (or nearly so) polarization. The boundaries separating domains are called *domain walls*.^[11] Figure 1- 2 represents the geometry of the polarization vectors in a poled rhombohedral perovskite in which the polarization vectors are 109° or 71° degrees apart. Different ferroelectric crystal structures have different number of possible polarization directions. Rhombohedral crystals from a cubic prototype group have 180° , 109° , and 71° domain walls. Tetragonal perovskites have 180° and 90° domain walls. Domain walls such as 109° , 90° , and 71° walls are referred to collectively as non- 180° domain walls. Figure 1- 3 illustrates some domain structures in ferroelectric materials.

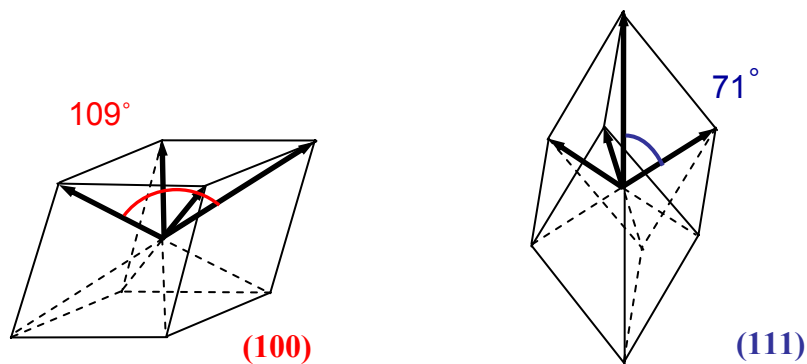


Figure 1- 2: A schematic showing the available polarization directions in two poled rhombohedral crystals of different orientations.^[6]

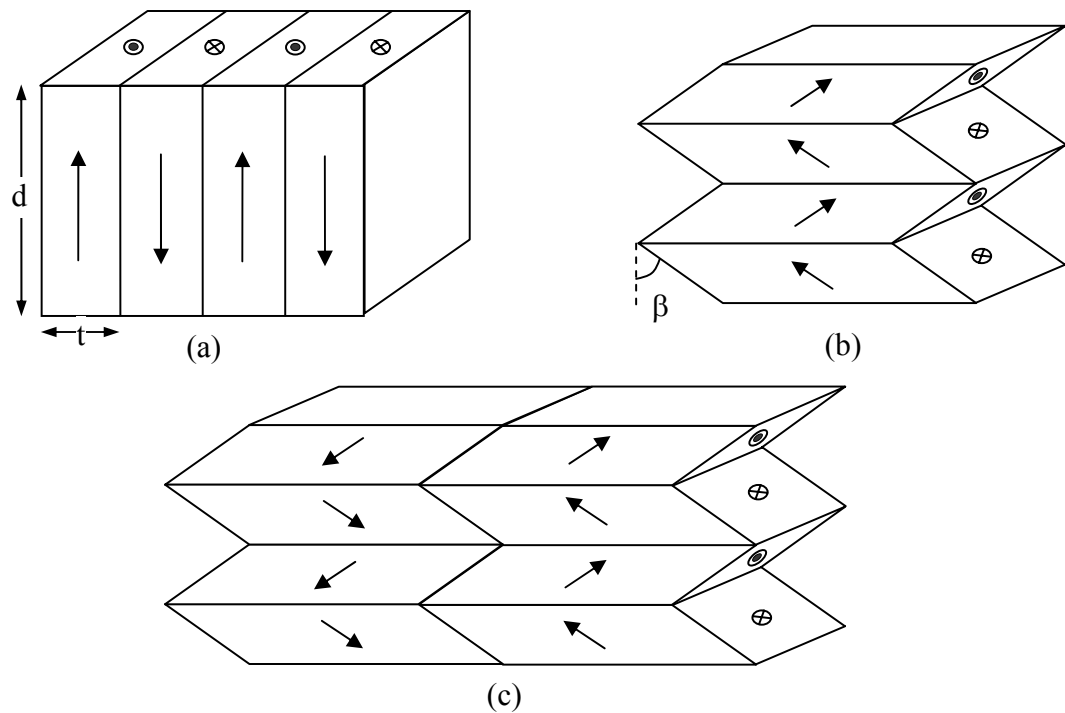


Figure 1- 3: Schematic showing domain walls in ferroelectric materials (a) 180° domain walls, (b) non- 180° domain walls, and (c) a mixture of 180° domain walls and non- 180° domain walls. ^[6]

1.2.1.2 Domain States in P-E Hysteresis Loop

Figure 1- 4 illustrates possible domain configurations at various points in a P-E hysteresis loop in an ideal ferroelectric crystal. Starting with an unpoled sample (point O), an appropriately oriented applied electric field can induce a perfectly poled state (point A). Typically, some reverse domains nucleate when the electric field is reduced to zero (point B). As the field is increased with the opposite polarity, domains with reversed polarization directions appear and grow (point B to point C). At $E < -E_c$ and $E > E_c$, large volumes of the sample begin to switch. Domains of the reverse polarization direction continue to grow (point D). Afterwards, a single domain state with reversed polarization direction may be achieved (point E). The material will

again show new domain nucleation with increasing electric fields (point F) followed by similar processes until saturation is reached at the original single domain state (point A).^[6]

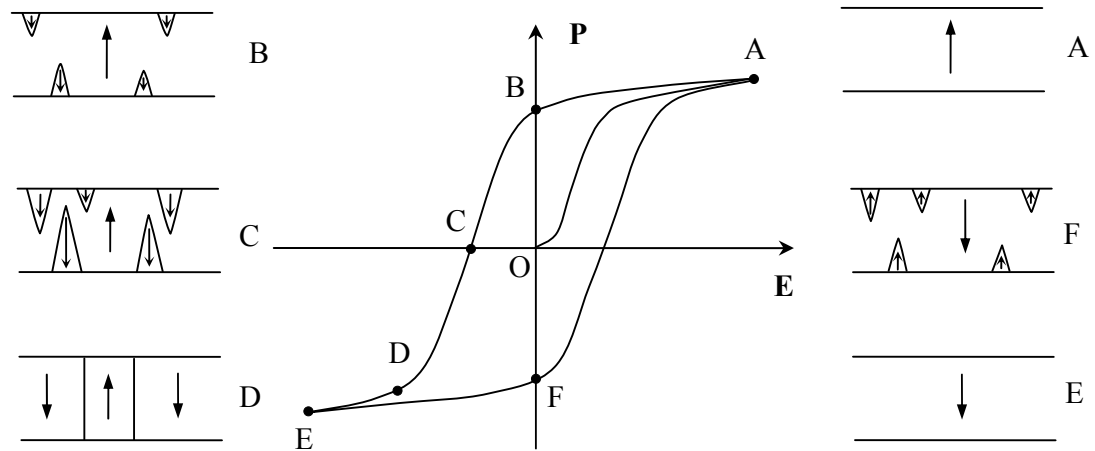


Figure 1- 4: The domain states in an ideal ferroelectric crystal at different electric fields in a polarization – electric field hysteresis loop. O = unpoled sample, A = perfectly poled sample in a single domain state, B and C = nucleation and growth of domains with opposite polarization direction, D = reverse oriented domains, E = perfectly single domain state with opposite polarization direction, and F = nucleation of reverse polarized domains.^[6]

1.3 PZT Solid Solution

Polycrystalline ferroelectric films are broadly used in non-volatile memory components,^[12, 13] microelectromechanical sensors and actuators,^[1] and capacitor applications.^[14] Of the available ferroelectric materials, the ones that are most widely exploited in MEMS are based on lead zirconate titanate (PZT) because of its high sensitivity in sensor applications and high output in actuator applications.^[1, 2]

The prototype crystal structure of PZT is the perovskite structure, as illustrated in Figure 1- 5. Above T_c , PZT is cubic. Below T_c , across the majority of the phase diagram, the crystal structure distorts to either a rhombohedral, monoclinic, or tetragonal phase depending on the

composition of PbZrO_3 and PbTiO_3 as shown in Figure 1- 6. When the structure distorts, the relative shift of the oxygen octahedra and the cations generates the electrical dipole moment in the ferroelectric phases.^[2, 15, 16] There are six possible orientations for the spontaneous polarization along the pseudocubic $\langle 001 \rangle$ and eight possible orientations along the pseudocubic $\langle 111 \rangle$ in the tetragonal and rhombohedral phases, respectively.^[2]

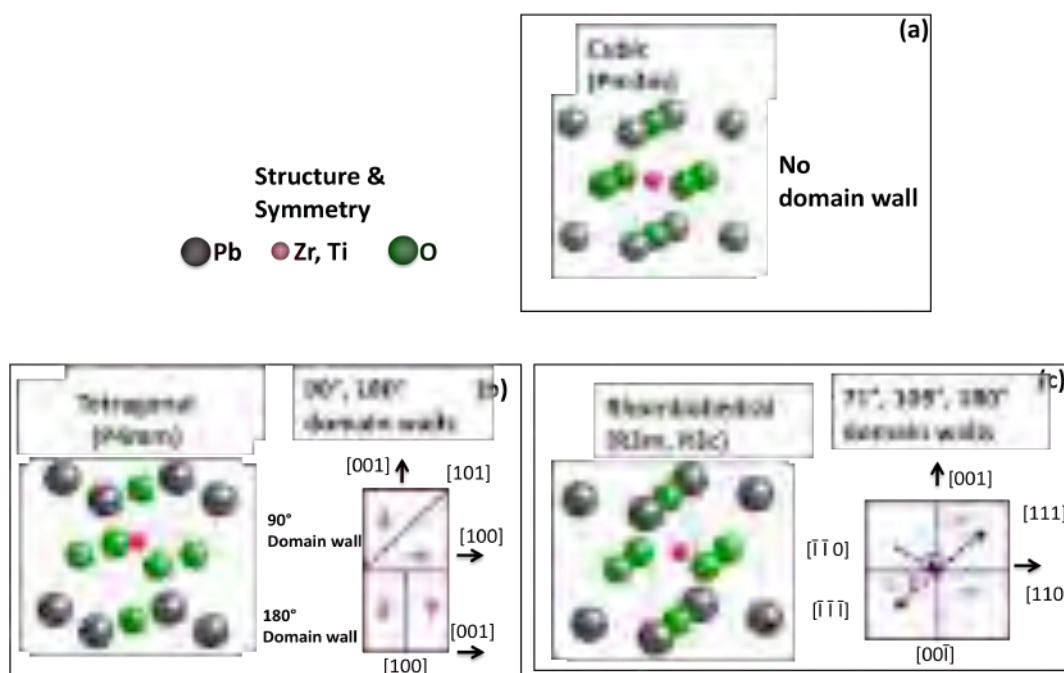


Figure 1- 5: PZT perovskite distortions and domains (a) cubic, above T_c no domains, (b) tetragonal, below T_c : 90° and 180° domain walls, and (c) rhombohedral below T_c 71°, 109°, and 180° domain walls, (Pm3m, P4mm, R3m, and R3c are the symmetry abbreviations. P = primitive lattice, R = rhombohedral lattice type, m = mirror plane, 3 and 4 = 3-fold and 4-fold rotations, c = glide plane parallel to 3.^[15]

The PZT phase diagram is shown in Figure 1- 6 (a). On the Ti-rich side of the phase diagram, the PZT structure is tetragonal and on much of the Zr-rich side, the structure is rhombohedrally distorted. The tetragonal and rhombohedral phases are separated by a morphotropic phase boundary (MPB). The ferroelectric and piezoelectric properties are strongly dependent on the composition and phase as shown in Figure 1- 6 (b). For robust piezoelectric

materials with large piezoelectric responses over a wide temperature range, a combination of an MPB with a high phase transition temperature is required.^[1, 15] In addition, domain wall motion is substantial at room temperature for PZT ceramics near the MPB. The superior piezoelectric properties of PZT ceramics near the MPB is thus due, in part, to the large extrinsic contributions to the properties.^[17]

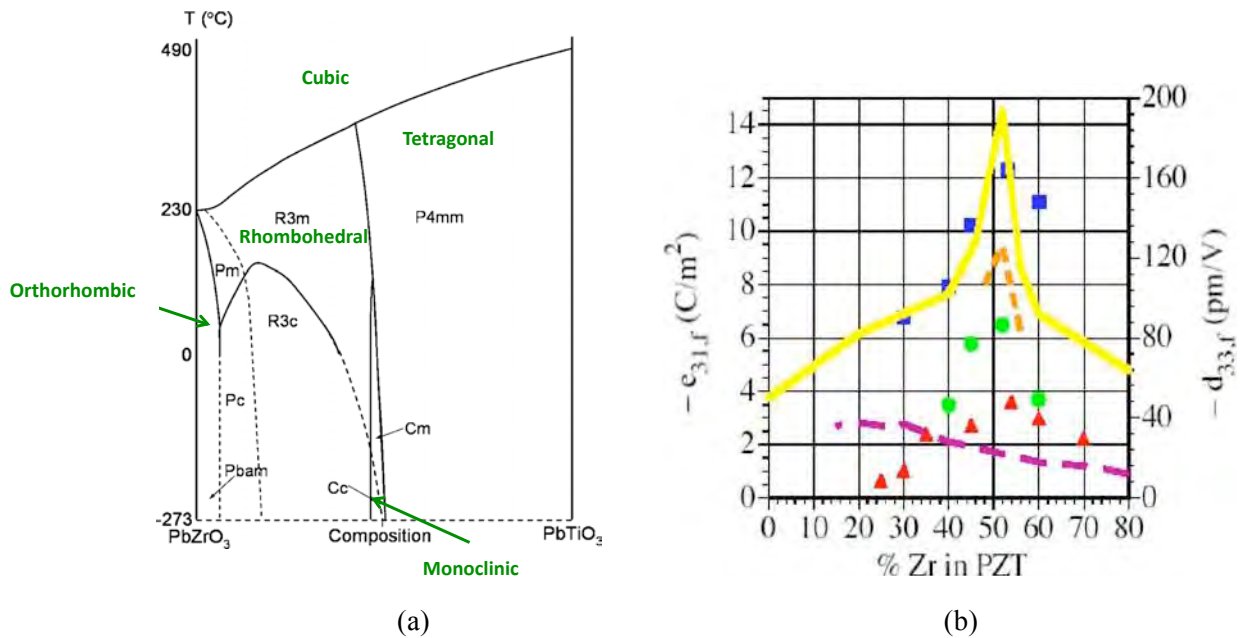


Figure 1- 6: (a) PZT phase diagram (Pm, R3m, P4mm, etc. are the symmetry abbreviations. Pm is a subgroup of R3m and Pbam, while Pc is a subgroup of Pm, Pbam, and R3c), (b and a = glide plane perpendicular to z axis, c= glide plane parallel to 3.^[15]), (b) Composition dependence of the relative piezoelectric response in PZT thin films^[1]

1.3.1 PZT Films

Generally, PZT films behave differently from bulk PZT ceramics. PZT films tend to have lower dielectric, ferroelectric, and piezoelectric properties because of substrate clamping, residual stresses, phase transformation stresses, grain size effects, and crystallographic orientation. The film is clamped to the substrate and it is not free to expand or contract in-plane in response to an applied electric field, resulting in the reduction of dielectric, ferroelectric, and

electromechanical responses. Residual stresses come from the high temperatures (e.g. 650-700°C) employed during the crystallization step. The difference in thermal expansion between the films and the substrates generates residual stresses at room temperature. The local stresses may reduce non-180° domain wall mobility.^[18] For this, and possibly other reasons, it is typically observed that the extrinsic contributions to the piezoelectric effect in ferroelectric films are limited.^[18, 19]

Additional differences between thin films and bulk ceramics arise from cracking and porosity problems. In chemical solution deposited films, cracking occurs due to shrinkage during heat-treatment steps and stresses, which arise from the thermal expansion coefficient mismatch between the PZT film and the substrate. Because films cannot contract in the plane of the substrate, volume changes during densification that cannot be accommodated by decreasing the thickness of the film lead to the development of tensile stresses in the film parallel to the interface with the substrate. In some cases, porosity is introduced to the films to overcome the cracking problems, but the porosity reduces the hardness and piezoelectric coefficient ($e_{ij,t}$) which governs the device performance in most MEMS structures.^[3, 19]

1.3.2 PZT Film Processing and Orientation Control for MEMS Applications

A wide variety of actuation mechanisms have been explored for microelectromechanical systems, including thermal, electrostatic, piezoelectric, or magnetostrictive approaches. Lead zirconate titanate, $\text{Pb}(\text{Zr}_{0.52}\text{Ti}_{0.48})\text{O}_3$, actuators are capable of large displacement, but require low driving voltages and powers. Moreover, many piezoelectric MEMS use PZT films due to their large displacements, fast response, and high sensitivity.^[1] As one example, recently it has been shown that rf MEMS switches using thin film PZT actuators have good temperature stability and driving voltages of about 5V. The series switch exhibited excellent isolation from DC up to 65

GHz with values better than 20 dB across the frequency band and as large as 70 dB below 1 GHz.^[20] For the switch actuator, the critical material property coefficient for low voltage, CMOS compatible operation is a high piezoelectric coefficient. The same PZT materials are also interesting for energy harvesting applications.^[21-24] In much the same way, in the energy harvesting application, it is essential to have high piezoelectric coupling coefficients, so that energy can be efficiently converted from mechanical motion to an electrical output.

The PZT films that are most widely utilized in MEMS are polycrystalline, with random orientation of the grains. The resulting $e_{31,f}$ coefficient is approximately -6 to -7 C/m² for a PZT 52/48 film. Higher piezoelectric coefficients (about -12 C/m²) can be achieved if significant $\{001\}$ texture is achieved, provided high remanent polarization values are retained.^[3, 25] For a randomly oriented film, a higher remanent polarization provides a higher piezoelectric coefficient. However, domain engineering can enhance the piezoelectric response due to polarization rotation even though the remanent polarization is smaller for orientations off the polar axis.^[26-28] Moreover, it has recently been shown that the piezoelectric response in films can be enhanced to -18 C/m² by decreasing Zr/Ti gradients.^[3, 25] Consequently, in optimizing thin films for piezoelectric MEMS applications, it is desirable to produce $\{100\}$ textured MPB films with small composition gradients.

There are many parameters that will influence texture in PZT films: pyrolysis temperature, post pyrolysis oxygen treatment, the RTA cycle, excess lead addition in the films, the presence of microcrystallization of the PbO (100) seed layer formed during pyrolysis in sol-gel films, high Ti content, as well as the orientation of substrates.^[29] In MEMS, where Si substrates are often desirable, and where elastic layers (often amorphous or polycrystalline) are needed for flexural structures, epitaxy cannot be routinely employed.

The pyrolysis steps remove the solvent and organic component in the films.^[30] Lakeman et al.^[31] reported that the films as-deposited were amorphous. At low heat treatment temperature,

the development of medium range order and the removal of solvent and the decomposition of residual organic species took place. The extent of inhomogeneity decreased with higher treatment temperatures, resulting in a uniform composition.^[31]

PbTiO₃ seed layer to control {001}-textured PZT films:

Several researchers reported that {001} PbTiO₃ can be used to template {001}-textured PZT films on (111) Pt/SiO₂/Si due to lattice parameter matching between PbTiO₃ and PZT.^[29] Calame and Murali^[25] achieved {100} orientated PZT films by using {100}-oriented PbTiO₃ seed layers with pyrolysis at 350°C for 20 sec and crystallization temperature at 650°C/sec in oxygen for 1 min by RTA (heating rate 15°C/sec). They used 10% Pb excess PZT solution for the first three layers and 30% Pb excess for last layer. Ledermann et al.^[3] deposited PZT on top of PbTiO₃ seed layers and pyrolyzed at 350°C for 15 sec. After four layers (first three layers with 10% Pb excess and last layer with 30% Pb excess), they thermally annealed at 650° for 1 min in oxygen by RTA (heating rate 15°C/sec). They reported that {100}-oriented PbTiO₃ seed layers enable {100}-textured PZT films from 1 μm to 4 μm in thickness. They also showed that {100} films near the MPB exhibit larger piezoelectric coefficients (up to -12.1 C/m²) than {111} films.^[3]

The same group also reported that a reduction in Zr/Ti gradients increases the piezoelectric constant. Ledermann et al. found that the composition of the individual crystallized layers had a Zr/Ti gradient with an amplitude of ±20% at the 53/47 MPB^[3] The fact that only a small volume of material is really at the morphotropic phase boundary degrades the properties. Consequently, Calame and Murali reported that a decrease in the Zr/Ti gradients increases $e_{31,f}$ and the dielectric constant to -18 C/m² and 1620, respectively.^[25]

Reaney et al. investigated how the pyrolysis temperature, the crystallization conditions (especially the heating rate), and post-pyrolysis oxygen treatment affect the film orientation.

They concluded that the lower temperature at 350°C favored (111) orientation, while the higher temperature as 420°C favored (100) orientation.^[32]

Heating rate during crystallization:

{001}-orientation tends to develop for slow heating rates while {111}-orientation prefers high heating rates during crystallization steps. It was hypothesized that the nucleation energy for the {001} PZT is lower than {111} PZT.^[29] Kalpat and Uchino^[29] found that (100) oriented PZT film can be prepared using heating rates less than 10°C/sec. It was found that (111) oriented PZT is preferred at heating rates above 60°C/sec, possibly because the higher rates do not provide as much time for nucleation.^[29] As a result, heterogeneous nucleation from the bottom electrode is favored at high heating rate.^[6, 19] Since Pt has a strong tendency to {111} orientation, and there is a good local structure match between {111} PZT and {111} Pt, this favors {111} oriented PZT films.^[29] Similarly, In PYbN-PT films, Gharb showed that slow heating rates (10°C/sec) favor {001} orientation of the films whereas higher heating rates (100°C/sec) favor (111) orientation.^[6] Moreover, Chen et al. suggested that (111) orientation is promoted by the formation of an intermetallic phase, Pt_{5.7}Pb, which forms when the local oxygen partial pressure is low. The lead platinide phase has an epitaxial relationship with both Pt (111) and PZT (111).^[33]

Substrates control orientation:

Substrates play an important role in controlling the orientation of the films. When there is a good structure match between the film and the substrate, the film orientation tends to follow the substrate orientation. Kushida et al. reported that PbTiO₃ films were fabricated on {001} SrTiO₃ single crystal disks, Pt-Si, and fused quartz. {001} oriented PbTiO₃ films showed a stronger c-axis orientation of the films on {001} SrTiO₃ than Pt-Si and fused quartz.^[34] The difference in domain populations is due, at least in part, to the different levels of residual stress

experienced by these films; tensile stresses favor a domain films, while compressive stresses favor c domain films.

1.4 Extrinsic and Intrinsic Contributions to the Piezoelectric Properties

The large piezoelectric response of PZT ceramics is comprised of both intrinsic and extrinsic contributions.^[18] The intrinsic piezoelectric response is associated with the lattice and corresponds to the average response of all single domains in the ceramic. The extrinsic piezoelectric response of bulk ceramics is primarily due to motion of non-180° domain walls or phase boundaries.^[1] Non-180° domain wall motion can be excited by electrical and mechanical fields, thus non-180° domain walls can contribute to both dielectric and piezoelectric properties. In contrast, 180° domain walls can be moved by electric fields, but not by uniform stresses. Figure 1- 7 illustrates the intrinsic and extrinsic contributions to piezoelectric.

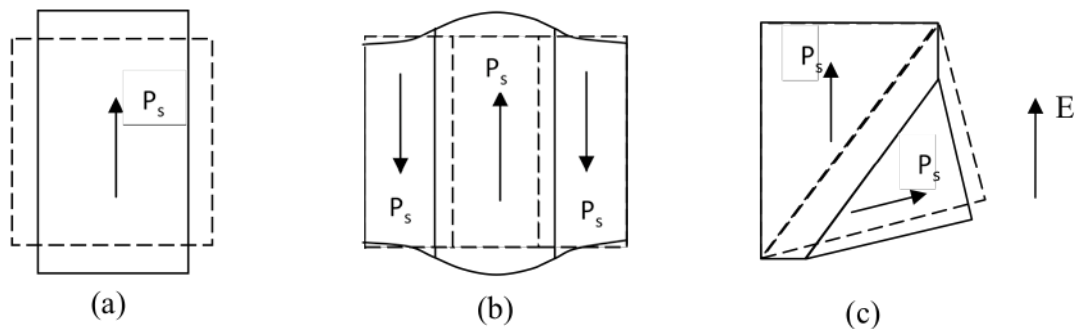


Figure 1- 7: (a) Intrinsic contribution from a single domain, (b) Extrinsic contribution from 180° domain wall motion, and (c) Extrinsic contribution from non-180° domain wall motion. The dashed lines represent the configuration before the application of the external electric fields.^[6]

Recently, Gharb and Trolier-McKinstry reported that 180° domain wall motion can also contribute to the extrinsic piezoelectric response in lead ytterbium niobate-lead titanate (PYbN-PT) films.^[6, 35] When the $d_{33,f}$ or $e_{31,f}$ coefficient is measured over a large area of electrode

covering many domain walls, the intrinsic piezoelectric response will be decreased by cancellation of the displacement in oppositely poled regions. In contrast, if d_{33} was measured with an electrode which is smaller than one domain, the intrinsic $|d_{33}|$ value will be maximum because there is no cancellation. Figure 1- 8 illustrates the schematic of the electrode size effects to the d_{33} amplitude. However, it is also important to remember that the extrinsic responses would be expected to be finite in the former case and zero in the case of measurement of a single domain.

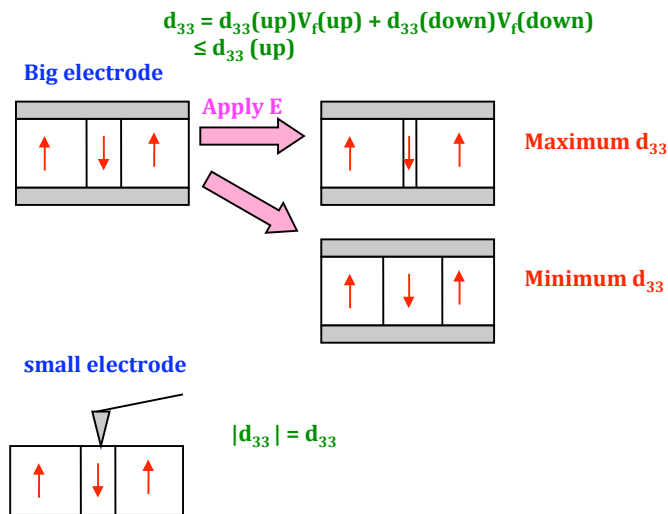


Figure 1- 8: Schematic of the electrode size effects to the amplitude of d_{33} in a system with only up and down polarization states. V_f is the volume fraction.

Gharb proposed that 180° domain wall motion could contribute to the piezoelectric coefficient as shown Figure 1- 9.^[6] At time A, the poled film shows a piezoelectric response defined as $d_{33,0}$. At time B, the remanent polarization is increased by an applied AC field parallel to P_r resulting in increasing the domain volume with this polarization direction. Therefore, the d_{33} is larger than $d_{33,0}$. At time C, the opposite effect happens if the domain state is not stable. The negative field shrinks the first domain and d_{33} is lower at time C than time A.

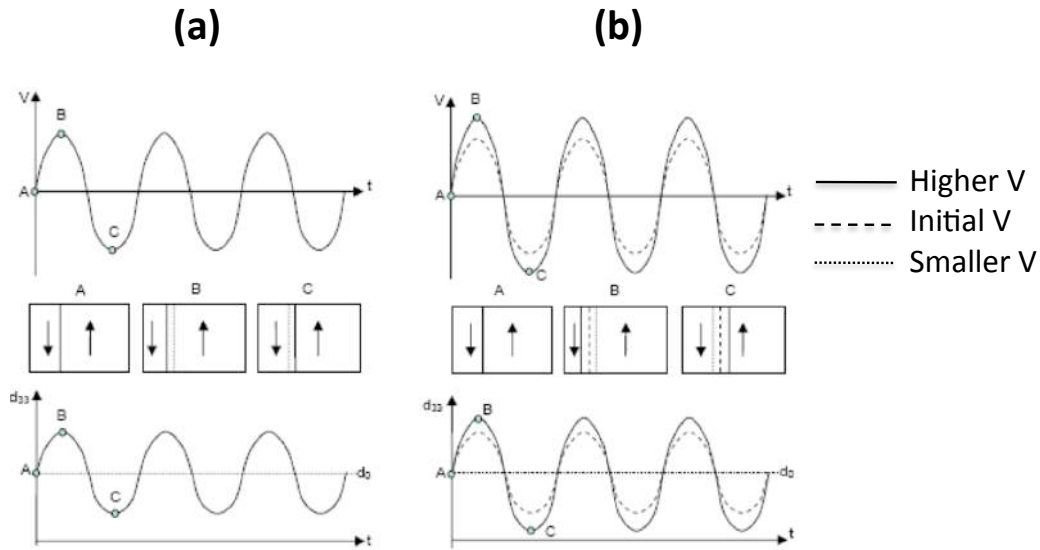


Figure 1- 9: (a) Schematic piezoelectric response of a poled ferroelectric crystal made of 2 domains with one 180° domain wall excited by ac voltage. (b) The piezoelectric response with higher amplitude excitation voltage.^[6]

Equation 1-8 shows the Rayleigh law.

$$x(E) = (d_{init} + \alpha_d E_0)E \pm \frac{\alpha_d}{2}(E_0^2 - E^2)$$

Equation 1- 8^[6, 35]

Using a Fourier expansion, Equation 1-8 is developed to Equation 1-9

$$x(E) = (d_{init} + \alpha_d E_0)E_0 \sin(\omega t) + \frac{4\alpha_d E_0^2}{3\pi} \cos(\omega t) + \frac{4\alpha_d E_0^2}{15\pi} \cos(3\omega t) - \frac{4\alpha_d E_0^2}{105\pi} \cos(5\omega t) + \dots$$

Equation 1- 9^[6, 35]

From Equation 1-9, it can be seen that only odd order harmonics of strain are present.

Equation 1-10 describes the case in which 180° domain wall motion contributes to the piezoelectric response. The reversible Rayleigh coefficient can be described as $d_{init} = d_0[1+(\beta+\beta'E_0)\sin\omega t]$ where β is a scaling factor. This can then be inserted into Equation 1-8 to produce:

$$\begin{aligned}
x(E) = & \beta d_0 E_0 + \beta d_0 E_0^2 + (d_0 + \alpha_d E_0) E_0 \sin(\omega t) + \frac{4\alpha_d E_0^2}{3\pi} \cos(\omega t) \\
& - \frac{\beta d_0 E_0 + \beta d_0 E_0^2}{2} \cos(2\omega t) + \frac{4\alpha_d E_0^2}{15\pi} \cos(3\omega t) \\
& - \frac{4\alpha_d E_0^2}{105\pi} \cos(5\omega t) + \dots
\end{aligned}$$

Equation 1- 10^[6, 35]

Equation 1-10 describes the time and field dependence of the response. It was concluded that a static term and a second order harmonic are created by the time and field dependent d_{init} . This is in contrast to a standard Rayleigh response, in which the second harmonic is absent as shown in Equation 1-9. Both domain wall motion and phase boundary motion could contribute to amplitude dependence of d_{init} . Thus, it is possible that 180° domain wall motion can contribute to the d_{33} .^[6, 35]

Dynamic poling will affect any property that relies on the remanent polarization. Hence, the dielectric constant should not show a domain wall motion-induced second harmonic response. Consequently, measurements of the magnitude of the second harmonic dielectric and piezoelectric response allow the relevance of dynamic poling model to a particular sample to be assessed.^[35, 36]

Landau-Devonshire phenomenological theory has been used to suggest that domain wall contributions in MPB-PZT account for more than half of the room temperature dielectric and piezoelectric responses.^[37, 38] The ability to understand the nonlinear properties is significant in predicting the behavior of devices.^[39]

There are several methods used to distinguish between intrinsic and extrinsic contributions: frequency dispersion in the dielectric or piezoelectric constants, property measurements near 0 K (where domain wall motion is frozen out), and field dependence in the properties.^[30, 37] In some high drive applications, the extrinsic contribution is not desirable

because it is nonlinear, hysteretic, and dispersive. However, the domain wall contributions significantly increase the net piezoelectric response of bulk ceramics, and so are desirable for many sensors and actuators. The extrinsic contribution is dependent on composition, crystal structure, dopants, and microstructure. The intrinsic response in thin films depends on the misfit strain and substrate clamping, as well as to the grain size and domain configuration.^[4]

Thus, among the factors that influence the observed piezoelectric response in thin films are:

Film orientation and phase: The intrinsic piezoelectric coefficients are a function of the crystallographic orientation. When rhombohedral or MPB PZT films are poled and driven along the crystallographic [001], they have extremely high piezoelectric coefficients, coupled with low hysteresis in the response.^[1] Wada and Tsurumi^[26] describe this as domain engineering. It has been reported that rhombohedral PZT films with the spontaneous polarization along $\langle 111 \rangle$ had the largest piezoelectric response measured along [001]. In contrast, films embedded deep in a tetragonal phase field have the spontaneous polarization along $\langle 001 \rangle$ and the largest piezoelectric response is measured along [001]. This behavior is true for some materials such as $\text{Pb}(\text{Zr}, \text{Ti})\text{O}_3$, BaTiO_3 , PMN-PT, and PZN-PT.^[40] Equation 1-11 and 1.12 show the details of d_{33} in case of rhombohedral and tetragonal phase.

Rhombohedral 3m group:

$$d_{33}^{r*}(\theta, \phi) = d_{15}^r \cos \theta \sin^2 \theta - d_{22}^r \sin^3 \theta \cos 3\phi + d_{31}^r \sin^2 \theta \cos \theta + d_{33}^r \cos^3 \theta \quad \text{Equation 1- 11}^{[40]}$$

Tetragonal 4mm group:

$$d_{33}^{t*}(\theta) = \cos \theta (d_{15}^t \sin^2 \theta + d_{31}^t \sin^3 \theta + d_{33}^t \cos^2 \theta) \quad \text{Equation 1- 12}^{[40]}$$

BaTiO_3 is good example to show piezoelectric anisotropy and the importance of proximity to a phase transition, as shown in Figure 1- 10 (a). Figure 1- 10 (b) illustrates how

orientation dependence changes the piezoelectric coefficient in the case of rhombohedral BaTiO₃ (calculated using Equation 1-12).

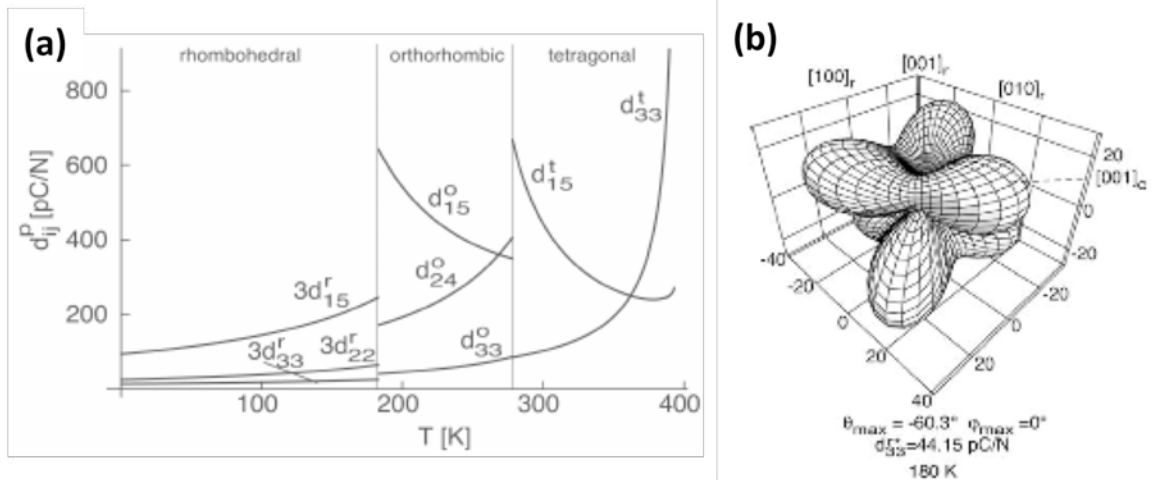


Figure 1- 10: (a) Piezoelectric coefficients as a function of temperature in all three ferroelectric phases of BaTiO₃ predicted by LGD theory. (b) Orientation dependence of $d_{33}^*(\theta)$ in the rhombohedral phase of BaTiO₃ at 180K. The $\langle 001 \rangle$ direction shows a higher d_{33} .^[40]

In Figure 1- 11 (a), it is shown for PZT at the MPB (where the polarization changes direction from the $[111]$ rhombohedral to $[001]$ tetragonal) that d_{15} can be used to increase d_{33} for some orientations. As can be seen in Figure 1- 11 (b), the piezoelectric coefficient is maximum at the compositions close to MPB. Figure 1- 11 (c) and (d) show the orientation dependence of piezoelectric coefficient for the rhombohedral side of MPB in PZT; it can be seen that the $[001]$ orientation has the highest piezoelectric coefficient.^[40]

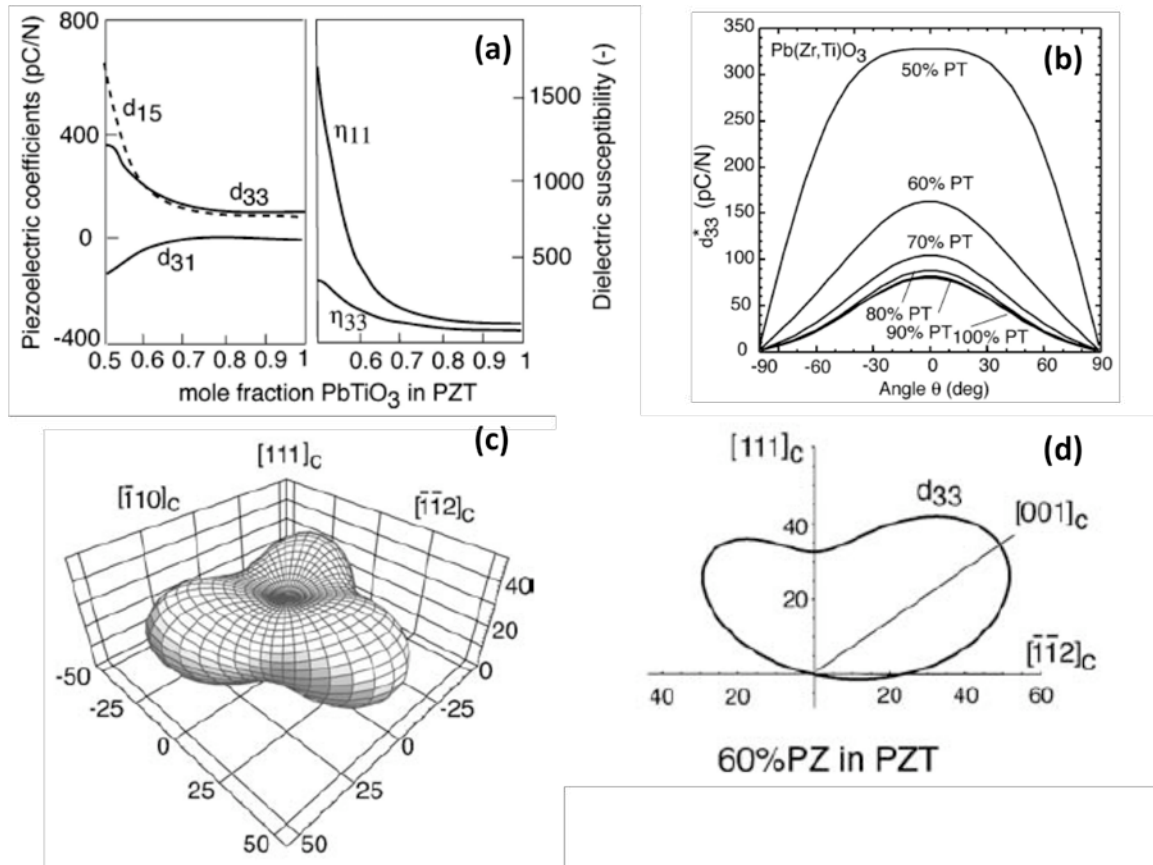


Figure 1- 11: Piezoelectric coefficient dependence of composition and orientation (a) Piezoelectric coefficient and dielectric susceptibilities in PZT crystals, (b) Orientation dependence of piezoelectric coefficient for PZT at room temperature as a function of PbTiO_3 concentration, (c) Orientation dependence of piezoelectric coefficient for rhombohedral PZT, and (d) A cross section of orientation dependence of piezoelectric coefficient for rhombohedral PZT from (c).^[40]

- Composition and phase:** There is some discrepancy in the literature regarding the importance of phase on the degree of domain wall motion. It was reported that films at the morphotropic phase boundary exhibit similar nonlinearity regardless of orientation.^[4, 26-28, 41] It has also been reported that tetragonal PZT films show less non- 180° domain wall motions than rhombohedral or MPB PZT films.^[39] In contrast, others claim larger amounts of domain wall motion in tetragonal films.^[42] It is not clear whether these differences result from differences in film quality.

- **Film thickness and microstructure:** Xu et al. reported that thinner films with smaller grain sizes show reduced non-180° domain wall contributions to the properties. Thick films (>5 μm) with large grain size exhibit domain wall contributions closer to those observed in bulk materials. They reported that the ferroelastic domain wall motion may be limited because of clamping by the substrate.^[4, 17] During cooling, the domain state is influenced substantially by the stress. When perovskite structured thin films are exposed to in-plane tensile stresses during cooling, they tend to have polar vectors parallel to the substrate. In contrast, when they are exposed to compressive stress, they tend to have polar components perpendicular to the substrate.^[1, 29] Kholkin also showed that in thick PZT films (~ 7-8 μm) 180° domain walls are more mobile than in thin PZT films (~0.25-0.4 μm).^[39]

- **Doping:** Soft PZT ceramics (donor doped) shows higher extrinsic contribution from the motion of domain walls than hard PZT ceramics (acceptor doped). Even low electric fields (about 0.1 kV/cm) can move domain walls in soft PZT ceramics while in hard PZT domain wall motion requires a higher threshold field as a result of the pinning effects from defects.^[39]

1.5 Rayleigh Law

In ferroelectrics, nonlinearity in the strain response to an applied electric field is dominated by domain wall or phase boundary motion. That is, in many cases, the electrostrictive contributions to the strain response are smaller than the domain-wall-induced nonlinearities. Under these circumstances, it is often found that the simplest link between the field dependence of the piezoelectric response and the observed hysteresis is through the Rayleigh law. Rayleigh – like behavior results when the planar domain walls in the material must move through a rough potential energy landscape (Figure 1- 12) that results in some pinning of the domain wall motion.

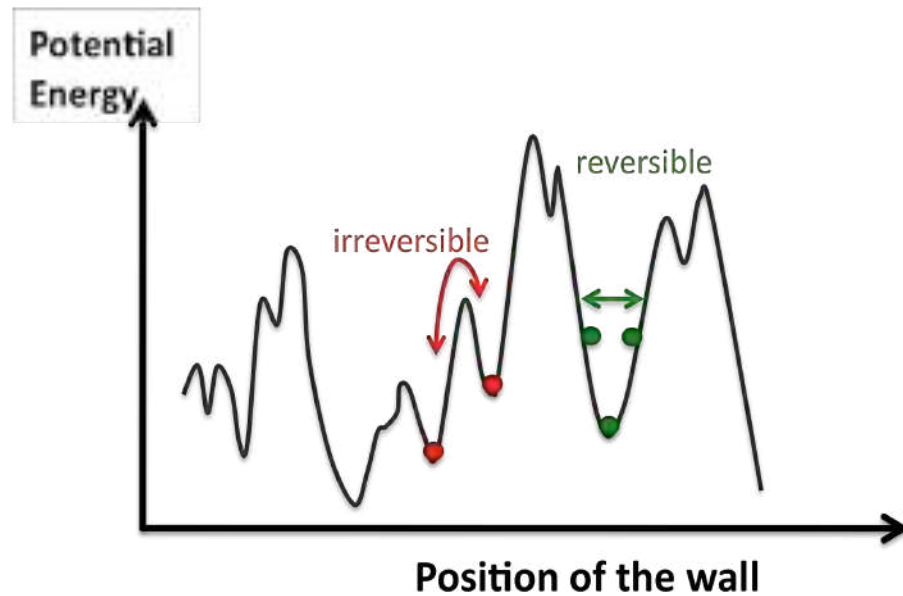


Figure 1- 12: A schematic showing the potential energy landscape for a moving domain wall as a function of position. For an ac electric field, there are the two possible types of domain wall motions: reversible and irreversible domain wall motions^[6]

The Rayleigh law is shown in Equations 1-13 and 1-14 for the dielectric constant and piezoelectric coefficient, respectively. Under sub-switching ac field excitation, the measured properties often increase linearly as a function of the amplitude of the field, E_0 .

$$\varepsilon = \varepsilon_{init} + \alpha E_0 \quad \text{Equation 1- 13}$$

$$d = d_{init} + \alpha E_0 \quad \text{Equation 1- 14}$$

ε_{init} and d_{init} include both the intrinsic contributions to the properties as well as a component due to reversible boundary motion. αE_0 is due to irreversible domain wall or phase boundary displacement. The Rayleigh law describes the situation that arises when there is a random distribution of potential wells that interact with the mobile interfaces. Reversible interface motion occurs around a local equilibrium position for the walls, while irreversible motion describes displacement of the interface from one potential energy well to another.

Moreover, the Rayleigh law predicts the development of odd order harmonics of strain and polarization.^[6]

Taylor and Damjanovic reported that about 21% of the total measured permittivity is due to irreversible domain wall displacement for a 1.3 μm thick PZT 45/55 film at $E_0 = 3 \text{ MV/m}$.^[43] Soft PZT ceramics show much higher nonlinearity than hard PZT as evidenced by the higher ratio of irreversible to reversible Rayleigh parameters.^[30] The dielectric $\alpha/\epsilon_{\text{init}}$ in films is believed to be lower than in bulk ceramics because of the small grain sizes, higher defect concentrations, and the lower concentration of mobile interfaces.^[30]

Xu et al.^[17] also showed different piezoelectric nonlinearities for films of different thicknesses. 1.5 μm PZT films showed little change in d_{33} as the applied AC field increased to 10 kV/cm. Above that field, only a small increase in the effective d_{33} was measured. In contrast, for 6.7 μm thick films, the effective d_{33} increased much more rapidly with AC fields above 4 kV/cm.^[17] The thicker film has less severe domain wall pinning.^[17]

1.6 Piezoelectric Force Microscopy (PFM)

While Rayleigh or Preisach descriptions are widely used to describe the collective behavior of many domain walls responding to applied fields, there is less information available on how this response develops locally. Consequently, one of the goals of this thesis was to begin to investigate local variations in domain wall mobility. Of the available techniques, piezoelectric Force Microscopy (PFM) is widely employed for characterization of ferroelectric materials due to the local measurements of electromechanical properties.^[8] The advent of PFM of capacitor structures^[44] allows real space probing of domain structures and polarization switching in active devices.^[45] Combined PFM and current studies of biased devices^[46, 47] allowed real space insight into in-situ device operation. Stolichnov et al. ^[48] have demonstrated that switching in capacitors

often occurs simultaneously across clusters of several grains, indicative of strong grain-grain coupling. This agrees with the observation that domain structures are often correlated across grain boundaries, presumably due to long range elastic and dipole interaction^[9] as well as with earlier reports on correlated switching via electron microscopy studied.^[49] Despite this progress, the polarization switching in the polycrystalline capacitors is relatively poorly understood, a limitation stemming from the fundamental resolution limitations on PFM imaging in capacitor and top electrode mediated strain effects on PFM imaging.^[50] In this research, polarization switching was studied in polycrystalline PZT capacitors using Switching spectroscopy PFM (SS-PFM).^[51, 52] SS-PFM is based on the acquisition of electromechanical hysteresis loops^[53, 54] on a closely spaced square grid. Subsequent analysis allows extraction of parameters such as coercive and nucleation bias, remanent and switchable response, and effective work of switching.^[55, 56] The details of each parameter will be described in Figure 2- 14.

The principle of the PFM method is to detect the response of piezoelectric materials under application of an ac electric field due to the converse piezoelectric effect as in Equation 1- 15.

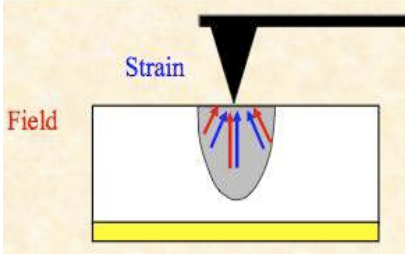
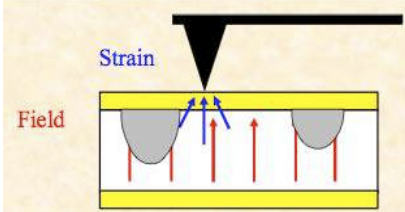
$$\Delta Z = d_{33}V \quad \text{Equation 1- 15}$$

where d_{33} is the longitudinal piezoelectric coefficient. The ΔZ is referred to as the out of plane or vertical PFM measurement. The magnitude and the phase of piezoelectric coefficient d_{33} depend on the ferroelectric polarization and polarization orientation, respectively. The resolution of PFM depends on the geometry of the sample. In this work, the resolution of PFM depends on the thickness of the top electrode and the thickness of the film. Kalinin et al. reported that the signal generation area in PFM is determined by the total thickness of the PZT structures with top electrodes. Thin top electrode is usually much thinner than the PZT film, resulting in a best-case PFM resolution of $0.2 * \text{PZT thickness}$.^[50]

In macroscopic systems, a statistical approach based on a Preisach model^[57] is often employed to describe the global response by providing a 2D distribution function of built in and coercive fields. Of particular interest is being able to map this distribution function onto real structures in the sample. Recently, magnetic force microscopy has been employed to probe the behavior of individual magnetic nanowires interacting through dipolar forces, and to construct a Preisach distribution from field dependent MFM images.^[58] Likewise, speckle microscopy measurements have been used to examine the spatial dependence of switching of magnetic memory material,^[59] allowing a direct link to statistical physics models.^[60] In ferroelectric materials, PFM observations of the fractal geometry of the domain wall and its evolution with thickness allowed a link to be established between statistical physics models with experimentally observed static wall geometries.^[61] PFM has also been used to image the deterministic energy landscape for nucleation in the highly localized SPM tip field, reconstruct the random field and random bond disorder in ferroelectric materials,^[62] and image individual defect centers on bare surfaces. PFM imaging of capacitor structures^[44] was used to visualize the nucleation sites in the films,^[63] and to probe the interplay the nucleation and wall motion.^[64]

Table 1- 1 compares two cases for PFM measurements: with and without a top electrode.^[8, 65, 66] In the case of PFM measurements without a top electrode, the ac field is applied between the PFM tip and the bottom electrode. The instrument detects the local deformation caused by the ac field.^[8] For PFM measurement with a top electrode, the ac field is applied across the top and bottom electrodes, the tip only detects the deformation from piezoelectricity.

Table 1- 1: Advantages and disadvantages of PFM measurement without and with a top electrode^[65, 66]

Method	Advantages	Disadvantages
<p data-bbox="285 443 618 470">PFM without a top electrode</p> 	<ul style="list-style-type: none"> • High lateral resolution • Correlation between domain patterns and microstructure • Analysis of domain wall structure and its interaction with microstructural features 	<ul style="list-style-type: none"> • Highly inhomogeneous electric field • Possible effect of surface contamination • Difficult to quantify absolute magnitudes of piezoelectric response • Asymmetric boundary conditions
<p data-bbox="285 800 581 827">PFM with a top electrode</p> 	<ul style="list-style-type: none"> • Homogeneous electric field • No electrostatic contribution • Quantitative characterization 	<ul style="list-style-type: none"> • Detrimental effect of top electrode on imaging resolution • Wafer flexure influences magnitude of apparent piezoelectric responses

Chapter 2

Experimental Procedures

This chapter describes the processing of $\text{Pb}(\text{Zr}_{0.52}\text{Ti}_{0.48})\text{O}_3$ and $\text{Pb}(\text{Zr}_{0.30}\text{Ti}_{0.70})\text{O}_3$ thin films, the characterization of their properties, and the deep reactive ion etching processes used to pattern the films. Several types of PZT thin films were prepared: mixed {001} and {111} orientation, {001}-textured films on Si, and {001}-textured films on SrRuO_3 coated single crystal SrTiO_3 . The processing used for each of these will be discussed. Characterization of the resulting films included measurement of thickness, morphology, dielectric permittivity, dielectric nonlinearity, the polarization – electric field (P-E) hysteresis loop, piezoelectric coefficients, piezoelectric nonlinearity, Switching Spectroscopy Piezoelectric Force Microscopy (SS-PFM), first order reversal curve (FORC), and nanoindentation.

2.1 Chemical Solution Deposition of PZT Films

There are several techniques that are routinely used to prepare PZT films: sputtering, screen printing, metal organic chemical vapor deposition (MOCVD), chemical solution deposition (CSD), and pulsed-laser ablation.^[67] The lead zirconate titanate thin films used in this research were prepared using a chemical solution deposition process described by Wolf and Trolrier-McKinstry.^[18] This technique was chosen due to the possibility of precise compositional control, good homogeneity, and uniformity over a large area.^[6, 68, 69] The thickness variation

across a 4-inch wafer is typically less than 3%.^[2] It has been reported that the films are thicker in the middle than near the edges.^[2, 18, 70]

It was found in early work that films prepared using a direct reproduction of the process reported by Wolf resulted in incorporation of porosity at each crystallization interface. Thus, first efforts were directed towards the production of denser films. This was achieved by modifying the pyrolysis and crystallization steps.

Once dense PZT films were achieved, {001}-textured PZT films were developed to obtain a larger transverse piezoelectric response ($e_{31,f}$). In particular, the intent was to prepare {001} oriented $\text{Pb}(\text{Zr}_{0.52}\text{Ti}_{0.48})\text{O}_3$ films on Si substrates. There are many ways to control PZT film orientation: tailoring the processing parameters during growth and crystallization, varying the crystallization step, and the use of oriented layers.^[29] The thrust of this work is to develop a means of reproducibly growing well-oriented PZT films with high piezoelectric coefficients on large area substrates for MEMS actuators and energy harvesting systems.

2.1.1 Solution Preparation

Figure 2- 1 shows the flow diagram for 10% Pb-excess $\text{Pb}(\text{Zr}_{0.52}\text{Ti}_{0.48})\text{O}_3$ solution preparation described by Wolf and Trolier-McKinstry.^[18] Zirconium (IV) propoxide solution, $\text{Zr}(\text{OCH}_2\text{CH}_2\text{CH}_3)_4$ 70 wt. % in 1-propanol (Sigma-Aldrich, Inc.), and titanium (IV) propoxide, $\text{Ti}[\text{OCH}(\text{CH}_3)_2]_4$ 97% (Sigma-Aldrich, Inc.) were dissolved in 2-methoxyethanol, $\text{CH}_3\text{OCH}_2\text{CH}_2\text{OH}$ CHROMASOLV[®], for HPLC, $\geq 99.9\%$ (Sigma-Aldrich, Inc.) and stirred at room temperature. In a separate container, lead acetate trihydrate, $\text{Pb}(\text{CH}_3\text{CO}_2)_2 \cdot 3\text{H}_2\text{O}$ 99.999% on a trace metals basis (Sigma-Aldrich, Inc.) was dissolved in 2-methoxyethanol and vacuum distilled at 120°C. After that, the mixture of Zr and Ti precursors were added to the Pb flask and the entire solution was refluxed for 2 hours at 120°C. Finally, the solution was vacuum distilled

and 22.5% volume of acetylacetone, $\text{CH}_3\text{COCH}_2\text{COCH}_3$ ReagentPlus[®], $\geq 99\%$ (Sigma-Aldrich, Inc.) was added to the PZT solution. Typically, the PZT solution was controlled to be 0.75 M.^[18]

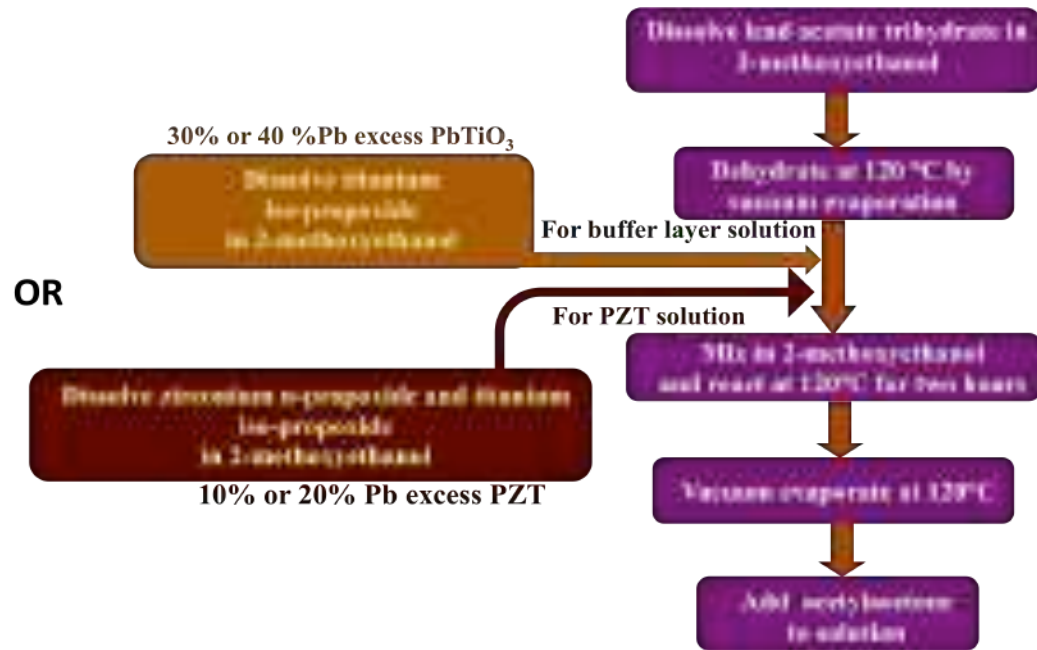


Figure 2- 1: Flow chart for preparation of 10% - 20 % Pb-excess PZT solution or 30 - 40% Pb-excess PbTiO_3 solutions

2.1.2 PZT Film Deposition

Figure 2- 2 (a) shows the flow diagram for PZT thick film deposition reported elsewhere.^[18] The substrates used were (111) Pt (1500 Å)/ Ti (200 Å) / SiO_2 /(100) Si from Nova Electronic Materials, Inc. First, the wafer surface was dehydrated by placing it sequentially on hot plates at 350° and 500°C for 1 min each. It was then exposed to a Rapid Thermal Annealing (RTA) step at 700°C for 1 min with a heating rate of 7°C/s. Immediately before deposition, 7% volume of acetic acid, $\text{CH}_3\text{CO}_2\text{H}$ CS reagent, $\geq 99.7\%$ (Sigma-Aldrich, Inc.) was added to the PZT solution for stabilization purposes.^[6] The solution was then spun onto the wafer at 1500 rpm

for 30 s, pyrolyzed at 350°C and 500°C for 1 min and 2 min respectively. For the first pyrolysis, the substrate was placed on 1 mm thick aluminum plate positioned above the hot plate about 1 cm. For the second pyrolysis step at 500°C, a 1 mm thick aluminum plate was positioned parallel to and 3.5 mm above the film surface to enhance heating. Afterwards, PZT films were crystallized at 700°C for 1 min by RTA. The RTA profile is shown in Figure 2- 3 (a). The steps were repeated until the desired thickness was achieved. Each spin step produces a layer of about 200 nm thickness for a 0.75 M solution.^[18]

In order to obtain dense and crack free PZT films, the pyrolysis and crystallization conditions were modified as shown in Figure 2- 2(b) and Figure 2- 3(b). First, the wafer was dehydrated by placing it sequentially on hot plates at 250°C and 400°C for 1 min each, and then exposing it to an RTA step at 700°C for 1 min with a heating rate of 4°C/s. Before spinning, 7% volume of acetic acid was added to the PZT solution for stabilization purposes. The solution was spun onto the wafer at 1500 rpm for 30 sec, pyrolyzed at 250°C and 400°C for 1 min each, and crystallized at 700°C for 1 min by RTA. In order to enhance the homogeneity of the hot plate temperature, especially for 4-6 inch wafers, 1 cm thick stainless steel plates were placed on top of two hot plates for the pyrolysis steps. It was found that the majority of the cracking and porosity development occurred during the initial heat treatment step. Some of this could be avoided by reducing the second pyrolysis temperature from 500°C to 400°C. In addition, as shown in Figure 2- 3 (b), adding a short temperature stabilization step at 500°C and reducing the heating rate in the RTA profile from 7°C/s to 3°C/s reduced cracking in the denser films. The steps were repeated until the desired thickness was achieved. Each spin step produces a layer of about 200 nm thickness for a solution molarity of 0.75 M.

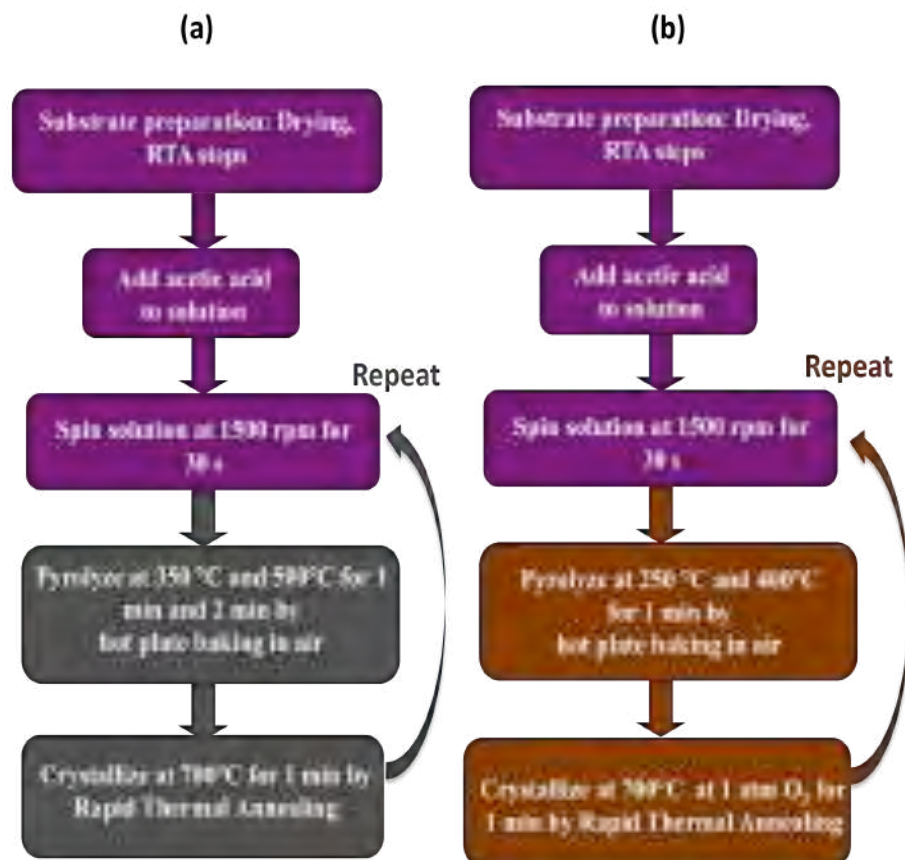


Figure 2- 2: (a) PZT film deposition used by Wolf and Trolier-McKinstry^[18] which was found to produce a layer of porosity for each RTA step, (b) Modified process for dense PZT films without strong levels of texture

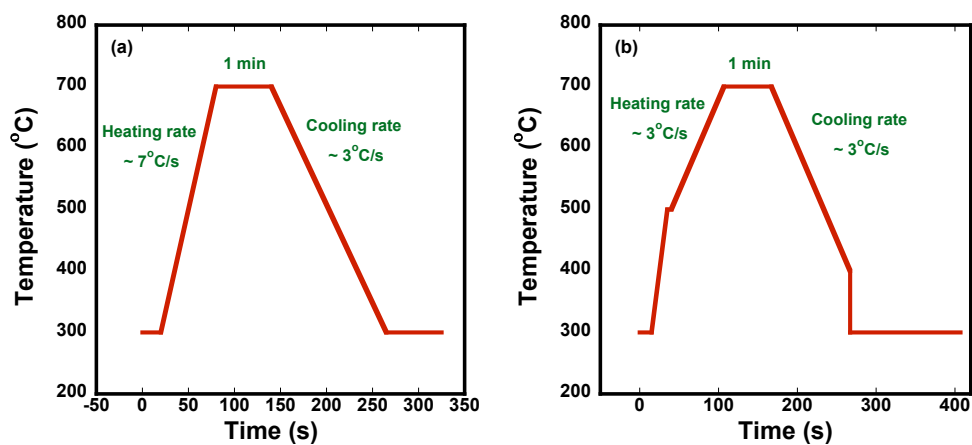


Figure 2- 3: Rapid Thermal Annealing (RTA) profile (a) previous condition^[18] (b) modified condition for dense PZT films

2.1.3 Processing of {001} Oriented PZT Films

In order to develop {001}-textured PZT films, PbTiO_3 buffer layers were chosen due to good lattice matching with PZT films, and the strong propensity for development of {001} orientation.^[29] The flow diagram for 30-40% Pb-excess PbTiO_3 solution preparation is shown in Figure 2- 1. The steps were comparable to those employed for PZT solutions.

2.1.3.1 PbTiO_3 Solution Preparation for {001}-Textured PZT Films

Figure 2- 1 shows the flow diagram for 30% and 40% Pb-excess PbTiO_3 solution preparation. Titanium (IV) propoxide was dissolved in 2-methoxyethanol and stirred at room temperature. In a separate container, lead acetate trihydrate was dissolved in 2-methoxyethanol and vacuum distilled at 120°C. After that, the Ti precursor was added to the Pb flask and the entire solution was refluxed for 2 hours at 120°C. Finally, the solution was vacuum distilled and 22.5% volume of acetylacetone was added. Typically, the PbTiO_3 solution was controlled to be 0.17 M.^[18]

2.1.3.2 PbTiO_3 Buffer Layer Deposition

Figure 2- 4 (a) shows the flow diagram for PbTiO_3 buffer layer deposition. The substrates used for this part were (111) Pt/ Ti/ SiO_2 / (100) Si from either Nova Electronic Materials, Inc. or Ramtron. First, the wafer surface was dehydrated by placing it sequentially on hot plates at 250°C and 400°C for 1 min each. It was then treated to an RTA step at 700°C for 1 min. Before spinning, 7% volume of acetic acid was added to the PbTiO_3 solution for stabilization purposes. The solution was spun onto the wafer at 1500 rpm for 30 s, pyrolyzed, and crystallized by RTA. Two pyrolysis steps were used. First, the film was pyrolyzed at 250°C for

1 min. The temperature of the second pyrolysis step was set to either 350°C or 400°C for 1 min. Afterwards, three crystallization temperatures were studied, with the temperatures chosen based on previous research^[29]: 535°C, 550°C, 580°C. The details of the experimental plan are shown in Table 2- 1.

Table 2- 1: Experimental plan of PbTiO₃ buffer layer condition study

Experiment	Pyrolysis Condition	Crystallization Condition
1	250°C + 350°C for 1 min	530°C
2	250°C + 350°C for 1 min	550°C
3	250°C + 350°C for 1 min	580°C
4	250°C + 400°C for 1 min	530°C
5	250°C + 400°C for 1 min	550°C
6	250°C + 400°C for 1 min	580°C

Once the optimized condition to obtain {001} PbTiO₃ was achieved, one PbTiO₃ buffer layer was spun on the substrate followed by PZT deposition. The PbTiO₃ film thickness is about 30 nm.

2.1.3.3 Deposition of {001}-Textured PZT Films

The PZT solution for {001}-textured PZT films was 0.4 M with 10 % Pb-excess. The pyrolysis conditions and heating rate for the crystallization step were then varied in an attempt to optimize the level of {001} orientation. Figure 2- 4 (b) shows the flow diagram of the optimization process for {001} PZT films. First, the wafer with the PbTiO₃ buffer layer was dehydrated by exposing it to an RTA step at 580°C for 1 min. Before spinning, 7% volume of acetic acid was added to the PZT solution. The solution was spun onto the wafer coated PbTiO₃

buffer layer at 1500 rpm for 30 s and pyrolyzed at 350°C for 20 s. After four layers, the PZT film was crystallized by RTA at 650°C for 1 min.^[25] In this research, heating rates from 10°C/s to 65°C/s were studied. The steps were repeated until the desired thickness was achieved. Four spin steps with one RTA produce a layer of about 80 nm thickness.

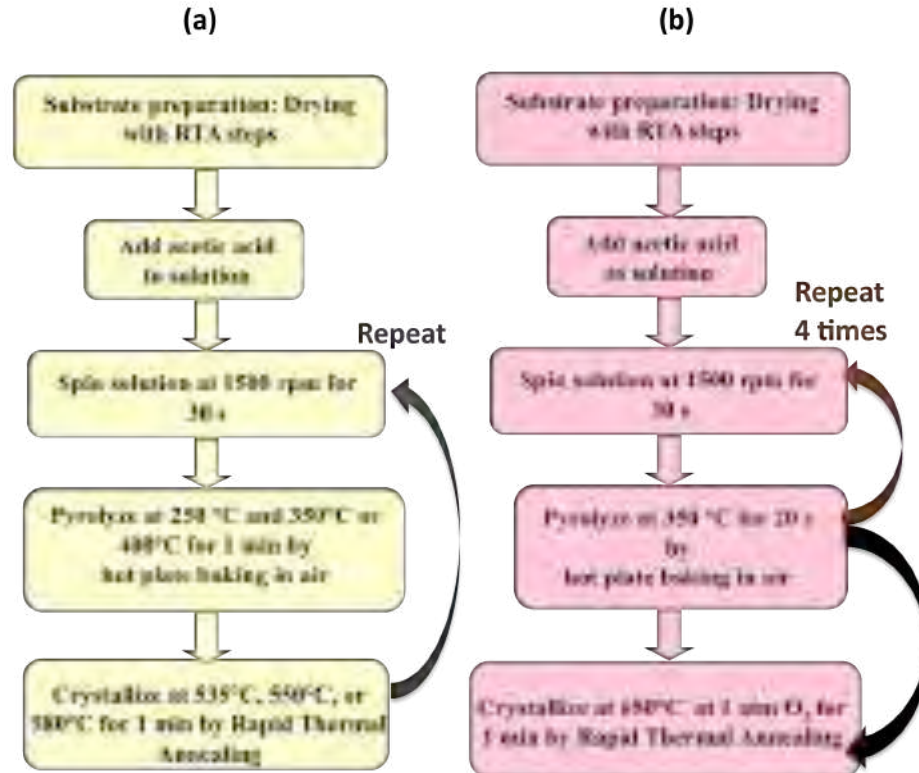


Figure 2- 4: (a) PbTiO_3 buffer layer deposition (b) The modified process for $\{001\}$ -textured PZT film deposition^[25]

2.1.4 PZT Films on $\text{SrRuO}_3/(100) \text{SrTiO}_3$

$\{001\}$ -oriented PZT films on single crystal SrTiO_3 coated with SrRuO_3 were also processed. (001) SrTiO_3 epitaxially polished wafers from MTI Corporation were coated with 150 nm SrRuO_3 by pulsed laser deposition at Penn State for use as a bottom electrode (by Dan

Tinberg). For films on SrTiO₃ substrates, no PbTiO₃ buffer layer was required before PZT deposition because the substrate controls the orientation.^[29, 34]

The PZT solution for these films was 0.4 M with 10% Pb-excess as shown in Figure 2- 1. For PZT deposition, 7% volume of acetic acid was added to the PZT solution before spinning for stabilization processes. The solution was spun onto the wafer at 1500 rpm for 30 s, pyrolyzed at 250°C and 400°C for 1 min each, and crystallized at 700°C for 1 min by RTA as shown in Figure 2- 5. The steps were repeated until the desired thickness was achieved. Eleven layers were deposited to prepare a 1 μm thick film.

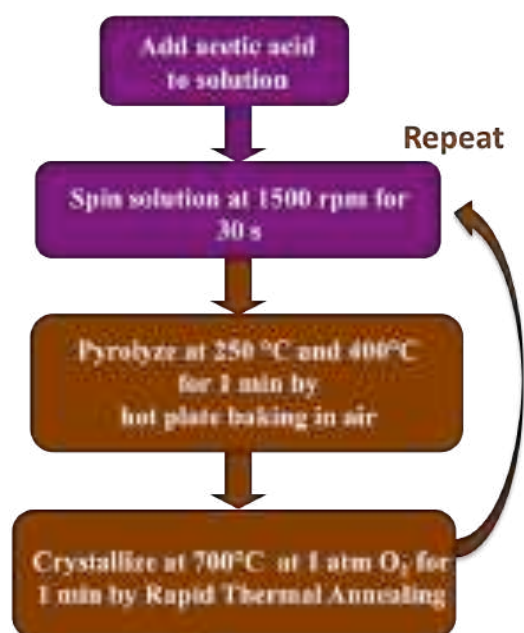


Figure 2- 5: PZT deposition process for {001} oriented films on single crystal SrTiO₃ coated with SrRuO₃

2.2 Structural Characterization

The structure and orientation of all films were characterized by X-Ray diffraction, XRD. A Scintag Pad V X-Ray Powder Diffractometer (Scintag Inc., Cupertino, CA) using CuK_α

radiation on a θ -2 θ goniometer was used. The XRD was equipped with a Ge liquid nitrogen cooled solid-state detector. The XRD generator was set at 35 kV and 30 mA. PZT films were scanned from 20 to 60 degrees 2 θ , with a step size of 0.02° and a 1.2 s count time. Table 2- 2 shows the numbers of the standard diffraction profiles from the powder database.

Table 2- 2: Powder diffraction file numbers used for XRD scan (from ICDD PDF-4 2007)

Material	PDF #
Pb(Zr _{0.52} Ti _{0.48})O ₃	00-033-0784
Pb(Zr _{0.30} Ti _{0.70})O ₃	01-070-4055
PbTiO ₃	00-040-0099 00-006-0452
SrRuO ₃	00-043-0472
Pt	01-087-0640

The quality of the PZT film orientation was quantified via the Lotgering factor shown in Equation 2-1.

$$f = \frac{(P - P^0)}{(1 - P^0)} \quad \text{where} \quad P = \frac{(I_{(100)} + I_{(200)})}{\sum I_{(hkl)}}$$

Equation 2- 1^[71]

where $I_{(100)}$ = the area under (100) PZT peak, $I_{(200)}$ = the area under (200) PZT peak, and $\sum I_{(hkl)}$ = the sums of the areas under all PZT peaks. P was used for the textured case and P^0 for a random sample of the same composition. Higher Lotgering factors correspond to improved {001} orientation. It has to be noted that the background was subtracted before determining the area

under the curves. This was important in particular for the 111 perovskite peak, as it typically appears on a large background due to the Pt 111 peak.

The formation of phases close to the film surface was characterized by grazing angle XRD. A schematic of the grazing angle XRD diffraction geometry is shown in Figure 2- 6. A Scintag X2 (Scintag, Cupertino, CA) using CuK_α radiation on a θ - θ goniometer equipped with a Si(Li) Peltier detector was employed. Grazing angles from 2° to 8° were studied for $\{001\}$ textured PZT films.

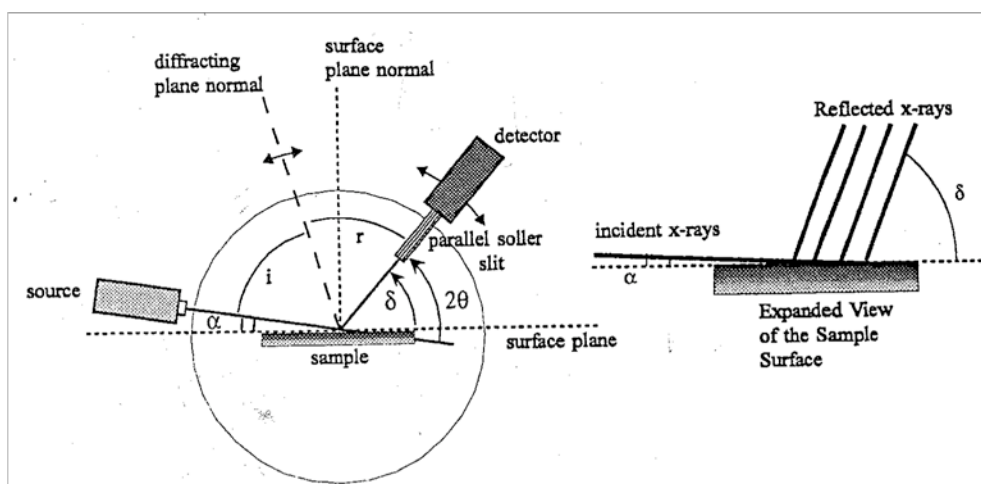


Figure 2- 6: Schematic of a grazing angle XRD^[72]

2.3 Thickness Characterization

The film thickness was characterized using an Alpha-Step 500 Surface Profiler (Tencor Instruments, CA). To create a step, wet etching was used to pattern the PZT film. HCl, HF, H_3PO_4 , HNO_3 , H_2SO_4 , NaOH, and KOH have been used in previous reports to etch PZT ceramics. In this work, a two step etch was used to pattern the PZT, as reported elsewhere.^[2] The majority of the film was removed using a solution of 10:1 BOE, buffered oxide etchant (ammonium fluoride (HN_4F)/hydrofluoric acid (HF), Transene Company Inc.) and water. Insoluble residues were then removed in HCl, 36.5-38% (J.T. Baker). This approach provides a

high etch selectivity of PZT over Pt. The remainder of the film and the wafer edges were protected with Shipley 1827 photoresist that had been baked on a hotplate at 115°C for 1 min. The average time required for the BOE etch is about 10 min for a 1 μm thick $\text{Pb}(\text{Zr}_{0.52}\text{Ti}_{0.48})\text{O}_3$ film, followed by HCl for 1 min to remove residues. For $\text{Pb}(\text{Zr}_{0.30}\text{Ti}_{0.70})\text{O}_3$ and $\text{Pb}(\text{Zr}_{0.52}\text{Ti}_{0.48})\text{O}_3/\text{PbTiO}_3$, wet etching required a longer time than for $\text{Pb}(\text{Zr}_{0.52}\text{Ti}_{0.48})\text{O}_3$ etching. Once the PZT etching was completed, successive rinses in acetone and isopropanol were used to remove the photoresist. The PZT film was then dried by placing it on a hot plate at 115°C for 1 min.

2.4 Microstructure Characterization

The cross section morphology was examined by using a Scanning Electron Microscope, SEM (S-3000H or S-3500H Hitachi, Hitachi Instruments, San Jose, CA). Before characterization, a thin gold film was sputtered for 30 s on the top of the PZT films in order to minimize charging artifacts.

2.5 Surface Morphology Characterization

The surface microstructure was characterized by Field-Emission Scanning Electron Microscope, FE-SEM (Jeol USA, Inc., Peabody, MA) and Atomic Force Microscope, AFM (Nanoscope IIIa, Digital Instruments Veeco Metrology Group, Chadds Ford, PA). The samples were cut to 5 mm x 5 mm pieces and placed on the AFM holder before characterization. The tapping mode was used to examine the grain size and surface roughness of PZT films. Silicon cantilevers, 160 μm long with a 300 kHz resonance frequency were used.

2.6 Dielectric Constant Characterization

To enable electrical characterization, 50 nm thick Pt top electrodes with sizes ranging from 200 μm to 1000 μm diameter were sputtered through a shadow mask on top of the PZT films. The top electrodes were annealed only in the case that the contact between top electrode and PZT films was not good resulting in high losses than 5%. The annealing condition was 400°C for 3 min on hot plate. The capacitances and loss tangents were measured using a Hewlett-Packard 4192A LF Impedance Analyzer, (Hewlett Packard, Palo Alto CA). Low field measurements were made from 0.1 kHz to 100 kHz with a 0.03 V oscillation voltages (rms). Point probes (Probing Solutions Inc. NV) were used throughout this study for making contacts to top and bottom electrodes. The capacitances were used to calculate the dielectric permittivity as shown in Equation 2-2.^[16]

$$C = \frac{\epsilon_r \epsilon_0 A}{d}$$

Equation 2- 2^[16]

where C = Capacitance, ϵ_0 = permittivity of vacuum (8.854×10^{-12} F/m), A = electrode area, and d = thickness of PZT film.

2.7 Polarization-Electric Field (P-E loops) Measurements

Polarization-electric field hysteresis loops (P-E loops) were characterized using an RT66A Standardized Ferroelectric Test System (Radiant Technologies Inc. Albuquerque NM). A 10 x external amplifier (AVC instrumentation 790 Series Power Amplifier) was connected to increase the output voltage of the RT66A system. The applied fields were from 50 kV/cm to 1100 kV/cm depending on the PZT film thickness. The P-E loops were used to determine the remanent

polarization (P_r) and coercive field (E_c). All polarization-electric field measurements were made at 100 Hz.

2.8 Piezoelectric Measurements

The piezoelectric effect is a linear coupling between electrical and mechanical energies and is useful for sensors, actuators, and ultrasound devices. There are two different approaches to measuring the piezoelectric response: current (or charge) measurement and strain (or displacement) measurement.^[3, 41] In this research two piezoelectric coefficients: $e_{31,f}$ and $d_{33,f}$ were measured. The transverse piezoelectric coefficients ($e_{31,f}$) were measured using the wafer flexure method at Penn State University. The piezoelectric coefficients ($d_{33,f}$) and polarization switching were measured by Piezoelectric Force Microscopy (PFM) and Switching Spectroscopy Piezoresponse Force Microscopy (SSPFM), respectively at Oak Ridge National Laboratory.

2.8.1 Wafer Flexure for $e_{31,f}$ Piezoelectric Coefficient Measurements

The transverse piezoelectric coefficients, $e_{31,f}$ were measured using the modified wafer flexure method. Small samples (less than 1 cm²) were glued to the center of a 3-inch silicon wafer and left to dry overnight. The wafer was then clamped on the top of a cylindrical cavity as shown in Figure 2- 7.^[6, 18, 73] First, the film was poled by applying about 3-5 times the coercive voltage to the film for 20 min. The charge and strain were measured while the pressure in the cavity was oscillated using an audio speaker. The pressure difference caused the sample to flex, applying an in-plane strain to the film. After that, a pre-wired strain gauge KFG-1N (KFG-1N-120-C1-11L3M3R) from Omega Engineering, Inc. (Stamford CT) was glued on top of the electrode used to measure the charge and dried overnight. The gauge factor (2.09 or 2.11) is

supplied by manufacturer and the gauge resistance is 120Ω . Thereafter, the strain was measured for the same pressure oscillation. Due to the non-uniformity of the sample size, a second strain measurement was made after gluing the strain gauge perpendicular to the previous direction. In addition, the film was poled to measure the charge again before the second strain measurement. The setting parameters of the lock-in amplifier (SR 830, Stanford Research Systems, Sunnyvale, CA) are 0 (phase), 4 Hz (frequency), $0.5 V_{\text{rms}}$ (Amp), and 1st (harmonic). In addition, poling and the $\epsilon_{31,f}$ aging studies were conducted.^[6]

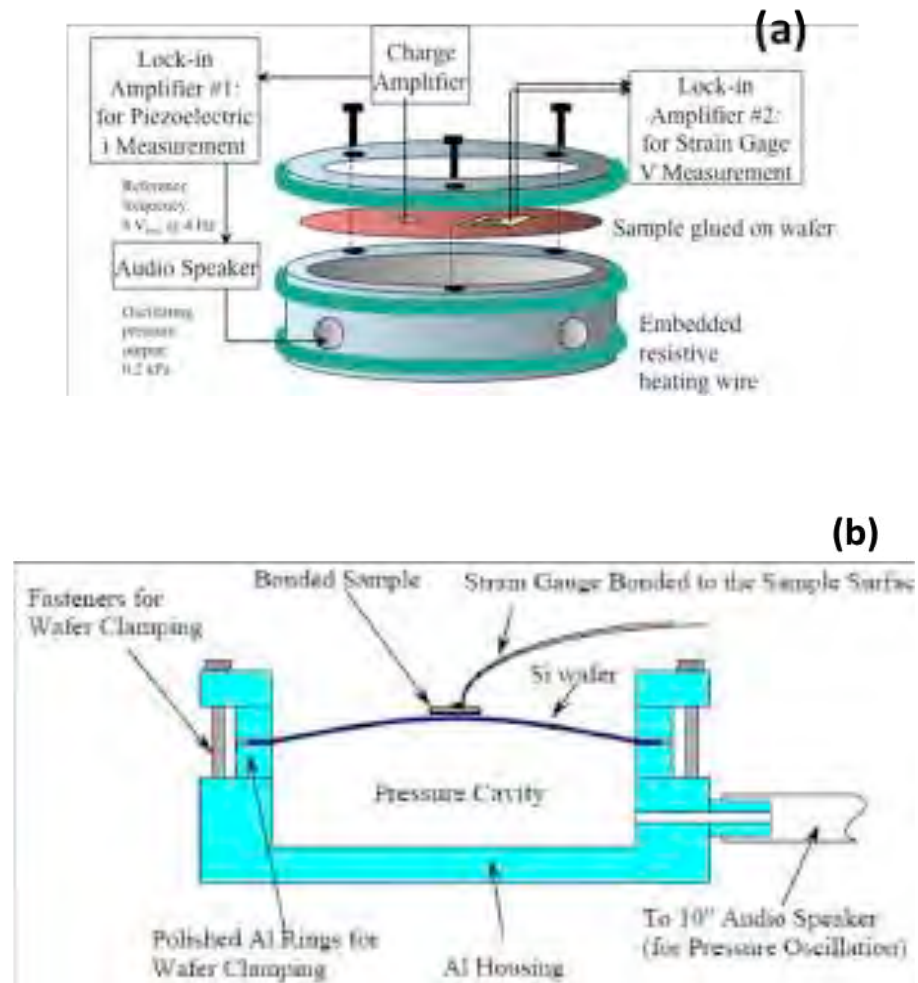


Figure 2- 7: Experimental set up for $\epsilon_{31,f}$ measurement (a) equipment set up and (b) sample with attached strain gauge ^[6, 73]

In addition, Figure 2- 8 illustrates the schematic of the quarter-bridge used for strain measurement. V_{in} is the +4 V input voltage, R is the resistance of the three known resistors in the quarter bridge circuit, ($120\ \Omega$ in this case); $R_g(\epsilon)$ is the resistance of the strain gauge. The output of this quarter bridge, V_{out} , is read through the connection to the lock-in amplifier.^[6]

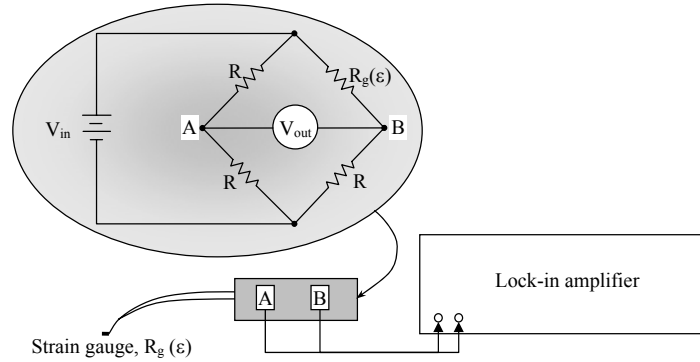


Figure 2- 8: Schematic of the quarter-bridge assembly used for strain measurement.

The converse piezoelectric coefficient was calculated using Equations 2-3 to 2-5.

$$\text{Strain} = \frac{(V_{out,1} + V_{out,2})(mV) \times 0.001}{\text{strain gauge factor} \times \left[1 + \left(\frac{(V_{out,1} + V_{out,2})(mV) \times 0.001}{2} \right) \right]}$$

Equation 2- 3

$$\text{Charge} = \frac{I_{out}}{\omega \sin \theta} = \frac{I_{out}}{2\pi(4) \sin(\theta)}$$

Equation 2- 4

$$e_{31,f} = \frac{\left(\frac{\text{Charge 1} + \text{Charge 2}}{2} \right)}{\text{area} \times \text{Strain}} \text{C/m}^2$$

Equation 2- 5

where $V_{out,1}$ and $V_{out,2}$ are the output voltages from the two perpendicular strain measurements. The strain gauge factor was supplied by the manufacturer of the pre-wired strain gauge. I_{out} is the collected charge.

2.8.2 Piezoelectric Force Microscopy for $d_{33,f}$ Piezoelectric Coefficients

Piezoelectric Force Microscopy (PFM) at Oak Ridge National Laboratory was used to characterize the piezoelectric nonlinearity and switching behavior in the PZT films. The samples were prepared as follows:

50 nm thick Pt top electrodes with sizes ranging from 200 μm to 1000 μm diameter were sputtered on top of the PZT films through a shadow mask. To facilitate electrical access, several electrode dots on the top surface of the film were wire-bonded to a DIP package. A wedge Bonder (K&S model 4123), Kulicke & Soffa Industries Inc. was employed for the wire bonding as shown in Figure 2- 9. To facilitate the PFM approach to the PZT film, a piece of bare silicon substrate was inserted between the sample and the attachment pad of the DIP package, so that the tip holder of the PFM would not hit the edge of the DIP package. An increased sample height will yield an increased bonding force on the sample, which can lead to an artificially high loss, possibly leading to shorting of the electrode. Consequently, the height of the sample holder was lowered to minimize the bonding force damage to the PZT film. The height and the temperature of the sample holder were set at ~ 8.3 cm and 44°C , respectively (Figure 2- 9(b)). The needle was placed in the needle holder so that it had a 1.5-2.0 mm tail above the top surface of the needle holder as shown in Figure 2- 9 (a).

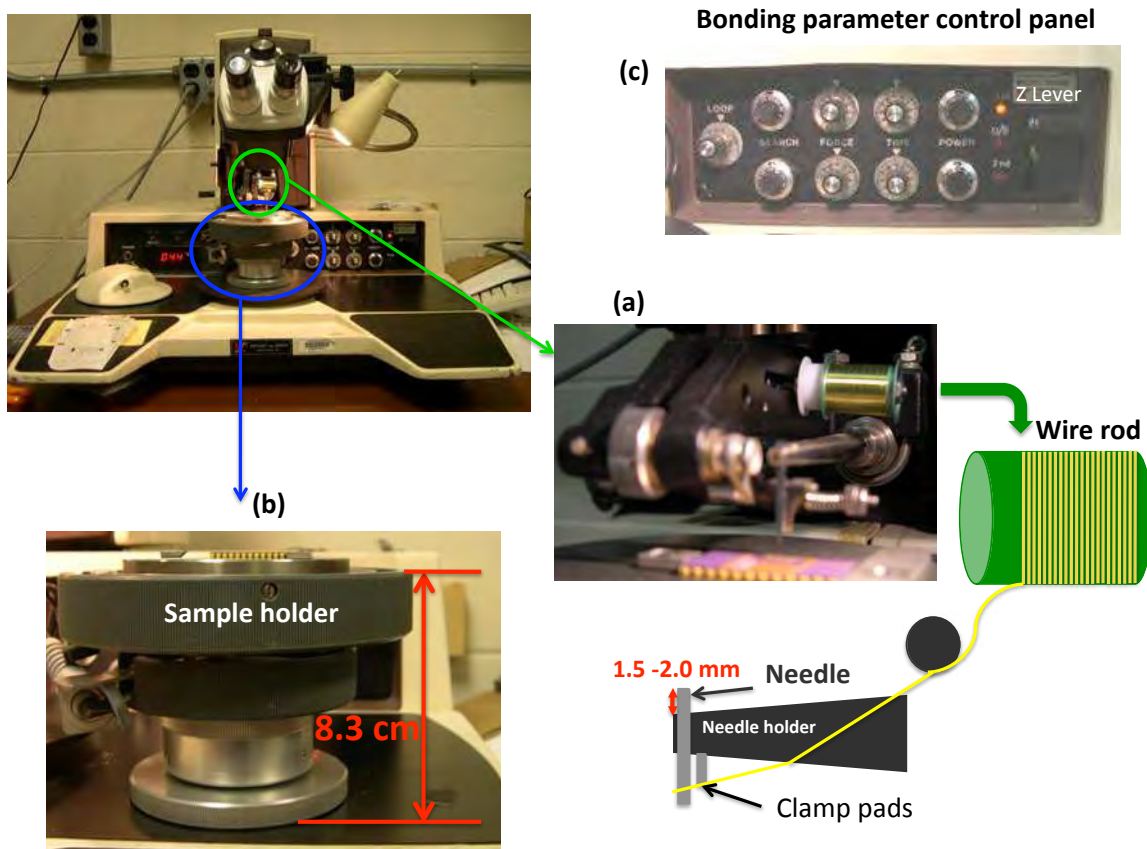


Figure 2- 9: A Schematic of wedge bonder for wire-bonding (a) wire and needle setting, (b) sample holder setting, and (c) bonding parameter control panel

When wire-bonding, the first bond was made to the dip package electrode pad. Prior to attempting to make the second bond, which has a stronger force associated with it, the wire was pressed against a bare section of the film. This cut the wire. The end of the wire was then manipulated over to the desired pad and the weaker first bond stage was used to bond to the top Pt electrode, see Figure 2- 10. All other parameters of the wedge bonder are shown in Table 2- 3.

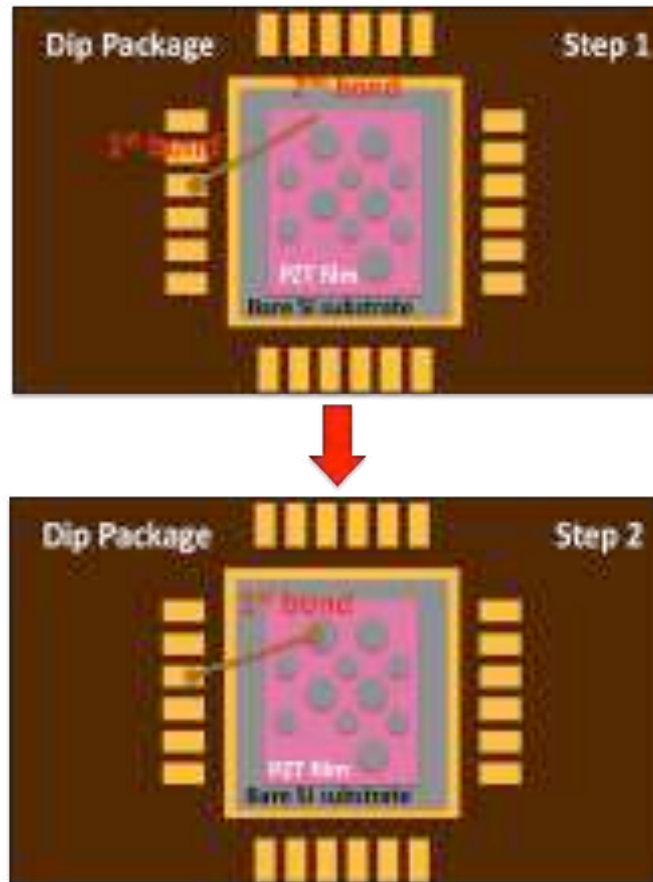


Figure 2- 10: Wire bonding technique

Table 2- 3: Wire-bonding parameters

Setting point	1 st bond	2 nd bond
Loop = 2.5		
Temperature = 44°C		
Search	2	1
Force	7.4	6.7
Time	5.8	4.8
Power	4	5

2.8.2.1 Piezoelectric Nonlinearity ($d_{33,f}$ vs. E_{ac})

The piezoelectric $d_{33,f}$ nonlinearity was measured by Piezoelectric Force Microscopy (PFM) at Oak Ridge National Laboratory. A commercial Asylum MFP-3D system equipped with a high voltage module (HVA220) and lock-in amplifier was used for the measurements. Figure 2-11 shows a schematic of the set up. The technique is based on the detection of mechanical surface deformation induced by an oscillating electrical bias applied across the sample. For the measurement, the tip of a scanning probe microscope is brought into contact with a top electrode on the film surface. The tip was lowered to the surface vertically until the deflection set point is achieved.^[52] The bottom electrode was grounded.

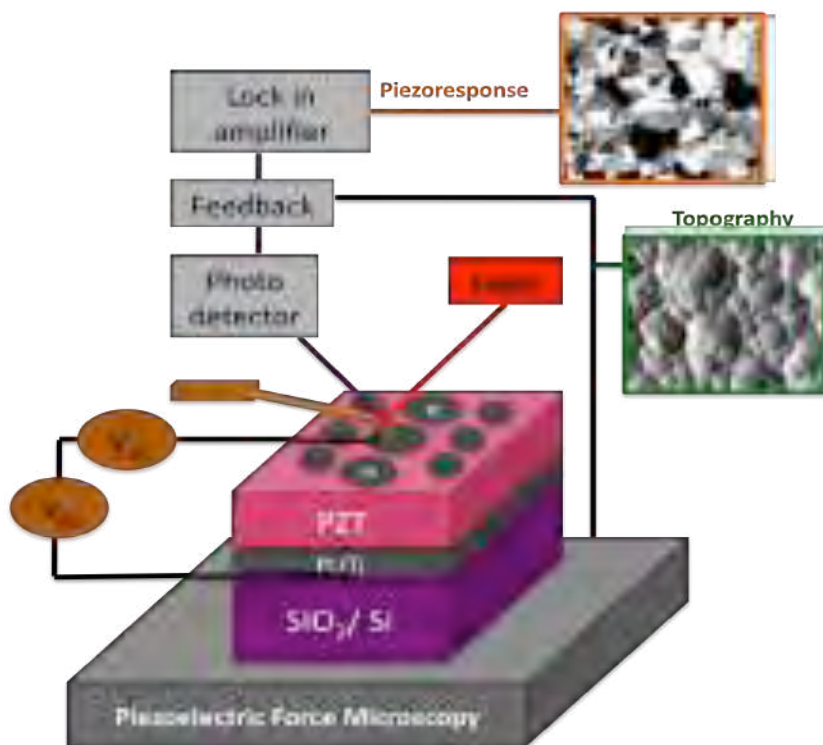


Figure 2- 11: Schematic of Piezoresponse Force Microscopy experimental set up for piezoelectric nonlinearity^[66]

The out-of-plane deformation of the PZT depends on the state of the polarization. The read out signal amplitude provides the magnitude of the effective piezoelectric coefficient. It should be noted, however, that due to the large area top electrode employed, the applied field leads to sample bending. Thus, the measured surface deflection is a combination of the true piezoelectric response of the film and substrate flexure. The phase provides information about the state of the polarization related to the piezoelectric coefficient sign.^[6] Before the nonlinearity measurements, the PZT films were poled by applying about 3 times the coercive voltage to the film for 20 min. Samples were then aged for at least 1 hour. Measurements were made of the effective $d_{33,f}$ vs. E_{ac} as a function of orientation and thickness. In addition, attempts were made to map the piezoelectric nonlinearity of the films to see how the domains behave locally.

A modified PFM approach, Band Excitation PFM (BE-SS-PFM), was employed for more quantitative measurements of the local piezoelectric nonlinearity to increase the signal to noise ratio^[74]. For this purpose, the cantilever was excited and the response detected over a selected frequency band rather than at a single frequency, as in conventional PFM. Figure 2- 12 illustrates the generic process of the BE method using a signal having a predefined Fourier amplitude density and phase content in the given frequency band. After that, the signal is Fourier transformed to generate an excitation signal in the time domain. The cantilever response is yielded from the ratio of the fast Fourier transform (FFT) of the response to the excitation signals.

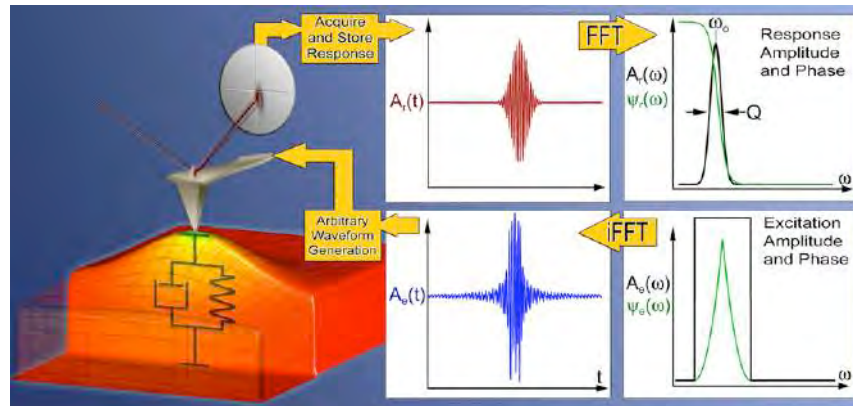


Figure 2- 12: The principle of band excitation SS-PFM: A = resonance amplitude, Ψ = phase, ω = resonance frequency, and Q = quality factor^[74]

The center frequency and frequency band were chosen based on the resonance frequency. In this experiment, a signal having a uniform amplitude within the band was used to collect the amplitude. More details on the measurement are provided elsewhere.^[74] The PFM tip for BE-PFM was from Olympus AC240TM, Electri-lever.

2.8.2.2 Switching Spectroscopy Piezoelectric Force Microscopy (SS-PFM)

Two main families of experiments were conducted by Switching Spectroscopy Piezoelectric Force Microscopy: spatially resolved spectroscopic mapping of polarization reversal and switching spectroscopy piezoelectric force microscopy of polycrystalline capacitor structures.

In piezoresponse force spectroscopy, a dc bias offset is applied to the tip, and the nucleation and growth of the ferroelectric domains and movement of existing domain walls below the tip are reflected in the change of the effective electromechanical response. The dependence of the response on prior dc bias yields the local electromechanical hysteresis loop. The spatial variability of the switching behavior is probed by switching spectroscopy PFM (SS-PFM), in which hysteresis loops are acquired at each point of a user-specified grid. The resulting 3 D data

array representing the hysteresis loops at each point of the sample is analyzed to yield 2D maps of maximal response, switchable polarization, nucleation and coercive biases, and work of switching.^[51]

2.8.2.2.1 Spatially resolved spectroscopic mapping of polarization reversal

In this experiment, the local polarization switching of 1.09 μm mixed {001} and {111} orientation PZT film was studied by Switching Spectroscopy Piezoelectric Force Microscopy (SS-PFM). Details on the development of SS-PFM are given elsewhere.^[52] A schematic of the set up is shown in Figure 2- 13 (a). A commercial Asylum MFP-3D system with an additional lock-in amplifier (Stanford Research Systems SR844) and function generators (SRSDS 345) was equipped with a high voltage module (HVA220). SSPFM maps of 50 x 50 pixels over 6 μm x 6 μm were performed at 400 kHz with the excitation windows of 3 V to 16 V. Here the “excitation bias window” refers to the range of dc bias values applied to the films between piezoelectric measurements. Each loop per pixel was taken in about 1.2 s with an ac probe bias of $3V_{pp}$. The SS-PFM maps were analyzed using standard procedures to extract 2D maps of local response, work of switching, remanent, and switchable response, and effective nucleation biases from hysteresis loops (piezoresponse-poling voltage), as defined in Figure 2- 14.^[52, 56] The piezoelectric hysteresis loops acquired in local measurements are different from hysteresis loops acquired using macroscopic top electrodes. First, the local hysteresis loops measured by PFM sample fewer domains compared to macroscopic hysteresis loops.^[52] The measurement volumes of PZT films in local and global measurements are shown in Table 2- 4. Secondly, SSPFM measurements are made at field after a “poling” field is applied, not at the applied bias, to avoid complications associated with the dc bias dependence of the piezoelectric response. A schematic

of the ac voltage dc voltage sequence is shown in Figure 2- 15.^[52, 62] In this measurement, the film was not poled before the measurement.

The volume samples in global and local measurements were calculated as followed:

Global volume sampled = Electrode area (πr^2) * PZT film thickness

Local volume sampled = Area of lateral resolution (πr^2) * PZT film thickness

where the lateral resolution was estimated as described by Kalinin et al.; that is the lateral resolution = $aH + bL$ (where H is PZT film thickness and L is top electrode thickness. The coefficients $a = 0.14$ and $b = 0.40$ were estimated from Equation 2-6 and Equation 2-7 with $d_{33} \sim 100$ pm/V, $d_{31} \sim -43$ pm/V, ν (Poisson's ratio) ~ 0.3 , and $\eta = 0.76$.^[73] More details of the calculation are described elsewhere.^[50, 73]

$$\tan^{-1}\left(\frac{a}{2}\right) + \frac{d_{33} + \nu d_{31}/2}{d_{33} + (1 + 2\nu)d_{31}} \left(\frac{a}{2}\right) \ln\left(1 + \frac{4}{a^2}\right) = \frac{\pi}{2} \eta$$

Equation 2- 6^[50, 73]

$$b = \eta \frac{\pi (d_{33} + (1 - 2\nu)d_{31})}{2 (d_{33} + \nu d_{31}/2)}$$

Equation 2- 7^[50, 73]

Table 2- 4: PZT volume sampled in global and local measurements

	Global measurement	Local measurement
Resolution (Φ)	0.2 mm – 1.0 mm	~ 60 – 585 nm (Depending on PZT thickness)
Volume	$(0.0314 - 0.785) \text{ mm}^2 * \text{thickness}$	~ $(0.00275 - 0.26933) \mu\text{m}^2 * \text{thickness}$
<u>PZT volume:</u>		
0.28 μm PZT film	$(8.79 \times 10^3 - 2.198 \times 10^5) \mu\text{m}^3$	~ $0.00077 \mu\text{m}^3$
0.53 μm PZT film	$(1.66 \times 10^4 - 4.16 \times 10^5) \mu\text{m}^3$	~ $0.0037 \mu\text{m}^3$
0.92 μm PZT film	$(2.88 \times 10^4 - 7.22 \times 10^5) \mu\text{m}^3$	~ $0.016 \mu\text{m}^3$
1.09 μm PZT film	$(3.42 \times 10^4 - 8.56 \times 10^5) \mu\text{m}^3$	~ $0.025 \mu\text{m}^3$
2.06 μm PZT film	$(6.47 \times 10^4 - 1.62 \times 10^6) \mu\text{m}^3$	~ $0.15 \mu\text{m}^3$
4.04 μm PZT film	$(1.27 \times 10^5 - 3.17 \times 10^6) \mu\text{m}^3$	~ $1.09 \mu\text{m}^3$

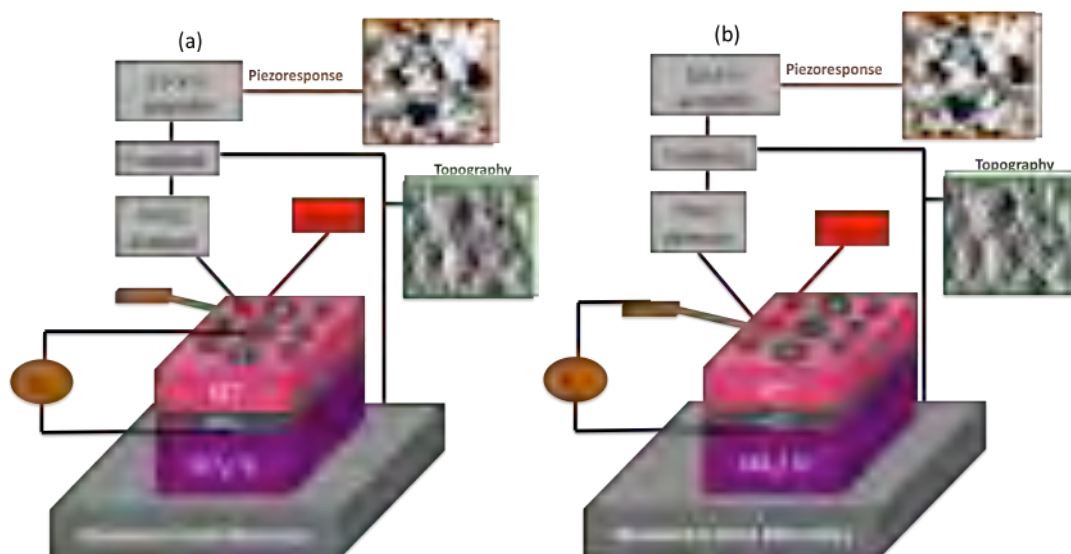


Figure 2- 13: Switching spectroscopy piezoresponse force microscopy measurements on a 1 μm thick, mixed $\{001\}$ and $\{111\}$ oriented PZT film (a) on electrode (b) on the PZT film directly

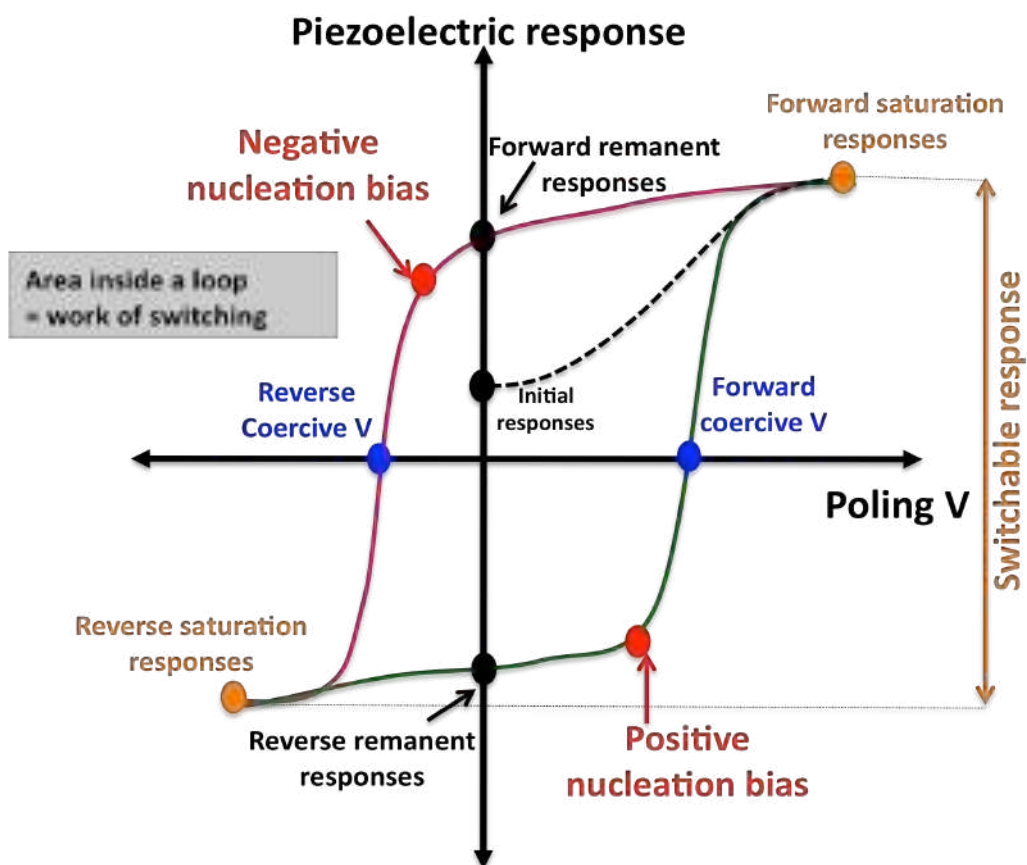


Figure 2- 14: A schematic of PFM hysteresis loop^[52]

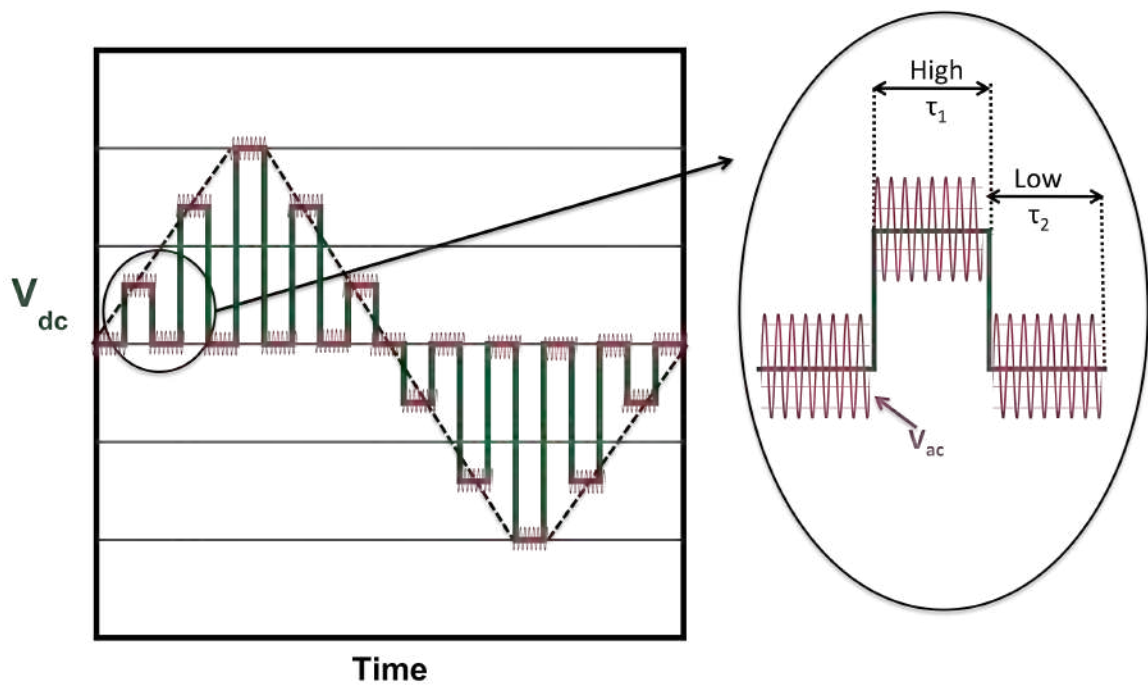


Figure 2- 15: The voltage waveform used for local hysteresis measurements^[52, 62]

2.8.2.2.2 Switching spectroscopy piezoelectric force microscopy of polycrystalline capacitor structures

The polarization switching behavior of 1.09 μm mixed $\{001\}$ and $\{111\}$ oriented PZT film was measured on and off the top electrodes by SS-PFM. For measurements made on electroded areas, as shown in Figure 2- 13 (a), the tip of the scanning probe microscope (Pt coated tips, Olympus Electrilever) detects the PZT deformation induced by the applied electric field across the top and bottom electrodes in contact mode. The bottom electrode was grounded. For measurements made on the PZT film surface as shown in Figure 2- 13 (b), the ac bias was applied directly to the PFM tip with the bottom electrode grounded. In this measurement, the coercive bias, nucleation bias, remanent, switchable response, and effective work of switching were acquired.^[55]

2.9 Macroscopic First Order Reversal Curve (FORC)

The first order reversal curves of mixed $\{001\}$ and $\{111\}$ orientation films, $\{001\}$ textured films on Si, and $\{001\}$ –textured films on single crystal SrTiO_3 were measured for a thickness series. The PZT films were taken to a negative saturation state, and were subsequently excited to progressively higher electric fields. After each excursion, the sample was then taken back to the negative saturation state. 42 minor to major loops were measured and analyzed in order to calculate the Preisach distribution function of the switchable units.

The Preisach distribution function describing global switching (large electrode, 200 μm to 1000 μm) was extracted from FORC data in the following manner. Consider a case in which a material is exposed to negative electric field to E_{-5} [Figure 2- 16 (a1)], which is high enough to reach negative saturation. Then, the field increases to E_{-4} and decreases to E_{-5} [Figure 2- 16 (b1) and Figure 2- 16 (c1)]. The difference between $P_{\alpha-4}$ and $P_{\alpha-4\beta-5}$ [Figure 2- 16 (b2) and Figure 2-

16 (c2)] corresponds to $p(\alpha_{-4}, \beta_{-5})\Delta\alpha\beta$. Next, the field increases to E_{-3} and decreases to E_{-4} [Figure 2- 16 (d1) and Figure 2- 16 (e1)]. The difference between $P_{\alpha_{-3}}$ and $P_{\alpha_{-3}\beta_{-4}}$ [Figure 2- 16 (d2) and Figure 2- 16 (e2)] corresponds to $p(\alpha_{-3}, \beta_{-4})\Delta\alpha\Delta\beta$. Then, the field decreases to E_{-5} [Figure 2- 16 (f1)]. The difference between $P_{\alpha_{-3}}$ and $P_{\alpha_{-3}\beta_{-4}}$ [Figure 2- 16 (f2)] corresponds to a summation of $p(\alpha_{-4}, \beta_{-5})\Delta\alpha\Delta\beta$ and $p(\alpha_{-3}, \beta_{-5})\Delta\alpha\Delta\beta$. Since $p(\alpha_{-4}, \beta_{-5})\Delta\alpha\Delta\beta$ is known, $p(\alpha_{-3}, \beta_{-4})\Delta\alpha\Delta\beta$ can be calculated.

To compare the results of switching over large areas (e.g. in a global measurement sampling thousands of grains) and local measurements, the FORC of 1.09 μm mixed $\{001\}$ and $\{111\}$ orientation PZT film were measured and modeled to produce a Preisach distribution function of the switchable units. This distribution function was subsequently used to calculate the average amount of switching expected for the excitation conditions employed in the PFM experiment.^[56] In particular, since the PFM measurements are made at zero dc bias, only the irreversible hysterons were utilized to calculate the expected change in switched polarization and hence remanent piezoelectric response. In this part, I would like to acknowledge Ichiro Fujii for his help in modeling the FORC data and calculating the Preisach distribution function.

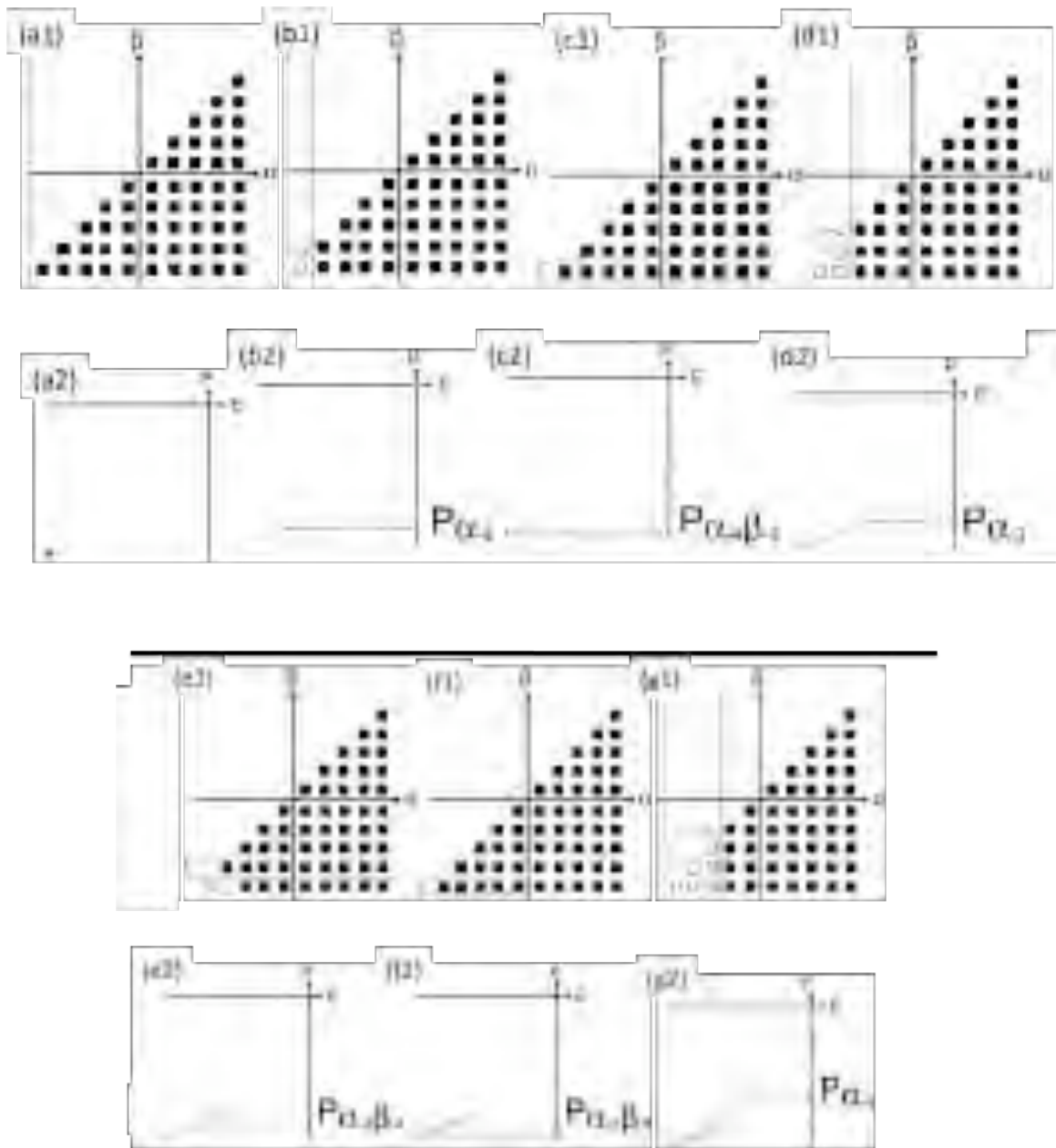


Figure 2- 16: The first order reversal curves method modeled by Ichiro Fujii

2.10 Nanoindentation Measurements on PZT Films

Nanoindentation measurements on PZT films with mixed $\{001\}$ and $\{111\}$ orientation (prepared using a standard processing route) were performed with a Hysitron Triboindenter with 500 nm radius conospherical diamond tip as shown in Figure 2- 17 by Amber Romasco. The method of Oliver-Pharr with pile-up height correction was performed for calculation. The elastic moduli were calculated from both the loading and the unloading curves.^[75, 76]

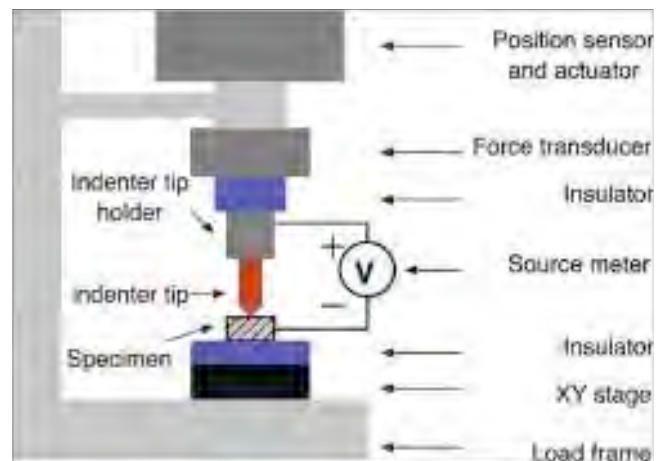


Figure 2- 17: Schematic illustration of the experiment setup for nanoindentation studies^[75, 76]

2.11 Dielectric Nonlinearity

The dielectric nonlinearity measurements were performed (1 kHz) using a Hewlett Packard 4248A precision LCR Meter (Agilent Technology, Palo Alto CA). The capacitance and loss tangent of the sample were measured as a function of ac voltage and converted to dielectric permittivity as shown in Equation 2-2.^[16] The dielectric nonlinearity was measured both before and after poling. The maximum AC voltage for each sample ranged from 0.01 V to half the

coercive field. In addition, the dielectric nonlinearity was characterized under applied bias fields from 0 V up to 3 times the coercive field.

2.12 Dry Etching of PZT Films

To explore dry etching of PZT using fluorine chemistries, PZT films (standard processing) were sputter coated with a Cr(100Å)/ Au(1000 Å) seed layer for electroplating. HMDS, Hexa-methyl-disilazine, was spun on the wafer at 4000 rpm for 40 s to promote adhesion of the photoresist. This was followed by spinning on Shipley 1827 photoresist at 4000 rpm for 40 s. The wafer was then placed on a hot plate at 115°C for 1 min for the soft bake to both remove solvent from the photoresist and help photoresist adhesion. After the photoresist was applied, the wafer was exposed to UV light through a photomask using an MA6 mask aligner and then developed in CD26 developer.^[77] The feature size and mask detail are shown in section 2.12.1. After this process, the wafer was electroplated with Ni as a hard mask, and then the photoresist was removed using acetone. The parameters and the schematic of sample preparation for DRIE are shown in Table 2- 5 and Figure 2- 18 (a) – (d), respectively.

Table 2- 5: Parameters of sample preparation for DRIE

Process	Condition
Cr/Au deposition by sputtering system	Cr(100Å)/ Au(1000 Å)
Phtolithography	
HMDS 1827 (thickness ~2.7 μm)	
Spin coating	4000 rpm for 40 s
Exposure time	12 s
Soft bake	110°C, 60 s
Develop by CD-26	1 min
Oxygen de-scum	1-5 min
Ni electroplating	Set I= 10 A Time = 22 min for 1 μm Ni thick
Remove Photoresist	Acetone rinse

The films were etched using an Inductively Coupled Plasma Reactive Ion Etcher (ICP-RIE), Alcatel AMS-100 Dielectric Etching I-Speeder. After etching, the Ni was removed with Transene Ni etchant type I (Ferric Chloride/ Hydrochloric acid/water) shown in Figure 2- 19(e) – (f).

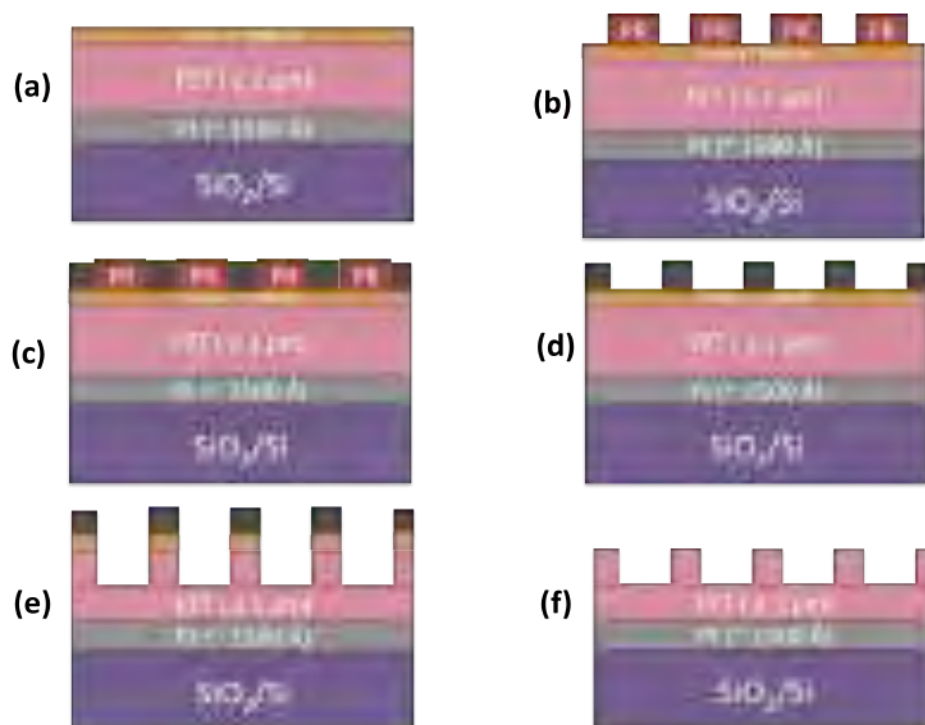


Figure 2- 18: Sample preparation and dry etching process steps (a) Sputter Cr/Au on PZT film (b) Lithographically pattern the resist on Cr/Au (c) Electroplate Ni (d) Remove photoresist (e) Dry etch PZT (f) Remove Ni

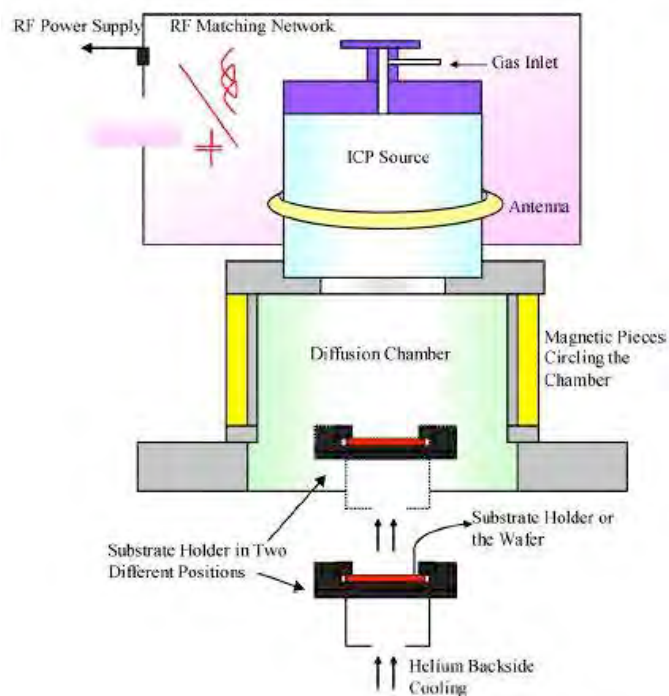


Figure 2- 19: Inductively Coupled Plasma Reactive Ion Etcher (ICP-RIE), Alcatel AMS-100 Dielectric Etching I-Speeder^[78]

Figure 2- 19 is a schematic of the ICP RIE chamber used in this research. The substrate is placed inside a reactor into which several gases are introduced. A plasma is struck in the gas mixture using an RF power source, breaking the gas molecules into ions. The ions are accelerated toward the surface of the material being etched and react, forming another gaseous material. This is known as chemical reactive ion etching. There is also a physical part, which is similar to sputtering. If the incoming ions have a high enough energy, they can knock atoms out of the material to be etched without chemical reaction.

In the etching process, variations in the gas flow rate, substrate holder power, operation pressure, spacing between feature sizes, repeatability, as well as the uniformity of etching have been investigated. In addition, the electrical properties of PZT films after etching were characterized as described above.

2.12.1 Mask Design and Feature Sizes for Dry Etching

There were three mask types used in this thesis. To investigate the effect of varying the gas flow rate, substrate holder power, operation pressure, as well as the repeatability, the PZT films used were patterned with feature sizes of $300\ \mu\text{m} \times 600\ \mu\text{m}$ with a pitch of $275\ \mu\text{m}$, as shown in Figure 2- 20.

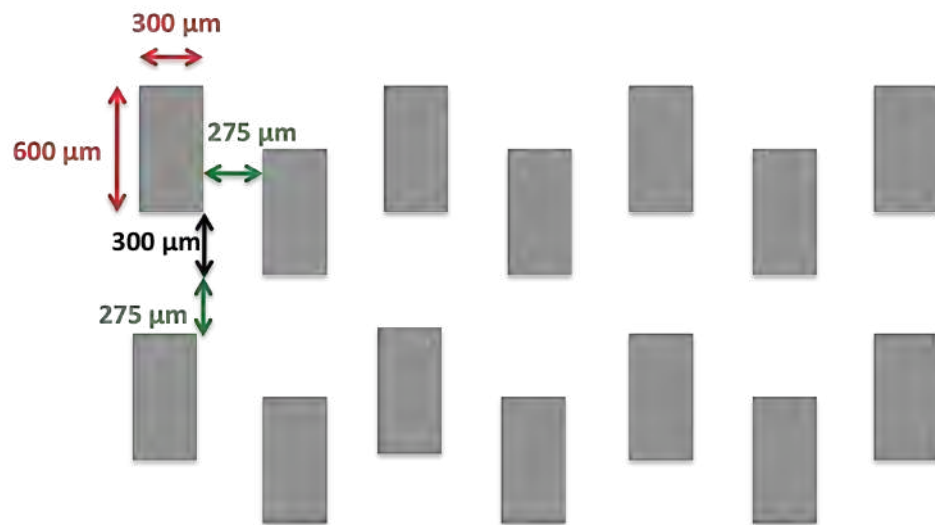


Figure 2- 20: Feature size and mask detail used in the etching process of variations in the gas flow rate, substrate holder power, operation pressure, and repeatability

To investigate different feature spacings, features with a size of $150\ \mu\text{m} \times 300\ \mu\text{m}$ and spacings of $50\ \mu\text{m}$, $30\ \mu\text{m}$, $20\ \mu\text{m}$, $10\ \mu\text{m}$, $5\ \mu\text{m}$, and $3\ \mu\text{m}$ were patterned on the PZT samples with the mask as shown in Figure 2- 21.

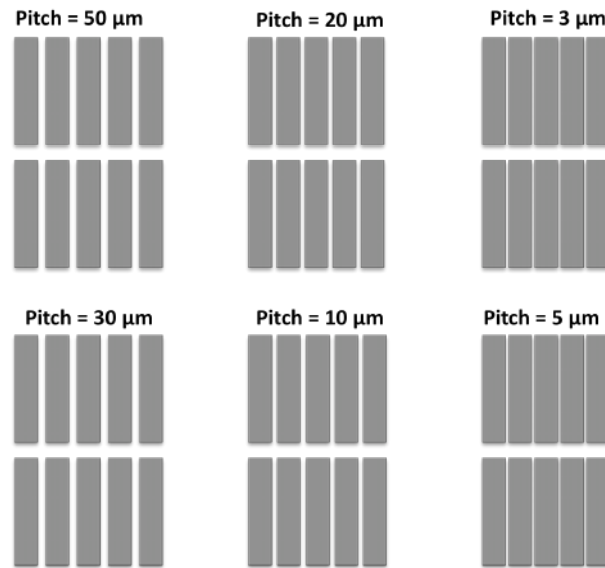


Figure 2- 21: Mask design for dry etching study of spacing variations of 50 μm , 30 μm , 20 μm , 10 μm , 5 μm , and 3 μm

Finally, Figure 2- 22 shows mask used for the uniformity of dry etching over 2 inch and 4 inch areas.

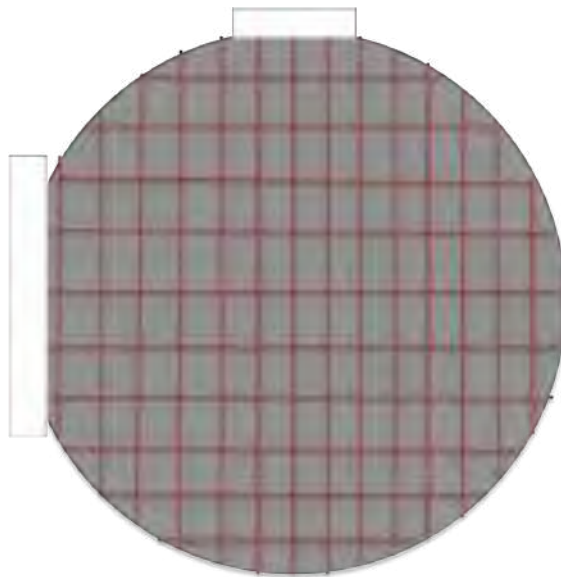


Figure 2- 22: Mask pattern for uniformity study

Chapter 3

Processing Control and Characterization of PZT Films with Mixed {001} and {111} Orientation and {001}-Textured PZT Films

This chapter describes work on the optimization of the process parameters for the deposition of the lead zirconate titanate films. Three types of PZT films were studied: PZT films with mixed {001} and {111} orientation, {001}-textured PZT films on Pt-coated silicon substrates, and PZT films on (100) single crystal SrTiO₃ coated with SrRuO₃. First, the pyrolysis and crystallization conditions as well as the lead source were optimized in order to obtain dense and crack free PZT films. Subsequently, the deposition process was modified to obtain {001}-textured PZT films. The characterization of highly {111} and {001} PZT films is then discussed in term of morphology, dielectric properties, Polarization-Electric field (P-E) loops, and the transverse piezoelectric coefficients ($e_{31,f}$).

3.1 Processing of PZT films with Mixed {001} and {111} Orientation

In this section, the processing of crack-free PZT films up to 5.8 μm in thickness was studied. Subsequently, the process was modified to enable films of higher density, resulting in improvement of the PZT film properties.

3.1.1 Processing Parameters, Crystallography, and Electrical Properties of PZT Films with Mixed {001} and {111} Orientation

Pb(Zr_{0.52}Ti_{0.48})O₃ thin films with mixed {001} and {111} orientation were fabricated using the procedures specified in sections 2.1.1 and 2.1.2. Figure 3- 1 shows a cross-sectional

micrograph of a 5.79 μm thick $\text{Pb}(\text{Zr}_{0.52}\text{Ti}_{0.48})\text{O}_3$ film prepared from a solution with 20% excess Pb with pyrolysis steps at 300°C, 1 min and 550°C, 2 min and an RTA step of 700°C, 1 min, heating rate 7°C/s. A boundary can be seen between each crystallized layer, where at least some of the contrast is due to pores at the interfaces.^[18] Attempts were made to estimate the porosity using the Image J program. However, it was found that it was not possible to accurately estimate the porosity in this way. For example, the calculated porosity of the 5.79 μm thick PZT film was approximately 14% of the total area. However, the measured dielectric permittivity is much higher than calculations using effective medium theory with this percentage porosity. Likewise, this film had a high $\epsilon_{31, f} = -8.2 \text{ C/m}^2$ as described in Table 3- 2. These discrepancies may arise, in part, because the fracture surfaces used in the micrographs may fail selectively at pore sites, leading to an over-representation of the porosity by this method. A second difficulty is that it was difficult to unambiguously assign particular contrast values in the micrographs to porosity (as opposed to roughness of the fracture surface). Thus, no further attempts were made to estimate the porosity using the software.

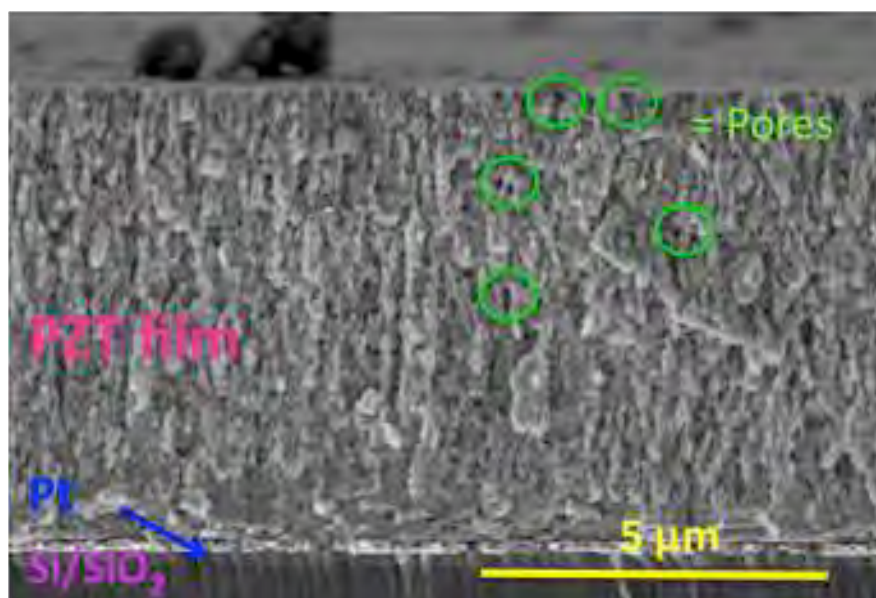


Figure 3- 1: 5.79 μm 20% Pb-excess $\text{Pb}(\text{Zr}_{0.52}\text{Ti}_{0.48})\text{O}_3$ films with pyrolysis at 300°C, 1 min and 550°C, 2 min and RTA 700°C, 1 min, heating rate 7°C/s

The surface morphology by Field-Emission SEM (Jeol 6700F) of the 5.79 μm 20% Pb-excess $\text{Pb}(\text{Zr}_{0.52}\text{Ti}_{0.48})\text{O}_3$ film is shown in Figure 3- 2. Subsequently, the Image J program was used to estimate the grain sizes. It was presumed that the grains were columnar, so that the surface “grain size” is the column diameter. The shortest and longest diameters of each grain were measured and averaged. At least 30 grains were characterized and given in a range of minimum and maximum grain size range. The grain sizes of this PZT film ranged from 50 to 237 nm (minimum grain size is 50 nm, maximum grain size is 237 nm, average grain size is 118 nm with standard deviation 49 nm. Pores are also visible.

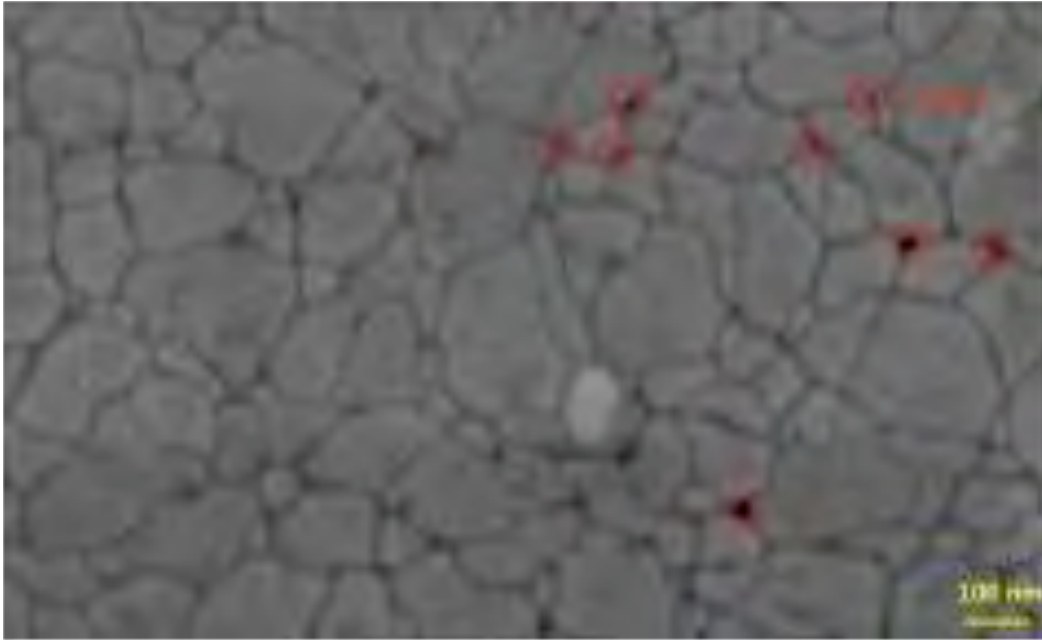


Figure 3- 2: Surface morphology showing grain sizes ranging from 50 nm to 205 nm for a 5.79 μm thick $\text{Pb}(\text{Zr}_{0.52}\text{Ti}_{0.48})\text{O}_3$ film prepared with pyrolysis at 300°C, 1 min and 550°C, 2 min and RTA 700°C, 1 min, heating rate 7°C/s

The dielectric constant as a function of frequency is shown in Figure 3- 3 (a). The dielectric constant of the film is 934 with $\tan \delta = 2.2\%$ at 10 kHz. The remanent polarization and coercive field of the films are 20 $\mu\text{C}/\text{cm}^2$ and 33 kV/cm, respectively, as seen in Figure 3- 3 (b). The comparatively low permittivity for such a thick film was attributed to the presence of pores. Thus, the pyrolysis temperature and crystallization were optimized to obtain dense PZT films with improved properties.

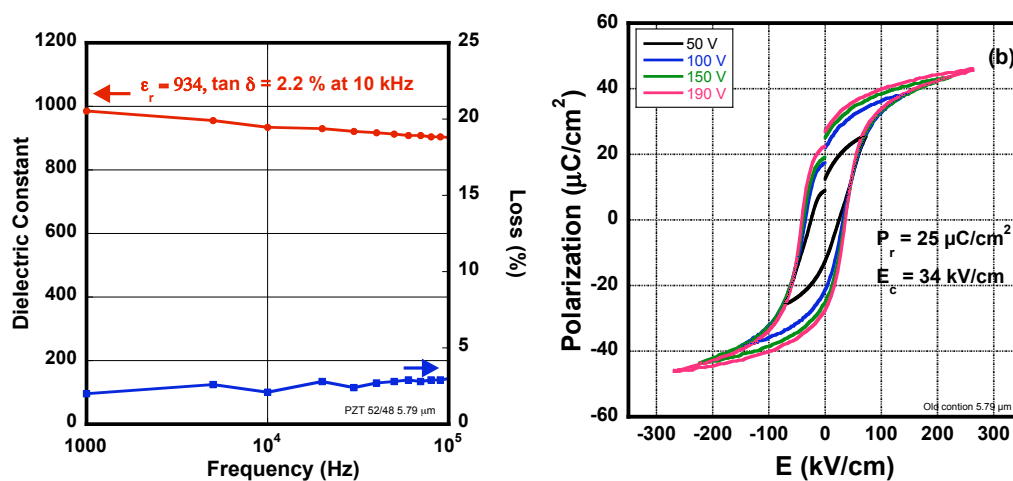


Figure 3- 3: Electrical properties of 5.79 μm Pb(Zr_{0.52}Ti_{0.48})O₃ films prepared using pyrolysis at 300°C, 1 min and 550°C, 2 min and RTA 700°C, 1 min, heating rate 7°C/s (a) dielectric constant vs. frequency and (b) polarization-electric field loop

In order to obtain denser films, the heat treatment was optimized. The temperatures of the two pyrolysis steps were varied over a range from 200°C to 500°C. Figure 3- 4 shows cross-sectional micrographs of a ~1 μm thick Pb(Zr_{0.52}Ti_{0.48})O₃ film prepared from a solution with 20% excess Pb with pyrolysis temperatures ranging from 200°C to 275°C, 1-2 min and 350°C to 500°C, 2 min and RTA 700°C, 1 min, heating rate 7°C/s.

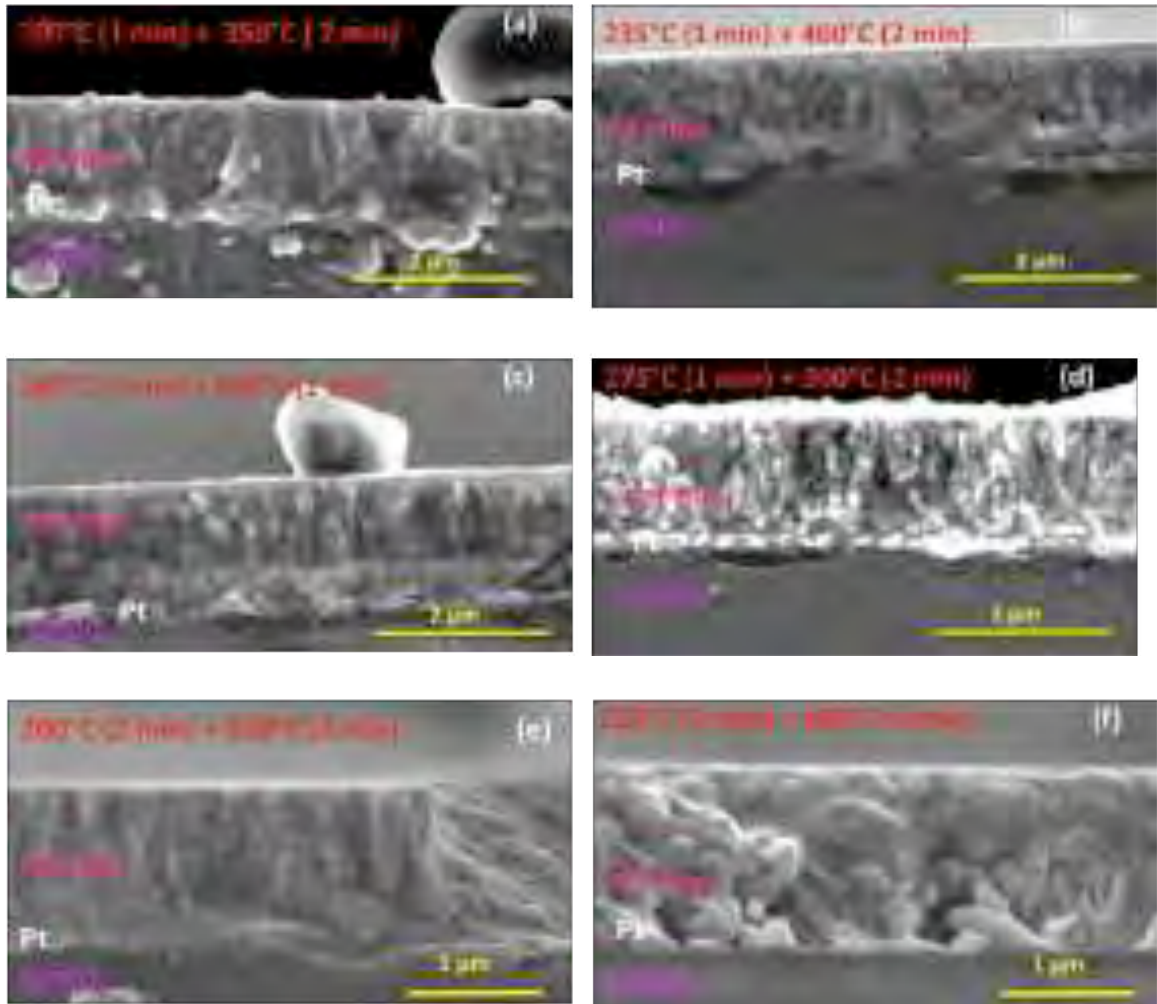


Figure 3- 4: Cross-sectional micrograph of $\sim 1 \mu\text{m}$ thick $\text{Pb}(\text{Zr}_{0.52}\text{Ti}_{0.48})\text{O}_3$ films prepared using the following pyrolysis steps: (a) 200°C , 1 min + 350°C , 2 min, (b) 235°C , 1 min + 400°C , 2 min, (c) 260°C , 1 min + 450°C , 2 min, (d) 275°C , 1 min + 500°C , 2 min, (e) 200°C , 2 min + 350°C , 2 min, and (f) 235°C , 2 min + 400°C , 2 min

The % porosity decreased as the second pyrolysis temperature decreased. The Lichtenecker rule was used to estimate the dielectric permittivity of the films as shown in Equation 3-1^[16].

$$\ln \epsilon_m = \sum_i V_{f_i} \ln \epsilon_i = (V_{f,PZT} * \epsilon_{PZT}) + ((V_{f,pores} * \epsilon_{pores})) \quad \text{Equation 3- 1}^{[16]}$$

where $V_{f,PZT}$ = Volume fraction of PZT films

ϵ_{PZT} = Permittivity of PZT films (in case of fully dense PZT films)

$V_{f, \text{ pores}}$ = Volume fraction of pores

ϵ_{pores} = Permittivity of pores

ϵ_m = Total permittivity

The calculated permittivity by Lichtenecker rule and the measured permittivity of PZT films are shown in Table 3- 1. The dielectric constant increased when the % porosity was minimized. It is also apparent that the image processing procedure significantly overestimated the level of porosity in some cases. Based on the electrical properties, a temperature of about 200 to 250°C for the first pyrolysis was chosen, followed by a second pyrolysis at about 350°C to 400°C.

Table 3- 1: Heat treatment condition of each experiment to obtain denser PZT films

Condition	Pyrolysis Step 1 (on metal plate)	Pyrolysis Step 2 (on hot plate)	Thickness (μm)	Porosity (%)	Calculated Dielectric Constant	Dielectric Constant (10 kHz)	Loss (%) (10 kHz)
1	300°C, 1 min	550°C, 2 min	5.79	13.9	564	934	2.2
2	200°C, 1 min	350°C, 2 min	1	2.9	1264	1270	4.7
3	235°C, 1 min	400°C, 2 min	1	10.3	736	1020	3.5
4	260°C, 1 min	450°C, 2 min	1	14.4	543	890	4.32
5	275°C, 1 min	500°C, 2 min	1	13.5	582	940	2.85
6	200°C, 2 min	350°C, 2 min	1	2.7	1291	-	-
7	235°C, 2 min	400°C, 2 min	1	2.5	1309	-	-
8	250°C, 1-2 min (on steel plate)	400°C, 1 min (on steel plate)	4.36	1.6	1390	1390	2.3

In order to enhance the lateral homogeneity of the pyrolysis temperature, especially for 4-6 inch wafers, 1 cm thick stainless steels were placed on top of both hot plates. The first

pyrolysis was set at 250°C for 1 min followed by second pyrolysis at 400°C for 1 min. The second pyrolysis was set at 1 min because the wafer did not need to be rotated to obtain homogeneity. In cases when the sample could not be transferred from the first pyrolysis to the second pyrolysis hotplate within 30 s, an additional one minute pyrolysis with an extra hot plate at 250 °C was required to prevent thermal shock that can cause film cracking. The thermal shock developed when films at room temperature were heated immediately to 400 °C. It was found that much denser films could be obtained when the pyrolysis steps were modified to 250°C, 1-2 min and 400°C, 1 min as shown in Figure 2-2 (b) (section 2.1.1) and the film was RTA at 700°C for 1 min in oxygen ambient at 1 atm. These are now used as the standard processing parameters of PZT films deposition at Penn State. Figure 3- 5 shows the cross-sectional micrograph of a 4.36 μm thick PZT 52/48 film prepared using this modified procedure. It is obvious that the film is denser compared to the film shown Figure 3- 1. It shows some features of a columnar microstructure, but there is no longer a clear boundary between each crystallized layer.



Figure 3- 5: $\text{Pb}(\text{Zr}_{0.52}\text{Ti}_{0.48})\text{O}_3$ films with optimized condition, 250°C, 1 min and 400°C, 1 min and RTA 700°C, 1 min, heating rate 4°C/s

Figure 3- 6 illustrates the dielectric constant as a function of frequency and the polarization-electric field loop of dense and crack free PZT films. The dielectric constant of the dense PZT film is increased to 1390 with $\tan \delta = 2.3 \%$ at 10 kHz. The hysteresis loop is essentially unchanged from that of the porous films, with a remanent polarization of $22 \mu\text{C}/\text{cm}^2$ and a coercive field of 29 kV/cm.

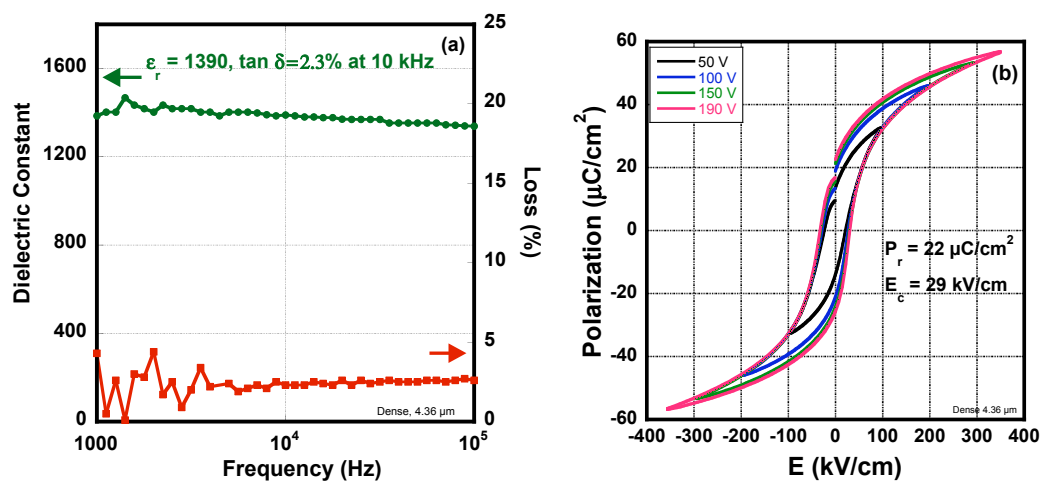


Figure 3- 6: Electrical properties of 4.36 μm thick, dense $\text{Pb}(\text{Zr}_{0.52}\text{Ti}_{0.48})\text{O}_3$ films (a) dielectric constant vs. frequency (b) polarization-electric field loop

The transverse piezoelectric coefficient, $e_{31,f}$ of films with and without visible porosity were characterized by the wafer flexure method and are shown in Table 3- 2 with $3E_c$ to $5E_c$ poling conditions. The $e_{31,f}$ values are comparable.

Table 3- 2: $e_{31,f}$ of 20% Pb excess $\text{Pb}(\text{Zr}_{0.52}\text{Ti}_{0.48})\text{O}_3$, 5.79 μm and 10% Pb excess $\text{Pb}(\text{Zr}_{0.52}\text{Ti}_{0.48})\text{O}_3$, 4.36 μm

PZT film conditions	$e_{31,f}$ ($\mu\text{C}/\text{cm}^2$) (poled at $3E_c$)	$e_{31,f}$ ($\mu\text{C}/\text{cm}^2$) (with poling $5E_c$)
20% Pb excess $\text{Pb}(\text{Zr}_{0.52}\text{Ti}_{0.48})\text{O}_3$, 5.79 μm	-8.1 ± 0.8	-8.5 ± 0.8
10% Pb excess $\text{Pb}(\text{Zr}_{0.52}\text{Ti}_{0.48})\text{O}_3$, 4.36 μm	-7.3 ± 0.7	-8.6 ± 0.8

This improvement in processing was generalizable to other compositions of PZT. PZT (30/70) is used for pyroelectric and piezoelectric sensor applications.^[1, 79] Figure 3- 7 shows the cross-sectional micrograph of 2.17 μm and 3.3 μm thick PZT 30/70 films. The films are dense

with a columnar structure. Table 3- 3 summarizes the properties of 20% Pb-excess $\text{Pb}(\text{Zr}_{0.30}\text{Ti}_{0.70})\text{O}_3$ films.

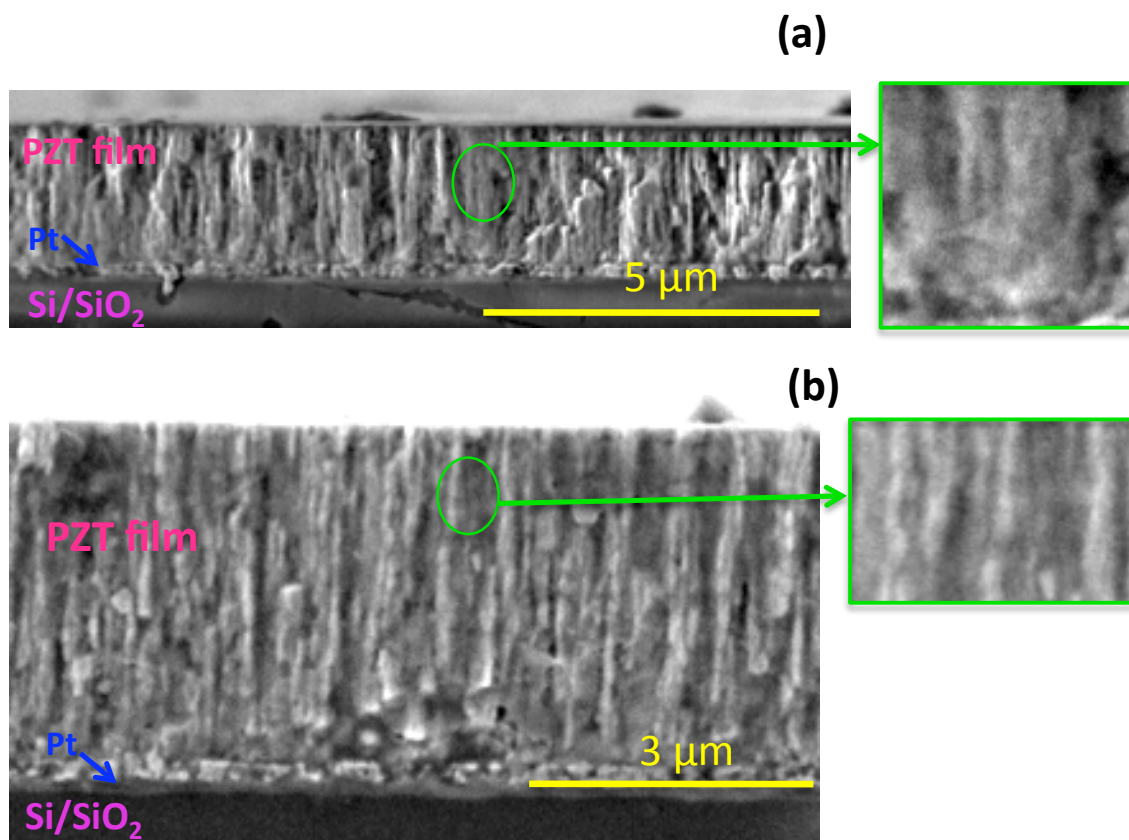


Figure 3- 7: 20% Pb-excess $\text{Pb}(\text{Zr}_{0.30}\text{Ti}_{0.70})\text{O}_3$ films (a) 2.17 μm thick film (b) 3.30 μm thick film

Table 3- 3: Electrical properties of 2.17 μm and 3.30 μm 20% Pb-excess $\text{Pb}(\text{Zr}_{0.30}\text{Ti}_{0.70})\text{O}_3$ films

$\text{Pb}(\text{Zr}_{0.30}\text{Ti}_{0.70})\text{O}_3$	Measured Dielectric Constant (10 kHz)	Loss (%)	P_r ($\mu\text{C}/\text{cm}^2$)	E_c (kV/cm)
2.17 μm	640	2.5	33	72
3.30 μm	664	1.7	38	83

Using the conditions, which produced dense films, PZT 52/48 films with thicknesses ranging from 0.28 μm to 4.4 μm were studied to track the thickness dependence of the electrical

properties, as well as the dielectric and piezoelectric nonlinearity. Figure 3- 8 illustrates the XRD patterns of dense PZT films with three different thicknesses: 0.28 μm , 1.09 μm , and 4.40 μm . These films were deposited on Pt-coated Si substrates purchased from Nova Electronic Materials using a 0.75 M solution with 10% Pb-excess. The result shows polycrystalline films with some {001} and {111} orientation and no pyrochlore. The relative intensities of the X-ray peaks substantially change with the film thickness, with a progressive evolution towards {100} texture observed. The texture of the film depends on the nucleation and growth of crystals during processing. It appears that using the processing conditions described here, the substrate dominated the nucleation of the PZT in thinner films, because the (111) Pt layer favors the (111) heterogeneous PZT nucleation from the substrate.^[34] As the thickness increases, the substrate does not play as significant role in orientation of the film.^[34, 80, 81]

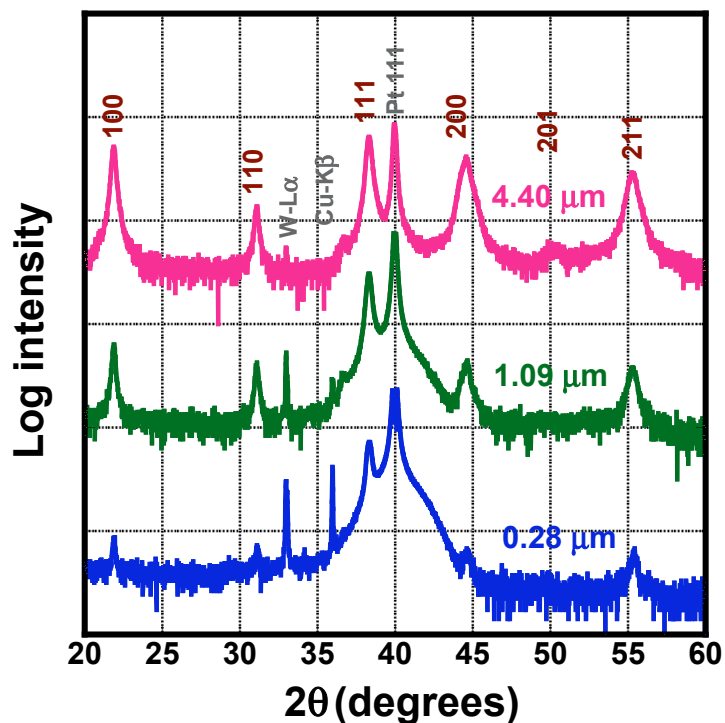


Figure 3- 8: XRD of $\text{Pb}(\text{Zr}_{0.52}\text{Ti}_{0.48})\text{O}_3$ films of various thickness deposited using a 0.75 M, 10% Pb-excess PZT solution

The electrical properties for films of different thickness are shown in Table 3- 4. Thicker PZT films show higher dielectric constant values; the loss tangent was low for all samples. There were no systematic changes in the remanent polarization, while the coercive field dropped somewhat as a function of thickness.

Table 3- 4: Remanent polarization and coercive field from hysteresis loops as a function of thickness

PZT film (μm)	ϵ_r (at 1 kHz)	$\tan \delta$ (%) (at 1 kHz)	P_r ($\mu\text{C}/\text{cm}^2$)	E_c (kV/cm)
0.28	1100	3.0	30	49
0.53	1070	3.3	24	70
1.09	1180	2.7	25	45
2.06	1240	2.4	25	36
4.04	1390	3.5	30	35
4.40	1370	4.6	27	32

3.1.2 Transverse Piezoelectric Coefficient ($e_{31,f}$) of PZT Films with Mixed {001} and {111} Orientation

Measurements were made of the $e_{31,f}$ coefficient of the PZT films with mixed {001} and {111} orientation. The $e_{31,f}$ was about $-5.9 \text{ C}/\text{m}^2$ to $-7.3 \text{ C}/\text{m}^2$, which is similar to reports from Wolf and Trolier-McKinstry^[18] and Ledermann et al.^[3]

Aging is the loss of polarizability or the loss of polarization with time in poled ferroelectric materials. Figure 3- 9 schematically illustrates the remanent polarization as a function of time. The rapid polarization decay at the beginning is related to the relaxation of dielectric, depolarization, or initial polarization loss and the aging is related to domain stabilization.^[82, 83]

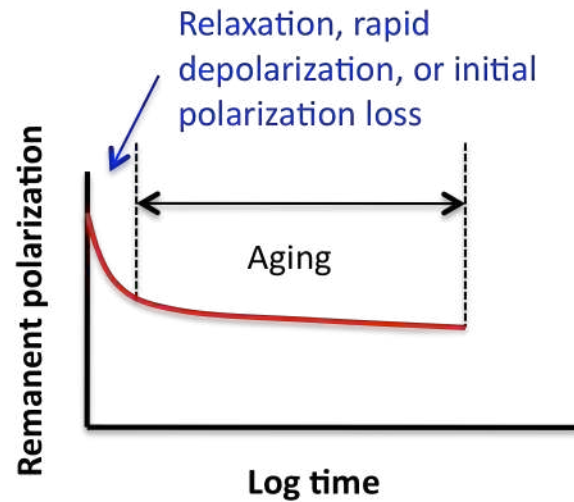


Figure 3- 9: The general curve of remanent polarization vs. log time.^[82]

In this thesis, the aging rate of dielectric permittivity (ϵ_r) was studied by monitoring the capacitance as a function of time after poling film for $3E_c$ for 20 min. The aging rate of permittivity was calculated from a logarithmic fit to the empirical data. In this experiment, a 1.09 μm mixed {001} and {111} orientation PZT (52/48) film was used. The aging rate of this film is about -1.1% / decade shown in Figure 3- 10, which agrees well with the values of -1 to -3 % / decade in reports by Pocalwich^[84] and Kholkin et al.^[85]

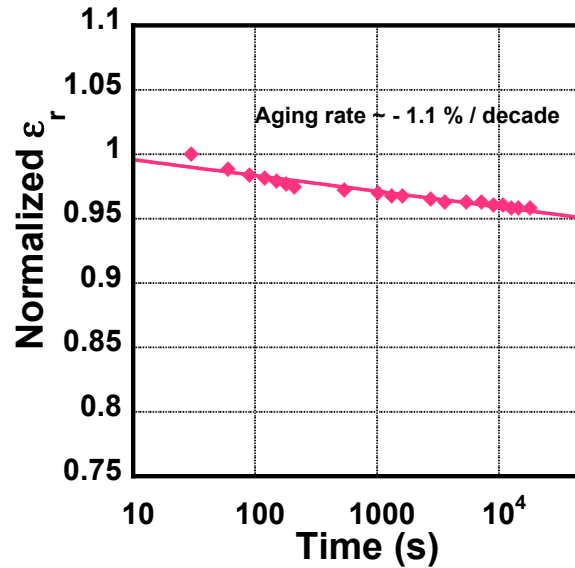


Figure 3- 10: Aging of the dielectric permittivity (ϵ_r) of 1.09 μm thick mixed $\{001\}$ and $\{111\}$ orientation PZT (52/48) film following poling

In addition, the aging rate of the transverse piezoelectric coefficient ($e_{31,f}$) was collected by monitoring $e_{31,f}$ as a function of time after poling. The aging rate of $e_{31,f}$ was calculated from a logarithmic fit to the empirical data.^[73] In this experiment, a 2.35 μm thick mixed $\{001\}$ and $\{111\}$ orientation PZT (52/48) film was used. The aging rate of this film is about -5% /decade, which is also slightly lower than the report from Polcawich^[84] and Kholkin et al.^[85], which are about -6 to -12% / decade. Kholkin et al. studied the aging of piezoelectric coefficient and dielectric permittivity of PZT thin films and PZT ceramics. They found that the aging rate of dielectric permittivity is lower than the aging rate of piezoelectric coefficient in PZT thin films. In contrast, the aging rate of both piezoelectric coefficient and dielectric permittivity of PZT ceramics are comparable.^[83, 85]

3.2 {001}-Textured Orientation Control Processing

As was described in section 2.1.3, strong {001} orientation in MPB PZT films increases the piezoelectric response. This section describes work on the optimization of the process parameters for the deposition of {001}-oriented PZT films. Two principal parts of the process were varied; first the role of the amount of lead excess, the pyrolysis temperature, and the crystallization temperature of the PbTiO_3 buffer layer were examined. Once a reasonable template layer was achieved, the heating cycle during the PZT crystallization was studied to optimize the orientation. The degree of orientation, electrical properties, and transverse piezoelectric coefficients ($e_{31,t}$) of the resulting films are discussed.

3.2.1 PbTiO_3 Buffer Layer Study

PbTiO_3 buffer layers were chosen due to good lattice matching with PZT films, and the strong propensity for development of {001} orientation.^[29] Ledermann et al.^[3] used 10 nm thick sputter deposited {001} oriented PbTiO_3 seed layers to texture PZT films. Calame and Murali^[25] achieved {001} oriented PZT films using a 20 nm thick {001} oriented PbTiO_3 seed layer deposited by a sol-gel technique. Kushida et al.^[34] demonstrated that the aging of the solution promotes (100) orientation of PbTiO_3 films on Pt/Si substrate due to the change of molecular size in solution and polymerization. They also studied the effect of the substrate on the film orientation.^[34]

In an attempt to reproduce this work, a study of the orientation of PbTiO_3 layers, with two different pyrolysis temperatures and three crystallization steps, was undertaken. First the PbTiO_3 films were pyrolyzed at 250°C for 1 min and pyrolyzed at 350°C or 400°C for 1 min as shown in sections 2.1.3.2 and 2.1.3.3. Thereafter, the PbTiO_3 films were crystallized at 535°C,

550°C, or 580°C for 1 min by RTA. Figure 3- 11 shows the XRD patterns of the resulting PbTiO₃ films.

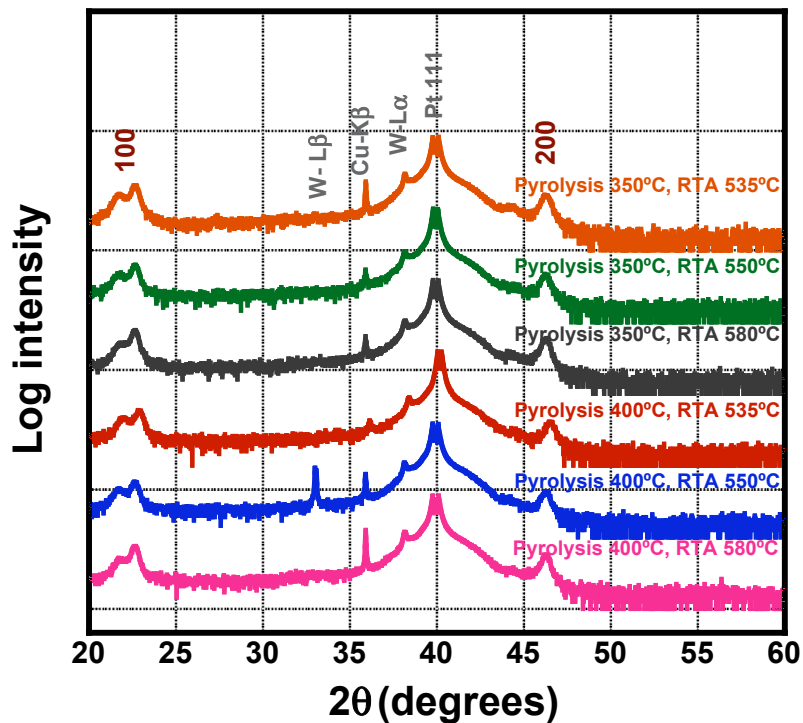


Figure 3- 11: XRD of 30% Pb-excess PbTiO₃ buffer layers for different pyrolysis and crystallization conditions

The results showed that there is no significant difference in orientation for different pyrolysis and crystallization temperatures; in all cases, high levels of {001} orientation were achieved. Therefore, this {001} PbTiO₃ is suitable for use as a template layer for {001}-textured PZT films.^[3] A second pyrolysis temperature of 400°C for 1 min and crystallization temperature at 580°C was chosen for subsequent buffer layer deposition. The thickness of PbTiO₃ buffer layer is about 30 nm thick.

3.2.2 PZT Films on PbTiO₃ Buffer Layers

After deposition of a 30 nm PbTiO₃ film, PZT solution was spun on to the wafer at 1500 rpm for 30 s, pyrolyzed at 250°C and 400°C for 1 min and crystallized at 700°C for 1 min by RTA (which are the conditions used for preparation of dense, PZT films with mixed {001} and {111} orientation) as described in section 2.1.2. The steps were repeated until the desired thickness was achieved. Figure 3- 12 shows XRD patterns of PZT films prepared in this manner with and without the PbTiO₃ layer. It is clear that the level of {001} orientation increases when the orienting layer is used, however, a large (111) peak is still apparent. Therefore, the heat-treatment conditions were modified to try and improve the orientation.

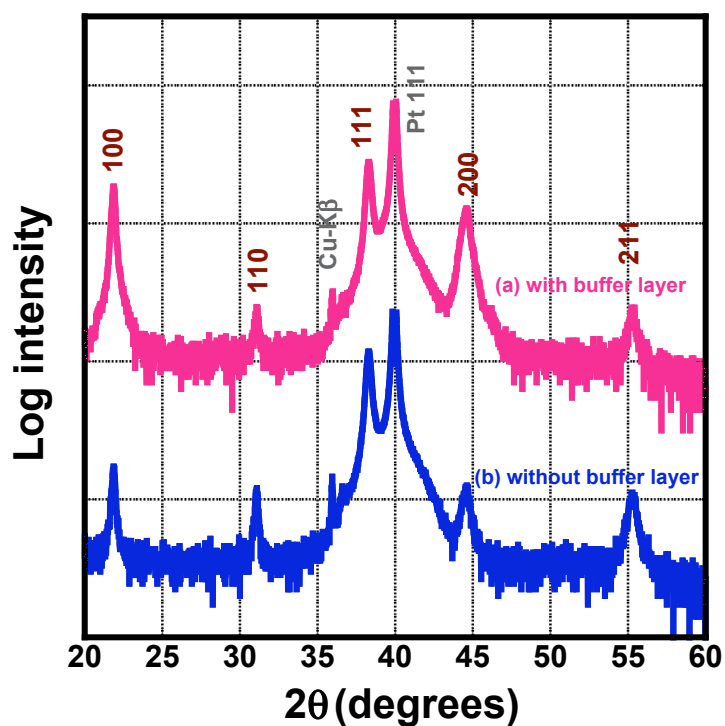


Figure 3- 12: XRD patterns of (a) PZT on a PbTiO₃ buffer layer (b) PZT film without PbTiO₃ buffer layer, with pyrolysis 250°C, 1 min and 400°C, 1 min and RTA 700°C, 1 min, heating rate 4°C/s

After PbTiO_3 buffer layer deposition, the 10% Pb-excess PZT solution was spun onto the wafer at 1500 rpm for 30 s and pyrolyzed at 350°C for 20 s, as described in section 2.1.3.3. The spinning and pyrolysis steps were repeated 4 times before crystallization. The PZT films were then crystallized at 650°C for 1 min by RTA. The heating rates were varied from 10°C/s to 65°C/s . Two Pt-coated silicon substrates were used: Nova substrates and Ramtron substrates.

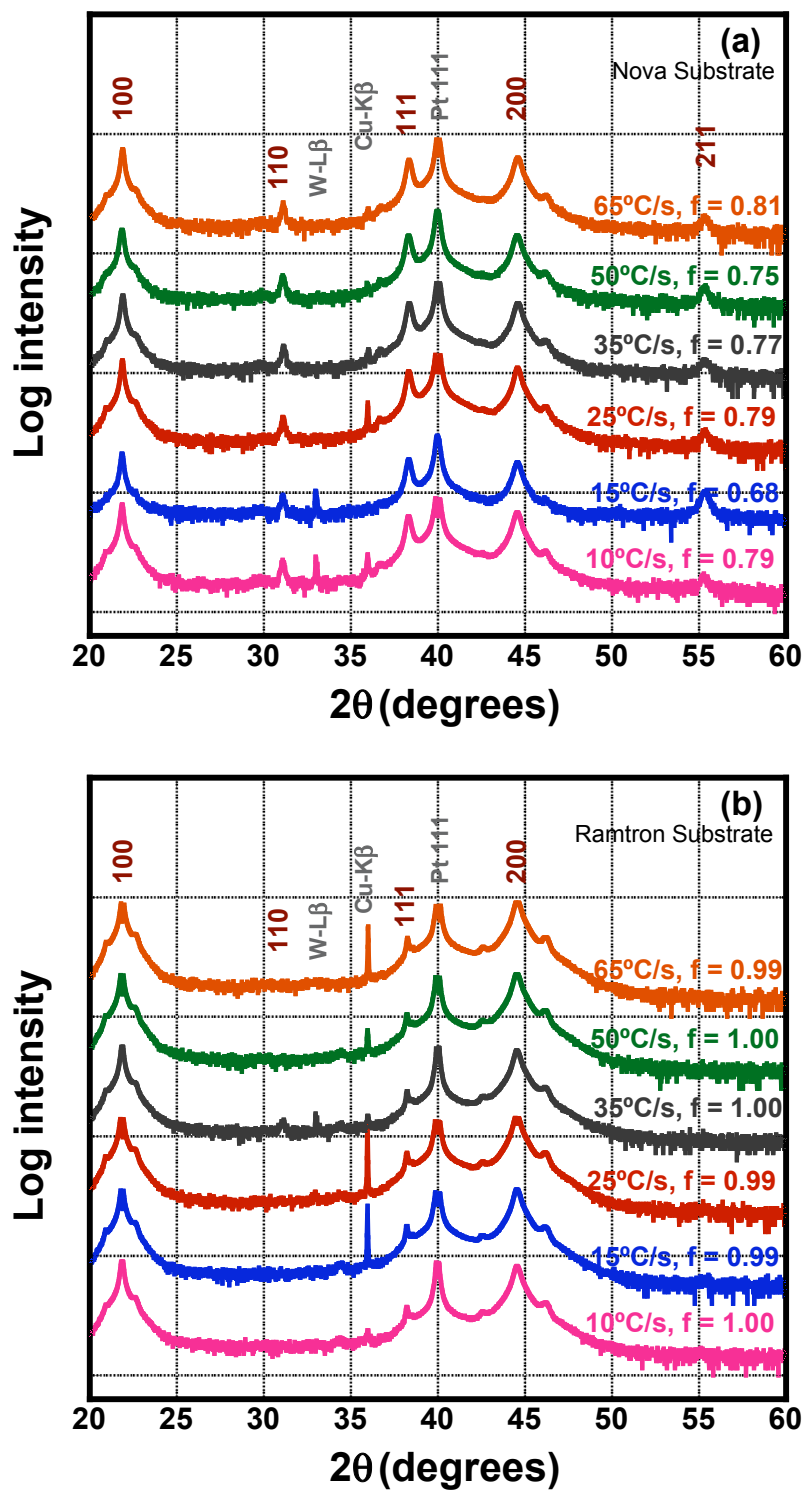


Figure 3- 13: XRD patterns of PZT films prepared with different heating rates on a PbTiO_3 layer on (a) Nova substrates (b) Ramtron substrates

Figure 3- 13 illustrates the XRD patterns of PZT films on PbTiO_3 layer as a function of the heating rate used during crystallization. The Lotgering factor (f) is used to estimate the quality of the PZT film orientation as described in section 2.2. Higher Lotgering factors correspond to improved $\{001\}$ orientation. In comparing the results shown in Figure 3- 12 and Figure 3- 13, it is obvious that both the orienting layer and the pyrolysis conditions influence the degree of $\{001\}$ orientation of PZT films, while the heating rate during the RTA step does not. These data contrast with previous reports that PZT films crystallized with high heating rates develop more (111) orientation than those prepared using a low heating rate.^[6, 29] The buffer PbTiO_3 layer used between the substrate and PZT films should decrease heterogeneous nucleation of (111) oriented grains from the substrate.^[6] However, some (111) orientation is still present in the films, as is a small volume fraction of pyrochlore. Therefore, subsequent experiments were undertaken to prepare better-oriented films with a minimum of second phase content, as will be described in section 3.2.3.

Figure 3- 14 shows the cross sections of $0.94 \mu\text{m}$ thick PZT films on Nova and Ramtron substrates, respectively. There is some columnar character to the grains. The dense, crack free films are similar to those of Ledermann et al. and Kalpat et al.^[3, 29]

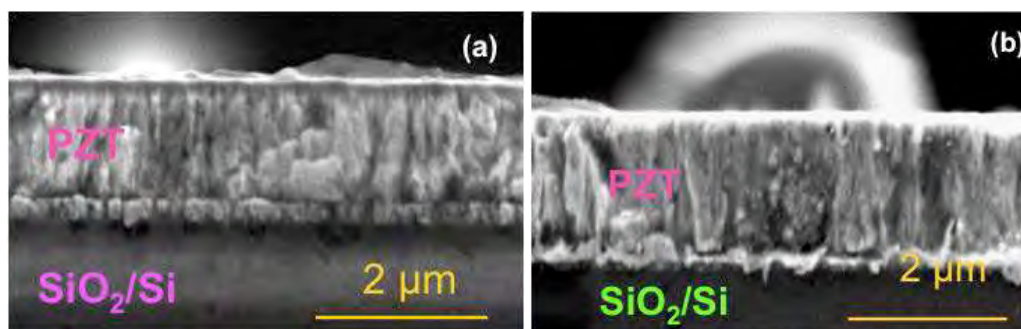


Figure 3- 14: Cross section of $\{100\}$ oriented PZT films on (a) a Nova substrate (b) a Ramtron substrate

The electrical properties of the partially {001}-oriented PZT films on Ramtron and Nova substrates are as follows. For the Ramtron substrate, the dielectric constant is 1140 with $\tan \delta = 3.3 \%$, at 1 kHz. For the Nova substrate, the dielectric constant is 1060 with $\tan \delta = 2.3 \%$, at 1 kHz. Comparing to Ledermann et al., the dielectric constants of both films in this work are higher than those of the reported PZT {001} 53/47, and the losses are lower.^[3]

Figure 3- 15 illustrates the hysteresis loops of partially {001}-oriented PZT films on Nova and Ramtron substrates. The P_r and E_c of PZT films on Nova substrates are $33 \mu\text{C}/\text{cm}^2$ and $45 \text{ kV}/\text{cm}$ and on Ramtron substrates are $25 \mu\text{C}/\text{cm}^2$ and $56 \text{ kV}/\text{cm}$, respectively. For equivalent levels of film texture, films with lower remanent polarization values have low $e_{31,f}$.^[1] The remanent polarization of the PZT film on the Ramtron substrate is lower than that on the Nova substrate. It is important to understand how this will affect the relative $e_{31,f}$ values. It was found that the $e_{31,f}$ of {001}-textured PZT films on Nova and Ramtron substrates were $-7 \text{ C}/\text{m}^2$ when the films were poled at $3E_c$ for 20 min.^[6] Improved results were obtained using an optimized poling process as described in section 3.2.5.

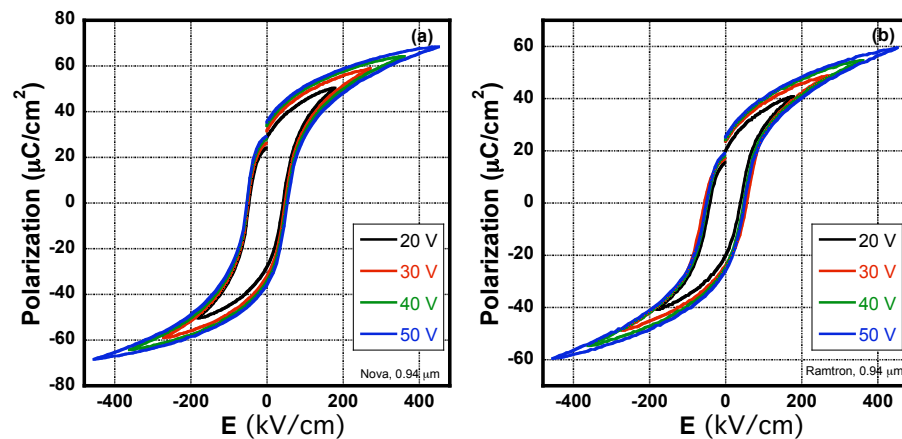


Figure 3- 15: Hysteresis loops of PZT films on PbTiO_3 buffer layer (a) Nova substrate (b) Ramtron substrate

3.2.3 Increased %Pb Content in PbTiO₃ Orienting Layer

The concentration of Pb-excess in the PbTiO₃ layer was also changed both in an attempt to reduce the amount of pyrochlore in the oriented films, and to understand the impact on the degree of {001} orientation. The high volatility of lead can create locally Pb-depleted zones, especially near the surface in Pb-based oxide thin films. The low lead content leads to formation of a parasitic pyrochlore phase that degrades the electrical and electromechanical properties.^[6] Reaney et al. found that addition of lead excess significantly improved the quality of the films in term of dielectric constant and remanent polarization.^[32]

Figure 3- 16 shows the result of 40% Pb-excess PbTiO₃ buffer layers prepared with pyrolysis temperature of 250°C and 400°C for 1 min with different crystallization conditions.

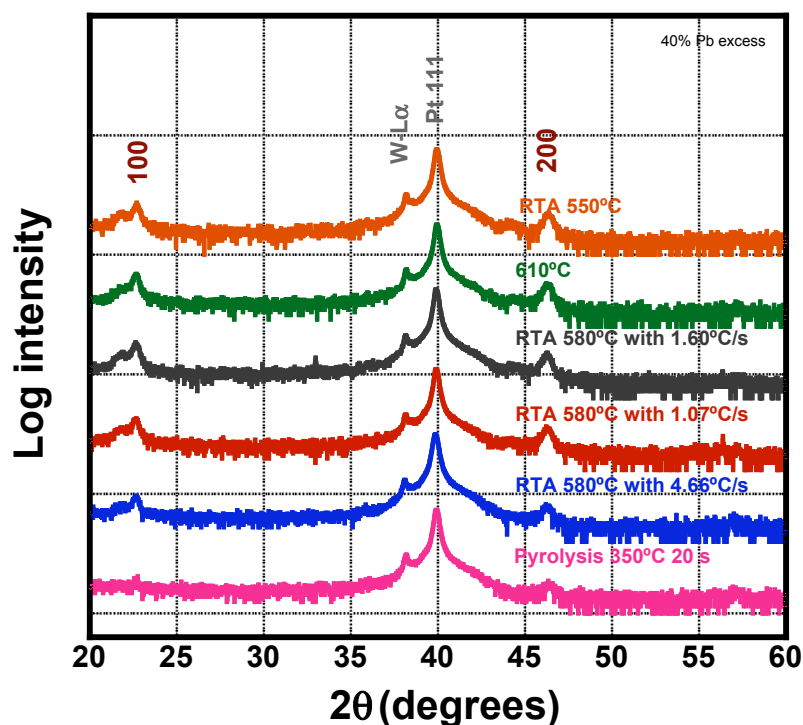


Figure 3- 16: X-ray diffraction scans of 40% Pb-excess PbTiO₃ buffer layers

There is no significant difference in orientation for different crystallization temperatures and heating rates. In all cases, high levels of $\{001\}$ orientation were achieved. Therefore, the 40% Pb-excess PbTiO_3 templates were used for PZT film deposition as shown in Figure 3- 17 (b). Figure 3- 17 shows the result of different PZT film thicknesses with a pyrolysis at 350°C for 20 s and crystallization with a heating rate of $10^\circ\text{C}/\text{s}$ on 40% Pb-excess PbTiO_3 layers (with pyrolysis temperature of 250°C and 400°C for 1 min) compared to the PZT films on 30% Pb-excess PbTiO_3 layers.

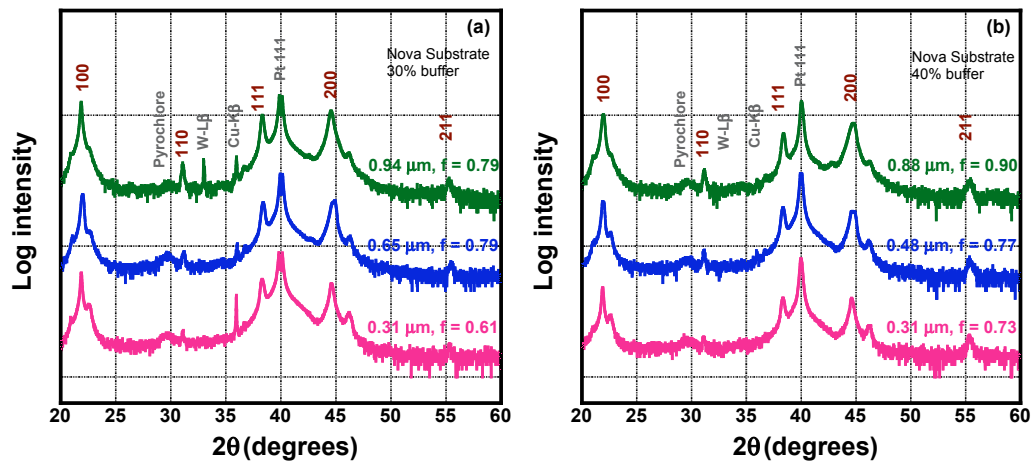


Figure 3- 17: PZT films on (a) 30% Pb-excess buffer layer (b) 40% Pb-excess buffer layer, Nova substrates

It can be seen that the Lotgering factor (f) of PZT films on 40% Pb-excess PbTiO_3 layers is higher than those on 30% Pb-excess PbTiO_3 layers. However, all films have some amount of pyrochlore phase in XRD pattern. It is important to eliminate the pyrochlore phase. The summary of electrical properties of those films is shown in Table 3- 5. The plots of dielectric constant vs. frequency and P-E loops are in Appendix A.

In addition, it has to be noted that there are some difficulties in obtaining repeatable levels of $\{001\}$ PbTiO_3 buffer layers for PZT films on (111) Pt/Ti/SiO₂/Si Nova Electronic

material substrates. Therefore, (111) Pt/TiO₂/SiO₂ Ramtron substrates were employed for PZT film deposition. Figure 3- 18 shows the comparison of 40% Pb-excess PbTiO₃ layers prepared with pyrolysis temperatures of 250°C and 400°C for 1 min on Nova and Ramtron substrates. Stronger {001} PbTiO₃ orientation was achieved on Ramtron substrates compared to Nova substrates. Thus, these were used for the remainder of the oriented PZT film depositions.

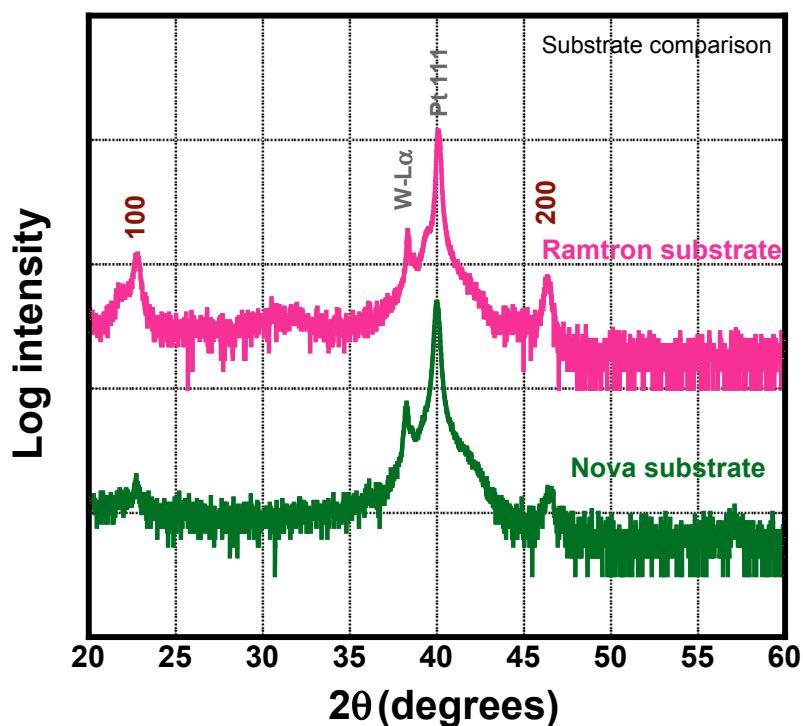


Figure 3- 18: X-Ray diffraction scans of 40% Pb-excess PbTiO₃ layers on Ramtron compared to Nova substrates

Figure 3- 19 illustrates the result for different PZT film thicknesses. The degree of orientation was quantified using the Lotgering factor. It can be seen that the Lotgering factor of {001}-textured PZT films on 40% Pb-excess PbTiO₃ / Ramtron substrates increases with thickness. However, the Lotgering factor of the thinnest sample (0.31 μm) was only 0.43.

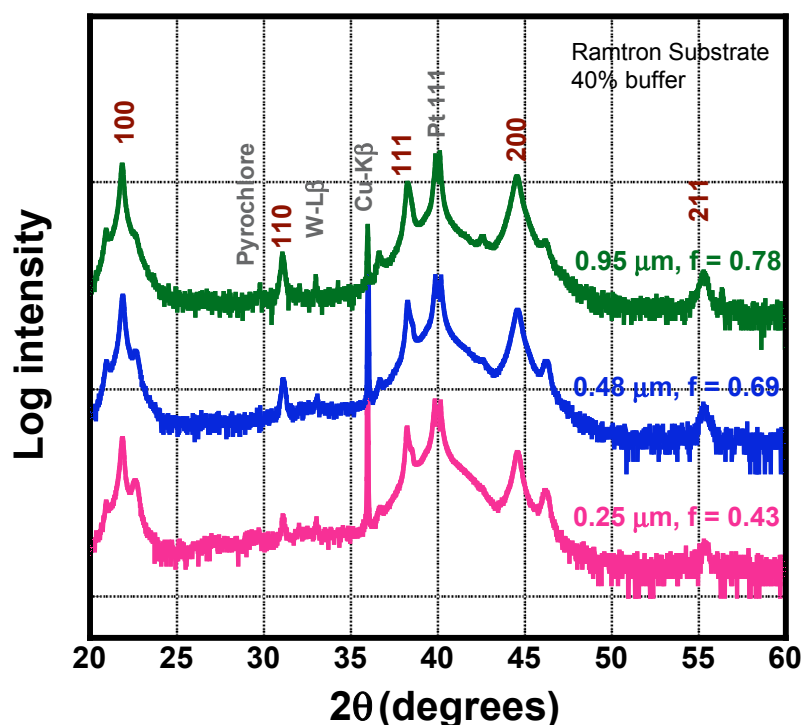


Figure 3- 19: PZT films on 40% Pb-excess buffer layer with Ramtron substrates. The second pyrolysis temperature was 350°C for 20 s and the crystallization was done using a heating rate of 10°C/s. The 40% Pb-excess PbTiO_3 layers were prepared with pyrolysis temperatures of 250°C and 400°C for 1 min on Ramtron substrates.

The dielectric constant and loss are shown in Table 3- 5 and the plots as a function of frequency are in Appendix A. The results reveal that the permittivity of the films drops as film thickness decreases. Comparing to Ledermann et al.^[3] and Tyholdt et al.^[38], the dielectric constant of the 0.95 μm thick film in this work is higher than those reported for {001} PZT 53/47. For the thinnest PZT films, the dielectric constants are low. The P-E loops are unusual, so the heat treatment of thinnest PZT films had to be modified as will be described in section 3.2.4.

In attempt to further improve the {001} orientation, the crystallization step was modified. Kalpat and Uchino^[29] found that {001} oriented PZT film can be prepared using heating rates less than 10°C/s. Moreover, they set a short plateau at 520°C to favor nucleation of {001} grains in the RTA step.

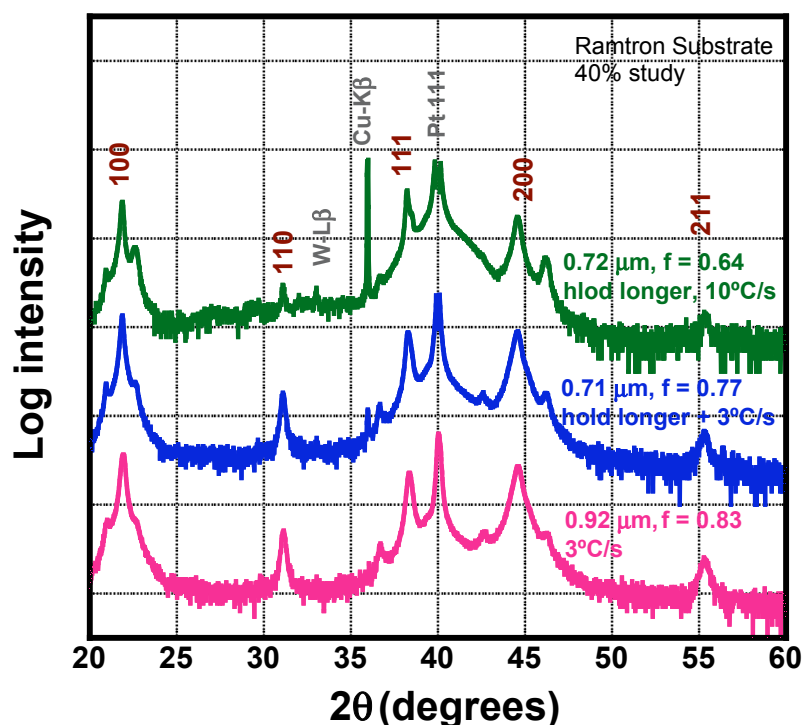


Figure 3- 20: PZT on 40% Pb-excess buffer layer with Ramtron substrates with different conditions: hold longer time was to hold at 520°C for 60 s and regular hold time was to hold at 520°C for 30 s

Figure 3- 20 illustrates the XRD patterns of PZT films on PbTiO_3 layers with longer holding times and slower heating rates of 3°C/s and 10°C/s during the crystallization step. The Lotgering factor of a 0.7 μm thick PZT film crystallized using a heating rate as 3°C/s and a longer hold time at 520°C is high compared to PZT films prepared with a heating rate of 10°C/s. The transverse piezoelectric coefficients were measured and are reported in section 3.2.6.

3.2.4 {001}-Textured Orientation Control Processing of Thin PZT Films ($\sim 0.24 \mu\text{m}$)

Using the processing described in the previous section, the $e_{31,f}$ and the dielectric constant of the thinnest samples ($\sim 0.25 \mu\text{m}$) were about -5 C/m^2 and 290-490, respectively. Thus, the heat treatments were modified for the thinnest PZT films to improve the $e_{31,f}$ and dielectric constant.

A {001} oriented PbTiO_3 film prepared using pyrolysis temperatures of 250°C and 400°C for 1 min was used as a template layer. After deposition of one layer of PbTiO_3 , PZT solution was spun onto the wafer at 1500 rpm for 30 s, and pyrolyzed at 350°C for 20 s. The spinning and pyrolysis steps were repeated 3 times before crystallization at 650°C for 1 min. The results were compared to those for a $0.24\ \mu\text{m}$ thick PZT film crystallized after each set of spin and pyrolysis steps (See Figure 3- 21). It can be seen that RTA'ing the film every layer produced a higher Lotgering factor than RTA'ing every 3 layers.

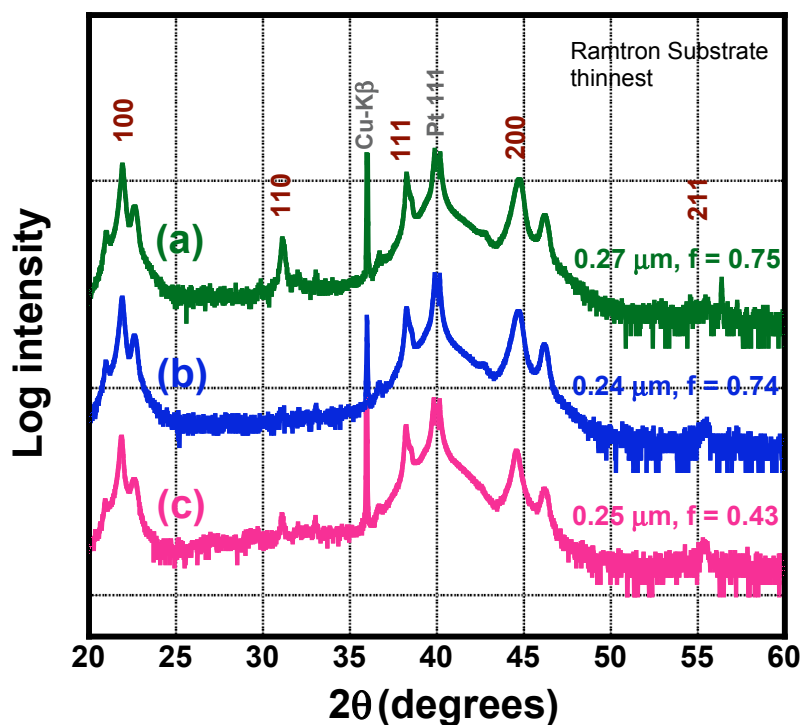


Figure 3- 21: X-Ray diffraction scans of thin PZT films (a) and (b) RTA every layer, and (c) RTA every 3 layers

One possible origin for the degraded electrical properties of the PZT film RTA'd every 3 layers is the existence of a low resistivity PbO phase. To assess this, a sample that had been RTA'd once was furnace annealed at 600°C for 30 minute in an attempt to remove any excess

lead. Figure 3- 22 shows that such an anneal does, indeed, increase the dielectric constant. Nonetheless, the dielectric constant of the thin PZT film that was prepared using an RTA step every layer provided the highest dielectric constant.

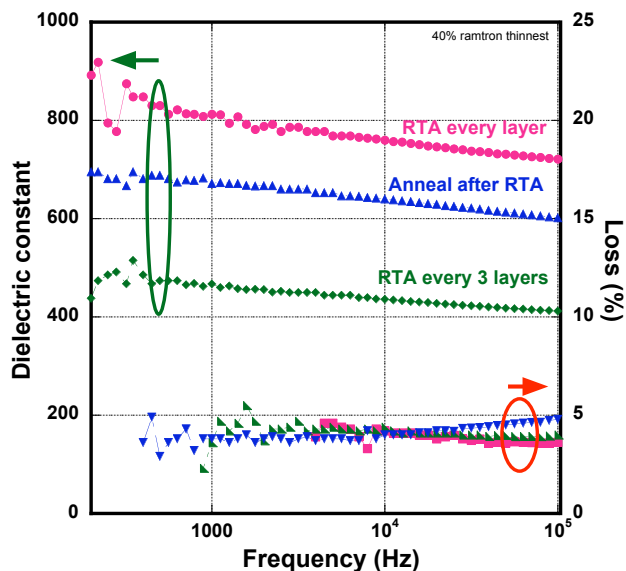


Figure 3- 22: Comparison of the dielectric constants and losses for PZT films on 40% Pb-excess buffer layer with RTA every layer, RTA ever 3 layers, and anneal at 600°C for 30 s after a single RTA step

Figure 3- 23 illustrates the P-E loops of the thin PZT films with different heat treatments. The cleanest hysteresis loops were obtained for the thin PZT films prepared with an RTA step every layer. The other thin films show evidence for a leakage pathway that is likely to be associated with excess PbO. The details of dielectric constant, remanent polarization, and coercive field are shown in Table 3- 5. The $\epsilon_{31,f}$ values for these films are shown in section 3.2.6.

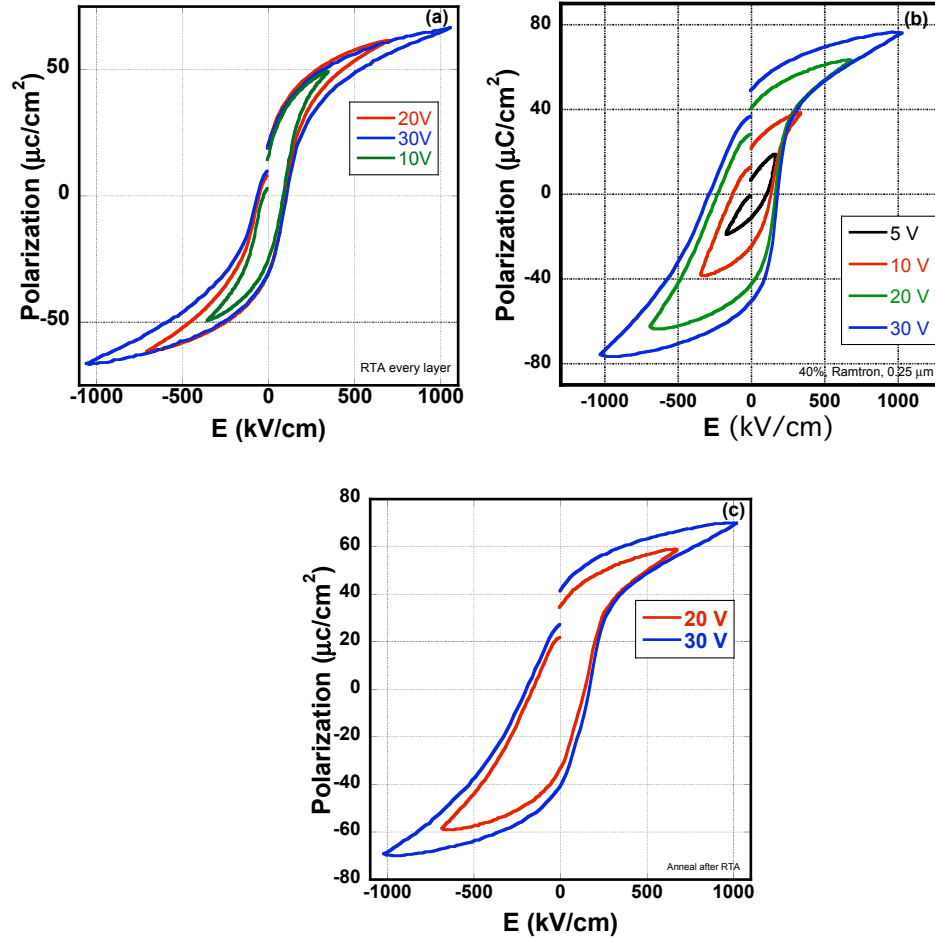


Figure 3- 23: P-E loops for thin PZT films on 40% Pb-excess buffer layer at different heat treatment (a) RTA every layer, (b) RTA every 3 layers, and (c) annealed after RTA step in (b)

3.2.5 Optimized Poling for {001}-Textured PZT Films

In order to achieve optimized $e_{31,f}$ values, a poling study was undertaken.^[3, 73] For this purpose, the top electrode was connected to a positive voltage and the sample was poled at each voltage for 10 min. The applied voltage was increased from 1 V until the measured $e_{31,f}$ saturated. On a second electrode, the bottom electrode was connected to the positive voltage and then the electrode was poled for each voltage for 10 min.^[73]

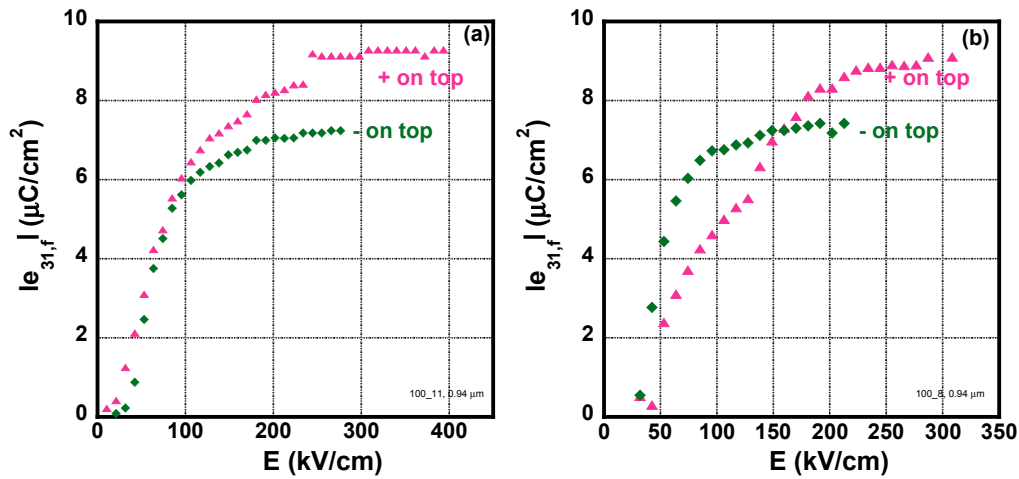


Figure 3- 24: $e_{31,f}$ poling study of PZT films (a) Nova substrates with Lotgering factor = 0.79 (b) Ramtron substrates with Lotgering factor = 1

Figure 3- 24 (a) and

Figure 3- 24 (b) show the effect of poling field on the measured $e_{31,f}$ value of {001}-textured PZT films on Nova and Ramtron substrates, respectively. The data indicate a rapid increase of e_{31} , for poling fields between about 50 and 100 kV/cm. For poling fields above 230 kV/cm, the rate of change in $e_{31,f}$ slows. The maximum value of $e_{31,f}$ achieved was -9.2 C/m^2 and -9.0 C/m^2 for Nova and Ramtron substrates, respectively. This represents a 30 - 50% increase in the piezoelectric coefficient relative to conventionally processed, PZT films with mixed {001} and {111} orientation of the same thickness. This is useful, as it suggests a comparable reduction in driving voltages for MEMS actuators. Thus, in subsequent work, {001}-textured PZT films were poled at 4 to 5 times the coercive voltage for 20 min.

3.2.6 Transverse Piezoelectric Coefficient of {001}-Textured PZT Films

Figure 3- 25 shows a comparison of $e_{31,f}$ values of all PZT films with mixed {001} and {111} orientation and PZT films on 30% Pb-excess and 40% Pb-excess PbTiO_3 buffer layers on

both Nova and Ramtron substrates. Piezoelectric coefficients, $e_{31,f}$ of -14.1 C/m^2 and -10 C/m^2 were achieved for the best oriented PZT films of $1.0 \mu\text{m}$ and $0.24 \mu\text{m}$ thickness, respectively.

These results are consistent with data from Ledermann et al.^[3]

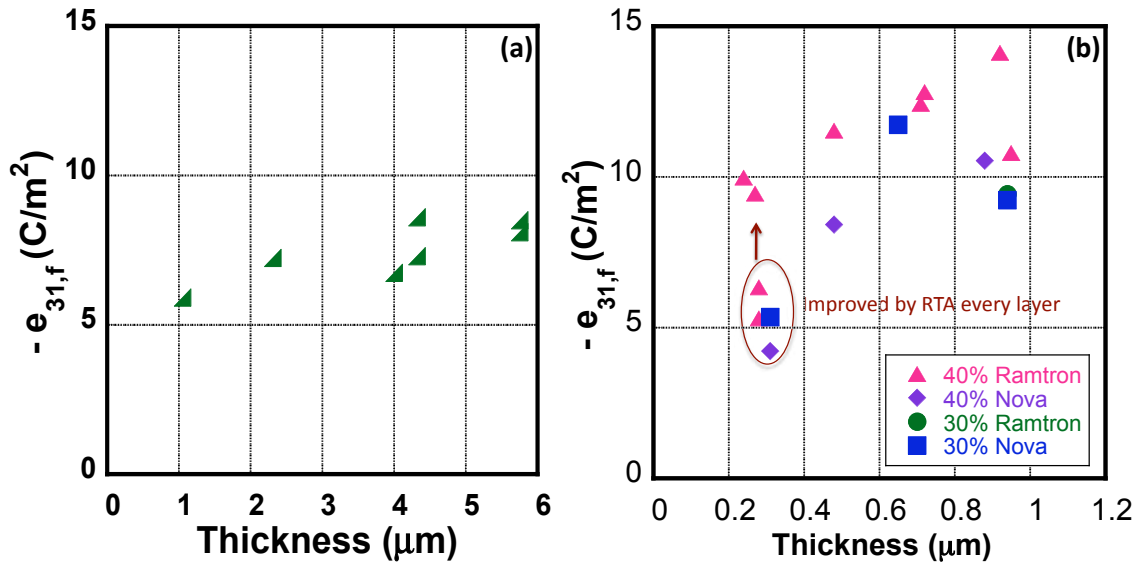


Figure 3- 25: (a) $e_{31,f}$ of PZT films with mixed $\{001\}$ and $\{111\}$ orientation and (b) $e_{31,f}$ of PZT films on 30% and 40% Pb excess PbTiO_3 layers on both Nova and Ramtron substrates as a function of PZT thickness

The $e_{31,f}$ of the poorly textured $0.25 \mu\text{m}$ thick PZT layers are about -5 C/m^2 on either Nova substrates and Ramtron substrates. It has to be noted that in measuring those samples, the poling field was limited to $2 - 3E_c$ due to their lower breakdown voltage. However, when deposition and crystallization steps of the thinnest $\{001\}$ -textured PZT were modified by utilizing an RTA step every layer, the quality of the texture increased considerably. The $e_{31,f}$ of the thinnest $\{001\}$ -texture PZT films improved from -5 C/m^2 to -10 C/m^2 as shown in Figure 3- 25 (b).

3.3 {001} PZT Thin Films on SrRuO₃/(100) SrTiO₃

PZT films were also prepared on (100) single crystal SrTiO₃ coated with SrRuO₃ to prepare {001} oriented PZT films without any buffer layers. It has previously been reported that stronger {001} orientation develops for PbTiO₃ on the SrTiO₃ single crystal rather than Pt coated Si or fused quartz substrates.^[34]

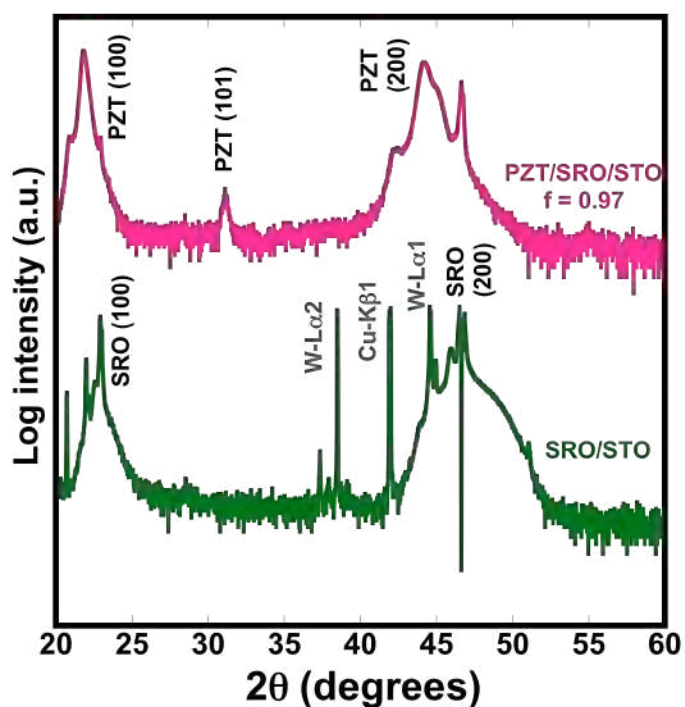


Figure 3- 26: X-Ray diffraction scans of PZT film on an SRO/STO substrate and SRO/STO substrate

Figure 3- 26 shows the result of X-Ray diffraction scans of the PZT film compared to the SRO/STO substrate before PZT deposition. It can be seen that the Lotgering factor of {001} PZT film on SrTiO₃ is 0.96. Consequently, this film can serve as a nearly fully textured endmember in a study of the effect of texture on properties. At 1 kHz, the dielectric constant and loss of this PZT film are 1322 and 4%, respectively. Figure 3- 27 demonstrates the hysteresis loops of this

PZT film. It shows a normal hysteresis loop with remanent polarization and coercive field of $32 \mu\text{C}/\text{cm}^2$ and $30 \text{ kV}/\text{cm}$, respectively.

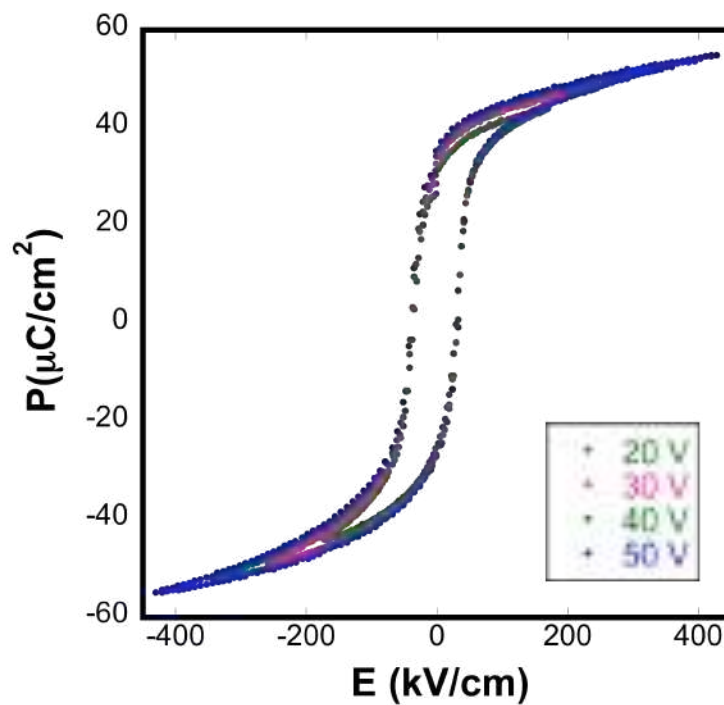


Figure 3- 27: P-E loops for PZT film on SRO/STO

3.4 Summary of Properties of PZT Films

The summary of the electrical properties and the transverse piezoelectric coefficients ($e_{31,t}$) of PZT films on 30% and 40% Pb-excess PbTiO_3 buffer layer with Nova and Ramtron substrates as a function of thickness and the PZT film on $\text{SrRuO}_3/\text{SrTiO}_3$ is shown in Table 3- 5.

Table 3- 5: Summary of $e_{31,f}$ and electrical properties of PZT films

PZT films	$e_{31,f}$ (C/m ²)	Permittivity (at 1 kHz)	$\tan \delta$ (%) (at 1 kHz)	P_r ($\mu\text{C}/\text{cm}^2$)	E_c (kV/cm)
<u>Nova substrates</u>					
PZT on 30% Pb-excess					
0.94 μm	-9.2 ± 0.9	1060	2.3	33	45
0.65 μm	-11.7 ± 1.2	1060	4.8	17	58
0.31 μm	-5.4 ± 0.5	290	1.8	40	226
PZT on 40% Pb-excess					
0.88 μm	-10.5 ± 1.1	1050	4.9	18	50
0.48 μm	-8.4 ± 0.8	790	3.8	18	73
0.31 μm	-4.2 ± 0.4	330	1.4	37	279
<u>Ramtron substrates</u>					
PZT on 30% Pb-excess					
0.94 μm	-9.4 ± 0.9	1140	3.3	25	56
PZT on 40% Pb-excess					
0.95 μm	-10.8 ± 1.1	1250	6.9	32	50
0.48 μm	-11.5 ± 1.2	800	2.6	28	87
0.25 μm	-5.3 ± 0.5	470	3.6	40	196
0.25 μm (anneal after RTA)	-6.3 ± 0.6	670	3.8	42	167
0.24 μm (RTA every layer)	-10.0 ± 1.0	810	3.9	21	107
0.92 μm (3°C/s)	-14.1 ± 1.4	1120	2.6	25	61
0.71 μm (hold longer + 10°C/s)	-10.4 ± 1.0	1040	3.6	29	70
0.72 μm (hold longer + 3°C/s)	-12.4 ± 1.2	1130	2.5	28	63
<u>SrTiO₃ substrate</u>					
1 μm	-	1320	4.0	32	30

In Table 3- 5, some films showed lower remanent polarizations, yet comparatively higher piezoelectric coefficients. There are many factors that influence the transverse piezoelectric coefficient (e.g. Young modulus, Poisson's ratio, etc) shown in Equation 3-2 and Equation 3-3.

$$d_{31} = 2Q\varepsilon_r P_r \quad \text{Equation 3- 2}^{[1, 11, 16]}$$

$$e_{31} = \frac{d_{31}Y}{1-\nu} \quad \text{Equation 3- 3}^{[1, 11, 16]}$$

where d_{31} = transverse piezoelectric coefficient

Q = electrostriction coefficient

ε_r = dielectric permittivity

P_r = remanent polarization

e_{31} = transverse piezoelectric coefficient

Y = Young's modulus

ν = Poisson's ratio

So, there are several possible factors that might complicate the typical relationship between the remanent polarization and the piezoelectric response. Firstly, the films shown in the table will not necessarily have identical microstructures, including grain size and levels of porosity. Secondly, it is difficult to guarantee that all of the PZT films are poled identically. Thirdly, some differences may be introduced because of variations in the aging rate due to internal field.^[11] It would be quite important in future work to determine which of these factors is dominant.

3.5 Grain Sizes of PZT Films

Many researchers observed that grain sizes affect the extrinsic contributions. Xu et al. reported that the properties of PZT films are dependent on film thickness and grain size.^[17] Damjanovic and Demartin reported that the domain wall contribution is larger in coarse grain than fine grain BaTiO₃ ceramics.^[86] Cao and Randall observed that ferroelastic domain size decreases with decreasing grain size, and that the piezoelectric response ultimately drops as the grain size decreases.^[49] It has also been reported that for some processing conditions, thicker films have bigger grains than thinner films.^[17]

Field Emission SEM was employed to observe the grain size of the PZT films in this work. Subsequently, the Image J program was used to estimate the grain sizes. The shortest and longest diameters of each grain were measured and averaged. In this thesis, the grain sizes are reported as a range of minimum and maximum grain sizes with an average grain size and a standard deviation. Figure 3- 28 shows surface micrographs of PZT with either mixed {001} and {111} orientation or {001} texture. It is quite difficult to determine the grain size in these two sets of the films (unlike the film prepared with the previous condition shown in Figure 3- 2). Two possible reasons are that these films are dense and pore free, and were prepared using only 10% lead-excess so that there is less thermal etching of the grain boundaries (the porous film had 20% lead-excess).

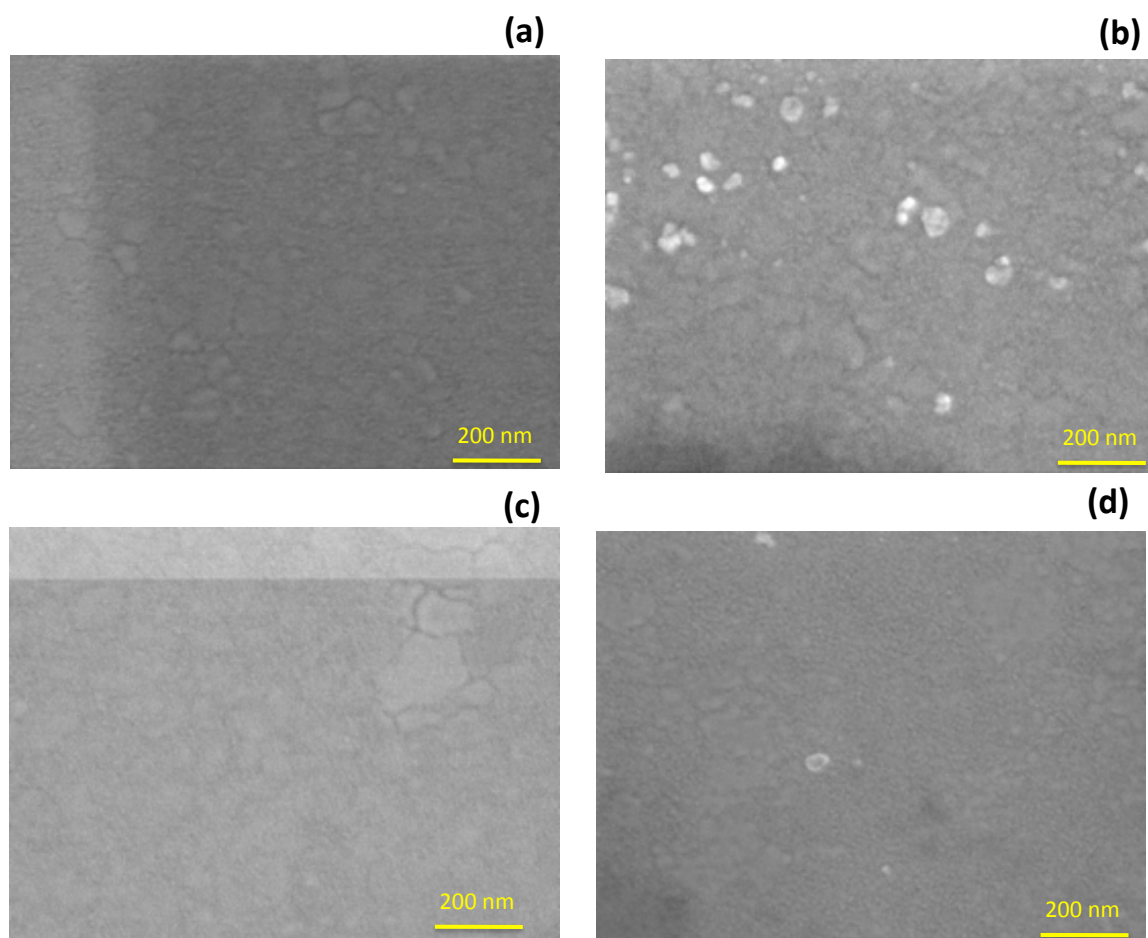


Figure 3- 28: Grain size observation by FE-SEM (a) 0.28 μm mixed $\{001\}$ and $\{111\}$ orientation PZT film, (b) 2.06 μm mixed $\{001\}$ and $\{111\}$ orientation PZT film, (c) 0.27 μm textured PZT film, and (d) 0.92 μm textured PZT film

Table 3- 6 summarizes the grain size of each film thickness. The grain sizes of PZT films with mixed $\{001\}$ and $\{111\}$ orientation vary between ~ 50 and 100 nm for thinner PZT films (~ 0.28 μm to 1.09 μm). When the thickness increased, the grain sizes ranged from 50 to 152 nm. $\{001\}$ textured PZT films have grain sizes from 50 to 210 nm for 0.27 to 0.92 μm thick PZT films. The top surface was used to estimate the grain size because the cross sections of PZT films show columnar grains as described in section 3.1.1.

Table 3- 6: Grain sizes for PZT films of mixed {001} and {111} orientation and {001} texture

PZT films	Grain size range (nm)	Averaged grain size (nm)	Standard deviation (nm)
PZT films with mixed {001} and {111} orientation			
0.28 μm	46 – 103	68	18
0.53 μm	56 – 96	71	12
1.09 μm	48 – 85	67	12
2.06 μm	57 – 130	84	19
4.04 μm	62 – 152	92	23
Textured PZT films			
0.27 μm textured PZT film	58 – 210	96	34
0.48 μm textured PZT film	57 – 123	83	16
0.92 μm textured PZT film	40 – 160	85	24

Chapter 4

Dielectric Nonlinearity

This chapter describes the dielectric nonlinearity of two families of $\text{Pb}(\text{Zr}_{0.52}\text{Ti}_{0.48})\text{O}_3$ thin films in the framework of the Rayleigh law. The thickness dependence, the orientation dependence, and the effects of DC bias fields are discussed.

The ac field dependence of the dielectric properties is important because at higher AC fields, extrinsic contributions become more prominent, resulting in increases in the measured permittivity and piezoelectric coefficients.^[6] In many ferroelectric materials, the extrinsic contributions to the dielectric and piezoelectric properties can be characterized by the Rayleigh law at sub-coercive fields. The Rayleigh law can be written as in Equation 4-1.

$$\boldsymbol{\varepsilon} = \boldsymbol{\varepsilon}_{\text{init}} + \boldsymbol{\alpha}_{\boldsymbol{\varepsilon}} \mathbf{E}_{\text{ac}} \quad \text{Equation 4- 1}$$

where $\boldsymbol{\varepsilon}_{\text{init}}$ is the initial permittivity, $\boldsymbol{\alpha}_{\boldsymbol{\varepsilon}}$ is the irreversible Rayleigh constant, and \mathbf{E}_{ac} is the ac electric field. The parameters $\boldsymbol{\varepsilon}_{\text{init}}$ and $\boldsymbol{\alpha}_{\boldsymbol{\varepsilon}}$ can be determined from the intercept and the slope, respectively of the ac electric field dependence of dielectric constant. $\boldsymbol{\varepsilon}_{\text{init}}$ is due to the intrinsic contribution of the lattice and any reversible domain wall contributions to the permittivity. $\boldsymbol{\alpha}_{\boldsymbol{\varepsilon}}$ is due to the irreversible displacement of the domain walls. The ratio $\boldsymbol{\alpha}_{\boldsymbol{\varepsilon}}/\boldsymbol{\varepsilon}_{\text{init}}$ can be used to quantify the relative importance of irreversible domain wall displacement to the total dielectric permittivity.

There are a few previous studies on the effect of film thickness on the dielectric nonlinearity. For example, Gharb et al.^[30] reported on the effect of dc electric field, film thickness, and temperature on domain wall motion in ferroelectric thin films. They concluded:

- A dc field stabilizes the domain structure and reducing depoling and switching. Therefore, the dielectric permittivity and loss increase more slowly with ac field, as the DC bias field is increased.^[30]
- As the film thickness increased, either the pinning site density or potential well depth drops, and the ac electric field that is required to change the domain structure or domain density is decreased. Thus, the Rayleigh parameters of PZT films increased with increasing film thickness up to about 1 μm and then saturated. Thinner films showed less ac field dependence in the dielectric response because of domain wall motion.^[30]
- Both the intrinsic dielectric permittivity and reversible domain wall motion increase with an increase in temperature toward T_c . Above T_c , the ϵ_{init} values are intrinsic values and extrinsic nonlinearity disappears.^[30]

To amplify the available database on nonlinearity in ferroelectric films, in this work, PZT films with different thicknesses and orientations were characterized at several DC bias fields. Prior to measurement, the samples were poled at room temperature at three to five times the coercive field for 20 minutes.^[6, 18] Dielectric data were collected at 1 kHz with a maximum ac field of about half of the coercive field.^[6, 87] All samples were aged for at least an hour before dielectric nonlinearity measurements.

4.1 Thickness and Orientation Dependence of the Dielectric Nonlinearity

Figure 4- 1 illustrates the amplitude dependence of permittivity as a function of film thickness and film orientations. All of the mixed $\{001\}$ and $\{111\}$ orientation, $\{001\}$ -textured,

and {001}-on SrRuO₃/SrTiO₃ PZT films showed a Rayleigh region for the dielectric permittivity. Up to electric fields of about half of the coercive field, a linear relation between dielectric constant and ac field is observed. Therefore, the PZT films can be described by the Rayleigh law.

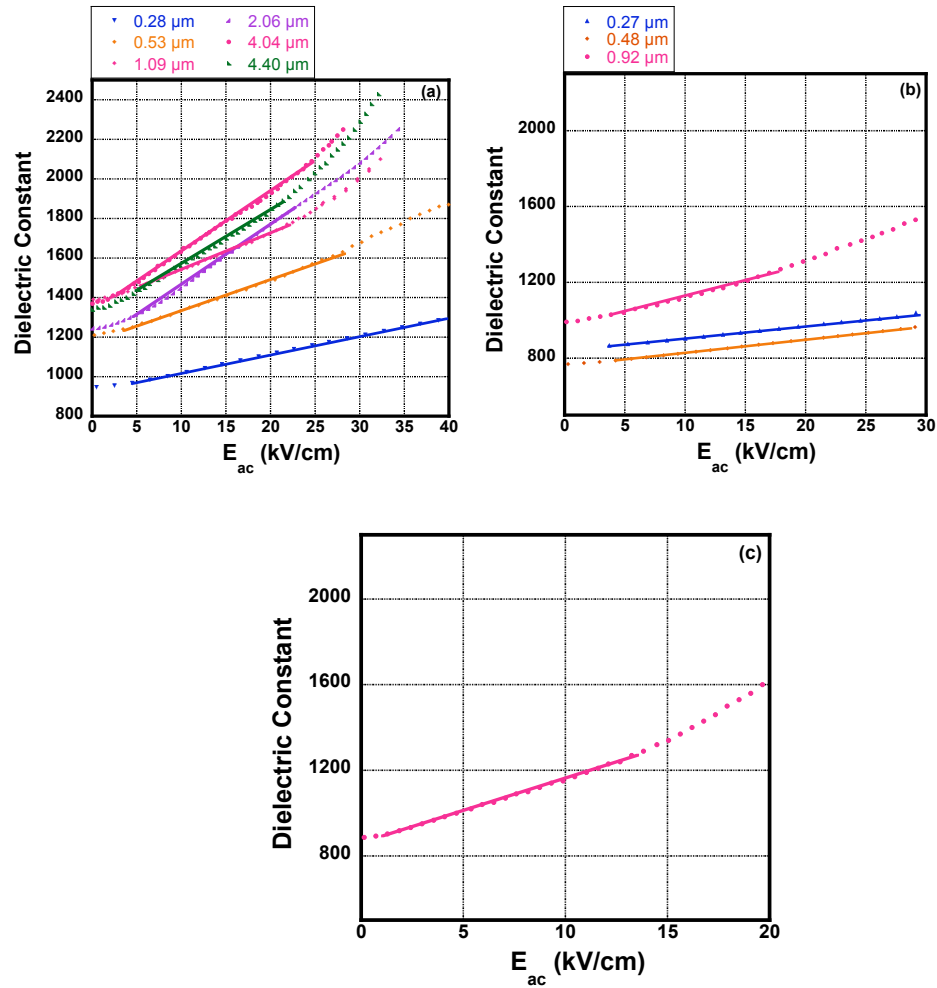


Figure 4- 1: The field dependence of the dielectric permittivity for films of different thickness (a) PZT films with mixed {001} and {111} orientation (b) textured PZT films and (c) {001} PZT film on SrRuO₃/SrTiO₃

The irreversible Rayleigh constant (α_e) and initial permittivity (ϵ_{init}) for PZT films of different thickness are shown in Figure 4- 2. It is clear that the thicker films exhibit higher extrinsic contributions related to the domain wall or phase boundary motion.^[87] This is consistent with previous reports.^[30] There are several possible reasons for the increased nonlinearity. First,

as the PZT film thickness increased, either the potential barriers for moving domain walls may decrease or the pinning site concentration may drop, resulting in a lower ac electric field being required to move the domain wall. A second possible contribution to the thickness dependence of the nonlinearity could be the presence of a second phase at an interface that dilutes the ac field dependence. The net response would be decreased Rayleigh parameters. The external dc bias field to the dielectric nonlinearity can be used to help distinguish between these two possibilities, as described in the next section.

The irreversible domain wall displacement contribution to the total dielectric permittivity can be evaluated using the ratio $\alpha_e E_0 / \epsilon$ where $\epsilon = \epsilon_{\text{init}} + \alpha E$.^[43] At an ac field of 20 kV/cm, for PZT films with mixed {001} and {111} orientation with thicknesses of 0.28 μm , 0.53 μm , 1.09 μm , 2.06 μm , 4.04 μm , and 4.4 μm , respectively, the irreversible response contributes $16.5 \pm 0.1 \%$, $21.2 \pm 0.2 \%$, $21.2 \pm 0.2 \%$, $35.2 \pm 0.2 \%$, $31.3 \pm 0.2 \%$, and $29.4 \pm 0.2 \%$ of the total measured permittivity. For {001} textured PZT films with thicknesses of 0.27 μm , 0.48 μm , and 0.92 μm , irreversible domain wall motion accounts for $14.0 \pm 0.2 \%$, $16.0 \pm 0.1 \%$, and $25.7 \pm 0.6\%$. For the 1 μm thick film on SrRuO₃/SrTiO₃, the ratio was $\sim 40.9 \pm 0.1 \%$ at the same field. The Rayleigh parameters (α_e) increased as the film thickness increased up to about 2 μm and then saturated. Therefore, the domain wall motion is apparently reduced for the film thickness below 2 μm .

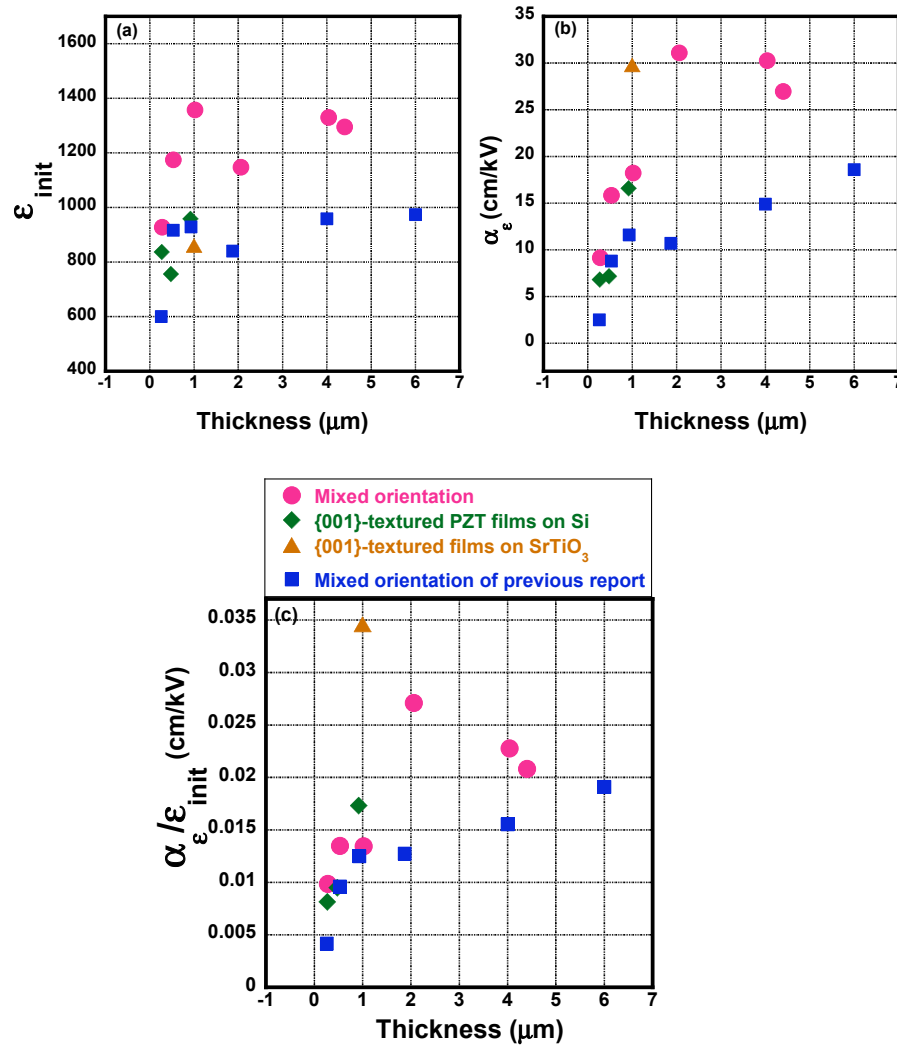


Figure 4- 2: (a) ϵ_{init} , reversible Rayleigh parameter, (b) α_{ϵ} , irreversible Rayleigh parameter and (c) ratio of irreversible to reversible Rayleigh parameters as a function of PZT film thickness and orientation. The previous report is the data from Gharb et al.^[30]

The thickness dependence of the extrinsic contributions in this work is consistent with the previous reports of Gharb et al. and Xu et al.^[17, 30] However, the PZT films here show somewhat higher irreversible to reversible ratios than the previous report.^[30] It is believed that that is because the PZT films in this work are very dense and pore free, which should improve the domain wall mobility.

4.2 Effects of External Bias Fields on the Dielectric Nonlinearity

In this section, the effects of an external dc bias field parallel to P_r on the dielectric nonlinearity were studied for films with different film thickness and different orientations. The results will be described separately for the mixed orientation PZT films and $\{001\}$ textured PZT films with different thickness.

Gharb reported that the application of a positive external dc bias field to both $\{001\}$ and $\{111\}$ oriented PYbN-PT ferroelectric films decrease the ratio of irreversible to reversible dielectric nonlinearity. In contrast, a small negative bias field led to higher reversible and irreversible parameters. They concluded that this was due to the presence of an internal field in the PYbN-PT films.^[6]

4.2.1 PZT Films with Mixed $\{001\}$ and $\{111\}$ Orientation

As can be seen in Figure 4- 3, the dielectric nonlinearity of PZT films with some degree of $\{001\}$ and $\{111\}$ orientation depends on the applied dc bias fields. With increasing external dc bias field, the ac field dependence of the dielectric response is significantly flattened for all PZT thicknesses. This arises from two sources: the tunability of the intrinsic dielectric response of a ferroelectric, and from the fact that the applied dc bias field stabilizes the domain structure, obstructing the depoling and switching.^[6]

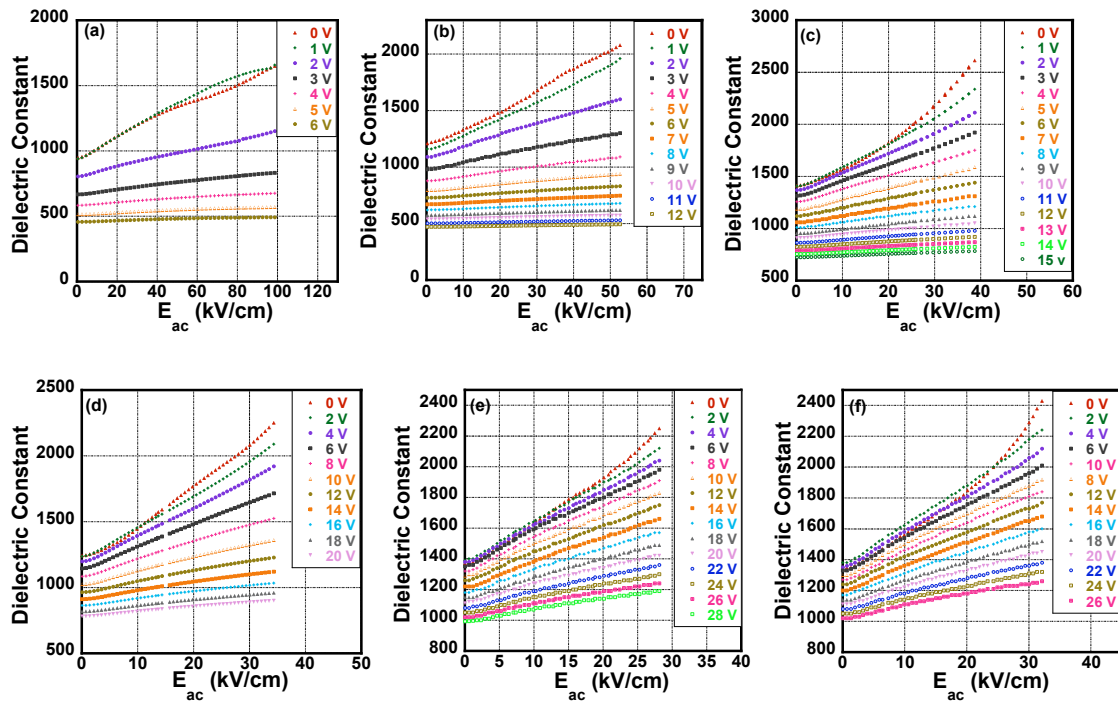


Figure 4- 3: The field dependence of the dielectric permittivity for different thicknesses of PZT films with mixed $\{001\}$ and $\{111\}$ orientation measured at 1 kHz with different dc bias fields. (a) 0.28 μm , (b) 0.53 μm , (c) 1.09 μm , (d) 2.06 μm , (e) 4.04 μm , and (f) 4.40 μm

Figure 4- 4 illustrates the ratio of irreversible to reversible Rayleigh coefficients as a function of external dc bias fields. Each mixed $\{001\}$ and $\{111\}$ orientation PZT film thickness shows that the irreversible to reversible ratio decreases as the external dc bias fields increase. Again, this is because an applied dc bias field stabilizes the domain configuration.

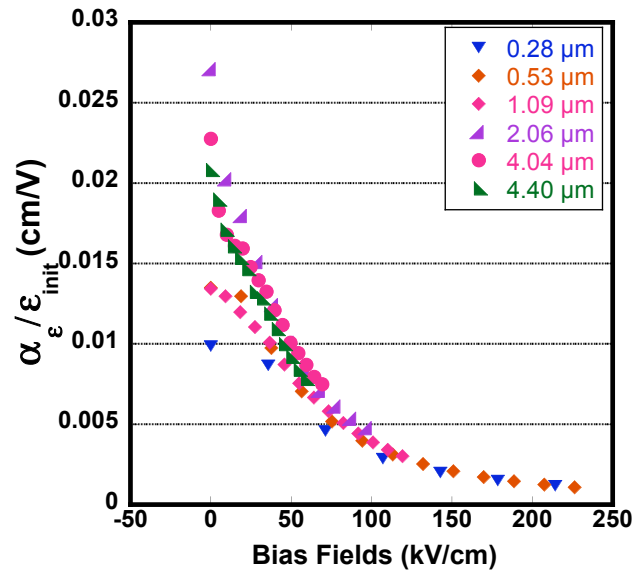


Figure 4- 4: The ratio of irreversible to reversible Rayleigh constants of PZT films with mixed {001} and {111} orientation as a function of applied dc bias fields at different film thicknesses.

4.2.2 {001}-Textured PZT Films on Pt-Coated Si Substrates

As can be seen in Figure 4- 5, the nonlinearity of {001}-textured PZT films on Pt-coated Si substrates depends on the dc bias field. With increasing dc bias, the dielectric permittivity is flattened for the same reasons described for the mixed orientation films.

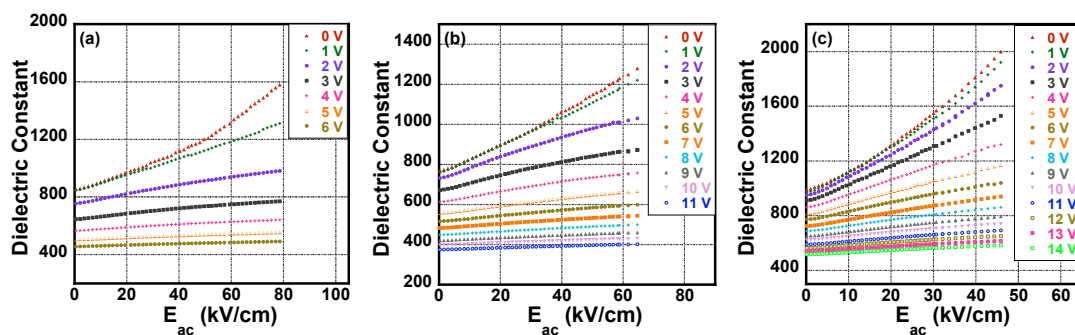


Figure 4- 5: The DC field dependence of the dielectric permittivity for different thicknesses of {001}- textured PZT films on Pt-coated Si substrates at 1 kHz (a) 0.27 μm , (b) 0.48 μm , and (c) 0.92 μm

Figure 4- 6 illustrates the effect of external dc bias fields of the ratio of irreversible to reversible Rayleigh constants in the case of {001}-textured PZT films on Pt-coated Si. For the 0.92 μm textured PZT film, the $\alpha_e/\varepsilon_{\text{init}}$ ratio initially increased and then dropped as the external dc bias field increased. This initial increase in the ratio of $\alpha_e/\varepsilon_{\text{init}}$ is likely to be a result of further poling. Afterwards, the external dc bias field tunes both the intrinsic and extrinsic contributions to the permittivity down. Similar behavior was observed in 0.45 μm , and 0.27 μm thick {001}-textured PZT films.

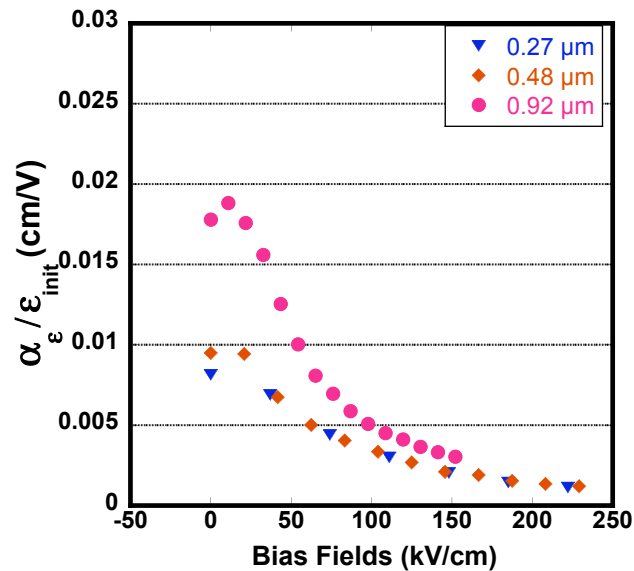


Figure 4- 6: The external dc bias fields dependence of irreversible to reversible Rayleigh ratio for 0.27 μm , 0.48 μm , and 0.92 μm thick {001}-textured PZT films on Pt-coated Si.

As mentioned in the section on the thickness dependence of dielectric nonlinearity, there were two possible reasons for the observed thickness dependence of the dielectric response: either changes in the domain wall concentration or mobility, or the presence of a second (non-ferroelectric) phase. The experiment of external dc bias field proves that thickness dependence is due to changes in domain wall concentration or mobility in thinner films. The same level of dielectric permittivity is observed with high dc bias fields for all of the PZT films. If a second

phase is present, the dielectric permittivity should decrease as calculated by one of the mixing rules, e.g., the Lichtenecker rule as shown in Equation 4-2^[16].

$$\ln \epsilon_m = \sum_i V_{f_i} \ln \epsilon_i = (V_{f,PZT} * \epsilon_{PZT}) + (V_{f,2^{nd} \text{ phase}} * \epsilon_{2^{nd} \text{ phase}})$$

Equation 4-2

where $V_{f,PZT}$ = Volume fraction of PZT films

ϵ_{PZT} = Permittivity of PZT films (in case of fully dense PZT films)

$V_{f, 2^{nd} \text{ phase}}$ = Volume fraction of 2nd phase

$\epsilon_{2^{nd} \text{ phase}}$ = Permittivity of 2nd phase

ϵ_m = Total permittivity

4.3 Summary of Dielectric Nonlinearity

Table 4- 1 summarizes the dielectric nonlinearity of PZT films with mixed {001} and {111} orientation, {001}-textured films on Si, and {001}oriented PZT films on single crystal SrRuO₃ coated SrTiO₃ in term of the reversible Rayleigh constant (ϵ_{init}), the irreversible Rayleigh constant (α_ϵ), and the ratio of irreversible to reversible ($\alpha_\epsilon/\epsilon_{init}$).

Table 4- 1: Summary of dielectric nonlinearity of mixed {001} and {111} orientation, {001}-textured PZT films

PZT films	ϵ_{init}	α_{ϵ} (cm/kV)	$\alpha_{\epsilon}/\epsilon_{\text{init}}$ (cm/kV)
<u>PZT films with mixed {001} and {111} orientation</u>			
0.28 μm	928 ± 1	9.15 ± 0.05	$0.0098 \pm .000051$
0.53 μm	1175 ± 3	15.84 ± 0.16	0.01349 ± 0.000142
1.09 μm	1358 ± 2	18.24 ± 0.12	$0.01343 \pm .000089$
2.06 μm	1148 ± 2	31.10 ± 0.13	$0.02710 \pm .000128$
4.04 μm	1330 ± 2	30.28 ± 0.15	0.02271 ± 0.000118
4.40 μm	1295 ± 2	26.97 ± 0.15	0.02082 ± 0.000122
<u>Textured PZT films</u>			
0.27 μm	837 ± 2	6.81 ± 0.07	0.00814 ± 0.000087
0.45 μm	756 ± 1	7.17 ± 0.04	0.00948 ± 0.000052
0.92 μm	958 ± 4	16.58 ± 0.35	0.017307 ± 0.00037

Chapter 5

Piezoelectric Nonlinearity and Switching Spectroscopy Piezoelectric Force Microscopy

This chapter first discusses the ac field amplitude dependence of the piezoelectric coefficient of mixed {111} and {001} orientation and {001}-textured $\text{Pb}(\text{Zr}_{0.52}\text{Ti}_{0.48})\text{O}_3$ films, as this will influence the effective coefficients needed to describe the operation of MEMs devices. In particular, the influence of grain size, thickness, and film orientation on the properties was assessed. To obtain better insight into these phenomena, the local map of piezoelectric coefficient ($d_{33,f}$) was studied by Piezoelectric Force Microscopy (PFM) and Band Excitation Piezoelectric Force Microscopy (BE-PFM) at Oak Ridge National Laboratory. Secondly, the local polarization switching was studied by Switching Spectroscopy Piezoelectric Force Microscopy (SS-PFM) at Oak Ridge National Laboratory and then compared with the global switching as characterized by a Preisach distribution^[35] function determined at Penn State University. The main difference in the two types of experiments is the ac field level used to drive the PZT films. In the piezoelectric nonlinearity measurements, the motion of domain walls was studied but the domain wall density was not changed. In the polarization switching, high enough ac fields were applied to change the domain density.

5.1 Piezoelectric Nonlinearity

Rayleigh-like behavior is expected when there are large ensemble averages of the material response (i.e. when large capacitors, which sample many domain walls, are

interrogated).^[30, 35, 36] It is also interesting to consider how the nonlinearity should be manifested on a much more local scale. Thus in this work, a local probe based technique was employed. Towards this end, the local nonlinearity in $d_{33,f}$ was measured by using a PFM at Oak Ridge National Laboratory. The samples were poled at three to five times the coercive field for 20 min and aged for a minimum of 1 hour before measurements.^[6] The maximum ac field applied to observe the piezoelectric nonlinearity is about $\frac{1}{3}$ to $\frac{1}{2} E_c$, thus the domain density should remain unchanged.

The piezoelectric nonlinearity measurements were made by PFM with two main types of experiments as follows:

- PFM with single frequency at 1 kHz as shown in section 5.1.1
- Band Excitation PFM (BE-PFM) as shown in section 5.1.2

5.1.1 Piezoelectric Nonlinearity by PFM with Single Frequency

In this section, the piezoelectric nonlinearity measurements were made at 1 kHz frequency with and without an applied ac bias. The bias serves two purposes. First, the piezoelectric response of the films decay with time due to aging, even after poling for long times.^{[6] [35]} The dc bias can minimize this time dependence by stabilizing the domain state. Secondly, the dc bias also tends to decrease nonlinearity.

There have been comparatively few attempts to make local measurements of the piezoelectric response previous to this work. Shvartsman et al.^[88] reported that the local nonlinearity differed from the one observed by double beam interferometry in 250 nm thick PZT 45/55 films. However, the local electric fields were somewhat ill-defined due to the use of the tip as a top electrode. These results do, however, suggest that mapping the nonlinearity may be possible.

5.1.1.1 Piezoelectric Nonlinearity of “Mixed {001} and {111} orientation” PZT Films

The piezoelectric coefficient was measured by the detection of mechanical surface deformation induced by an oscillating electrical bias applied across the sample while the bottom electrode was grounded. The PFM set up details were described in section 2.8.2. For each measurement, the maximum ac voltage was half of the coercive field. For each data set, the amplitude and phase angle for each oscillation voltage were collected and analyzed. Only the data points with phase angles of $\geq 150^\circ$ and $\leq -150^\circ$ were used. However, the data show some scatter, and thus the confidence limits on the calculated Rayleigh parameters are quite high as shown in Figure 5- 1. Figure 5- 1 shows the ratio of the irreversible (α) to reversible ($d_{33,r}$) piezoelectric Rayleigh coefficients for 4 μm , 1 μm , and 0.53 μm thick PZT films as a function of bias field and a normalized field $E_{\text{normalized}} = E_{\text{bias field}} / E_c$, respectively. All three films show an initial increase in response, followed by a gradual drop under higher dc bias levels. It is believed that this initial increase is associated with an increase in the poling in the film, while the successive drop-off in nonlinearity is due to the fact that under dc biases, the domain state becomes more stable. Thus, it becomes more difficult for a small ac field to perturb the domain state. As a result, the nonlinearity drops.

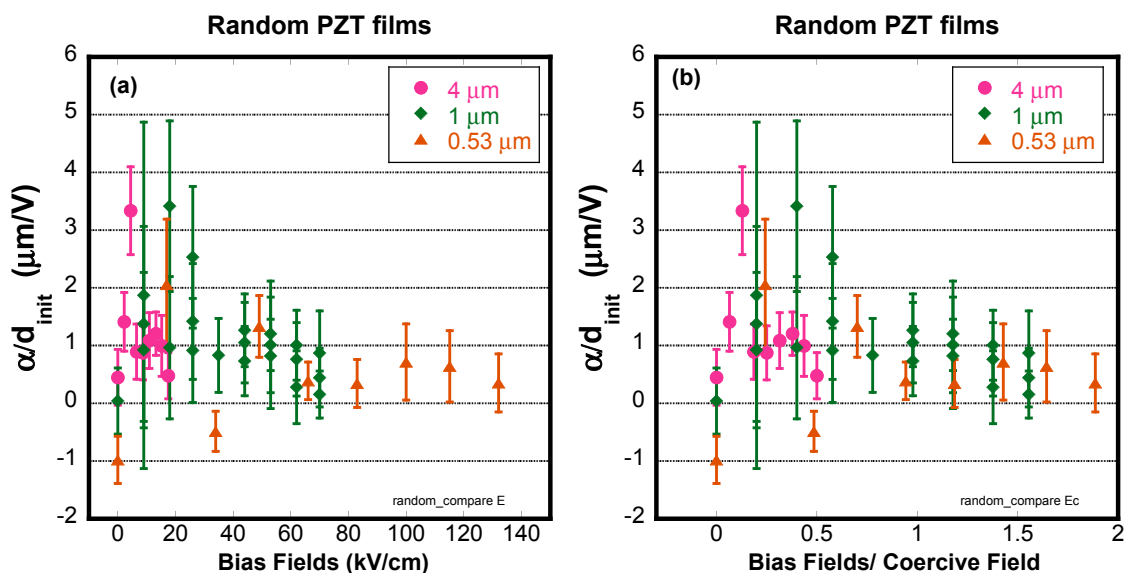


Figure 5- 1: The ratio of irreversible to reversible piezoelectric response of PZT films with mixed $\{001\}$ and $\{111\}$ orientation at 1 kHz (a) as a function of bias field (b) data from (a) plotted as a function of normalized field (bias field/coercive field)

It is also clear that the piezoforce microscopy measurements at a single frequency well below the cantilever resonance do not provide as clear a signature of the thickness dependent nonlinearity as is achieved with other tools. Xu et al.^[17] and Kholkin^[39] for example, used double beam interferometry to demonstrate unambiguously that thicker films showed larger levels of piezoelectric nonlinearity. This was attributed to less severe domain wall pinning in thicker films.^[17] There are two principal reasons why the thickness dependence may have been more difficult to identify in the PFM experiments. The first, trivial, possibility is a significantly poorer signal to noise ratio in the local measurements. In this particular set of measurements, a software lock-in amplifier was used to determine the piezoelectric response, using an averaging time of 32 s. This, in turn, leads to larger confidence limits, which obscure the true thickness dependence. This could be ameliorated using a longer time sample and detect the response. The second, more interesting possibility is that the scatter in the local measurements is a result of sampling a much small volume, with fewer domains walls. The double beam interferometry measurements of

piezoelectric nonlinearity reported by Xu et al.^[17] and Kholkin^[39] employed electrodes hundreds of microns in diameter, and so sample many more domains than the PFM measurements in this work. In this case, the scatter would arise from the fact that there are too few walls and pinning centers for the statistics required to properly apply the Rayleigh law. Further investigations in this area were made using band excitation measurements as described in section 5.1.2.

A second important observation is that the amplitude of piezoelectric coefficients, $d_{33,f}$ of PZT films are lower than the expected values. Usually, the $d_{33,f}$ of PZT 52/48 films are on the order of 70 - 100 pm/V.^[1, 39] One likely contribution to this is an artifact associated with wafer bending induced by using comparatively large (200 μm to 1000 μm diameter) top electrodes. To assess the impact of wafer bending, the piezoelectric coefficients were measured across an electrode, as shown in Figure 5- 2. In this case, the electric field was applied between the top and bottom electrodes, and the tip was used only to map the deflection. It is apparent that there are variations of d_{33} from point to point on the electrode. Moreover, the bare PZT film (off electrode) should not show any $d_{33,f}$ response because there was no electric field in that area. Experimentally, however, the bare PZT film shows an apparent $d_{33,f}$ of approximately 10 to 15 pm/V. This is direct confirmation that the entire wafer was bent by the piezoelectric effect.

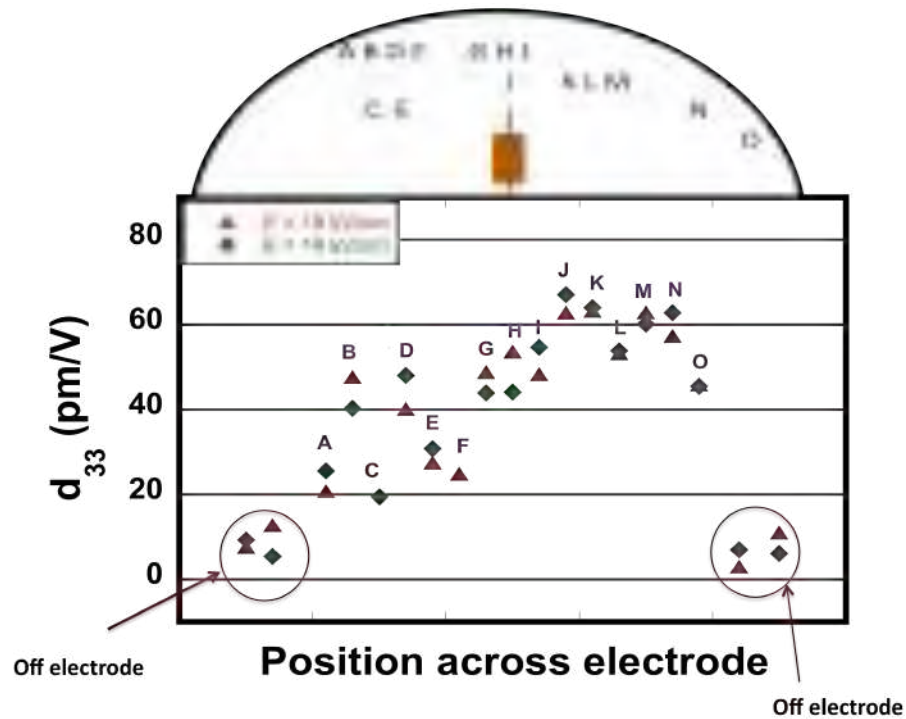


Figure 5- 2: Measurement of apparent piezoelectric coefficients ($d_{33,p}$) across an electrode and on bare PZT film at two different E_{ac} amplitudes. The points from A to O were measured on the top electrode. “Off electrode” means the measurement was made on bare PZT films when only the electrode (rather than the tip) was driven.

It has previously been demonstrated that sample flexure is important in measurements of the piezoelectric response from a single surface. Equation 5.1 shows the displacement (δ_b) for unimorph and bimorph structures.

$$\delta_b \sim \frac{d_{31}VL^2}{t^2} \quad \text{Equation 5-1}$$

where d_{31} is the piezoelectric coefficient, V is bias, L is bimorph length of order of capacitor size, and t is substrate thickness. In comparison, the piezoelectric expansion is $\delta_p = d_{33}V$. A simple comparison indicates that the bending effect can be very significant, as determined by the capacitor mounting, and can be eliminated only when the top electrode is much smaller than that

used in these experiments.^[89] Figure 5- 3 illustrates the importance of wafer bending when the piezoelectric coefficient was collected by PFM.

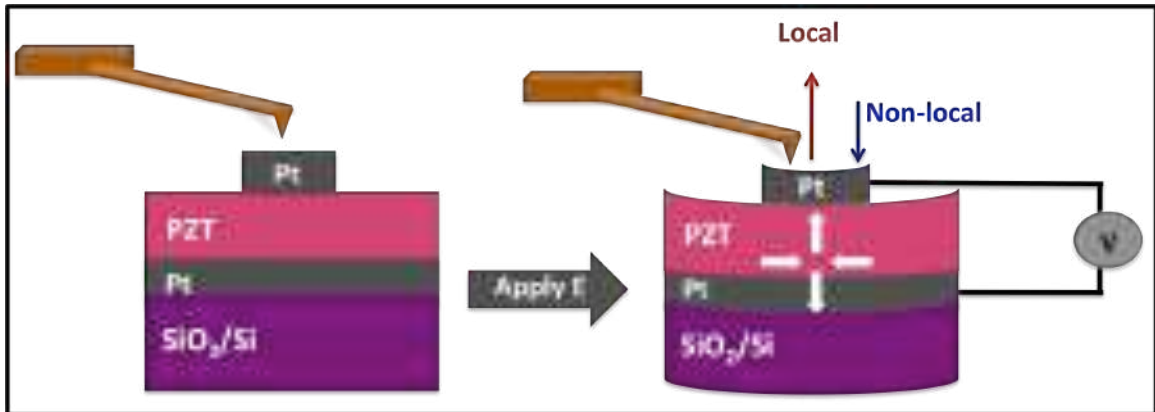


Figure 5- 3: Schematic of the experimental PFM set up and bowing due to use of a large top electrode. The piezoelectric strains results in local surface motion due to local piezoelectric response and bending due to a bimorph effect.^[55, 56]

Kholkin et al.^[83] showed comparable unimorph-like bending in a 520 nm thick PZT film on a Si substrate by single beam interferometry. Figure 5- 4 (a) shows a schematic of the influence of bending on the apparent surface displacement in their experiment. The clamping force between the substrate and the holder affects the results, as shown in Figure 5- 4 (b). If the substrate is totally clamped (ideal case), the measured displacement corresponds to the electric field - induced change of the film thickness. However, if the clamping force drops, bending of the wafer dominates the surface displacement. Figure 5- 4 (c) illustrated the displacement of 520 nm PZT film on Si substrate with 1.5 mm diameter electrode. Errors due to unintended wafer flexure can be at least partially ameliorated by using epoxy resin to glue the substrate exactly under the electrode as shown in Figure 5- 4 (d).^[83] It is apparent that the data measured by PFM in this work shows similar behavior to the report by Kholkin et al. Thus, the observed surface displacement is a convolution of the true piezoelectric dilation of the film and wafer bending. Moreover, this means that the observed nonlinearities are effective numbers only. It would be

important in the future to take a comparable data set using much smaller top electrodes (to eliminate the wafer bending).

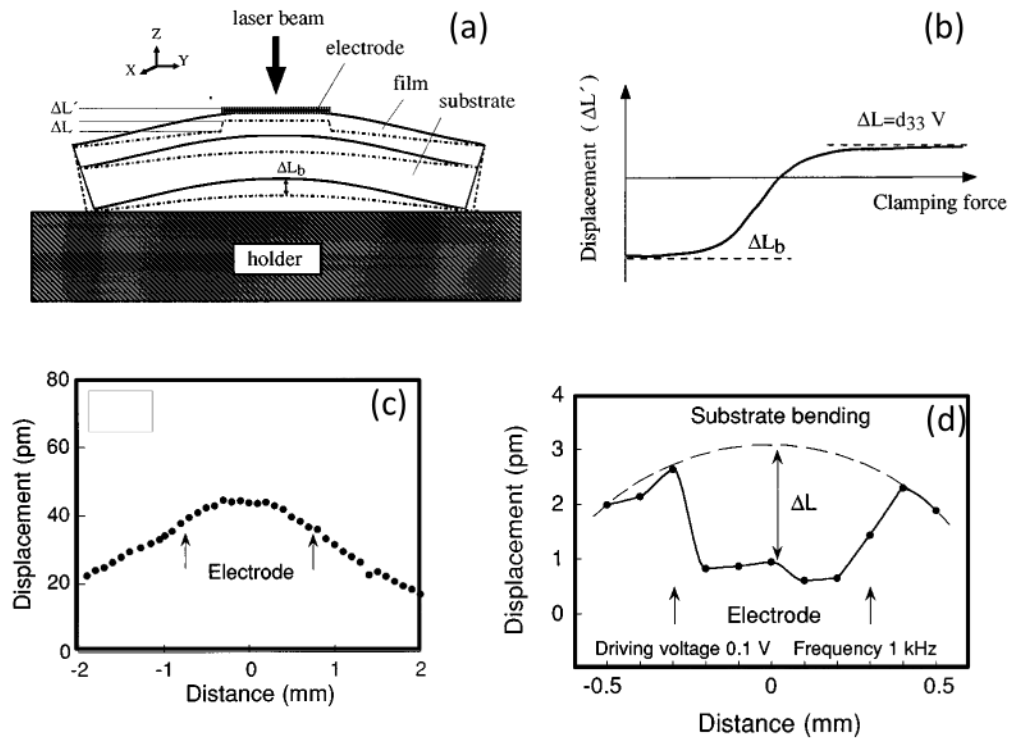


Figure 5- 4: (a) Schematic of the effect of substrate bending on the measured displacements by a single beam interferometer (b) Schematic behavior of the displacement vs. substrate clamping (c) Deformation of the PZT/Si induced by piezoelectric effect across electrode, and (d) Displacement for a PZT film on a partially clamped Si substrate^[83]

5.1.2 Piezoelectric Nonlinearity by Band Excitation SS-PFM

Unfortunately, it was found that conventional PFM measurements could not provide quantitative measurements of the piezoelectric nonlinearity, particularly compared to the dielectric nonlinearity data described in section 5.1.1 To circumvent this difficulty, Band Excitation Piezoelectric Force Microscopy (BE-PFM) was utilized, where resonant enhancement of the cantilever was used to measure the piezoelectric nonlinearity to increase the signal to noise ratio.^[74]

The analysis of BE-PFM is as follows. The point spacing in the frequency domain is $\Delta f = 1/T$, where T is the pulse duration. In this measurement, the pulse duration was set at 4 ms with 16 waveforms per step. Thus, the duration for each measurement is $16 \times 4 = 64$ ms. The frequency resolution is nearly 240 Hz. For example, if the bandwidth is set at almost 60 kHz, approximately 240 data points were recorded per resonance peak.^[74] The resonance frequency of the tip/sample system was set as the center frequency. Table 5- 1 summarizes the setting parameters for the center frequency, bandwidth, and maximum ac field amplitude in the BE-PFM measurement. In general, voltages corresponding to $\frac{1}{3}$ - $\frac{1}{2}$ of the coercive field were used to excite the film to ensure that the domain density is not changed. This was checked by monitoring the time dependence of the piezoelectric response. If a progressive drop in the magnitude of the piezoelectric coefficient was observed, the film was reoled and the measurements were retaken at a lower excitation.

Table 5- 1: Setting resonance frequency and excitation ac field in BE-PFM experiment

PZT films	Center frequency (kHz)	Bandwidth (kHz)	Maximum ac voltage (volts)	Maximum E_{ac} (kV/cm)
<u>Mixed {001} and [111] orientation</u> 4.04 μm	657	60	8.1	20 (~ 0.58 E _c)
2.06 μm	353 – 380	40	1.65	8 (~ 0.22 E _c)
1.09 μm	340 – 375	40	1.42 2.18	13 (~ 0.3 E _c) 20 (~ 0.5 E _c)
0.53 μm	326 – 354	13	1.54	29 (~ 0.41 E _c)
<u>Textured PZT film</u> 0.92 μm textured	350 – 385	40	2.56	27.8 (~ 0.46 E _c)

The response signals were collected using a fast data acquisition card (NI-6615) and Fourier transformed to provide amplitude – frequency and phase – frequency curves. The collected data were fit to a simple harmonic oscillator (SHO) model with three independent parameters; resonance frequency, amplitude at resonance, and quality factor as shown in Equation 5-2 and Equation 5-3.^[74]

$$A(\omega) = \frac{A^{\max} \omega_0^2}{\sqrt{(\omega^2 - \omega_0^2)^2 + (\omega \omega_0 / Q)^2}} \quad \text{Equation 5- 2}^{[74]}$$

$$\tan(\varphi(\omega)) = \frac{\omega \omega_0 / Q}{\omega^2 - \omega_0^2} \quad \text{Equation 5- 3}^{[74]}$$

where ω is angular frequency, ω_0 is the resonant frequency, which is related to the tip-surface force gradient, and is not identical to the resonant frequency of the free cantilever, A is the resonance amplitude, and Q is quality factor. Before starting the experiments on each sample, the ratio of the Fourier transforms of the piezoelectric response and excitation signal was checked. This ratio of signal gave the transfer function of the system within the selected frequency band. This allowed the true excitation voltage applied to the film to be determined.

5.1.2.1 Piezoelectric Nonlinearity of Mixed Orientation PZT Films by BE-PFM

The piezoelectric response as a function of ac field amplitude was observed to study the piezoelectric nonlinearity of several PZT films. During measurement, the cantilever response amplitude for each excitation ac voltage was observed. It is important to remember that in these measurements, the intent was to measure the amplitude dependence of the piezoelectric response. Consequently, it was important that potential nonlinearities associated with the tip-sample resonance itself not interfere with the measurements. As is described in texts on non-linear vibration response, if a resonant system is driven at large enough amplitudes, linear approximations of the response are no longer adequate, and the system can either soften or harden, resulting in a frequency dependence of the resonant frequency (See Figure 5- 5).^[90]

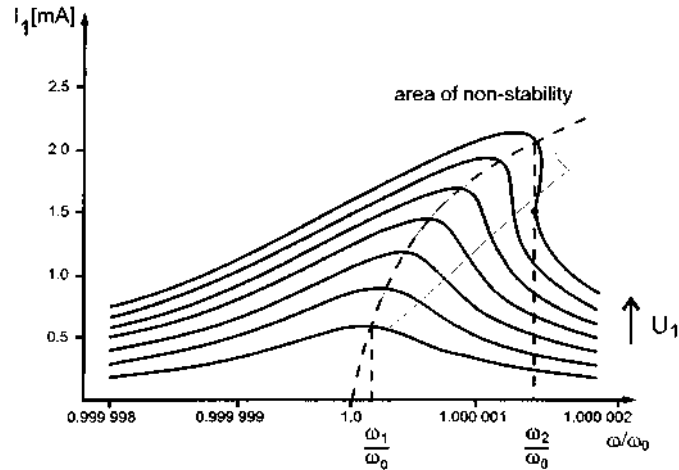


Figure 5- 5: A set of resonant characteristics, where different curves show different amplitudes for the driving field. In this case, the resonant frequency increased with drive amplitude.^[90]

To insure that the nonlinearities of the resonant system (e.g. the cantilever itself or the tip - sample contact) did not dominate the response, stiff cantilevers were employed. Prior to making any series of measurements, the amplitude – frequency response was examined as a function of driving voltage. Only measurements where it could be demonstrated that the resonant frequency was not a strong function of the excitation ac voltage were used, as in Figure 5- 6. In this way, nonlinearities in the resonant system should not dominate the results.

The amplitude calculated from the area under the peak for each excitation ac field as a function of ac field amplitude over the selected frequency band was then plotted and curve-fit by the polynomial equation shown in Equation 5-4. Note that in this case, the amplitude is directly proportional to the sample surface displacement. When the Equation 5-4 is differentiated (Equation 5-5), the Rayleigh law is obtained as in Equation 5-5.

$$\text{Amplitude} = a_1 + a_2 V_{ac} + a_3 V_{ac}^2 \quad \text{Equation 5- 4}$$

$$\frac{\partial(\text{amplitude})}{\partial V_{ac}} = \beta a_2 + 2\beta a_3 V_{ac} \quad \text{Equation 5- 5}$$

$$\beta d_{33,f} = \beta d_{33,f,init} + 2\beta\alpha_d V_{ac} \quad \text{Equation 5- 6}$$

where a_1 , a_2 , and a_3 are the polynomial coefficients, V_{ac} is ac voltage, β is scaling factor related to Q and of the transfer function of the PFM tip, $d_{33,f}$ is the total piezoelectric coefficient, $d_{33,f,init}$ is the initial piezoelectric coefficient (which includes both the intrinsic response and any reversible domain wall contributions), and α_d is the irreversible Rayleigh coefficient. Because the constant β is unknown, only the ratio of $\alpha_d/d_{33,f,init}$ is quantitative in these measurements. Thus, the local piezoelectric nonlinearity was analyzed in term of the irreversible to reversible ratio shown in Equation 5-7.

$$\frac{\alpha_d}{d_{33,f,init}} = \frac{\text{Irreversible}}{\text{Reversible}} \quad \text{Equation 5- 7}$$

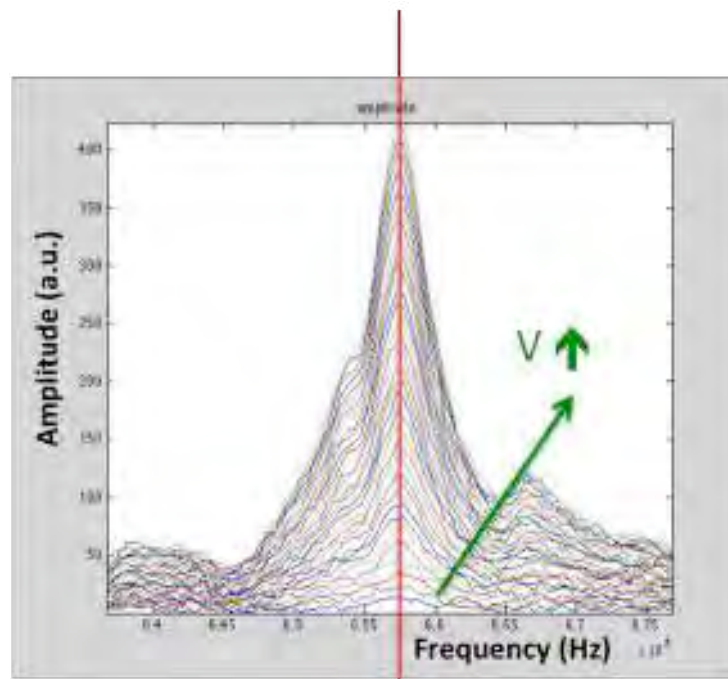


Figure 5- 6: Amplitude signal as a function of frequency over the frequency band employed in the band excitation measurement. Data where there was little drive amplitude dependence of the resonant frequency were chosen for quantitative measurements.

The importance of using the resonance enhancement to improve the measurement of the piezoelectric nonlinearity is clear from Figure 5- 6. At the resonant frequency, there is a systematic trend in the cantilever response as a function of drive amplitude. However, well away from the resonant frequency, a much noisier response is apparent.

One hundred consecutive piezoelectric nonlinearity measurements were taken at one single point on a 4.04 μm mixed $\{001\}$ and $\{111\}$ orientation PZT film to determine how reproducible the measurements were by BE-PFM. Figure 5- 7 shows the first 15 and last 4 of these 100 measurements. The E_c of this sample is 35 kV/cm. The film was excited with an ac field about 0.5 E_c . It is clear that the confidence limits for $d_{33,\text{init}}$, α_d , and the irreversible to reversible ratio are significantly lower than the results measured by the PFM acquired at a single

frequency. Thus, this appears to be a much more viable means of making quantitative measurements.

The ratio of irreversible to reversible of piezoelectric nonlinearity compared to dielectric nonlinearity is the average value from the single measurement of 20 measurements as shown in Figure 5- 7. The irreversible to reversible ratio of piezoelectric nonlinearity compared to irreversible to reversible ratio of dielectric nonlinearity is as follows.

$$\left[\frac{\alpha_d}{d_{33,init}} \right] = 0.0168 \pm 0.0006 \left(\frac{cm}{V} \right)$$

$$\left[\frac{\alpha_\epsilon}{\epsilon_{init}} \right] = 0.0227 \pm 0.0001 \left(\frac{cm}{V} \right)$$

The magnitudes of the irreversible to reversible ratio from the dielectric and piezoelectric measurements are on the same order in the 4.04 thick PZT films with mixed {001} and {111} orientation.

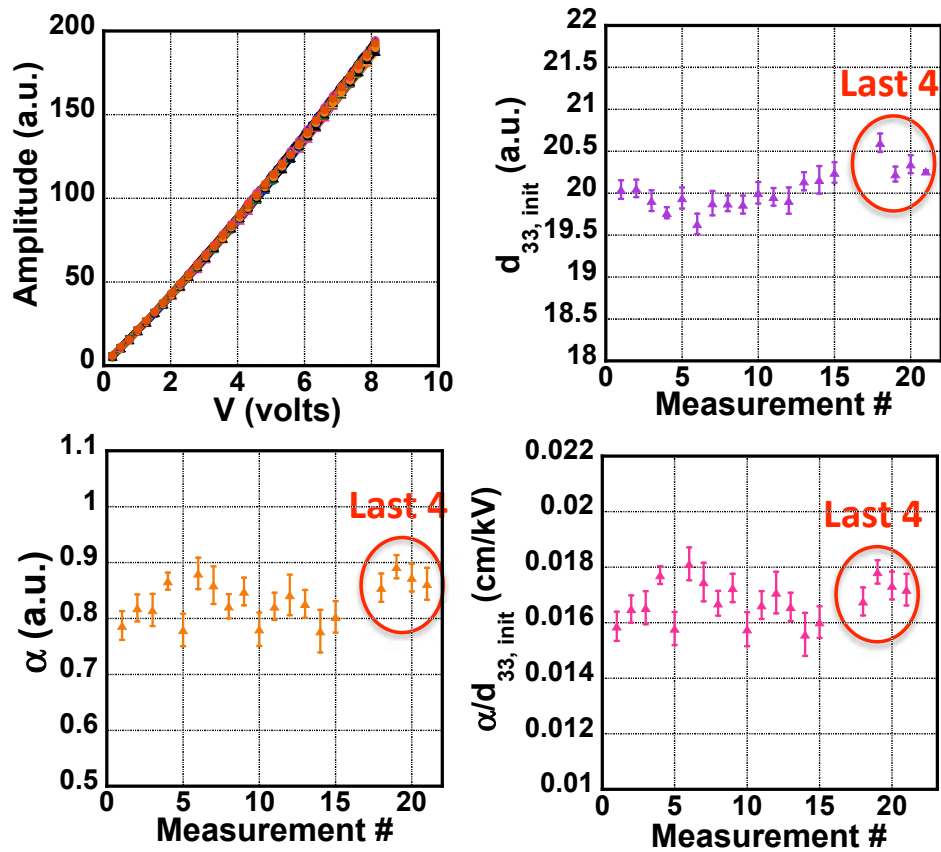


Figure 5- 7: The piezoelectric nonlinearity of 4.04 μm PZT films with mixed $\{001\}$ and $\{111\}$ orientation measured at a single point with the first 10 and last 4 measurements out of 100 times shown (a) Displacement (arbitrary units) as a function of ac voltage, (b) Initial piezoelectric coefficient ($d_{33, \text{init}}$), (c) Rayleigh coefficient (α_d), and (d) Irreversible to reversible ratio ($d_{33, \text{init}}/\alpha_d$)

PZT ferroelectrics have both intrinsic and extrinsic contributions to the piezoelectric response. The intrinsic contribution is due to the averaged response of single domains to the ac field excitation. The extrinsic contribution is due to domain wall and phase boundary motion. 180° domain walls are ferroelectric, while non- 180° domain walls are both ferroelectric and ferroelastic.^[17, 35, 36, 83, 91] Much of the previous work on the thickness dependence of piezoelectric nonlinearity in films assumed that all of the extrinsic contributions were due to non- 180° domain wall motion.^[17, 35, 36, 83, 91] However, Gharb and Trolier-McKinstry recently described a

mechanism whereby 180° domain walls can contribute to the piezoelectric response.^[35, 36] Thus, it becomes interesting to investigate whether 180° domain wall motion or non- 180° domain wall motion contributes a larger fraction to the piezoelectric nonlinearity shown by the PZT films in this work. This could be accomplished in future work by quantifying the extent of the non- 180° domain wall motion in the films. First attempts to do so are given in Chapter 6 of this thesis.

The major goal in this work was to be able to understand how the nonlinearity of PZT films changes spatially as a function of film thickness and orientation. The spatial maps of the irreversible to reversible ratio of $4.04\ \mu\text{m}$ mixed $\{001\}$ and $\{111\}$ orientation PZT film are shown in Figure 5- 8. Modest variations in the response are apparent as a function of position (e.g. changes on the order of $\pm 10\%$). As mentioned above, it is important in these measurements that the results be dominated by the voltage dependence of the piezoelectric strain, rather than some nonlinearity in the tip-sample contact. Thus, the spatial variation in the apparent irreversible/reversible Rayleigh coefficient ratio was compared to maps of both the resonance frequency and topology. No correlations between topology and resonance frequency are apparent. Moreover, the shift of the center resonance frequency during the measurement (from 650 to 655 kHz) is negligible.

For this $4.04\ \mu\text{m}$ thick film, the spatial variation in the irreversible/reversible Rayleigh constants is small, and is probably on the order of the accuracy with which the ratio can be determined. The volume sampled of this measurement is about $1.09\ \mu\text{m}^3$. This suggests that over the volume sampled, the degree of extrinsic contributions is nearly uniform. This, in turn, suggests that it may be possible to scale piezoelectric MEMS structures from polycrystalline films to very small lateral sizes before point-to-point variations in the piezoelectric response renders one device substantially different from the next.

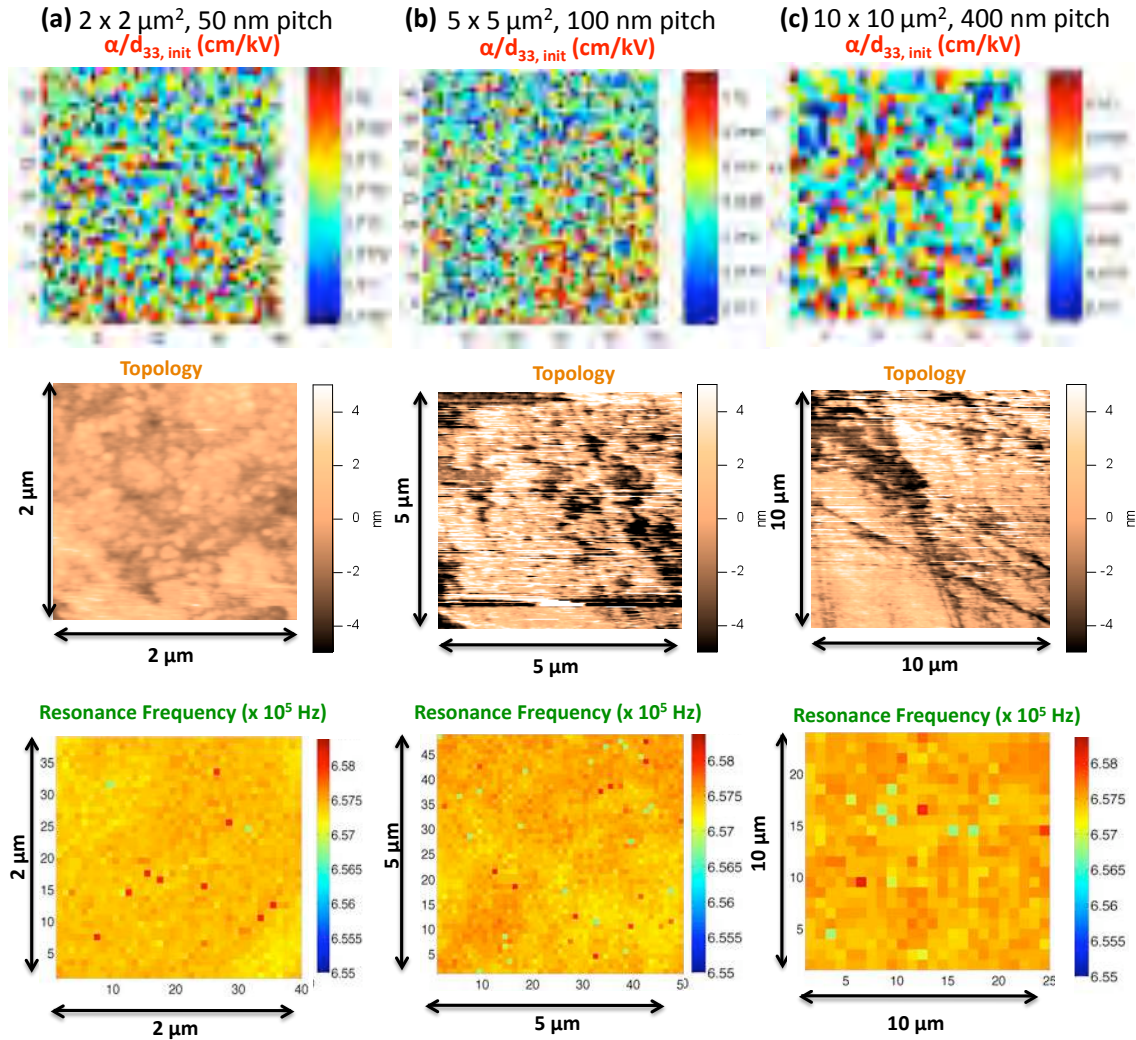


Figure 5- 8: Irreversible to reversible ratio, topology, and resonance frequency maps of $4.04 \mu\text{m}$ PZT films with mixed $\{001\}$ and $\{111\}$ orientation (a) $2 \mu\text{m} \times 2 \mu\text{m}$ area with 50 nm pitch (b) $5 \mu\text{m} \times 5 \mu\text{m}$ with 100 nm pitch, and (c) $10 \mu\text{m} \times 10 \mu\text{m}$ with 400 nm pitch. The maximum ac field was 20 kV/cm ($0.58 E_c$).

As has been described elsewhere, the volume sampled in a PFM measurement with top electrodes is a function of the film thickness^[55, 56]. Thus, thinner films should provide an improved ability to resolve any local variations in the extrinsic contributions to the properties.

Figure 5- 9 and Figure 5- 10 illustrate the spatial map of piezoelectric nonlinearity measured with $\sim \frac{1}{3} E_c$ and $\sim \frac{1}{2} E_c$, respectively, for a 1.09 μm thick PZT film with some degree of $\{100\}$ and $\{111\}$ orientation. In the 1.09 μm thick, mixed $\{001\}$ and $\{111\}$ orientation PZT film, it is clearly observed that there is clustering in the irreversible/reversible ratio. One possible reason is BE-PFM sampled a lower volume in any one measurement for the thinner film. The calculation of the volume probed in the PFM measurement for each PZT film thickness was shown in Table 2- 4. In this film, the center resonance frequency shifted across any one map from 360 to 365 kHz. There are some correlations between topology and resonance frequency. However, it is clear that the clustering observed in the irreversible/reversible ratio is not simply an artifact associated with cross-talk from topology or resonance frequency. It is very important to do the correlation function on the irreversible to reversible ratio as is proposed in the future work section.

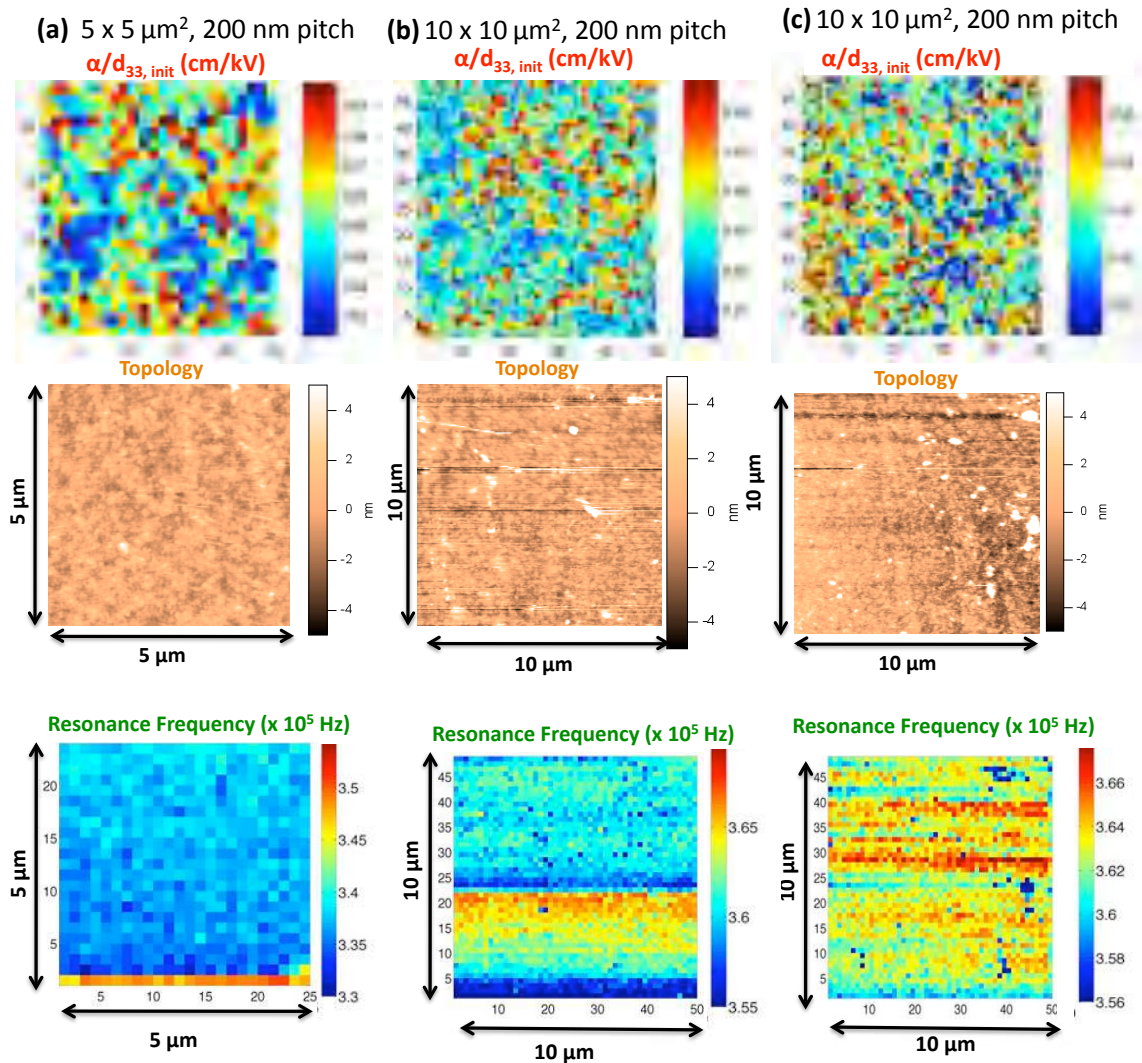


Figure 5- 9: Irreversible to reversible ratio, topology, and resonance frequency maps for the 1.09 μm thick PZT films with mixed $\{001\}$ and $\{111\}$ orientation (a) $5 \mu\text{m} \times 5 \mu\text{m}$ area with 200 nm pitch (b) $10 \mu\text{m} \times 10 \mu\text{m}$ with 200 nm pitch, and (c) $10 \mu\text{m} \times 10 \mu\text{m}$ with 200 nm pitch. The maximum ac field was 13 kV/cm ($0.3 E_c$).

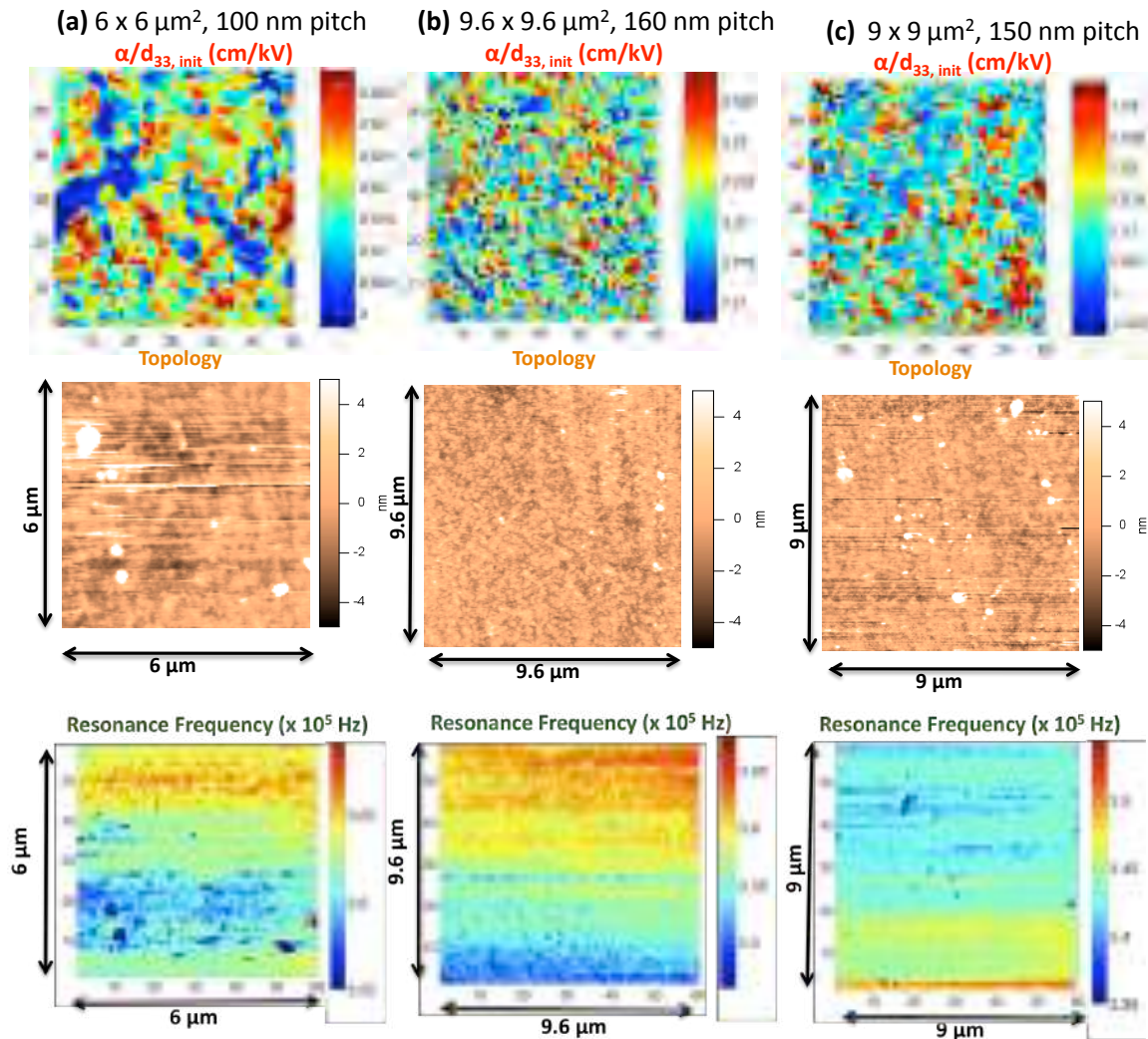


Figure 5- 10: Irreversible to reversible ratio, topology, and resonance frequency map of 1.09 μm PZT films with mixed $\{001\}$ and $\{111\}$ orientation (a) 6 μm x 6 μm area with 100 nm pitch (b) 9.6 μm x 9.6 μm with 160 nm pitch, and (c) 9 μm x 9 μm with 150 nm pitch. The maximum ac field was 20 kV/cm (0.47 E_c).

The irreversible to reversible ratio of piezoelectric nonlinearity of 1.09 μm mixed $\{001\}$ and $\{111\}$ orientation PZT film is comparable to that measured in the dielectric nonlinearity measurements of the same sample, especially when PZT film was excited with the same ac field ($\frac{1}{2} E_c$) as shown in Figure 5- 10 (see Table 5- 2). It is suggested that the same domain walls contribute to both the dielectric and piezoelectric nonlinearity.^[35, 36]

Figure 5- 11 shows the ratio of irreversible to reversible piezoelectric response, topology, and resonance frequency for a 2.06 μm thick, mixed $\{001\}$ and $\{111\}$ orientation PZT film. In this experiment, especially for the 9.6 μm x 9.6 μm map at 160 nm pitch, there is some cross-talk from the resonance frequency to the piezoelectric response. A line at row 40 should be ignored as an observation of piezoelectric nonlinearity. The fact that the entire row appears to be in error would suggest some change in the tip (perhaps contamination). The 2.06 μm mixed $\{001\}$ and $\{111\}$ orientation PZT show clustering behavior which is intermediate between that of the 4.04 μm and the 1.09 μm PZT films with mixed $\{001\}$ and $\{111\}$ orientation. This is believed to be directly related to the sampling volume of the measurement, as calculated in Table 2- 4. The volume sample of 2.06 μm and 1.09 μm are $\sim 0.15 \mu\text{m}^2$ and $\sim 0.025 \mu\text{m}^3$, respectively.

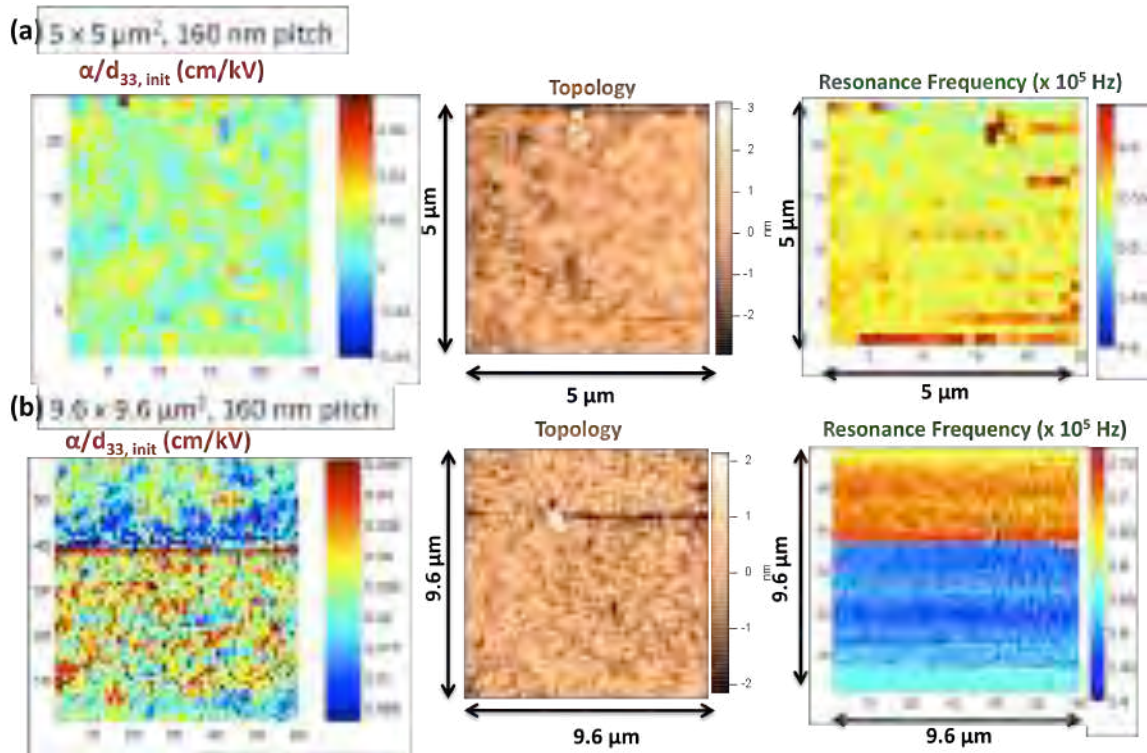


Figure 5- 11: Irreversible to reversible ratio, topology, and resonance frequency map of 2.06 μm PZT films with mixed $\{001\}$ and $\{111\}$ orientation (a) 5 μm x 5 μm area with 160 nm pitch and (b) 9.6 μm x 9.6 μm with 160 nm pitch. The maximum ac field was 8 kV/cm (0.22 E_c).

Xu et al. showed that the effective $d_{33, f}$ nonlinearity of thinner PZT films is much lower than that in thick PZT films.^[17] To examine this behavior locally, Figure 5- 12 illustrates the ratio of irreversible to reversible piezoelectric response in a 0.53 micron thick mixed $\{001\}$ and $\{111\}$ orientation PZT film. Some areas show a negative value of the ratio, which probably points mainly to difficulties in detecting the lower d_{33} nonlinearity, as well as smaller displacements.

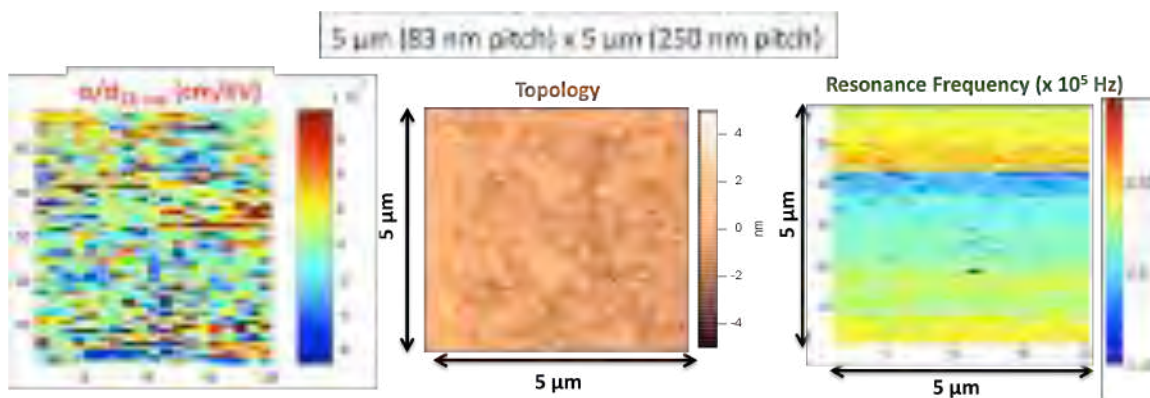


Figure 5- 12: Irreversible to reversible ratio, topology, and resonance frequency map of $0.53 \mu\text{m}$ PZT films with mixed $\{001\}$ and $\{111\}$ orientation, $5 \mu\text{m}$ (83 nm pitch) \times $5 \mu\text{m}$ (250 nm pitch). The maximum ac field was 29 kV/cm ($0.41 E_c$)

5.1.2.2 Piezoelectric Nonlinearity of Textured PZT Film by BE-PFM

$\{001\}$ oriented rhombohedral perovskite films have four ferroelastic domain states that are energetically equivalent with respect to an ac field along $[001]$.^[26] Hence, there should be no driving force for ferroelastic wall motion due to the AC field. Thus, it might be expected that if ferroelastic wall motion is important, the piezoelectric nonlinearity of a textured film (even one at the morphotropic phase boundary, as those measured here) might be lower than in a mixed $\{001\}$ and $\{111\}$ orientation film. Figure 5- 13 showed the results of piezoelectric nonlinearity including topology and resonance frequency during measurement of a $0.92 \mu\text{m}$ thick $\{001\}$ oriented film. Some areas (shown in red in Figure 5- 13 (b)) show clusters with similar irreversible to reversible ratios as those shown for the dielectric nonlinearity of the same film. However some areas (light blue in the Figure 5- 13 (b)) shows lower piezoelectric nonlinearity. Unfortunately, there does appear to be a stronger correlation with topology in the set of data, possibly due to the larger grain sizes in the oriented films. It would be useful to take a comparable set of data on a smoother oriented film.

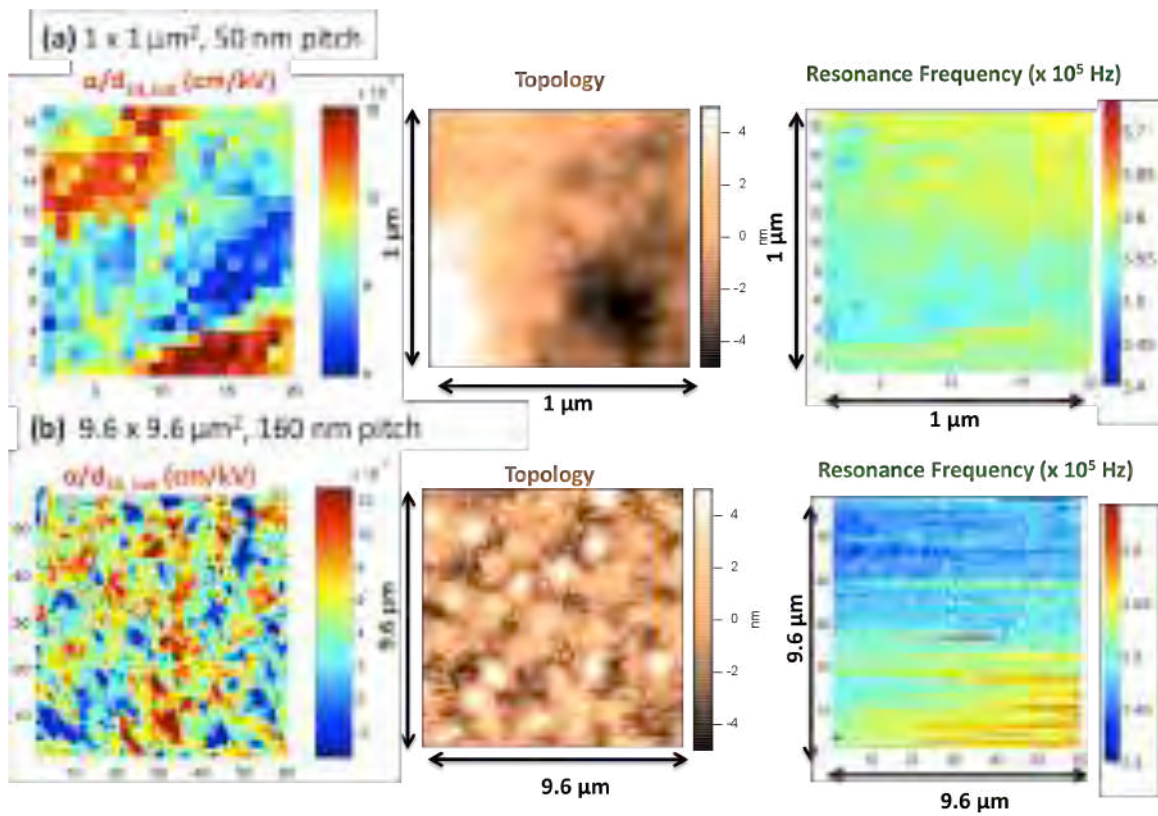


Figure 5- 13: Irreversible to reversible ratio, topology, and resonance frequency map of $0.92 \mu\text{m}$ textured PZT films (a) $1 \mu\text{m} \times 1 \mu\text{m}$ with 50 nm pitch and (b) $9.6 \mu\text{m} \times 9.6 \mu\text{m}$ with 160 nm pitch. The maximum ac field was 27.8 kV/cm ($0.46 E_c$)

5.1.3 Summary of Dielectric Nonlinearity and Piezoelectric Nonlinearity Comparison

Table 5- 2 summarizes the piezoelectric nonlinearity in term of average and median, of $\alpha_d/d_{33, r_{init}}$ for each spatial map compared to the dielectric nonlinearity.

Table 5- 2: Comparison between average local piezoelectric nonlinearity and global dielectric nonlinearity

PZT films	Map size	$\alpha_d/d_{33, f \text{ init}}$ Average (cm/kV)	$\alpha_d/d_{33, f \text{ init}}$ Median (cm/kV)	Dielectric nonlinearity $\alpha_g/\epsilon_{\text{init}}$ (cm/kV)
4.04 μm (mixed orientation)	2 x 2 μm^2	0.0184	0.0184	0.0227 \pm 0.0001
	5 x 5 μm^2	0.0186	0.0185	
	10 x 10 μm^2	0.0186	0.0186	
2.06 μm (mixed orientation)	5 x 5 μm^2	0.0169	0.0167	0.0271 \pm .0001
	9.6 x 9.6 μm^2	0.0246	0.0237	
1.09 μm (mixed orientation)	5 x 5 μm^2	0.0553	0.0540	0.0134 \pm .0001
	10 x 10 μm^2	0.0357	0.0327	
	10 x 10 μm^2	0.0311	0.0315	
1.09 μm (mixed orientation)	6 x 6 μm^2	0.0191	0.0195	0.0135 \pm 0.0001
	9.6 x 9.6 μm^2	0.0232	0.0230	
	9 x 9 μm^2	0.0139	0.0111	
0.53 μm (mixed orientation)	5 x 5 μm^2	0.0029	0.0022	0.0135 \pm 0.0001
0.92 μm (textured)	1 x 1 μm^2	0.0075	0.0069	0.0173 \pm 0.0004
	9.6 x 9.6 μm^2	0.0050	0.0049	

5.2 Global Switching Measurements

In the previous section, the field dependence of the piezoelectric response using relatively small ac fields was studied. In this section, larger fields, which would be expected to cause switching in the films, were also explored. As a reference for the PFM data, global switching measurements were made for a 1.09 μm thick, $\text{Pb}(\text{Zr}_{0.52}\text{Ti}_{0.48})\text{O}_3$ film with mixed $\{111\}$ and $\{100\}$ orientation. The macroscopic switching behavior was studied using hysteresis loop measurements, ac amplitude measurements and the first-order-reversal curve (FORC) method.^[56]

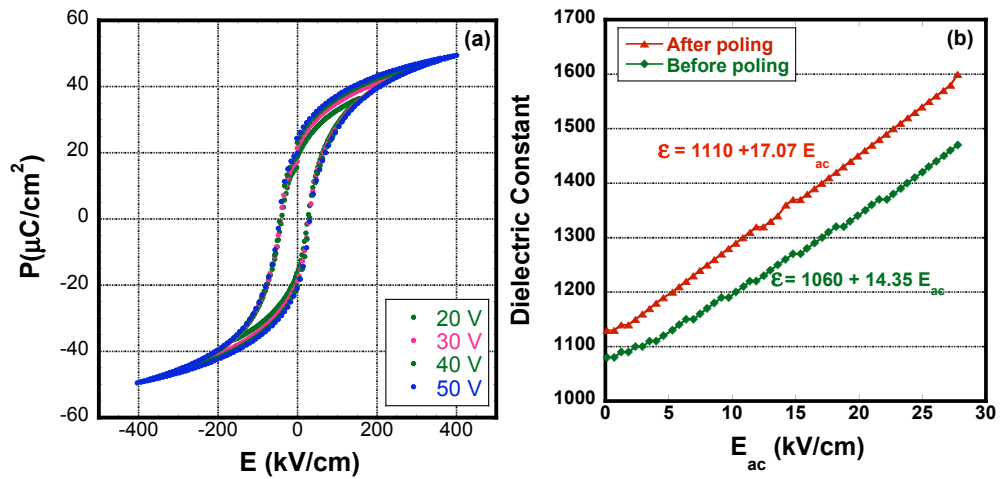


Figure 5- 14: (a) Polarization-electric field hysteresis loop measurement and (b) Rayleigh-like dielectric response of 1.09 mixed {001} and {111} orientation PZT thin film

Figure 5- 14 illustrates the global P-E loop measurement and the dielectric nonlinearity measured using large area electrodes, from 200 μm to 1000 μm in diameter. For ac electric fields < 27 kV/cm (corresponding to ~2.7 V_{ac}), the dielectric response could be well-described using a Rayleigh model.^[91, 92] In this regime, the permittivity increased linearly with the amplitude of the applied electric field, as shown in Equation 5.8.

$$\epsilon_r = \epsilon_{init} + \alpha E_{ac} \quad \text{Equation 5- 8}$$

The same constant α describes the experimentally measured minor polarization hysteresis loops. The Rayleigh-like behavior suggests that for the large capacitor, the Preisach density sampled for small ac excitations is nearly uniform.

For higher ac field levels, the Rayleigh approach breaks down, and first order polarization reversal curves were employed to determine the Preisach distribution as shown in Figure 5- 15.^[93] The Preisach distribution function was subsequently used to calculate the average amount of macroscopic switching expected for the excitation conditions employed in the PFM experiments.

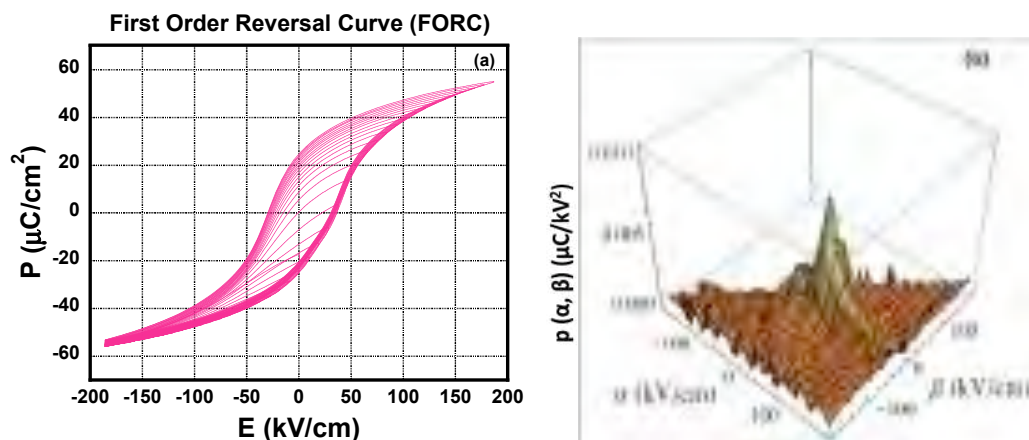


Figure 5- 15: (a) First order polarization reversal curves measured using large area electrodes and (b) Preisach density measured using large capacitor structures

A comparison of the Preisach distribution functions for PZT films with mixed orientation, $\{100\}$ orientation on Pt-coated Si, and $\{100\}$ orientation on SrTiO₃ was also made. All FORC data were smoothed using a binomial algorithm with an average of 3 points to minimize the noise from the equipment. Figure 5- 16 showed the calculated Preisach distribution functions for a thickness series of PZT films with mixed $\{001\}$ and $\{111\}$ orientation. The up-switching field is α and the down-switching field is β . The Preisach density shows a sharp peak for films above about 2 μm thickness. In thinner PZT films (0.28 μm , 0.53 μm , and 1 μm), the peak Preisach density is significantly lower, suggesting less well-defined switching fields.

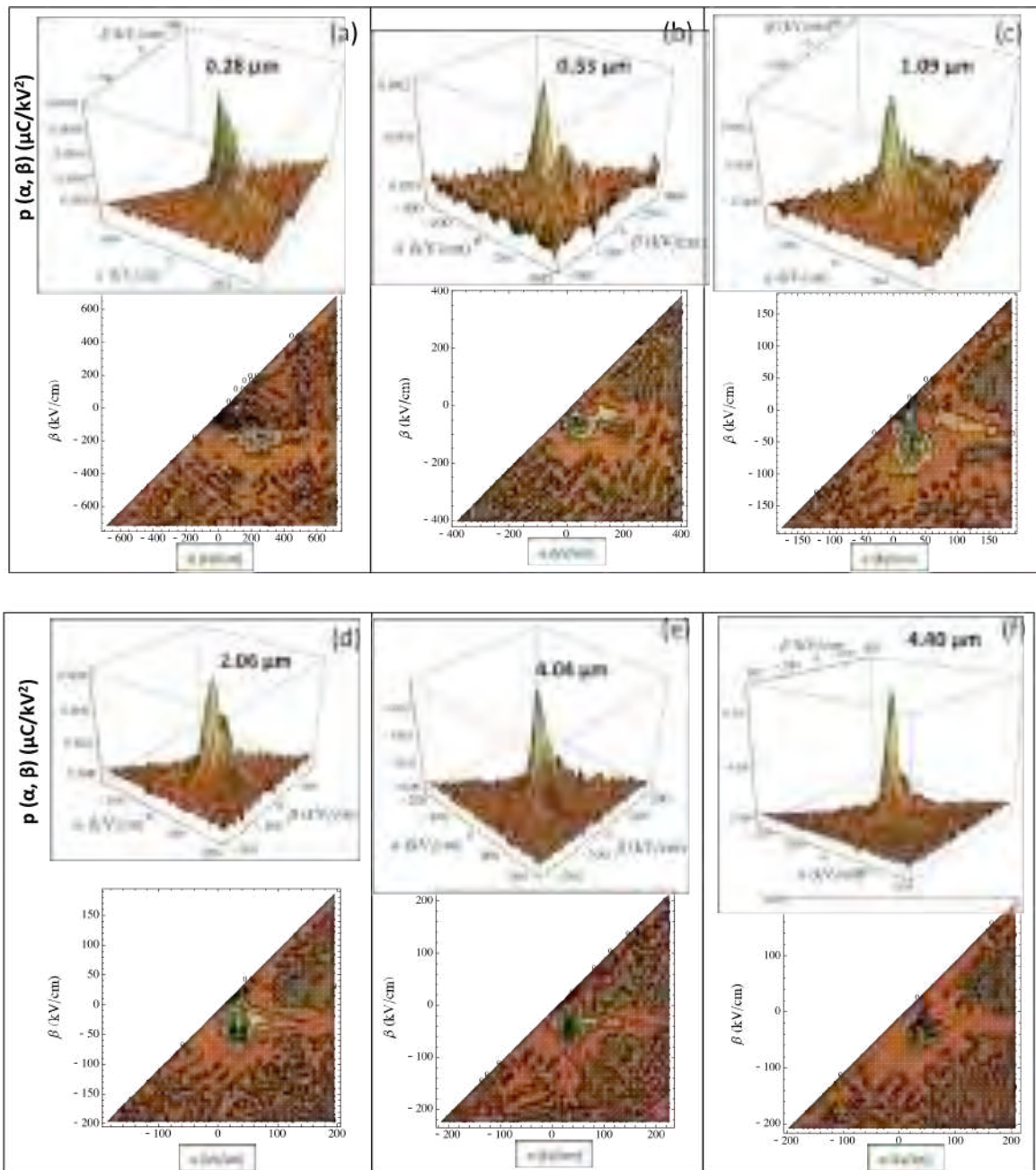


Figure 5- 16: Preisach distribution density of PZT films with mixed $\{001\}$ and $\{111\}$ orientation in thickness series (a) $0.28 \mu\text{m}$, (b) $0.53 \mu\text{m}$, (c) $1.09 \mu\text{m}$, (d) $2.06 \mu\text{m}$, (e) $4.04 \mu\text{m}$, and (f) $4.40 \mu\text{m}$

Figure 5- 17 and Figure 5- 18 illustrate the Preisach distribution density of $\{001\}$ -textured PZT films on Pt-coated Si and SrRuO_3 coated SrTiO_3 , respectively. The Preisach density of the $\{001\}$ -textured PZT film on Pt-coated Si shows a sharp peak at $1 \mu\text{m}$ thick, similar to the

mixed $\{001\}$ and $\{111\}$ orientation case. Many hysterons switch with comparable values of the switching fields at the Preisach distribution peak. The peak is more pronounced in thicker films compared to thinner ones.

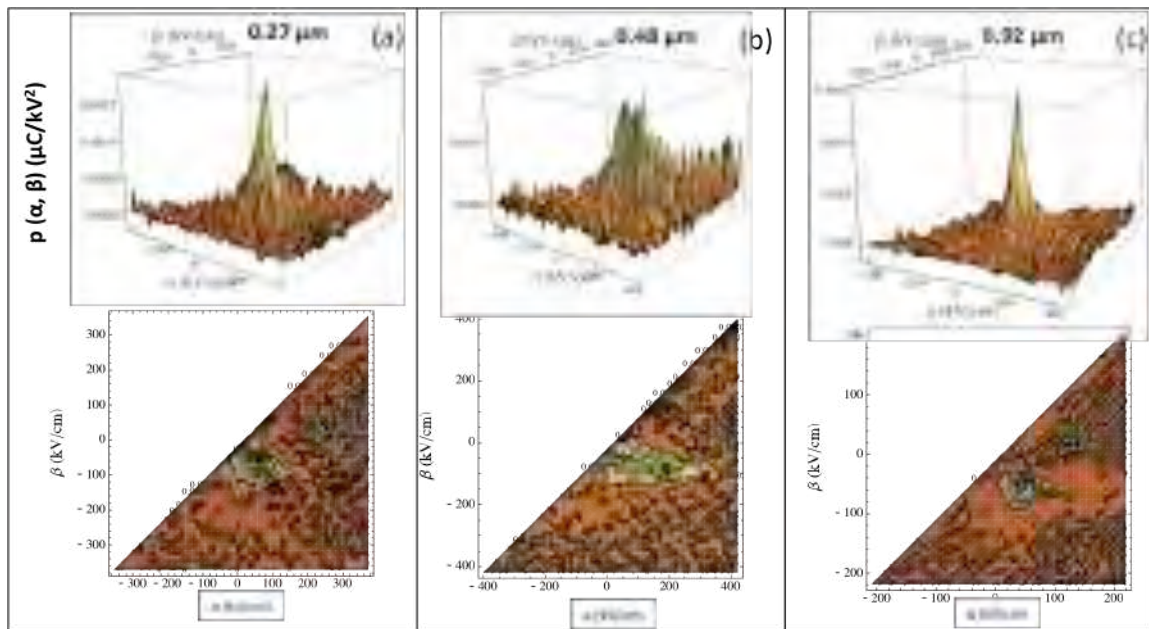


Figure 5- 17: Preisach distribution density of $\{001\}$ -textured PZT films in thickness series (a) 0.27 μm , (b) 0.48 μm , and (c) 0.92 μm

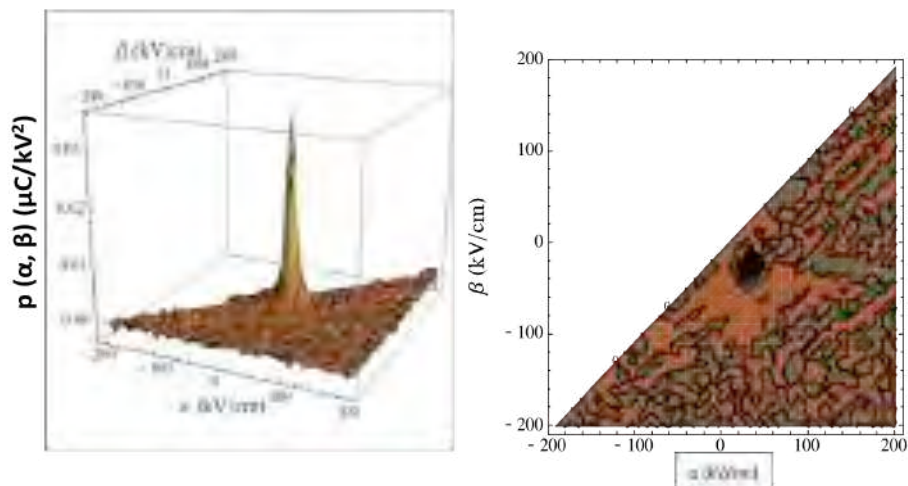


Figure 5- 18: Preisach distribution density of 1 μm thick PZT film on SrRuO_3 coated SrTiO_3

5.3 Switching Spectroscopy Piezoelectric Force Microscopy (SS-PFM)

To make a comparison between the local and global response of PZT films, a 1.09 μm thick, $\text{Pb}(\text{Zr}_{0.52}\text{Ti}_{0.48})\text{O}_3$ film with mixed $\{111\}$ and $\{100\}$ orientation on Pt-coated Si substrates prepared by chemical solution deposition described in Chapter 2 was examined by SS-PFM. A composition close to the morphotropic phase boundary was chosen to maximize the number of possible domain orientations and minimize the characteristic domain size.^[94] For this purposes, 50 nm thick Pt top electrodes with diameters ranging from 200 μm to 1000 μm were sputtered through a shadow mask on top of the PZT films. To facilitate electrical access, several electrode dots on the top surface of the film were wire-bonded to DIP package as shown in section 2.8.2.

SS-PFM provides information on the polarization dynamics at two levels: the locally measured PFM hysteresis loops provides information on the polarization dynamics within a probing volume (below the spatial resolution limit), while the spatially resolved maps provides information on the variability of switching behavior on length scales above the resolution limit.

5.3.1 Spatially Resolved Spectroscopic Mapping of Polarization Reversal

In SS-PFM measurements, a dc bias offset is applied over top and bottom electrode, and the nucleation and growth of the ferroelectric domains and movement of existing domain walls below the tip are reflected in the change of the effective electromechanical response. The dependence of the response on prior dc bias yields the local electromechanical hysteresis loop. The spatial variability of the switching behavior is probed by switching spectroscopy PFM (SS-PFM), in which hysteresis loops are acquired at each point of a user-specified grid. SS-PFM maps were analyzed to extract 2D maps of remanent piezoelectric response and switchable response, work of switching, and nucleation biases.^[51] In this discussion, focus is placed on the analysis on the

remanent piezoelectric response and the switchable piezoelectric response.^[51] The measured switchable response represents the changes in electromechanical response due to changes in the domain state within the signal generation volume of the probe. In a capacitor geometry, the signal is averaged spatially over a distance $\sim (0.2-0.5)H+(0.5-1)L$, where H is PZT film thickness and L is Pt top electrode thickness, R is tip radius, and $(H+L) \gg R$. So, the spatial resolution is $\sim 100-300$ nm, well above the grain size. In contrast, the lateral resolution of the global measurement is about 200-1000 μm depending on the electrode size.^[56] Table 2- 4 shows the comparison of the volume probed on switching behavior between global and local measurements. Figure 5- 19 and Figure 5- 20 illustrate the spatial distribution of the remanent piezoelectric response and switchable response, respectively, as well as the maximum and median hysteresis loops at a single point. The remanent polarization image is similar to the standard PFM images as expected from resolution considerations due to the reduction of the signal generation volume.^[95] The remanent polarization images shown in Figure 5- 19 (c-h) remains almost identical after multiple switching cycles, suggesting that at the end of the switching cycle each pixel returns to the initial mesoscopic state, approximately the same average polarization state, corresponding to nearly ideal return point memory. This is reasonable given that the PZT geometry, all pixels except the very first have already been exposed to the field cycle before measuring.^[56]

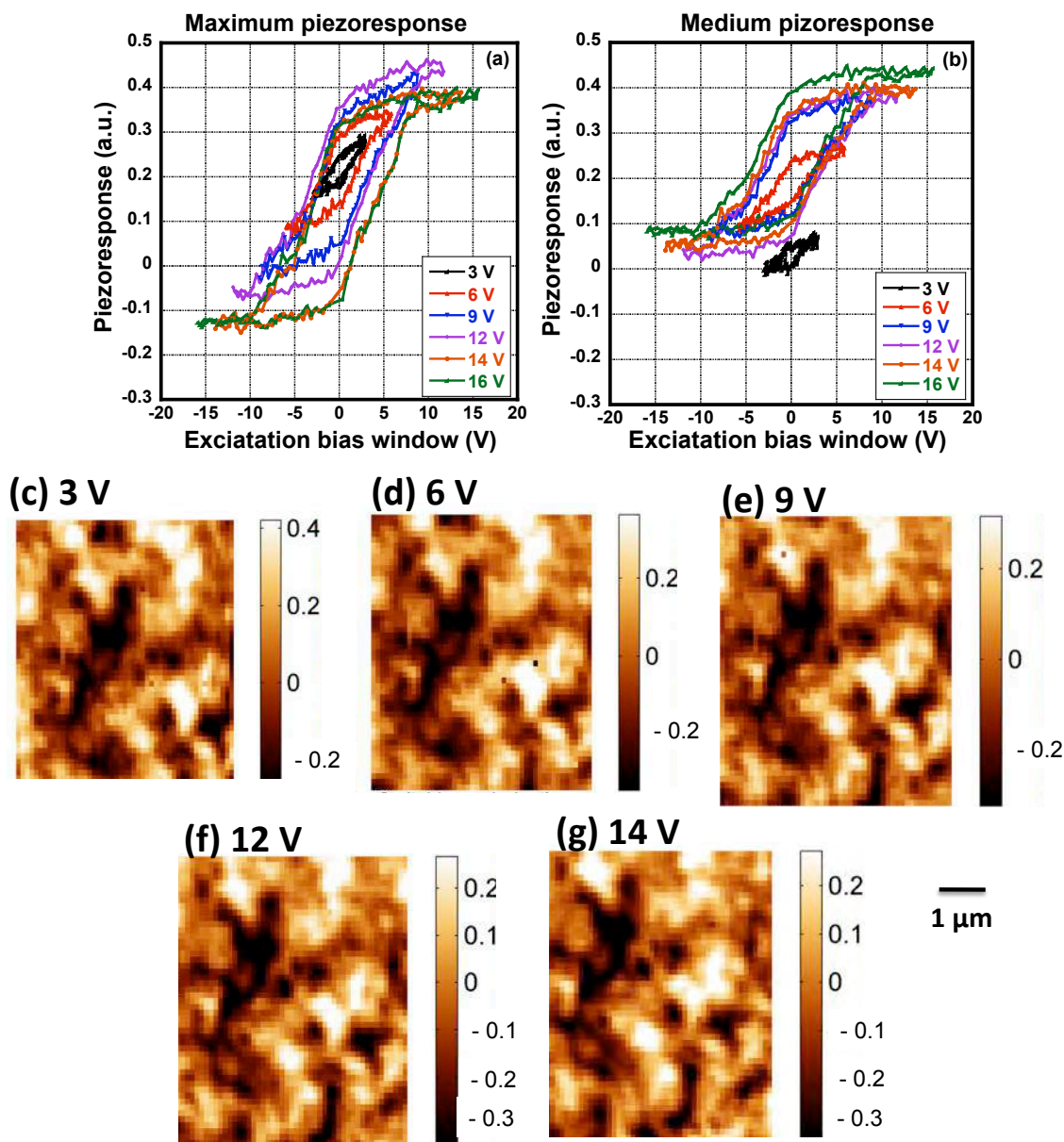


Figure 5- 19: (a-b) Single point hysteresis loops from areas with maximum and medium piezoresponse and (c- g) Positive *remanent* piezoresponse maps with increasing excitation bias window^[56]

Figure 5- 20 illustrates the measurement of the amount of the switchable response maps with increasing excitation bias window. The “excitation bias window” refers to the range of dc bias values applied to the film between SS-PFM measurements. The switchable response shows a gradual evolution with increase in the excitation bias window. The amount of switchable

response is relatively small for the small electric field ranges. This is a manifestation of the observation that the switchable response is small for minor loops, as would be expected for excitation at field levels well below the coercive field. As the excitation bias increased, a larger volume of PZT films switches, the switched response increases progressively, indicating progressive opening of the hysteresis loop. The corresponding image develops a clearly visible contrast, which is different from the piezoelectric response images, thus excluding possible cross-talks in signal acquisition or hysteresis loop analysis.^[55, 56]

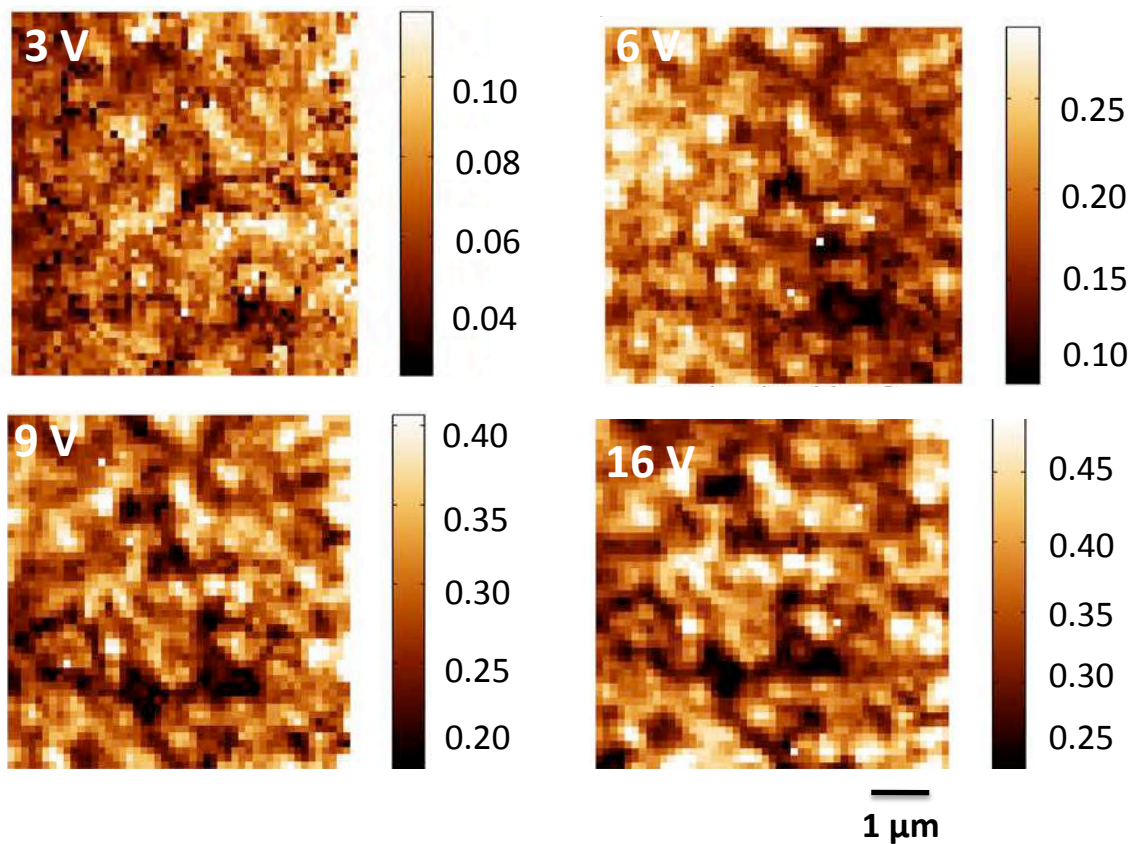


Figure 5-20: *Switchable* response maps with increasing excitation bias window^[56]

The spatial variability of switching behavior measured using a top electrode is illustrated in Figure 5-21, where the images show the (a) initial piezoresponse, (b) imprint, (c) work of switching (area within the loop), (d) switchable polarization, (e) positive nucleation bias defined

at 5% threshold, and (f) negative nucleation bias with the schematic of hysteresis loops (switchable response vs. poling voltage). All images show clear details within the scan area, with regions of high contrast with typical feature size of the order of 0.2 – 2 μm , approximately an order of the magnitude larger than the grain size shown by topography of PZT film shown in Figure 5- 21 (g). That is, the SS-PFM images taken using large top electrodes show regions that are substantially larger than the grain size that display similar contrast in the nucleation bias, indicating correlated switching behavior of these regions. In many cases, these regions are characterized by a comparatively low nucleation bias. This, in turn suggest than within the volume probed, a region of material switches, and that cross-granular drives switching in adjacent grains. As shown in Figure 5- 22, transgranular coupling of domain structures is well-documented in the case of PZT ceramics^[49]

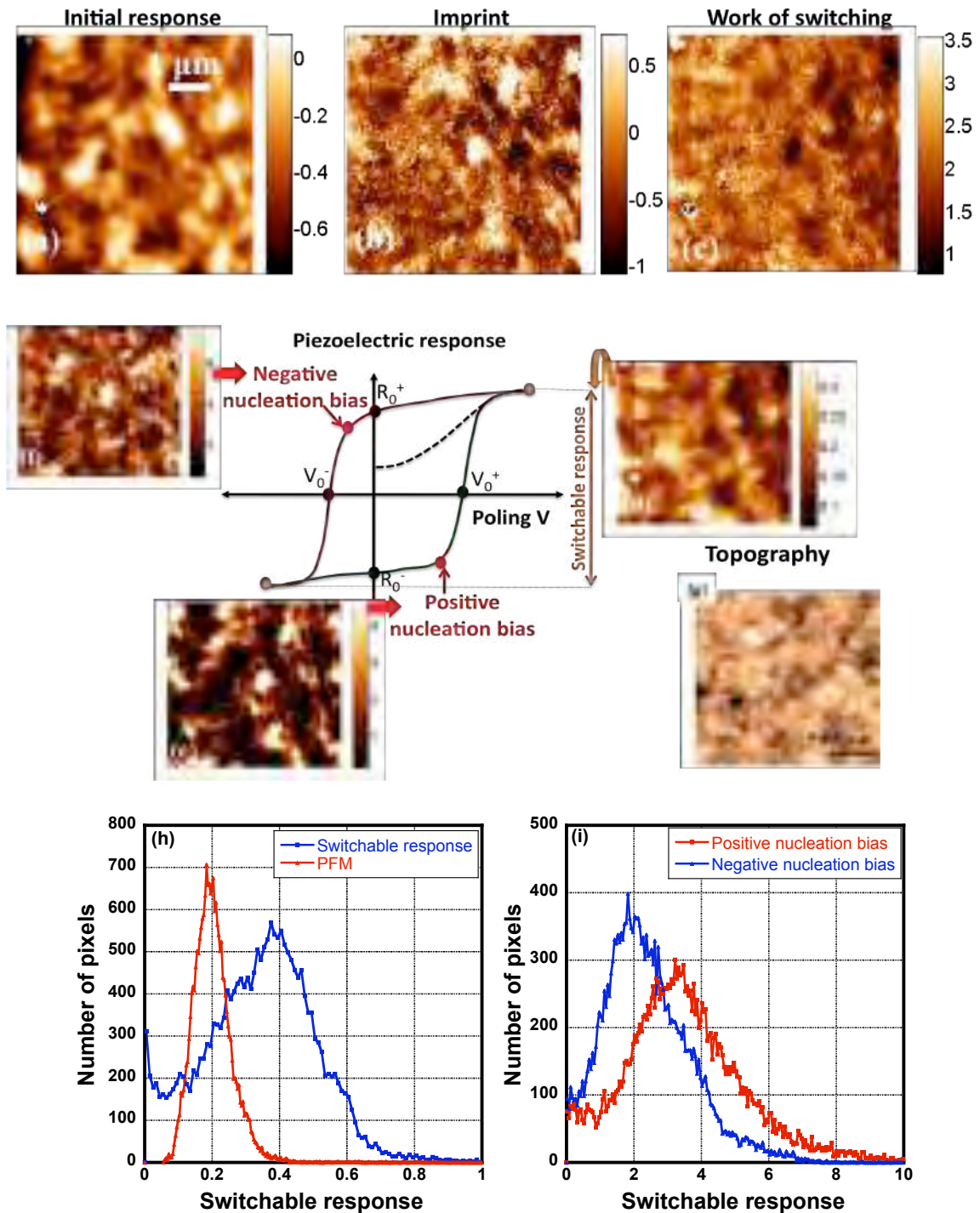


Figure 5-21: Spatial maps of ferroelectric switching parameters SS-PFM from the electrode area (a) initial piezoresponse, (b) imprint, (c) work of switching, (d-f) Schematic of the hysteresis loop switching parameters of switchable response, positive and negative nucleation bias, (g) topography of PZT films, (h) statistical distributions of PFM signal and switchable response, and (i) statistical distribution of positive and negative nucleation biases.^[55]



Figure 5- 22: An example of transgranular coupling in a PZT ceramic. DW denotes domain wall^[49]

The grain-grain coupling can be attributed both to short range effects due to electrical or mechanical coupling between adjacent grains, as well as possibly through a long-range elastic coupling through the substrate. These studies then provide the first measure of the lateral size of correlated switching in PZT films, which is of the order of 1-2 μm from spatial image analysis, corresponding to clusters consisting of 10^2 - 10^3 grains. The distribution functions for each of the loop parameters are shown as insets and are Gaussian in nature. The positive nucleation bias shows a broader distribution than the negative. This may be a consequence of the fact that on top electrodes, all but the first pixel have already seen the field excursion, and so will start the measurement partially pre-poled. It would be intriguing to compare these results for films of different compositions, defect densities, and levels of texture, to assess how the volume of correlated switching changes.

5.3.2 SS-PFM On and Off the Top Electrode

To understand further the origin of the correlated switching, a comparison of SS-PFM on and off the top electrode was made. Figure 5- 23 shows examples of nucleation bias maps with several hysteresis loops acquired from the bare PZT film surfaces and from electrode surfaces.

Figure 5- 23 (a) shows the result of SS-PFM directly on the bare PZT surfaces with the tip electrode. The shapes of local hysteresis loops are found to be generally similar for different areas of the sample, as reflected by the lack of correlated features in the SS-PFM maps and relatively small deviations from the average. Generally, the loops are smooth, and in nearly all cases have a small vertical shift. A small number of anomalous loops were observed. The lack of defined features within the image suggests that on the length scale of the pixel (150 nm), there is no strong correlation between switching behavior at neighboring points. This is consistent with models showing that for a tip electrode, the electric field is strongly confined to the area underneath the tip.^[55]

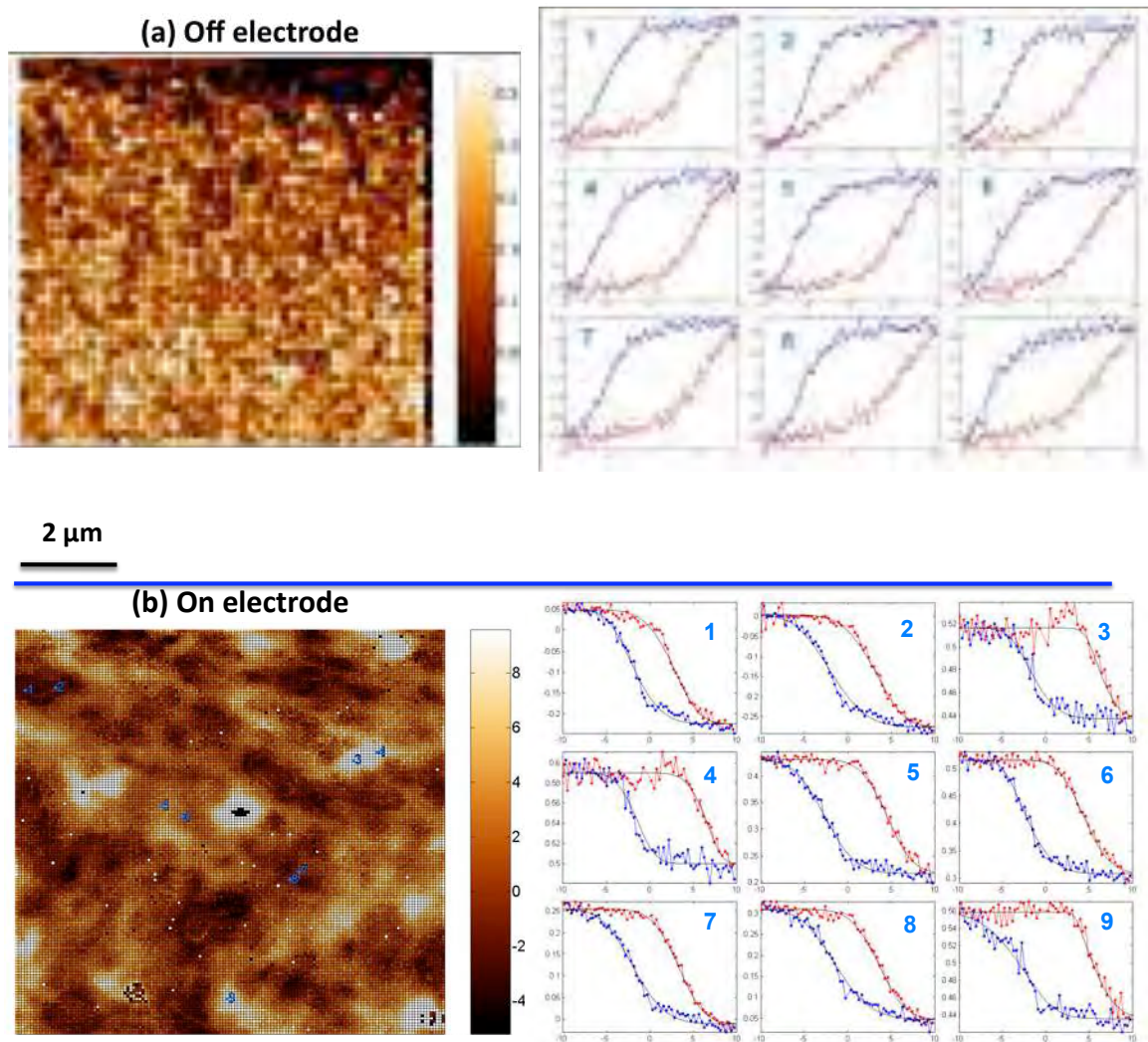


Figure 5- 23: Positive nucleation bias maps and hysteresis loops from several location acquired from (a) a bare PZT film sample surface and (b) the electroded surface^[55]

Figure 5- 23 (b) shows the SS-PFM on top electrode where the bias is applied across the entire area underneath the top electrode, the tip is used only to detect the vertical piezoresponse. In this case, the characteristic hysteresis loop shape is markedly different. The loops have somewhat better defined nucleation biases than samples without a top electrode. It is speculated that this may arise due to some combination of the training the sample, as the measurements are

made on the majority of pixels after multiple exposures to the driving field, and the influence of clusters of switching.

It should also be noted that the loops measured in a capacitor geometry generally show a strong vertical shift. Figure 5- 24 (a-b) illustrates the comparing hysteresis loops averaged over ~10,000 location for bare PZT film and on electrode surfaces. This behavior is most likely attributable to the global bending of the capacitor structure, bimorph like response as described in section 5.1.1.

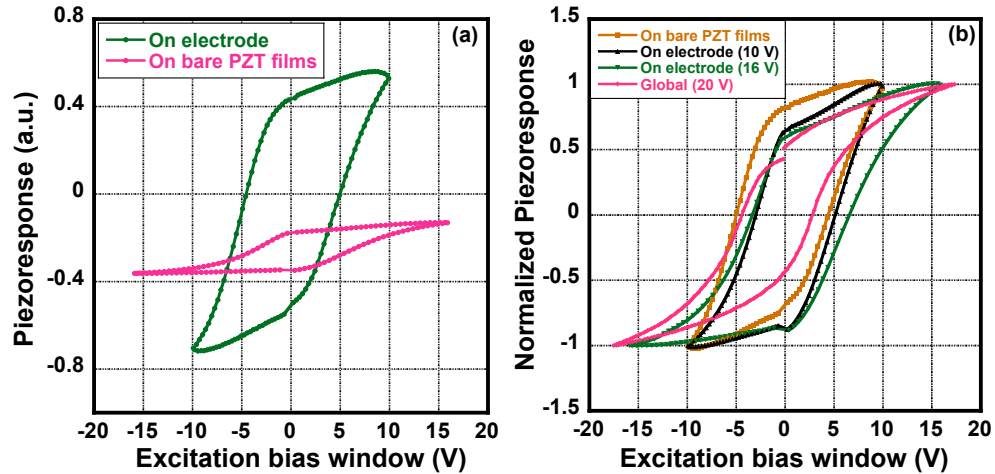


Figure 5- 24: Piezoelectric hysteresis loops obtain from SS-PFM averaged over an 8 x 8 μm area for bare PZT films (tip as top electrode) (b) comparison of normalized hysteresis loop of global, and local (on and off electrode) measurements

The measured piezoelectric response $PR_m(V)$ is shown in Equation 5.9. ^[55]

$$PR_m(V) = PR_l(V) + [PR_l(V)]_k \quad \text{Equation 5- 9}$$

where $PR_l(V)$ is the local piezoresponse, averaged over signal generation volume of 100-200 nm and $[PR_l(V)]_k$ is the signal averaged over a characteristic lateral length. In the limit of low frequencies (below ~ 1 kHz in this case), the wafer bends in the static regime and averaging occurs on the scale of the capacitor shown in Figure 5- 3 (c), while at higher frequencies, higher-

order modes and surface acoustic waves are excited. The averaging area k in this case is of the order of the corresponding wavelength. For the imaging frequencies used here, $k \gg 10 \mu\text{m}$ and hence the bending effect may result in a uniform vertical shift of the hysteresis loops, which now is not related to the presence of unswitchable polarization.^[56]

The result of statistical analysis of the switchable response images is illustrated in Figure 5- 25. The 2500 individual loop parameters were processed to obtain distribution functions for each parameter by using about 150 bins of equal size. The resulting distributions are well approximately by a Gaussian function shown in Equation 5-10.^[56]

$$y = \frac{A}{w\sqrt{\frac{\pi}{2}}} \exp\left[-2\frac{(x - x_c)^2}{w^2}\right]$$

Equation 5- 10

where A = total number of data points, not depend on the bias window

x_c = the average value of the switchable response within the image

w = the dispersion of the switchable response values

The evolution of the switchable response on excitation bias from minor to major loops is shown in Figure 5- 25.

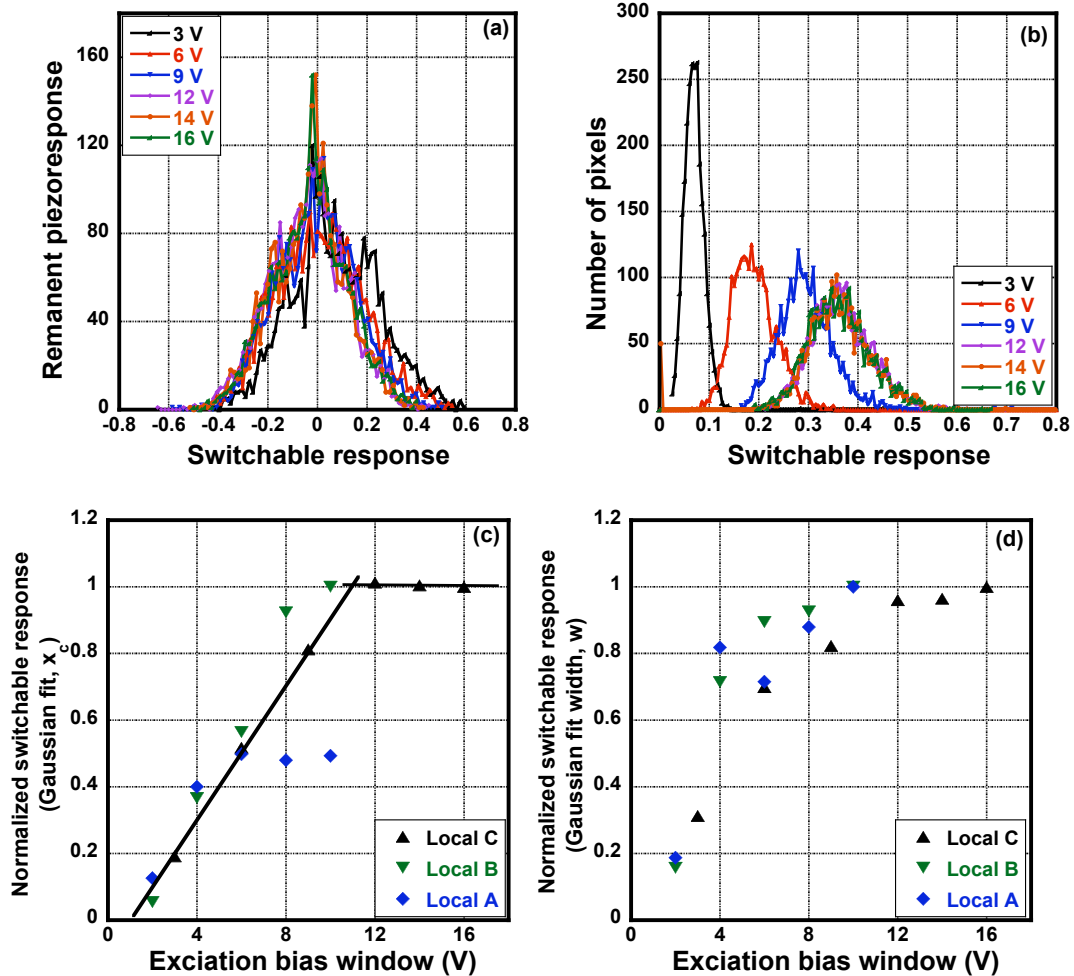


Figure 5- 25: (a) Distribution of remanent piezoelectric response for different excitation windows showing similarity of behavior, (b) Distribution of switchable response showing Gaussian profiles, (c) Evolution of average switchable response, and (d) Evolution of deviation width of switchable response^[56]

The dependence clearly delineates three regions. For excitation windows $< 1 - 2$ V, the switched response on the volume and time scale of the PFM measurement is small. This correlates with the Rayleigh-like region of the film behavior in macroscopic capacitor measurements, and with the understanding that in the Rayleigh regime, the excitation should leave the density and structure of the domain walls unchanged by the field cycling. Apparently, the local domain wall motions associated with the Rayleigh behavior in small ac fields does not

change the average piezoelectric response measured at zero bias after relaxation. For excitation bias windows between 1 and 10 V, the switched response increases approximately linearly with the excitation bias window, indicative of the increasing volume of material with irreversible changes of domain structure. The observed transition from Rayleigh – like to Preisach behavior (see Figure 5- 26) for the macroscopic capacitor at this field range may thus be associated with collective domain dynamics at these mesoscopic scales. Finally, for excitation windows above 11 V, the switchable response measured via PFM saturates. In this case, polarization switching is induced through the entire volume of the sample. These observations thus provide direct insight into bias-dependent evolution of reversible and irreversible polarization components.^[56] Figure 5- 26 shows the comparison of local switching piezoresponse from SS-PFM and global switching polarization from Preisach distribution. Even though the global and local switching behaviors are not perfectly matched, they are comparable. Therefore, the combination of global measurements and local spectroscopy allows the characteristics length scales corresponding to the transition from Rayleigh to Preisach behaviors to be determined.

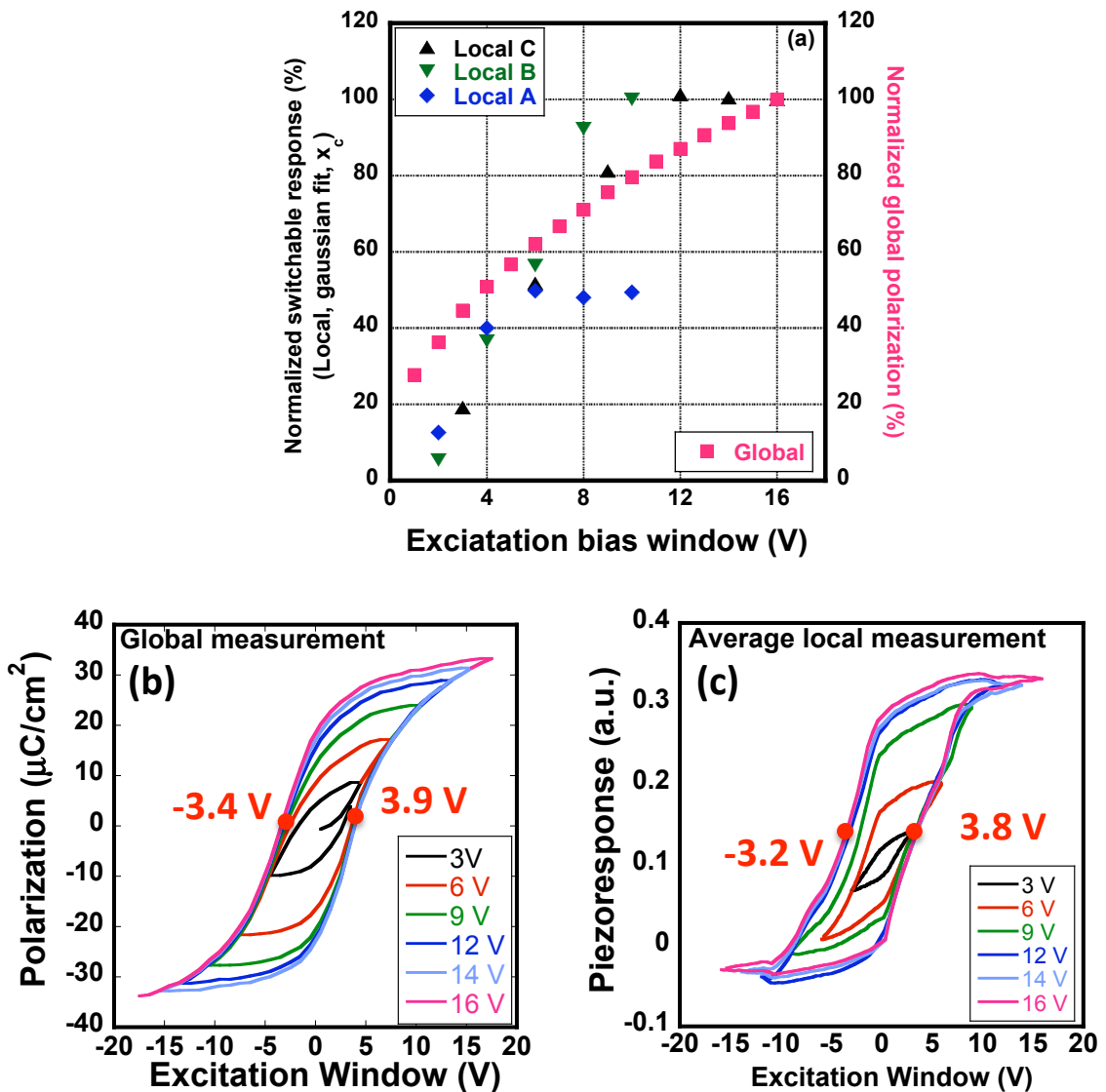


Figure 5- 26: (a) The comparison of global and local switching vs. excitation bias window, (b) A series of minor and major hysteresis loops calculated from the irreversible part of the Preisach density assuming the sample was depoled prior to the field excitation, and (c) Averaged local SS-PFM loops for similar excitation bias window^[56]

At the same time, when all of the loops are averaged, see Figure 5- 26, no preferred polarization is apparent and the resulting behavior matches closely with the Preisach calculations for the same field excursions. These observations strongly suggest that observed Preisach behavior for macroscopic capacitors originates on length scales above the resolution limit of PFM.

To obtain insight into the spatial distribution of switching regions as a function of the excitation window, high resolution SSPFM maps and bare film and electrode topography are shown in Figure 5- 27. Figure 5- 27 (a), clearly shows large scale (0.1 – 1 μm as compared to ~ 55 nm pixel size) features in the switchable response images. To quantify the length scales observed in the images, we calculate the spatial autocorrelation functions (CF) (radial), defined as in Equation 5-11.

$$CF = \frac{F(r) * F(r + dr)}{[F(r)]^2} - 1 \quad \text{Equation 5- 11}$$

The average size of the features in the positive nucleation bias map is ~ 200 nm, estimated as the full width at half maximum (FWHM) of the correlation function. From the topography image, the average feature size is significantly smaller, ~ 50 nm. Correlations at large length scales are also evident through the presence of additional maxima in the correlation function at length scales greater than 1 μm . These can also be directly observed in the switchable response images as micron sized areas with comparable switching properties. From Figure 5- 27 (d), the feature of 1.5 μm size observed in the switching polarization maps persist through changes in the excitation bias window from 7-16 V and likely represent the collective correlated response of regions with $\sim 10^2$ - 10^3 grains.^[55, 56]

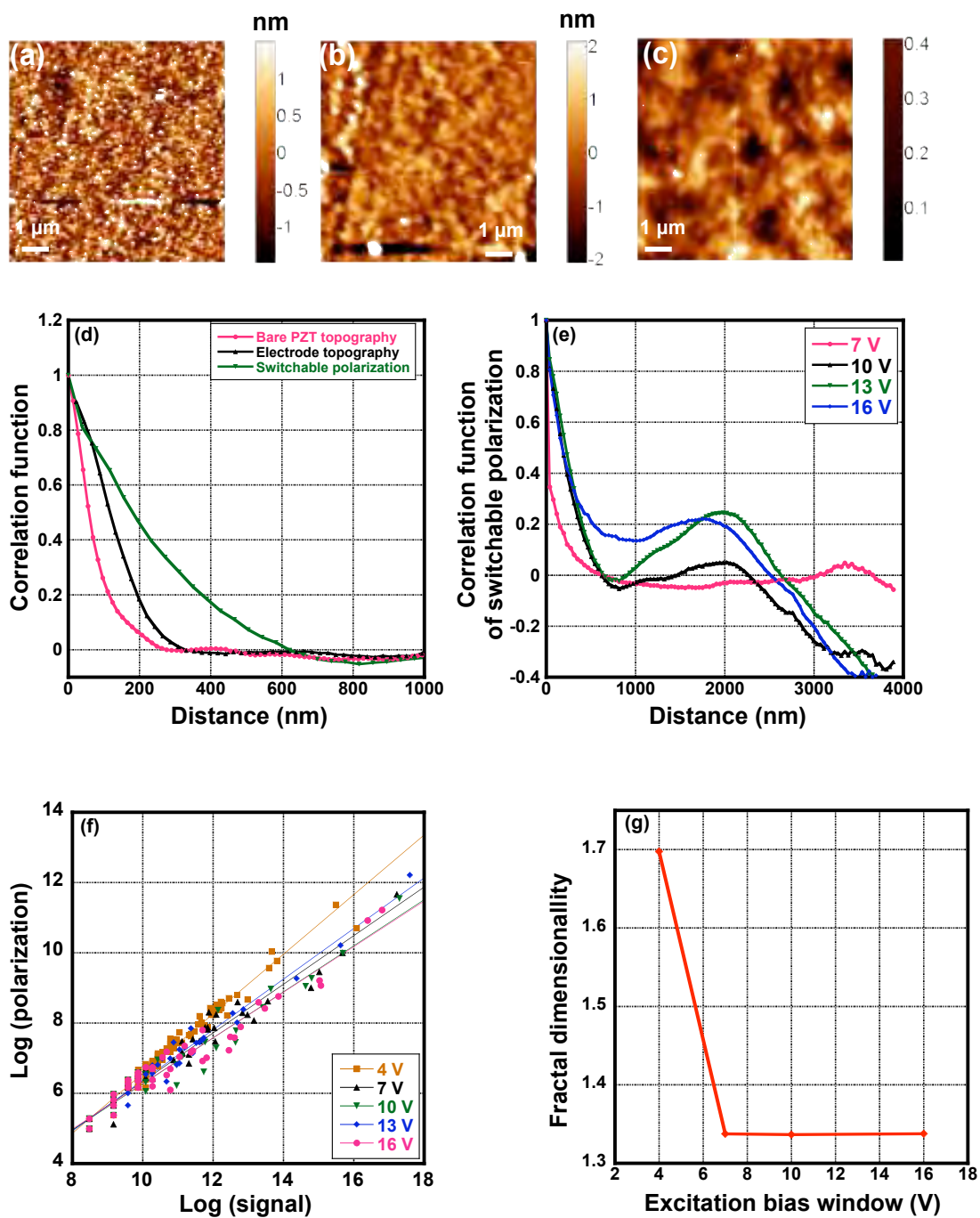


Figure 5- 27: (a) Topography of bare PZT films, (b) Topography of electrode film, (c) Positive nucleation bias map at an excitation window of 7 V, (d) Correlation function of bare PZT films, electrode, and switchable polarization, (e) Correlation function at different bias voltages, (f) Fractal analysis of switchable polarization images for different excitation bias window, and (g) Excitation bias window dependence of fractal dimensionality^[56]

Fractal analysis of the switchable response images based on perimeter and surface area calculations are shown in Figure 5- 27 (g) for the high resolution data sets. For each image, the switchable response average value was chosen as the threshold to distinguish between high and low values and the resulting fractal dimension is defined in Equation 5.12 and Equation 5.13.

$$D = 2\alpha \quad \text{Equation 5- 12}$$

$$P = \mu S^\alpha \quad \text{Equation 5- 13}$$

where P is the perimeter of high switchable response features, S is the surface area, μ is a prefactor, and α is the scaling coefficient.

The fractal dimension remains fairly constant with change in the excitation bias window, suggesting universality of the cluster geometry. The value of $D = 1.3$ is close to that expected for ferroelectric materials controlled by bond disorder, presumably pinning at grain boundaries in the presence of dipolar interactions, as analyzed by Paruch et al.^[96]

In summary, the local switching behavior in ferroelectric PZT capacitors and thin films was studied using spatially resolved hysteresis loop measurements. While macroscopic polarization hysteresis measurements and the tip-induced switching are insensitive to macroscopic substrate bending, the hysteresis loops in capacitors often exhibit significant vertical offset and changed amplitude due to excitation of bimorph-like modes of the structure at low frequencies and possibly surface acoustic waves at high frequencies. In the frequency range utilized here, these effects are likely to provide vertical signal offset uniform within the measured area. The spatial variability of SS-PFM maps indicate the correlated switching behavior across $\sim 1\text{-}2 \mu\text{m}$ sized clusters comprised of $10^2\text{-}10^3$ grains, as evidenced in nucleation bias and switchable polarization images. These correlations are likely driven by non-local elastic

interactions mediated by coupling through the top electrode and substrate, as well as local elastic and polarization coupling across grain boundaries. Jointly, these local and global interactions result in collective dynamics between the grains at mesoscopic 0.1-10 μm length scales.^[55, 56]

For the spatially resolved mesoscopic polarization dynamic in polycrystalline ferroelectric films, the method allows observation of irreversible polarization dynamics on the length scales below spatial resolution ($\sim 200\text{-}300\text{ nm}$) through bias evolution of hysteresis loops, and on the larger length scales through real space mapping of the switchable and remanent polarization component as a function of the excitation bias window. The Rayleigh behavior is associated with locally ($\sim 50\text{ nm}$) reversible polarization dynamics, while a transition to the Preisach regime is associated with large inhomogeneity of switching behavior. Large scale ($\sim 1\ \mu\text{m}$) regions of distinctly correlated switching behavior were observed. The corresponding roughness exponent corresponds to bond disorder, presumably due to pinning at grain boundaries. Neither the characteristic cluster size nor the fractal dimension depends on the excitation window, which is indicative of the universality of the observed dynamics.^[56]

Chapter 6

Nanoindentation Studies of PZT Films

This chapter describes the results of nanoindentation of $\text{Pb}(\text{Zr}_{0.52}\text{Ti}_{0.48})\text{O}_3$ films with mixed $\{111\}$ and $\{100\}$ orientation using a Hysitron Triboindenter with a 500 nm radius conospherical diamond tip. Several methods are utilized to measure the mechanical properties of thin films, such as the impulse acoustic method, atomic force microscopy, Brillouin light scattering, and nanoindentation.^[97] Nanoindentation has high sensitivity, high resolution, and is comparatively simple.^[97-100] Nanoindentation is able to evaluate the mechanical behavior of films while they are still adhered to the substrate.^[100] In this work, the nanoindentation technique was utilized to study the hardness and elastic modulus of PZT films with mixed $\{001\}$ and $\{111\}$ orientation. Of particular interest was whether there would be any indication of motion of non-180° domain walls in the films.

In general, the application of a stress to a ferroelectric material can cause both linear and nonlinear constitutive (i.e. stress-strain) behavior. Figure 6- 1 shows typical strain (ϵ) and depolarization behavior of a ferroelectric ceramic under a compressive stress (σ) applied parallel to the poling direction. At small compressive stresses (A-B), the compressive strain increases linearly, while the polarization linearly decreases. At compressive stresses higher than the coercive stress (σ_c), ferroelastic domains will switch, causing additional strain and depolarization, and resulting in a decrease in the elastic moduli. Eventually, many of the domains will switch so that the polarization direction is perpendicular to the compressive stress. Afterwards, linear behavior will be restored as the compressive stress can no longer cause domain switching. A

reversible process is observed if the polarization state recovers to its original state on unloading the compressive stress. However, irreversibility is observed if the domains remain switched during unloading the compressive stress. In the irreversible case, remanent strain referred to plastic strain and depolarization are observed.^[101]

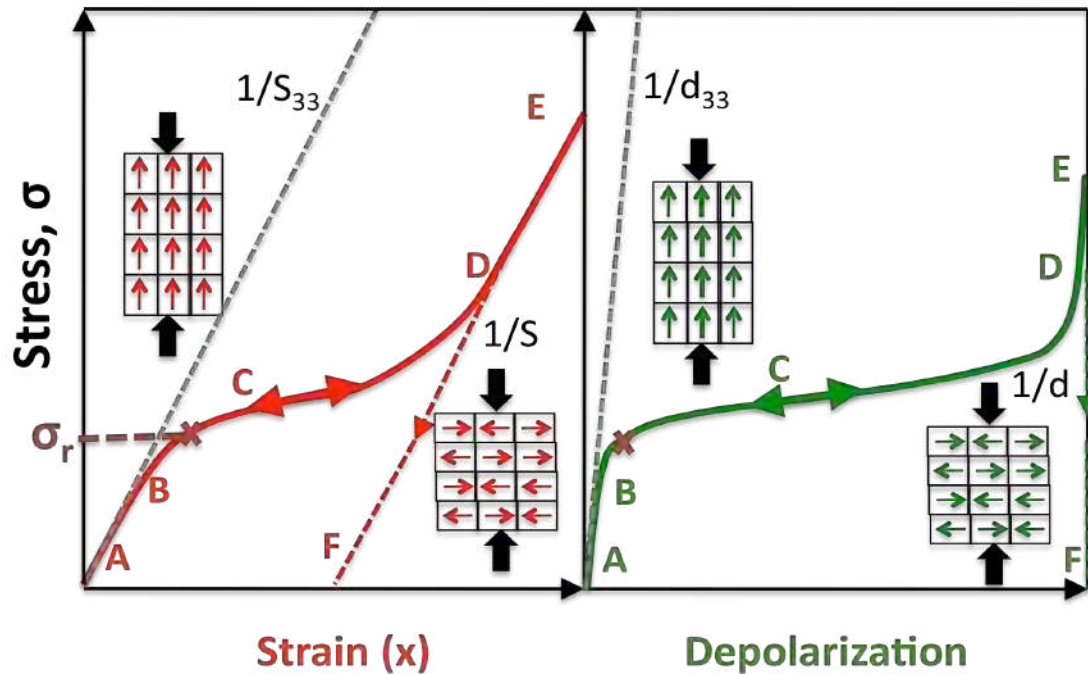


Figure 6- 1: Typical strain and depolarization behavior for a uniaxial stress applied parallel to the poling direction in PZT ceramics, A-B linear behavior before domain switching, B-D, domain switching, D-E, linear behavior after all domains have been switched perpendicular to stress. E-A is the case of reversible domain switching, and E-F is the case of irreversible domain switching. After reference ^[101]

6.1 Loading and Unloading Elastic Curves

In this work, the Oliver-Pharr method was employed to model the elastic behavior of PZT films with mixed $\{001\}$ and $\{111\}$ orientation as shown in Figure 6- 2. The calculations are described in Equation 6-1 to Equation 6-2. The stiffness can be identified from the slope of the loading or unloading curve and used to calibrate the contact area to determine the reduced elastic

modulus and hardness.^[76] The sensitivity of the properties to strain rate can be observed by varying the loading conditions and reduced elastic modulus and hardness.

$$\frac{1}{E^*} = \frac{1 - \nu_s^2}{E_s} + \frac{1 - \nu_i^2}{E_i} \quad \text{Equation 6- 1}^{[100, 102]}$$

$$H = \frac{P_{\max}}{A_c} \quad \text{Equation 6- 2}^{[100, 102]}$$

where E^* is reduced contact modulus, E_s is elastic modulus of sample, E_i is elastic modulus of indenter tip, ν_s = Poisson's ratio of substrate, ν_i = Poisson's ratio of indenter tip, Equation 6-2 is a Meyer's hardness approach, where H is the hardness, P_{\max} is the maximum force, and A_c is the projected contact area. The contact area was calculated by using a known tip geometry as a function of plastic or contact indentation depth as shown in Equation 6-3.

$$A_c = C_0 h_p^2 + C_1 h_p + C_2 h_p^{1/2} + C_3 h_p^{1/4} + \dots + C_n h_p^{1/2^{n-1}} \quad \text{Equation 6- 3}^{[100]}$$

where A_c is contact area, C_i are constants reflecting the tip geometry and h_p is the indentation contact depth.

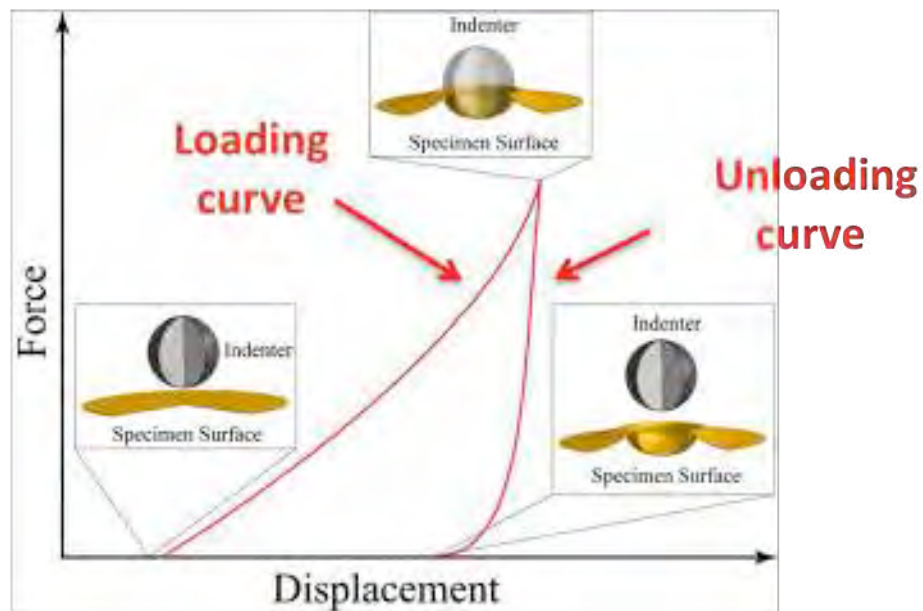


Figure 6- 2: Schematic loading and unloading curves measured using nanoindentation.^[100]

6.2 Pile-Up

The Oliver-Pharr method is not directly applicable to materials that have pile-up behavior. In Figure 6- 3, the cases of pile-up and sink-in in nanoindentation are shown, where a is the projected tip radius at the plane of the underformed surface of the film, $a_{c, \text{sink-in}}$ is the pile-up projected contact radius when the material sinks in, $a_{c, \text{pile-up}}$ is the projected contact radius when the material piles-up, h_i is the maximum indentation depth, h_p is the plastic indentation depth, $h_{\text{pile-up}}$ is the pile-up height, and R is the radius of indenter tip.^[100] In order to obtain accurate material properties, any pile-up must be included in the plastic indentation depth, otherwise the reduced elastic modulus and hardness can be overestimated substantially.^[99, 100]

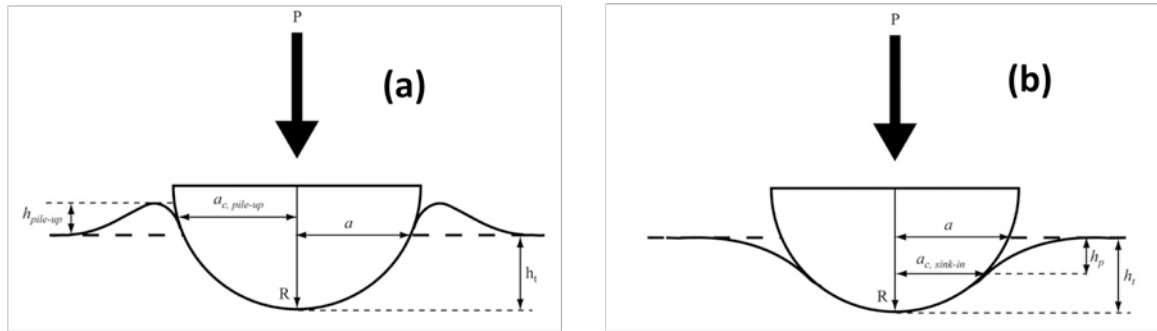


Figure 6- 3: Schematic of material response during indentation test (a) image depicting a material that shows pile-up and (b) material that sinks in.^[100]

In the indentation experiments of this work, it was found that the PZT film interacts with the indenter tip by pile-up. The amount of pile-up was directly linked to the amount of plastic deformation. The in-situ image obtained immediately after indentation test was used to calculate pile-up height (h_{pu}). First, the image was flattened using the plane correction tool in Scanning Probe Image Processor (SRIP) software. A 3rd order polynomial fit was employed over the entire image with the Matlab program to find the minimum point on the image. Then, the pile-up height was determined by minimum on the image and maximum point along eight evenly spaced radii. More details of pile-up calculations were described elsewhere.^[100] The average pile-up from 8 locations around the indent was used. Figure 6- 4 shows the pile-up results for PZT films. For lower loads, pile-up is indistinguishable from surface roughness. For the highest load at about 3800 μN , the pile-up is about 10% of plastic indentation depth. Therefore, pile-up is not large for PZT films.

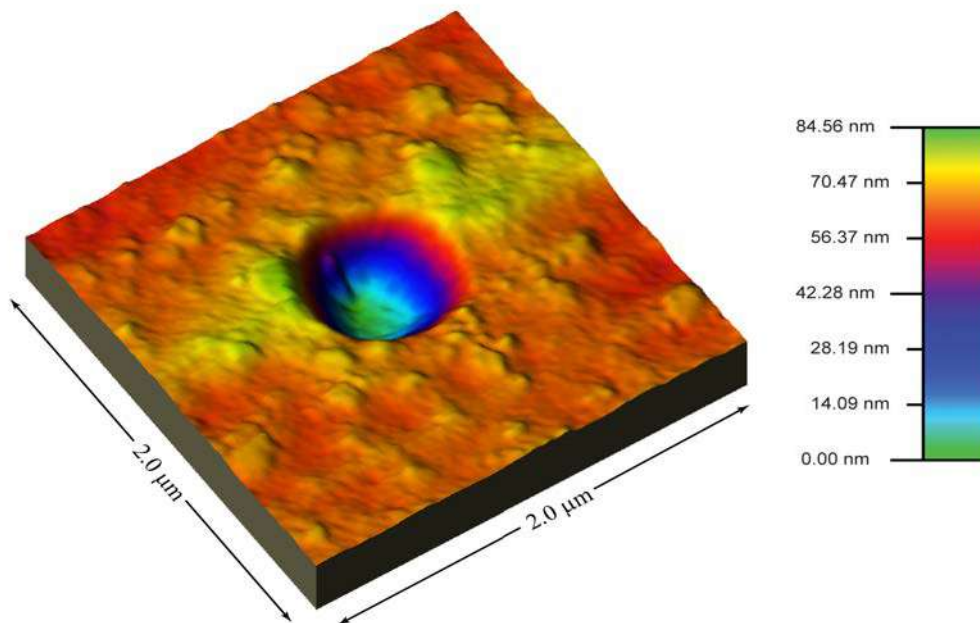


Figure 6- 4: A scanning probe microscope image of Pile-up results for a PZT film

6.3 Residual Stresses

Residual stresses can also affect the results of nanoindentation tests. In general, films have residual stresses as a result of the processing used in the film preparation. The stresses can be either tensile or compressive. In this work, the residual stresses in all of the PZT films are expected to be approximately the same, since all of the films were prepared by the same chemical solution deposition processing conditions at the same time. The majority of the residual stress has been shown to be due to the thermal expansion mismatch between the film and the substrate; the stresses of the PZT films should be tensile, since the thermal expansion coefficient of Si is smaller than that of PZT, particularly above the phase transition temperature.^[18, 19] For that reason, each PZT film should have the same level of residual stresses ($\sim 100 - 150$ MPa)^{[18] [1, 18]}

6.4 Nanoindentation Tests on PZT Films with Mixed {111} and {100} Orientation

The first experiment conducted was to study the effect of the strain rate on the reduced modulus and hardness on 0.28 μm PZT films with mixed {001} and {111} orientation. Afterwards, a strain rate was selected and performed on the thickness series of PZT films with mixed {001} and {111} orientation to obtain a self-consistent set of reduced modulus and hardness measurements. All measurements and analyzes were made by Amber Romasco.

6.4.1 The Indentation Depth Set Up

The indenter loading depth is useful to study how PZT films will respond when large stresses are applied to films. As the indentation depth increases, it would be anticipated that the substrate will contribute more to the overall mechanical response. The forces for each nanoindentation experiment were selected to produce indents corresponding to 10%, 20%, 25% and 50% of the film thickness (e.g. 700 μN , 1300 μN , 1750 μN , and 3800 μN). The selected loading rates were 10 $\mu\text{N/s}$ and 100 $\mu\text{N/s}$ with a 10 s holding time.^[100]

Table 6- 1: Nanoindentation loading parameters tests for PZT films with mixed {001} and {111} orientation

PZT film thickness	Indent depth
0.28 μm	28 nm, 53 nm, 70 nm, 140 nm,
0.53 μm	28 nm, 53 nm, 70 nm, 133 nm, 140 nm, 240 nm
1.09 μm	28 nm, 53 nm, 70 nm, 102 nm, 140 nm
2.06 μm	28 nm, 53 nm, 70 nm, 140 nm, 206 nm
4.4 μm	28 nm, 53 nm, 70 nm, 140 nm, 240 nm

Figure 6- 5 shows the reduced modulus and hardness tests measured at two strain rates. Systematic loading rate tests were used to determine the strain rate sensitivity. The results reveal that there is insignificant sensitivity to strain rates over this range, because both sets of data produce about the same results (within 3% of data distribution). In this work, since there is not much sensitivity in strain rate of PZT films, the 10 $\mu\text{N/s}$ loading rate was used in nanoindentation measurements.

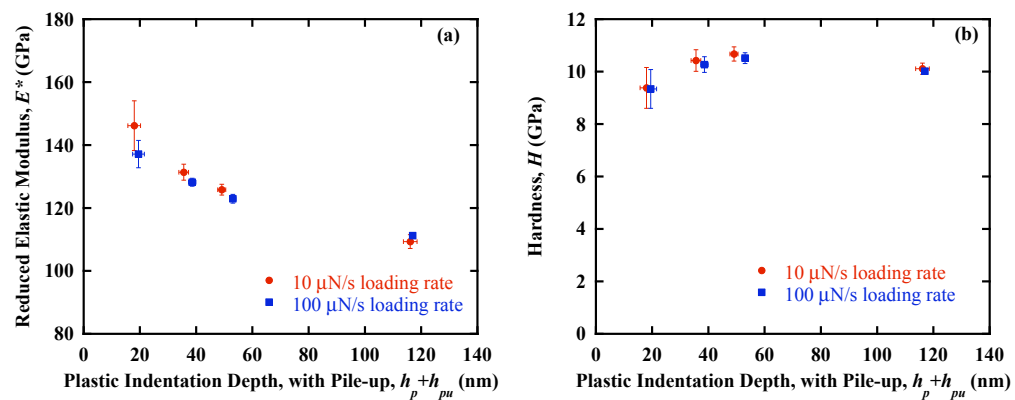


Figure 6- 5: (a) The strain rates with reduced modulus and (b) The strain rates with hardness as a function of plastic indentation depth of 0.28 μm mixed {001} and {111} orientation PZT film

6.4.2 Reduced Modulus and Hardness of PZT Films

Nanoindentation measurements were performed on PZT films with mixed $\{111\}$ and $\{100\}$ orientation for a thickness series of 0.28 μm , 0.53 μm , 1.09 μm , 2.06 μm , and 4.40 μm . Figure 6- 6 illustrates the force as a function of displacement showing the loading and unloading curves.

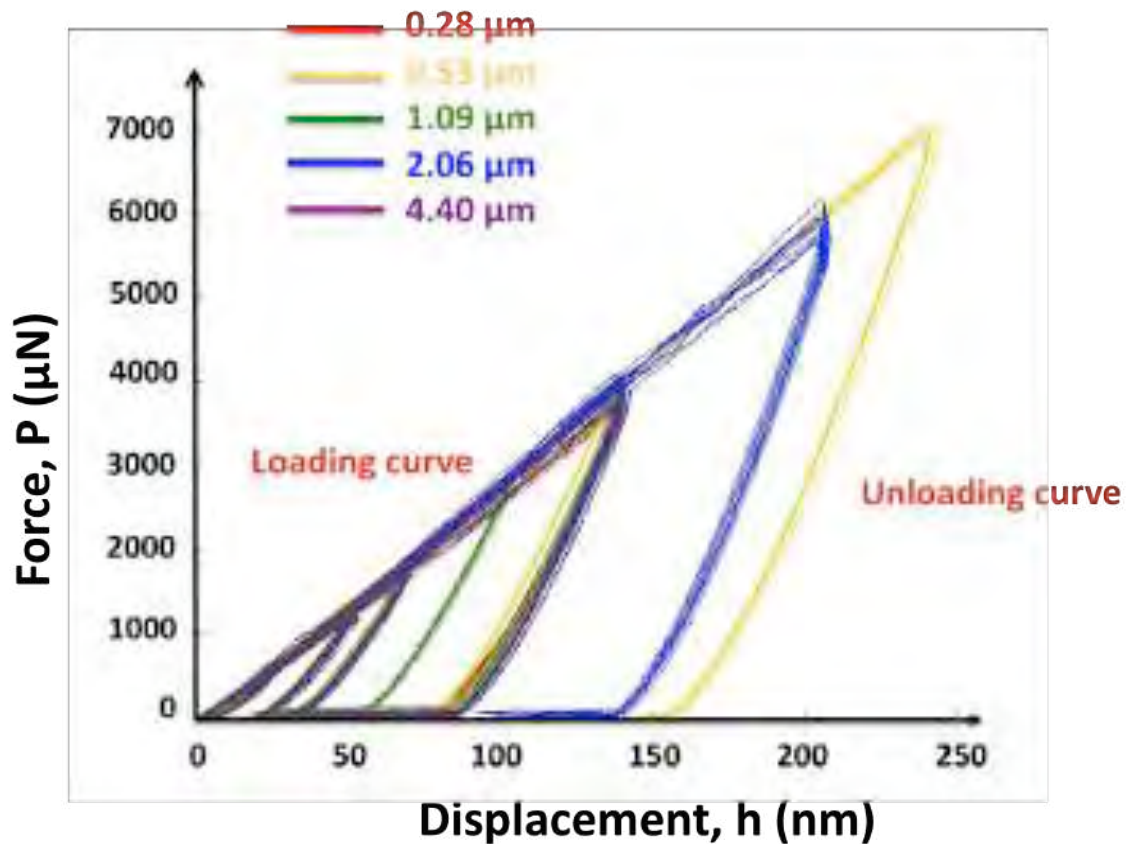


Figure 6- 6: Force as a function of displacement showing loading and unloading curves, as well as the reproducibility of the measurements

The reduced elastic modulus was resulted from the loading and unloading curves as shown in Figure 6- 7. The loading and unloading curves for each film thickness are shown in Appendix C. The loading moduli were taken from the initial portion of the force-displacement curves; here although the indentation depths are quite shallow, the nominal von Mises stresses

pressures are large – on the order of a GPa.^[100, 103] The unloading moduli were taken from the initial portion of the unloading curve; again, the stresses are expected to be on the GPa order based on flow stress-hardness correlations such as the Tabor relationship.^[100, 103] Two different families of curves are apparent in Figure 6- 7. On loading, the reduced modulus is on the order of 80 GPa. Typically, hard PZT ceramics have elastic modulus on the order of 80 GPa due to limited (but finite) non-180° domain wall mobility. In soft PZT ceramics, where the non-180° domain wall motion is easier, the elastic modulus is typically ranges from 40 – 60 GPa. Thus, the reduced modulus (elastic modulus/(1-Poisson's ratio²)) measured in the loading curves appears to be consistent with a finite amount of ferroelastic domain wall motion, when the samples are stressed heavily (~GPa in this experiment)^[100]. As the loading proceeds, one would expect all of possible ferroelastic wall motion to be exhausted. Upon subsequent unloading, the reduced elastic modulus is much higher presumably because there is no contributions from mechanical softening associated with non-180° domain wall motion.^[104-106]

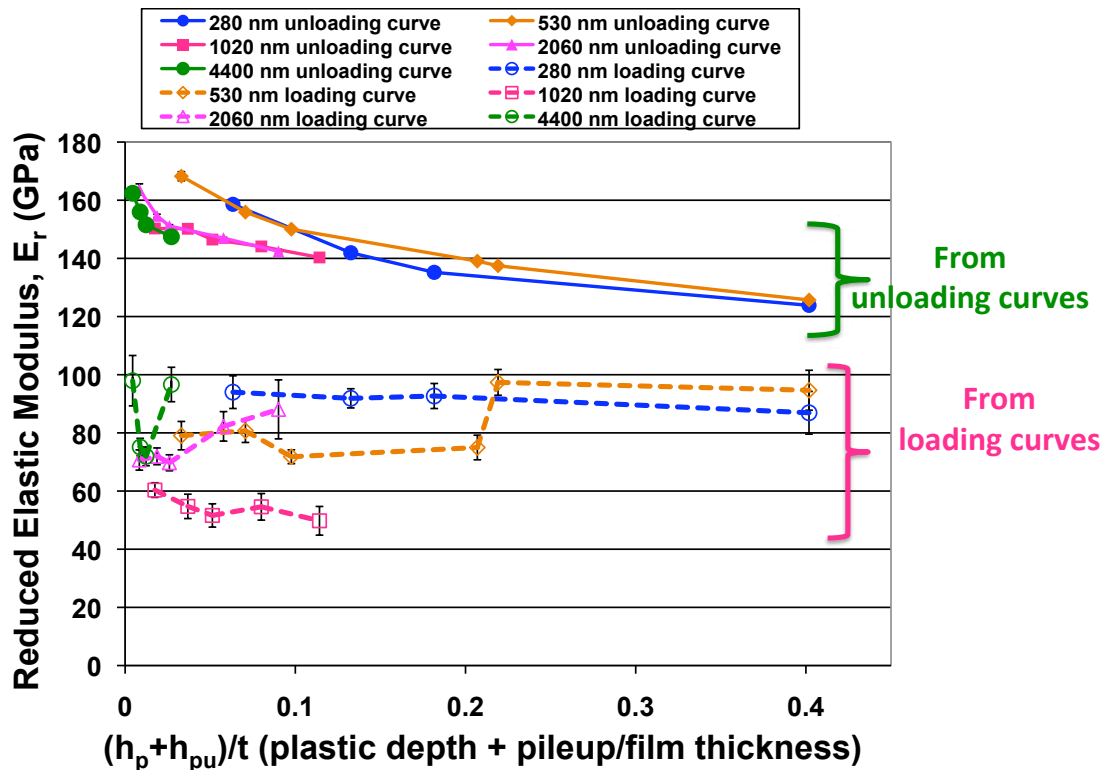


Figure 6- 7: The elastic modulus as a function of percent indentation depth normalized by film thickness calculated from unloading curves and loading curves for each mixed {001} and {111} orientation PZT film thickness.

It is intriguing that the reduced moduli on unloading are of the same order as that of PZT ceramics above the phase transition temperature, where all domain walls are eliminated. Bouzid et al., Bourim et al., and Zarycka et al. reported measurement of elastic modulus as a function of temperature for PZT ceramics for several compositions, including PZT 52/48.^[104-106] Theoretically, at temperatures below the transition temperature (T_c), the PZT crystal structure can be rhombohedral, tetragonal, or monoclinic depending on the composition of Zr/Ti. There are 180° , 109° , and 71° domain walls for the rhombohedral and 180° and 90° domain walls for the tetragonal crystal structures. Above T_c , the PZT crystal structure is cubic and no domains are present. Typical data for bulk PZT ceramics are shown in Figure 6- 8. Below T_c , the ferroelastic walls can be moved by applied stresses, and the Elastic Modulus is about 70 GPa to 90 GPa

depending on the phase. In contrast, there is no mobility of ferroelastic walls in PZT at temperature higher than T_c , resulting in an increase in Elastic modulus > 120 GPa in the case of PZT ceramics.^[101]

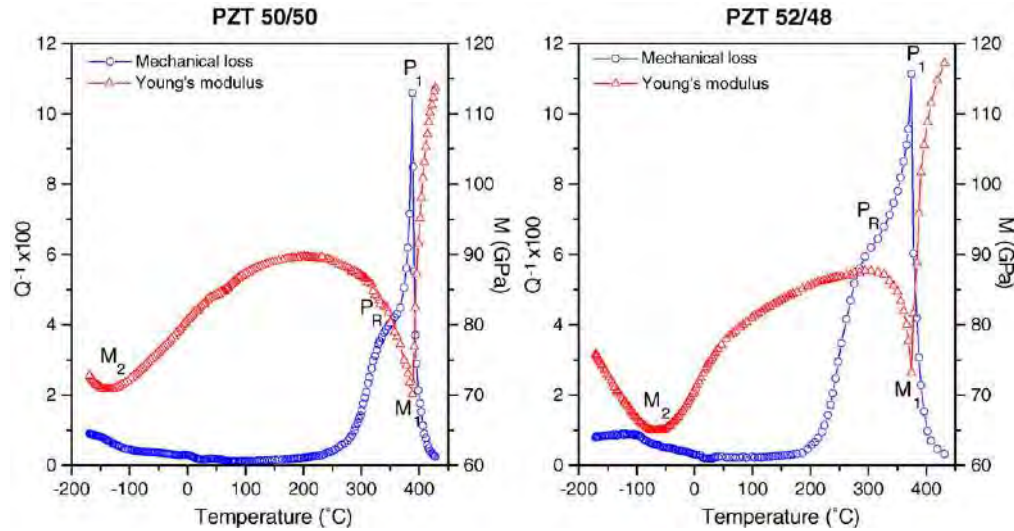


Figure 6- 8: The Elastic modulus for PZT 50/50 and PZT 52/48 ceramics. M_1 and M_2 represent Elastic modulus. P_1 and P_2 represent mechanical losses^[105]

As can be seen in Figure 6- 7, there is no trend in reduced elastic modulus extracted from loading curves in terms of thickness dependence. Two possible explanations could be concluded. The first is that all samples have comparable levels of non- 180° domain wall mobility. Secondly, there could be insufficient precision in the nanoindentation measurements to detect differences in the non- 180° domain wall motion. This point should be examined in detail in future work.

It should also be noted that the nanoindentation results here are comparable to those in previous reports.^[104-106] Delobelle et al. reported the modulus of 0.2 to 3 μm thick MPB PZT thin film prepared by sputtering deposition. Those PZT films have grain sizes of 0.2 μm and 1-4 μm for (111) and (110) orientation, respectively. They analyzed the nanoindentation results to obtain a modulus using the Oliver and Pharr method as shown in Figure 6- 9. The biaxial elastic

modulus is independent of thickness and grain size measured at low pressures. With higher loads, the elastic modulus drops. This would be consistent with the supposition that ferroelastic domain wall motion is easier for larger grain size samples. The elastic modulus decreases as ferroelastic domains reorient under the pressure of the tip.^[97]

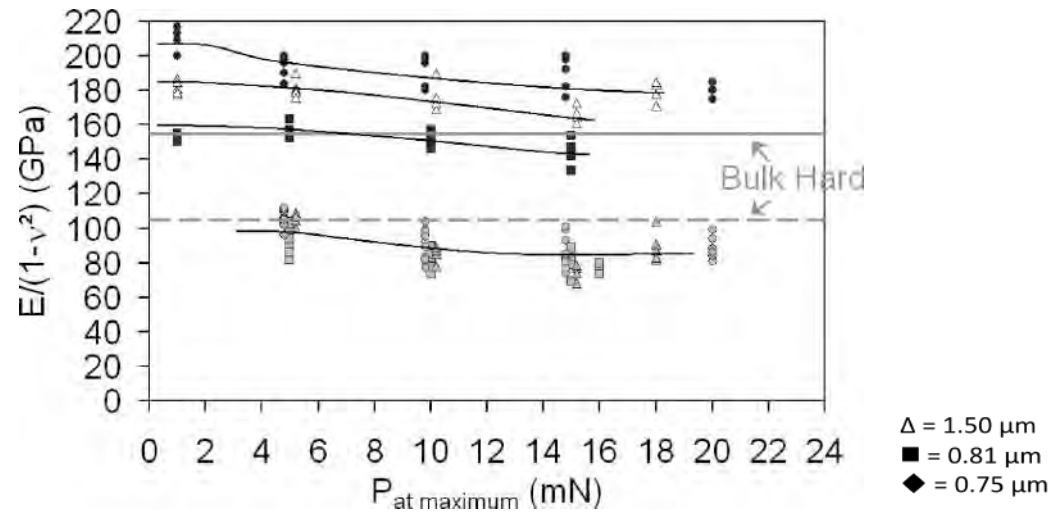


Figure 6- 9: Biaxial elastic modulus vs. maximum applied force on the tip.^[97]

Subsequently, Delobelle et al. also reported the mechanical properties by nanoindentation of PZT and PMN. They reported the reduced elastic modulus for films of these two materials as a function of the maximum force and grain sizes. It was found that the bigger the grain size, the lower the elastic modulus shown in Figure 6- 10. This would be due to an increase in domain wall motion. The (unloading) modulus of those films is close to those of hard bulk ceramic.^[98]

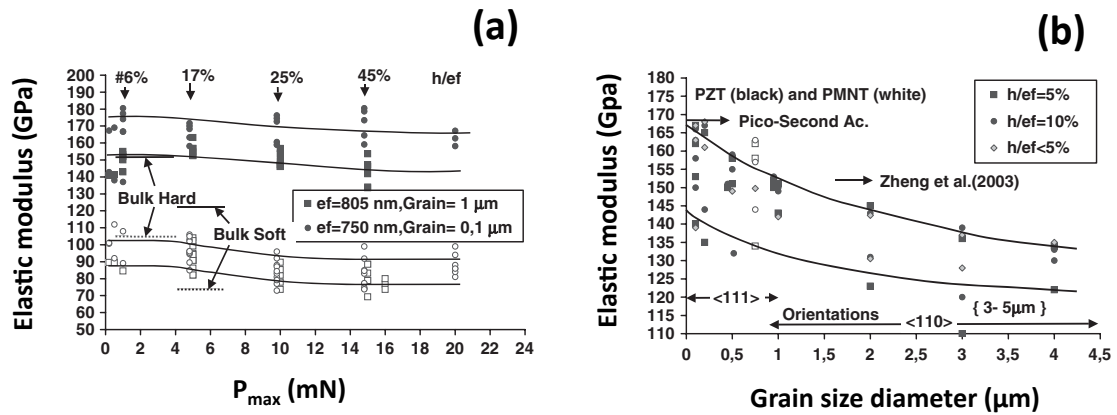


Figure 6- 10: (a) Elastic modulus as a function of load and (b) Elastic modulus as a function of grain size diameter, h = indentation depth and ef = film thickness^[98]

Fang et al. observed nanomechanical properties of 500 nm thick PZT (52/48) films prepared by RF magnetron sputtering. They found the elastic modulus and hardness of the films varied because each film has a different grain size. In contrast to the Delobelle results, they claim that films with bigger grain size show higher Elastic modulus and hardness. The elastic modulus and the hardness ranges are 109 – 260 GPa and 6.5 – 16.6 GPa, respectively.^[107]

Wu et al. investigated the mechanical properties with nanoindentation of 200 nm PZT (52/48) films with $\langle 111 \rangle$, $\langle 100 \rangle$ and random orientation prepared by sol-gel technique. They used load displacement curves and the Oliver and Pharr method to analyze the elastic modulus and hardness of PZT film. They observed that the modulus increases when the indentation depth rises from 0 up to ~ 20 - 30 nm (~ 10 % of film thickness). Afterwards, the indentation modulus and hardness of the samples dropped slightly as the indentation depth increases, as shown in Figure 6- 11 (a) due to influence from the substrate. Figure 6- 11 (b) shows the hardness of PZT films as a function of indentation depth. The apparent hardness increases with the indentation depth up to 20 – 30 nm (~ 10 % of film thickness) and becomes constant or further increases with deeper indentation depth. They suggested that the constant hardness observed for deeper indents

is due to the substrate effect when the indenter is close to the PZT / Pt interface. Increased hardness with deeper indents was attributed to dislocations producing deformation in materials with a grain size of less than 60 nm.^[108]

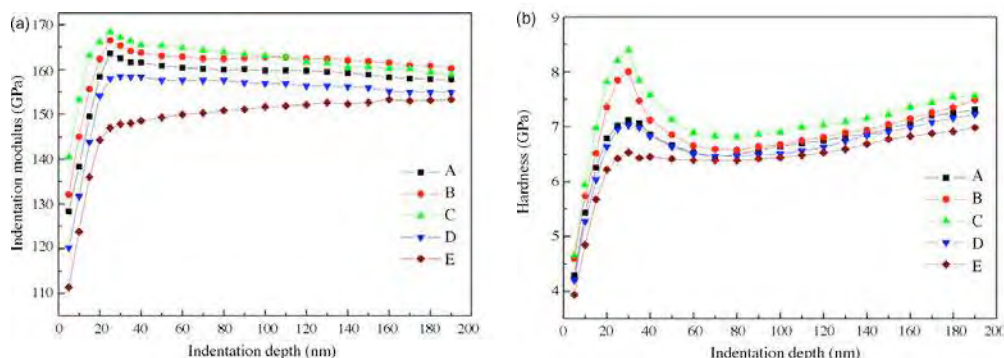


Figure 6- 11: Nanoindentation of 200 nm PZT (52/48) films by Wu et al. (a) Indentation modulus vs. indentation depth and (b) Hardness vs. indentation depth. A = $\langle 111 \rangle$ with 32 nm grain size, B = $\langle 111 \rangle$ with 49 nm grain size, C = $\langle 111 \rangle$ with 58 nm grain size, D= random, E = $\langle 100 \rangle$ ^[108]

Figure 6- 12 shows the hardness of the PZT films from this work. For all PZT film thicknesses, the hardness test shows the same trend. At low indentation depths, the hardness increases slightly, and becomes constant at deeper depths. There are two possible reasons. First, when the indentation depth increases, the hardness is affected from the substrate. Second, the larger indentation depths may result in more dislocations, making the materials harder. The hardness behavior of PZT film was also investigated. The same trends are reported by Wu et al., as shown in Figure 6- 11 (b), and Delobelle et al. as shown in Figure 6- 13. Delobelle et al. showed that the hardness of PZT and PMNT are not dependent on grain size.

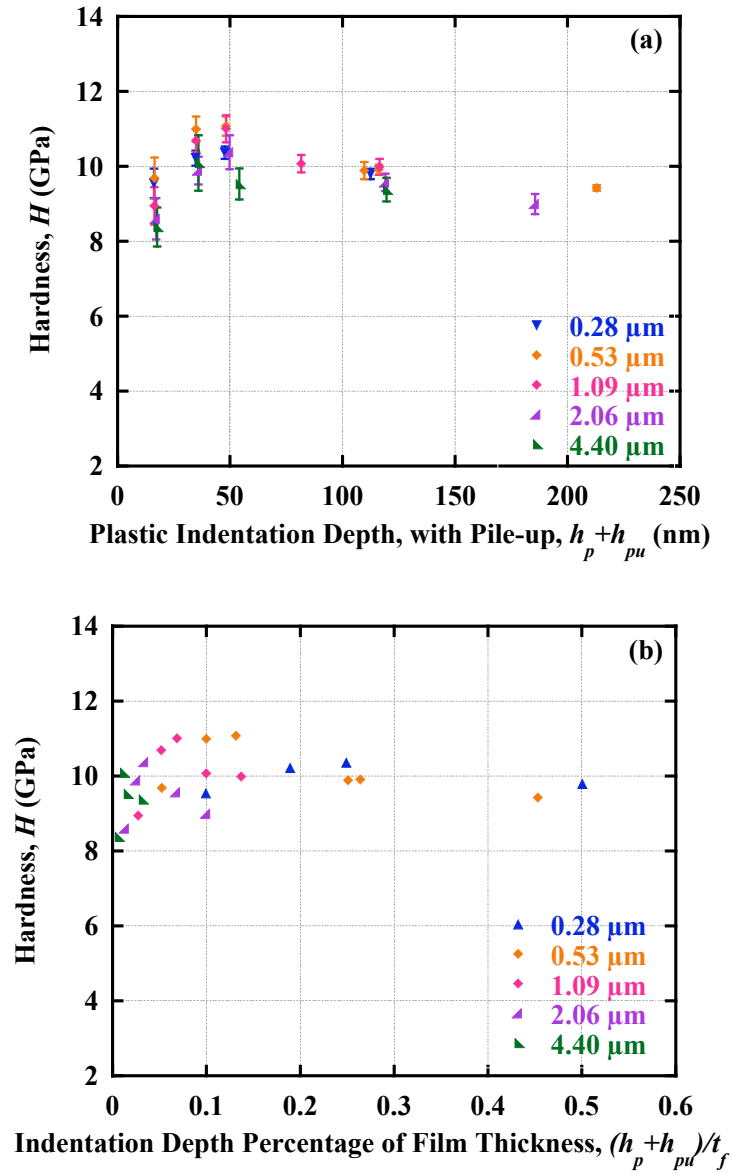


Figure 6- 12 (a) The hardness as a function of plastic indentation depth of different mixed $\{001\}$ and $\{111\}$ orientation PZT film thickness (b) The hardness as a function of percent indentation depth normalized by the film thickness of different mixed $\{001\}$ and $\{111\}$ orientation PZT film thickness.

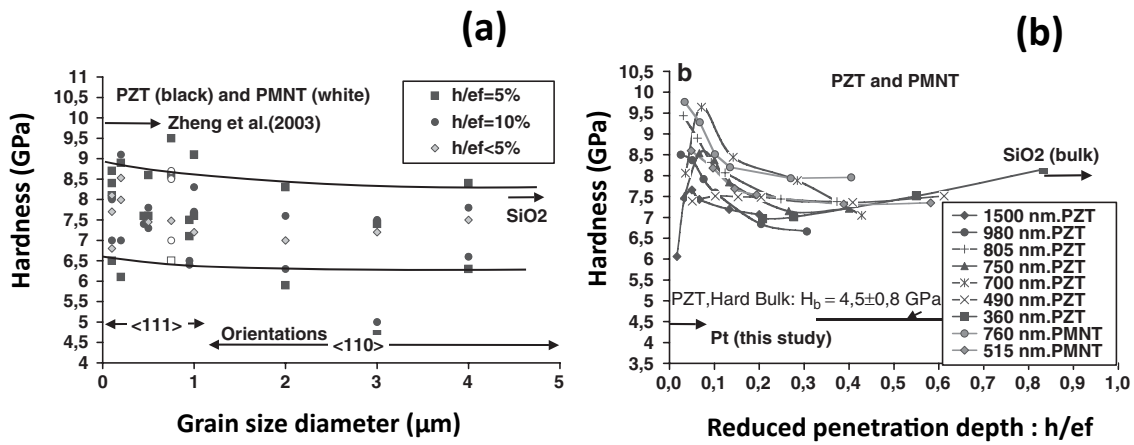


Figure 6- 13: (a) The hardness as a function of grain size diameter and (b) the hardness as a function of reduced penetration depth of PZT and PMNT films^[98]

Chapter 7

Dry Etching of PZT Films

This chapter presents the results of Deep Reactive Ion Etching (DRIE) of PZT films. Dry etching of PZT films is interesting for a wide variety of memory and MEMS devices. However, the literature typically concentrates on the etching of very thin films (often well below a micron in thickness), where slow etch rates are not problematic. Thus, in this work the parameters that influenced the etching characteristics were studied for higher etching rate conditions. It is known that the source power, substrate holder power, substrate self-bias, operation pressure, and the variation of gas mixture affect the etching rate^[78, 109]. In the chamber, the source power generates the plasma while the substrate holder power accelerates the ions. In this research, the ICP source power was kept constant at 2000 W. The gas mixture, the substrate holder power, and the operating pressure were varied to assess the effect on the etch rate. In addition, the uniformity over a 4 inch diameter wafer, repeatability, and the etch rates of SiO₂ and Pt were investigated.

From a practical standpoint, the ability to deposit and characterize piezoelectric thin films is not adequate for processing of many MEMS devices. Another critical step is patterning of the films. Although in a limited number of cases, direct writing of the functional structures is possible^[14], in many cases, patterning is achieved by etching. There are two principal families of etching techniques: dry etching and wet etching. The reactant phase in wet etching is liquid while dry etching uses a gas.^[2] Wet etching is typically a fast, inexpensive method to etch large areas; patterning with wet etching is most readily employed where a mask material is available that will not erode faster than the materials to be etched. One challenge is that wet etching can cause undercutting as shown in Figure 7- 1.^[2, 110] In contrast, dry etching is able to produce fine-line semiconductor devices and is appropriate for deep etching with better anisotropy.

The etching process can be isotropic or anisotropic. Isotropic etching occurs when the material etches with the same etch rate in all directions. On the other hand, anisotropic etching occurs when there are different etch rates for different directions.^[2, 110] Figure 7- 1 and Figure 7- 2 illustrate isotropic and anisotropic etching.

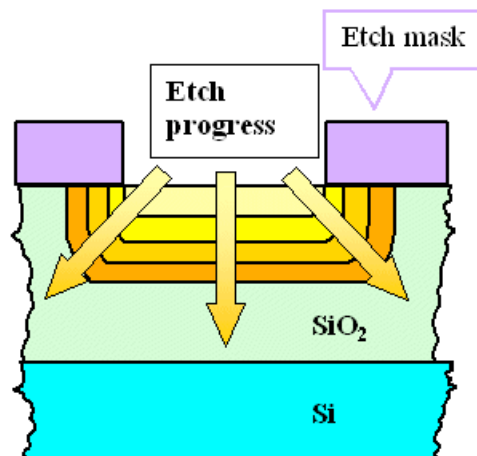


Figure 7- 1: A schematic of isotropic etching. The arrows show the etching time dependence.^[110]

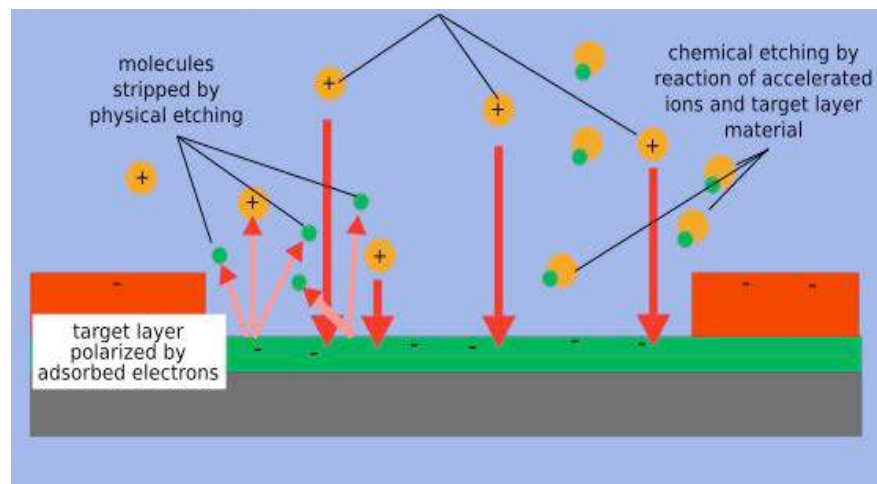


Figure 7- 2: A schematic of anisotropic etching by a dry etching process^[110]

During the manufacture of devices, the ability to pattern PZT anisotropically, to enable high aspect ratios, is important. In this thesis, Deep Reactive Ion Etching (DRIE) was employed for this purpose.

Reactive ion etching (RIE) is a combination of chemical and physical etching. For the chemical removal component, gas molecules are broken into ions, which are accelerated towards the wafer. A chemical reaction at the surface results in etching, with material removal accomplished by volatile reaction compounds. For physical removal, incident ions with high energy knock atoms out of the material to be etched without chemical reaction. Traditional RIE tools are limited by the substrate power and RF plasma power, which can result in limited etch depths, non-uniform etching across the wafer, low-density plasma, and restricted control over processing conditions. Therefore, deep reactive ion etching (DRIE) with a radio frequency inductively coupled plasma source (ICP RIE) was introduced. In an ICP RIE, the substrate power controlling the energy of etchant and the coil power controlling the plasma density are independent of each other, so it provides excellent control. DRIE provides higher etch rates compared to conventional RIE due to the high plasma densities ($\geq 10^{11}$ ions/cm³) available at low pressure (1-20 mTorr).^[78, 111]

Table 7- 1 summarizes previous work on reactive ion etching of PZT along with a few other ferroelectrics in term of the tool, gas used in the etching process, material etched, etch rate, and sidewall angles achieved.

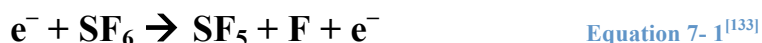
Table 7- 1: Previous work in Reactive Ion Etching (RIE) and Deep RIE (DRIE) of PZT

Tool	Gas Selection	Material	Material: Etch rate	Sidewall angle (°)	Reference
DRIE (ICP, Alcatel)	Ar/SF ₆	Bulk PZT	0.269 μm/min	-	Subasinghe et al. [109]
RIE, High Temperature etch	Cl ₂ /O ₂	Ir/Ir ₂ film	0.05 (100°C)- 0.12 (500°C) μm/min	10 (100°C) 90 (500°C)	Marks and Almerico [112]
	Cl ₂ /SF ₆ /O ₂ /Ar	PZT film	0.01 (100°C)- 0.11 (500°C) μm/min		
DRIE (ISM)	Cl ₂ / C ₄ H ₈	PZT film	0.19 μm/min	62	Kokaze et al. [113]
RIE, Plasmatherm	SF ₆	PZT film	0.065 μm/min	80	McLane et al. [114]
DRIE (ICP)	Ar/Cl ₂ /CF ₄	PZT film	0.197 μm/min	70	Kang et al. [115]
RIE, Samco	Ar/ChClFCF ₃	PZT film	0.030 μm/min	-	Pan et al. [116]
RIE	CHF ₃ /Ar	PZT film	0.013 μm/min	-	Peng and Xi [117]
RIE, Plasmatherm	HC ₂ ClF ₄	PZT film	0.030 μm/min	70	Zarkar et al. [118]
DRIE, Planar ICP	CH ₄ /Ar	PZT film	0.143 μm/min	-	Efremov et al. [119]
RIE, 1C-Etcher	CCl ₂ F ₂	PZT film	0.030 μm/min	-	Vijay et al. [120]
RIE, Oxford	SF ₆	Bulk PZT	0.20 μm/min	72	Bale et al. [121]
DRIE, Oxford	Cl ₂ /Ar C ₂ F ₆ /Ar Cl ₂ /C ₂ F ₆ /Ar HBr/Ar SF ₆	PMN-PT	0.09-0.13 μm/min	50-80	Jiang et al. [122]
			0.12 μm/min	85-90	
DRIE (ICP)	HBr/Ar	PZT film	0.09 μm/min	70	Chung et al. [123]
DRIE (ICP)	Cl ₂ /C ₂ F ₆ /Ar	PZT film	0.13 μm/min	78	Chung et al. [124]
RIE, Oxford	SF ₆	PZT plate	0.16 μm/min	-	Bale and Plamer [125]
DRIE (ICP)	SF ₆	PZT plate	0.30 μm/min	75	Wang et al. [126]
DRIE, Planar ICP	Cl ₂ /Ar CF ₄ /Ar	PZT film	0.145 μm/min	-	Efremov et al. [127]
			0.143 μm/min		
DRIE (ICP)	Cl ₂ /Ar BCl ₃ /Ar	PZT film	0.160 μm/min 0.179 μm/min	-	Koo et al. [128]
RIE (ICP)	Cl ₂ /CF ₄ /Ar Cl ₂ /CF ₄ /O ₂	PZT film	0.145 μm/min	-	Kim et al. [129]
			0.110 μm/min		
RIE (ICP)	Cl ₂ /O ₂ /Ar	PZT film	0/030 μm/min	70	Chung and Chung [130]
RIE (ICP)	Ar/O ₂ /Cl ₂ /CF ₄	PZT film	0.146 μm/min	-	Lim et al. [131]
DRIE (ICP)	BCl ₃ /Ar/Cl ₂	PZT film	0.245 μm/min (at 80°C)	-	An et al. [132]

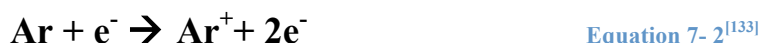
7.1 The Mechanism of PZT Etching

A *radical* is 1 or more atoms with unsatisfied chemical bonding, which is uncharged, e.g. F, O, CF_x. A *positive ion* is an atom, radical, or stable molecule that lost electrons, leaving the particle with positive charge, e.g. Cl⁺, SF₅⁺, HF⁺. A *negative ion* is an atom, radical, or stable molecule which has captured an electron, leaving the particle with a negative charge, e.g. F⁻, Cl⁻, SF₅⁻.^[133]

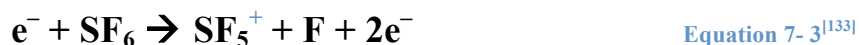
Electron impact dissociation: The process of dissociation converts relatively unreactive etch gas molecules into very reactive radicals. Equation 7-1 shows an example of dissociation of SF₆.^[133]



Electron impact ionization: Equation 7-2 shows an example of electron-impact ionization. This is important process for electron – molecule collision. Electron impact ionization provides the positive ions and the electrons needed to maintain the plasma.^[133]



Dissociation and ionization may both occur in one collision via *dissociative ionization*, as shown in Equation 7-3.



Dissociative electron attachment: Molecules tend to capture low energy electrons and form negative ions as shown in Equation 7-4.^[133]



Electron impact excitation: This mechanism involves exciting an electron to a large radius orbit about the nucleus and is treated as incomplete ionization. The lifetime of excited electron is very short (10⁻⁶ to 10⁻⁹ s) and the electron rapidly decays to a lower energy state, emitting a photon as shown in Equation 7-5 and Equation 7-6^[133]. This very short lifetime makes

that electron of these species will survive long enough to reach a surface. Thus, this contribution can be neglected.^[133]



Volatile product: When the etching of PZT film was accomplished using fluorine gases, the volatile products are given in Equation 7-7 to Equation 7-9.^[112]



7.2 Etching Effect of Substrate Holder Power

The substrate holder power accelerates the charged species in the plasma towards the sample, and so determines the kinetic energy of the ions bombarding the PZT films. The effect of variation of substrate holder power from 250 W to 400 W in an Alcatel AMS-100 Dielectric I-Speeder etcher was studied as shown in Figure 7- 3. In this experiment, the source power was 2000 W, the Ar gas flow rate was 42.5 sccm, and the SF₆ gas flow rate was 5 sccm. It is expected that as the substrate holder power is increased, the higher energy ion bombardment will cause an increase in etch rate by facilitating rapid physical removal of nonvolatile etch products from the surface of PZT films.^[78, 109] The physical sputtering by the unidirectional energetic ions efficiently breaks bonds at the surface of PZT films preferentially to the sidewall. This process is called surface damage induced anisotropy.^[109] These reaction products are then removed from the surface from energetic ion sputtering. In addition, the local temperature at the sample surface is expected to increase due to the physical bombardment by energetic ions even though the substrate holder was kept at a constant temperature of 20°C. The elevated local temperature increases the

kinetics of the chemical reactions, and so increases the etch rate. ^[78, 109] The result of this experiment showed that as the substrate holder power is increased, the PZT etch rates increased. This observation is consistent with the reports of Subasinghe et al., Goyal et al. and Kodaze et al. ^[78, 109, 113] The selectivity for PZT removal compared to Ni was good.

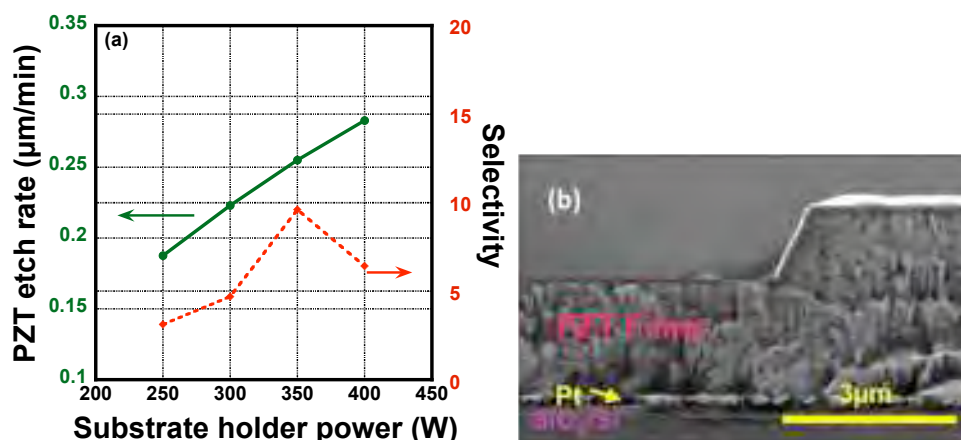


Figure 7- 3: (a) PZT etch rate vs. substrate holder power variation at source power = 2000 W, Ar flow rate = 42.5 sccm, SF₆ flow rate = 5 sccm (b) SEM of PZT cross section after etching at source power = 400 W

7.3 Effect of Operating Pressure on Etching

The operation pressure is also important for the etching process. A low operation pressure is desirable to facilitate rapid removal of etch products. ^[78] Moreover, a low operation pressure tends to improve anisotropy by decreasing the collision probability of the plasma species and increasing the mean free path. ^[78, 109] To investigate this, the operation pressure was varied from 2.7, 3.6, to 5 mTorr. It was found that changes in the operation pressure over this range had little effect on the etch rate, as shown in Figure 7- 4. In this set of experiments, the source power was 2000 W, the substrate holder power was set at 400 W, the Ar gas flow rate was 42.5 sccm, and the SF₆ gas flow rate was 5 sccm.

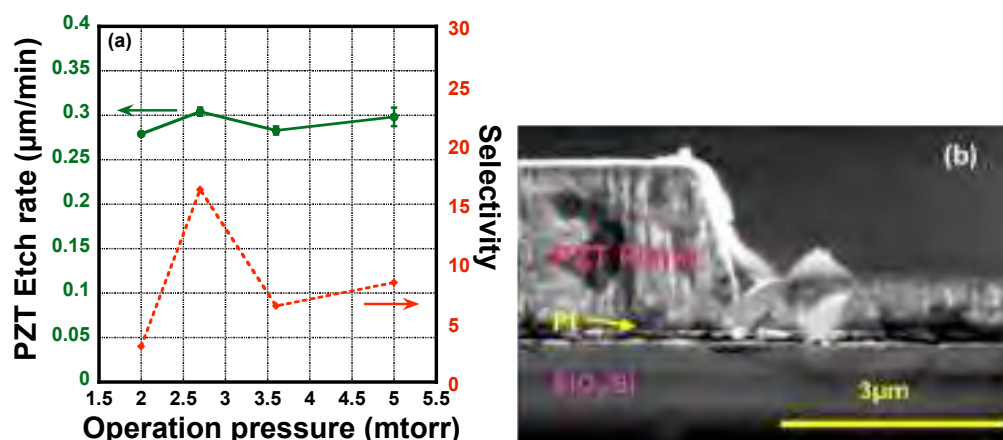


Figure 7- 4: (a) PZT etch rate vs. operating pressure at a source power = 2000 W, substrate holder power = 400 W, Ar = 42.5 sccm, SF₆ = 5 sccm (b) SEM of PZT cross section after etching at pressure of 2.7 mTorr

7.4 Effect of Gas Chemistry on DRIE of PZT Films

In this research, a mixture of Ar and SF₆ was employed as the etch gas. SF₆ is widely used in etching of silicon, bulk PZT and PZT thin films. SF₆ has safety advantages relative to chlorine chemistries, but the chlorinated process gases produce higher volatility compounds in PZT etching.^[112] The etching products of PZT produced from SF₆ etching are PbF₂, TiF₄, and ZrF₄.^[117] Ar is responsible for physical etching by ion bombardment. Increasing the reaction of fluorine ions and radicals with the surface and the removal of non-volatile reaction products by sputtering will raise the etch rate. For these experiments, the source power was set at 2000 W, the substrate holder power at 400 W, and the operation pressure was 3.6 mTorr. Figure 7- 5 and Figure 7- 6 illustrate the PZT etch rates as a function of variations in the Ar gas flow rate and SF₆ gas flow rate, respectively. In addition, the % Ar gas flow rate to overall gas is shown in the figures.

The variation of Ar gas flow: Figure 7- 5 summarizes experiments in which the Ar gas flow rate was varied from 0-50 sccm while the SF₆ flow rate was kept constant at 5 sccm. The

PZT etch rate increases as the Ar gas flow rate was increased from 0 to 20 sccm. The etch rate increases because as the Ar content was increased, there is more physical sputtering by Ar ions that breaks bonds on the surface of the PZT films. SF_6 provides reactive fluorine ions and radicals, which generates a chemical component of the etching as fluoride compounds of lead, zirconium, and titanium are removed. Raising the Ar content above 20 sccm does not significantly increase the etch rate because there are not sufficient reactive fluorine ions and radicals. Thus, the physical sputtering rate saturated.^[78, 109]

The percent Ar gas to overall gas in Figure 7- 5 and Figure 7- 6 is calculated from Equation 7-10:

$$\%Ar \text{ gas to overall gas} = \frac{Ar \text{ gas flow rate}}{[(Ar \text{ gas flow rate}) + (SF_6 \text{ gas flow rate})]}$$

Equation 7- 10

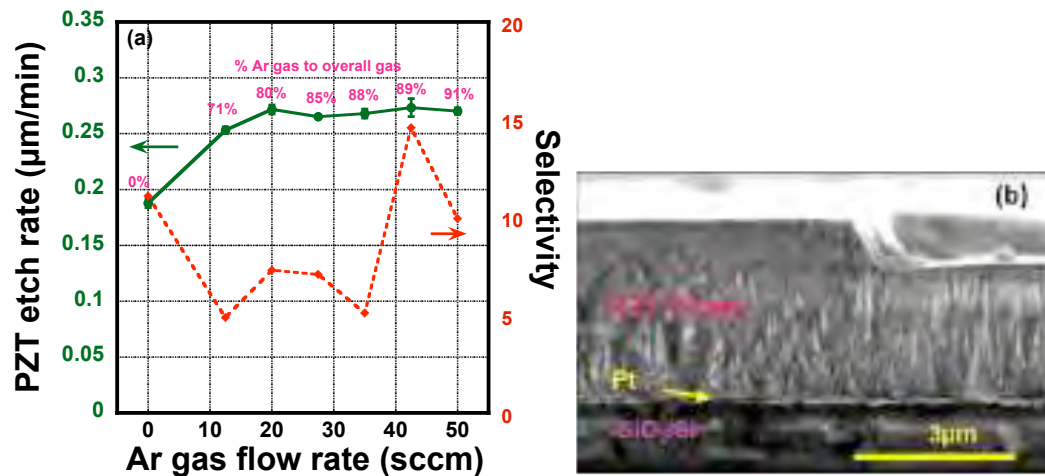


Figure 7- 5: (a) PZT etch rate vs. Ar gas flow rate at a substrate holder power = 400 W, source power = 2000 W, SF_6 = 5 sccm (b) SEM of PZT cross section after etching at Ar = 42.5 sccm

The variation of SF_6 gas flow: Figure 7- 6 shows the PZT etch rate as a function of SF_6 flow rate with the Ar flow rate kept constant at either 5 sccm or 42.5 sccm. As the SF_6 content is

increased, there are more reactive fluorine ions and radicals generated, which in principle could increase the chemical component of the etching and result in a higher etch rate. However, it was observed that reduction in the % Ar in the gas mixture led to insufficient sputtering at the PZT film surface. Thus, the PZT etch rate decreases as the SF₆ flow rate rose.

For a higher Ar flow rate of 42.5 sccm, the PZT etch rate is constant as the SF₆ flow rate rises from 10 sccm to 20 sccm, but it decreased for an SF₆ flow rate of 30 sccm. The reduction in etch rate is believed to be due to a decrease in sputter removal of low volatility compounds, as described above. Finally, it can be seen that as the % Ar flow rate was increased to 68% (SF₆ at about 20 sccm + Ar = 42.5 sccm), the etch rate increases to a maximum of 0.31 μm/min.

These results are consistent with those reported by Sabasinghe's group. They obtained the maximum etch rate of bulk PZT at about 70% Ar flow ratio to overall gas while the source power and the substrate holder power were set at 2000 W and 400 W.^[109]

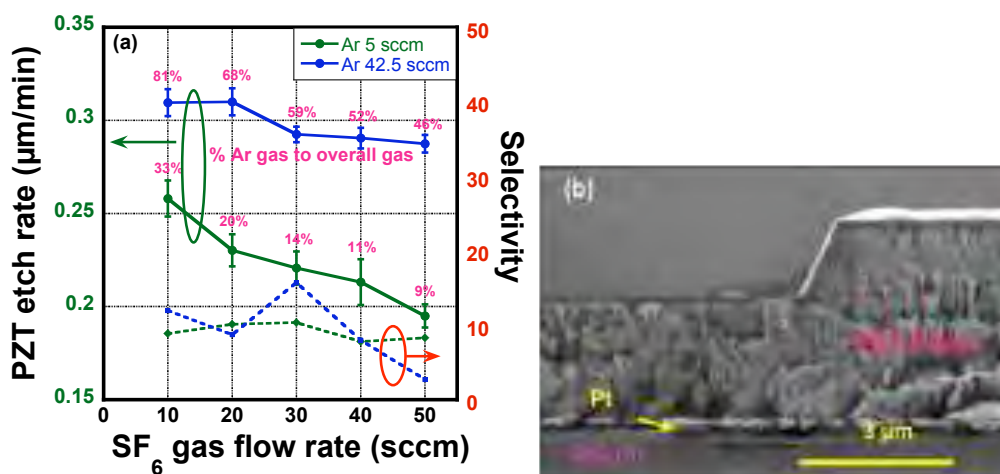


Figure 7- 6: (a) PZT etch rate vs. SF₆ variation at source power = 2000 W, substrate holder power = 400 W, Ar = 42.5 sccm (b) SEM of PZT cross section after etching at SF₆ = 20 sccm. The solid curves are for the etch rate, while the dashed lines are for the selectivity.

7.5 Etch Rate as a Function of Feature Spacing

The etch rate was also investigated as a function of feature spacing. Richad et al. found that in Si and SiO₂, larger diameter contact windows etch more rapidly than smaller contact windows.^[134] In this study, the feature spacing was varied from 3 μm to 150 μm as shown in Figure 7- 7. The source power was set at 2000 W with the substrate holder power at 400 W and the Ar and SF₆ flow rates at 42.5 sccm and 5 sccm, respectively. It has to be noted that the step profilometer is not able to characterize spacing less than $\sim 20 \mu\text{m}$; thus for finer spacings, the etch rates were characterized by SEM images. It can be seen that etch rates do not significantly change with spacing. It was found, however, that there are residues (TiF₄ or TiZr₄) in narrow trenches after etching (confirmed by XRD) as shown in Figure 7- 8.

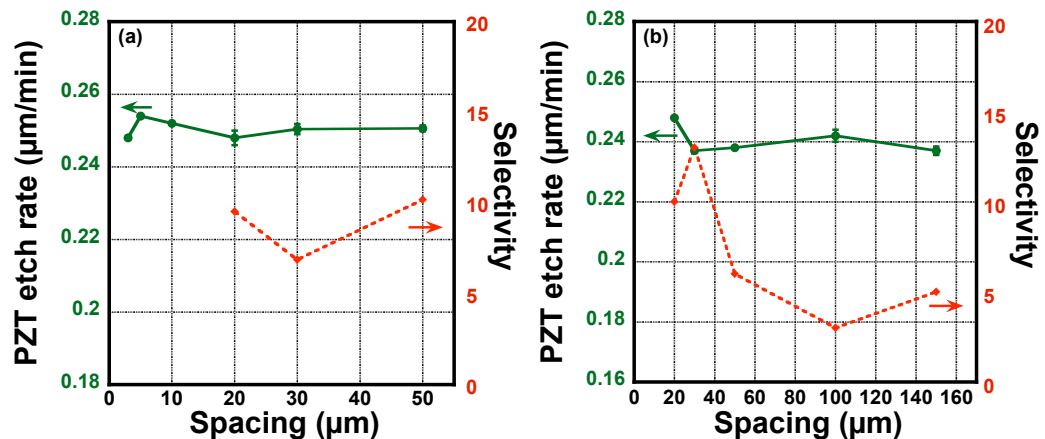


Figure 7- 7: PZT etch rate vs. spacing (a) Spacing from 3 μm to 50 μm (b) Spacing from 20 μm to 150 μm . The selectivity is given in the dashed lines.

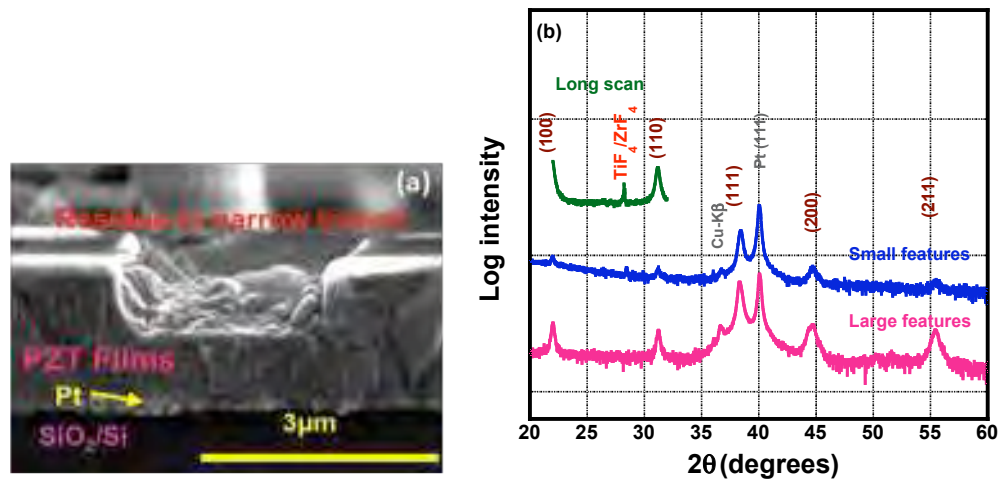


Figure 7- 8: (a) SEM of PZT film after etching with 3 μm spacing (b) XRD pattern of PZT films after etching of different feature sizes

7.6 The Repeatability of Dry Etching

The repeatability of the dry etching is shown in Figure 7- 9. The source power was set at 2000 W with a substrate holder power at 400 W and the mixture of Ar and SF_6 at 42.5 sccm and 5 sccm, respectively.

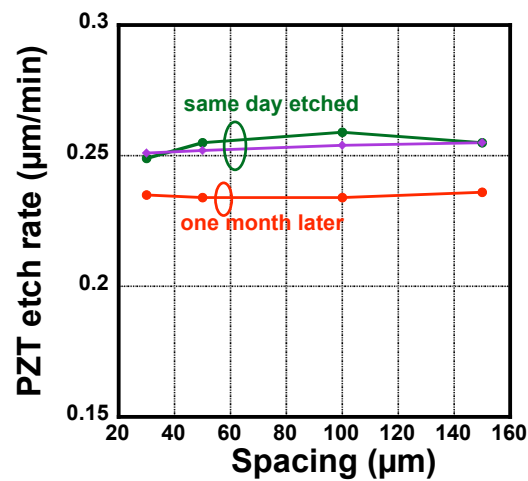


Figure 7- 9: Repeatability of PZT film etch rate

7.7 Etch Uniformity over 4 inch Wafer

The cross-wafer uniformity of the etching is important in manufacturing. For many MEMS applications, device performance depends on its physical dimensions.^[135] The uniformity across the wafer leads to the variability of the device performance resulting in yield loss.^[135] Surendra et al.^[136] studied the silicon oxide etch rate uniformity in an RF ICP system. They found that nonuniformity in the radio frequency coupling to the substrate from a biased substrate holder led to about a 20% higher etch rate at the wafer center than the edge. It has been previously reported that the uniformity can be improved through equipment modifications.^[136]

Table 7- 2 shows the PZT etch uniformity over the middle 2 and 3.5” of a 4” wafer with high and low etch rates. The variation over a 3.5-inch area is about 15 % and results from the machine design. In the DRIE machine, there are 14 magnets circling the chamber. The high power magnets increase the density of the plasma. The plasma density at the wafer center is higher than at the edge, resulting in slower etch rates at the edge of the wafer.^[109]

Table 7- 2: Etch uniformity over 2 inch and 3.5 inch areas

Etch rate ($\mu\text{m}/\text{min}$)	Etch rate ($\mu\text{m}/\text{min}$) within 2 inch area	Etch rate ($\mu\text{m}/\text{min}$) within 3.5 inch area
Uniformity of PZT etch Source power = 2000 W Substrate power = 400 W Ar = 42.5 sccm, SF ₆ = 5 sccm Operation pressure = 5 mTorr	$0.68 \pm 0.01 \mu\text{m}$ % variability = 5.3%	$0.65 \pm 0.04 \mu\text{m}$ % variability = 9.7 %
Source power = 2000 W Substrate power = 250 W Ar = 42.5 sccm, SF ₆ = 5 sccm Operation pressure = 3.6 mTorr	$0.45 \pm 0.02 \mu\text{m}$ % variability = 6.3 %	$0.42 \pm 0.04 \mu\text{m}$ % variability = 15.0 %

7.8 Influence of Substrate Holder Voltage

The substrate holder voltage is important in reactive ion etching. In deep reactive ion etching systems, an radio frequency (RF) voltage is applied between the two electrode plates, generating free electrons. Electrons oscillate and collide with the gas molecules, leading to the plasma in the system. The collisions also ionize the gas molecules. The substrate holder voltage (also called self bias) is automatically generated from the impact of electrons on the substrate holder because electrons move faster than ions.^[111] The negative potential of the substrate holder power controls the direction of the ions and extracts the ions from the plasma, leading to the etching sample. The substrate holder voltage depends on the substrate, RF power, chamber pressure, and gas type. However, the plasma is not constant over the entire 4-inch wafer because of variations in the ion density in the plasma leading to different incident angle (α) of ions on the substrate shown in Figure 7- 10.^[137] From this reason, non-uniform etching over the entire wafer was observed in section 7.7.

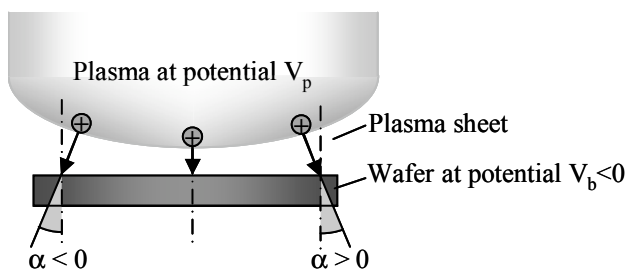


Figure 7- 10: Schematic overview of plasma sheet thickness and the resulting angular deviation including substrate holder voltage^[137]

In this work, the substrate holder voltage with the PZT etch rate was recorded as a function of the variation of substrate holder power and % Ar gas to overall gas, as shown in Figure 7- 11. Figure 7- 11 (a) shows the effect of variation of substrate holder power from 250 W to 400 W in the Alcatel AMS-100 Dielectric I-Speeder etcher. In this experiment, the source

power was 2000 W, the Ar gas flow rate was 42.5 sccm, and the SF₆ gas flow was 5 sccm. The experiment showed that as the substrate holder power increased, the PZT etch rates increased, as did the substrate holder voltage.

Figure 7- 11 (b) and (c) show the result of substrate holder voltage and PZT etch rate as a function of % Ar gas to overall gas. It can be seen that the variation of % Ar gas to overall gas does not produce large changes in the substrate holder voltage. It implies that the ion bombardment from Ar does not show a one to one correlation to the gas composition, providing the substrate voltage is constant. Because the physical etching (from Ar gas) plays a more important role than chemical etching (from SF₆ gas) in this DRIE Alcatel tool, the PZT etch rate increased as % Ar gas to overall gas increased. In contrast, the PZT etch rate decreased as the SF₆ gas flow rate increased.

It is also important to consider the sputtering yield. The sputtering yield is defined as the number of sputtered atoms / incident particle and is a measure of the efficiency of sputtering. The sputter yield of Ar and F is related to the mass too. The mass of Ar (39.948 amu) is heavier than F (18.998 amu). This, in combination with the negative bias developed by the substrate, is the reason that Ar plays a bigger role in the physical component of etching, than does F in this system.^[138]

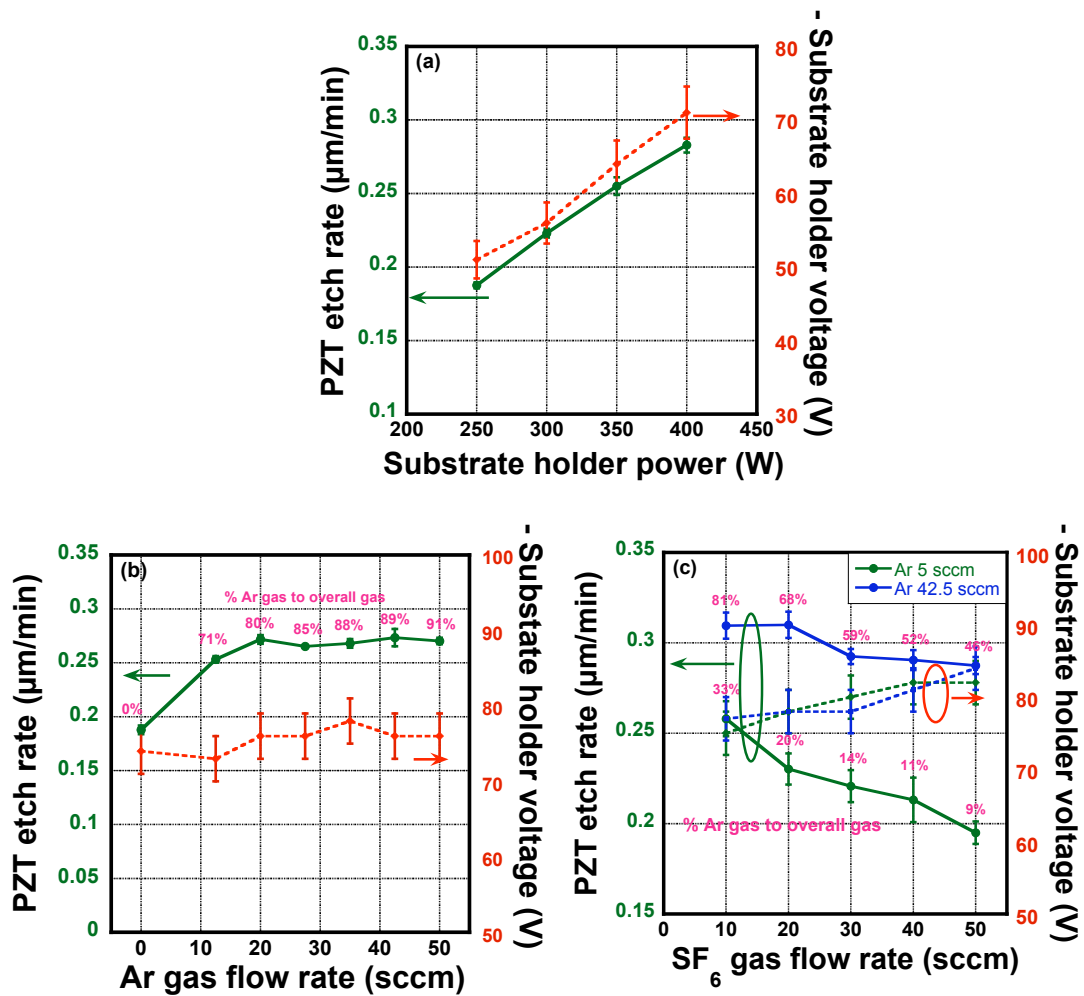


Figure 7- 11: (a) PZT etch rate and substrate holder voltage (self-bias) vs. substrate holder power variation at source power = 2000 W, Ar flow rate = 42.5 sccm, SF₆ flow rate = 5 sccm (b) PZT etch rate and substrate holder voltage (self-bias) vs. Ar gas flow variation at a substrate holder power = 400 W, source power = 2000 W, SF₆ flow rate = 5 sccm, and (c) PZT etch rate and substrate holder voltage (self-bias) vs. SF₆ gas flow variation at source power = 2000 W, substrate holder power = 400 W, Ar = 42.5 sccm

7.9 Etch Rate of SiO₂ and Pt

In order to make electrical contact to piezoelectric devices, top and bottom contacts are needed. Thus, it is useful to understand the etch rate of the Pt bottom electrode to assess whether it will be straightforward to stop an etch on it. To assess how much over-etching can be tolerated,

the Pt and SiO₂ etch rates were also investigated as shown in Figure 7- 12. Because there is a strong physical component to the PZT etch, it is difficult to stop on the Pt bottom electrode. The results show that the Pt etch rate was about 0.188 ± 0.006 $\mu\text{m}/\text{min}$, which is similar to that of PZT. The SiO₂ etch rate was 0.40 ± 0.01 $\mu\text{m}/\text{min}$, approximately double the PZT etch rate. In this experiment, the source power was 2000 W, the substrate holder power was 400 W, and operation pressure was 5 mTorr, the SF₆ flow rate was 5 sccm, and the Ar flow rate was 42.5 sccm. These results imply that careful control will need to be exercised during the PZT etch to avoid unintentionally milling through the bottom electrode. Indeed, it may be preferable to remove the majority of the PZT using this DRIE process, but finish any etch with a short, wet etch with superior selectivity (though inferior aspect ratio control).

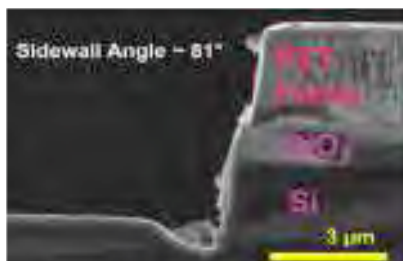


Figure 7- 12: Cross section of Pt and SiO₂ etching

7.10 Electrical Properties of PZT Films after Etching

After etching, the electrical properties of the PZT films were determined and then compared to the properties before etching (see Table 7- 3). The electrical properties of PZT films directly exposed to the plasma after etching are similar to the electrical properties of PZT before etching. Thus, the PZT films were not significantly degraded after plasma etching. In particular, no pinching of the hysteresis loop was observed following etching, as seen in Figure 7- 13. Several authors have reported degradation of the hysteresis loops following high energy etch

processes.^[139, 140] In each case photoresist was used as a mask.^[115, 140] The properties of etched samples could be at least partially recovered by annealing the samples in O₂ gas.^[115] It is interesting to speculate on why no such damage was observed in this work. One possibility is that the photoresist mask was associated with the damage, possibly due to the liberation of hydrogen. In this work, Ni hard masks were used. Therefore, the reason for the observed lack of change in the electrical properties of the PZT film etched will be investigated in the next section.

Table 7- 3: The electrical properties of PZT films before and after etching

Substrate Holder Power (W)	ϵ_r (10 kHz)	Loss (%) (10 kHz)	P_r ($\mu\text{C}/\text{cm}^2$)	E_c (kV/cm)
<u>Substrate Holder Power = 250 W: $0.188 \pm 0.001 \mu\text{m}/\text{min}$</u>				
Before Etching	1260	3.0	17.3	28
After Etching	1220	3.0	17.1	34
<u>Substrate Holder Power = 400 W, $0.283 \pm 0.005 \mu\text{m}/\text{min}$</u>				
Before Etching	1360	4.3	27.1	32
After Etching	1300	3.0	29.8	39

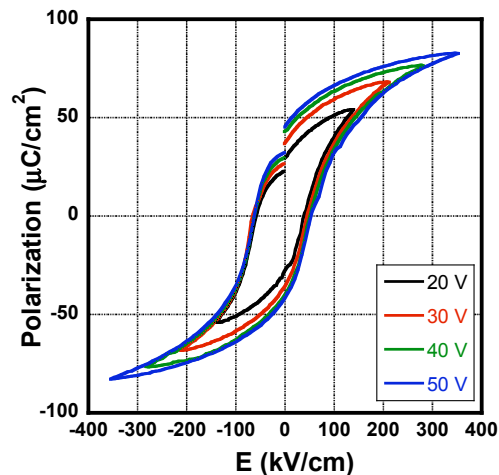


Figure 7- 13: The hysteresis of PZT film after etching without annealing

7.10.1 Impact of Etching Induced Point Defects of PZT Films

Many reports showed that the electrical properties of PZT films, especially the hysteresis loops, are degraded after dry etching as described above.^[115, 139, 140] It is important to find the origin of the property destruction resulting from dry etching. One possible cause of the property degradation could be associated with the use of photoresist as a mask for dry etching.^[115, 140] When photoresist is exposed to the harsh etch conditions used to pattern PZT, it typically degrades, so that complete removal of the polymer residues is difficult. This polymer may degrade the PZT films as found by Soyer and Kang.^[115, 140, 141] Alternatively, it is possible that hydrogen released from the photoresist is responsible for the strong pinning of the polarization.

In this section, photoresist masks were used to investigate the effect from polymer residue damaging the properties of PZT films after etching. Because the selectivity of photoresist to PZT is very low compared to that of the Ni mask, the etch time of this experiment was much shorter than those used for PZT films with a Ni mask. To investigate the degradation of electrical properties of PZT films, three types of masks were used: a Ni mask, a negative photoresist KMR 1100 mask, and a positive photoresist Shipley 1827 mask. The P-E loops before and after etching were compared. Following etching, a top electrode was deposited. No annealing was used after the electrode deposition in order to avoid redistributing any point defects created. The etching time was about 5 to 7 min. The remaining PZT thickness was measured by wet etching (BOE, 0.1 μm /min + HCl, 1 min) some PZT film area down to bottom electrode. The high etch rate and low etch rate were determined by the previous experiment described earlier in this section. Figure 7- 14 shows the P-E loops of PZT films before etching. In order to examine more subtle effects, the minor loops were also investigated. The minor loops of PZT films before etching are shown in Figure 7- 14. It can be seen that the minor loops of PZT films are normal.

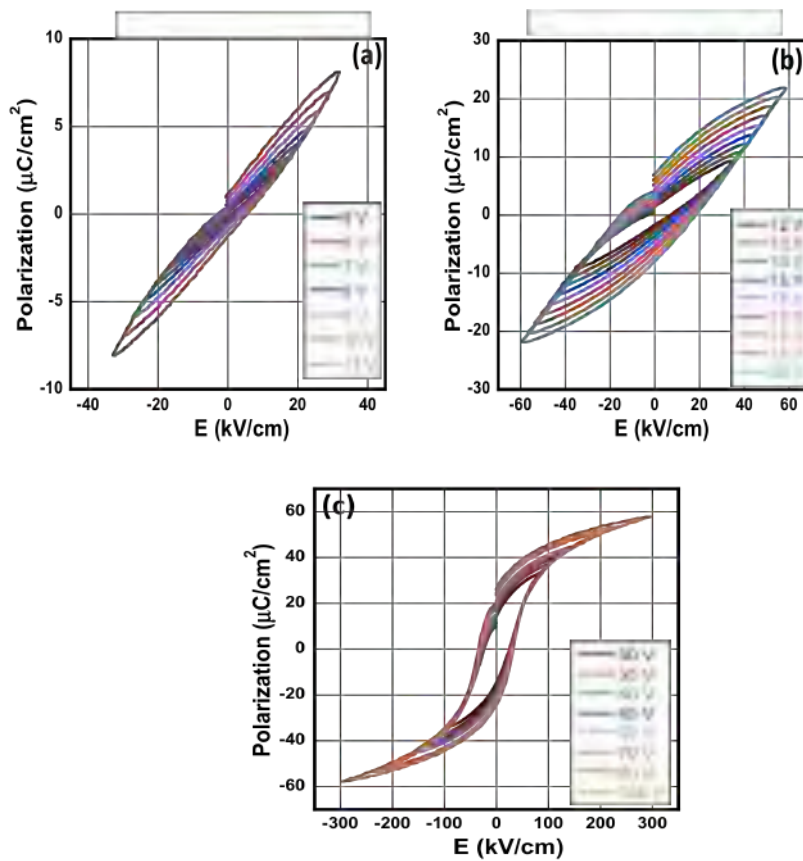


Figure 7- 14: The P-E loops of PZT films before etching

Figure 7- 15 illustrated the major loops of PZT films after etching at two different etch rates $0.188 \pm 0.001 \mu\text{m}/\text{min}$ and $0.283 \pm 0.005 \mu\text{m}/\text{min}$ with the different masks. The major hysteresis loops are essentially unchanged after dry etching, even when the films were directly exposed to the plasma. It is possible that the domain wall pinning may be weak and the high electric field can overcome the influence of any defect dipoles, so that the polarization reverses during the measurement. To assess more subtle changes, the minor loops were also characterized.

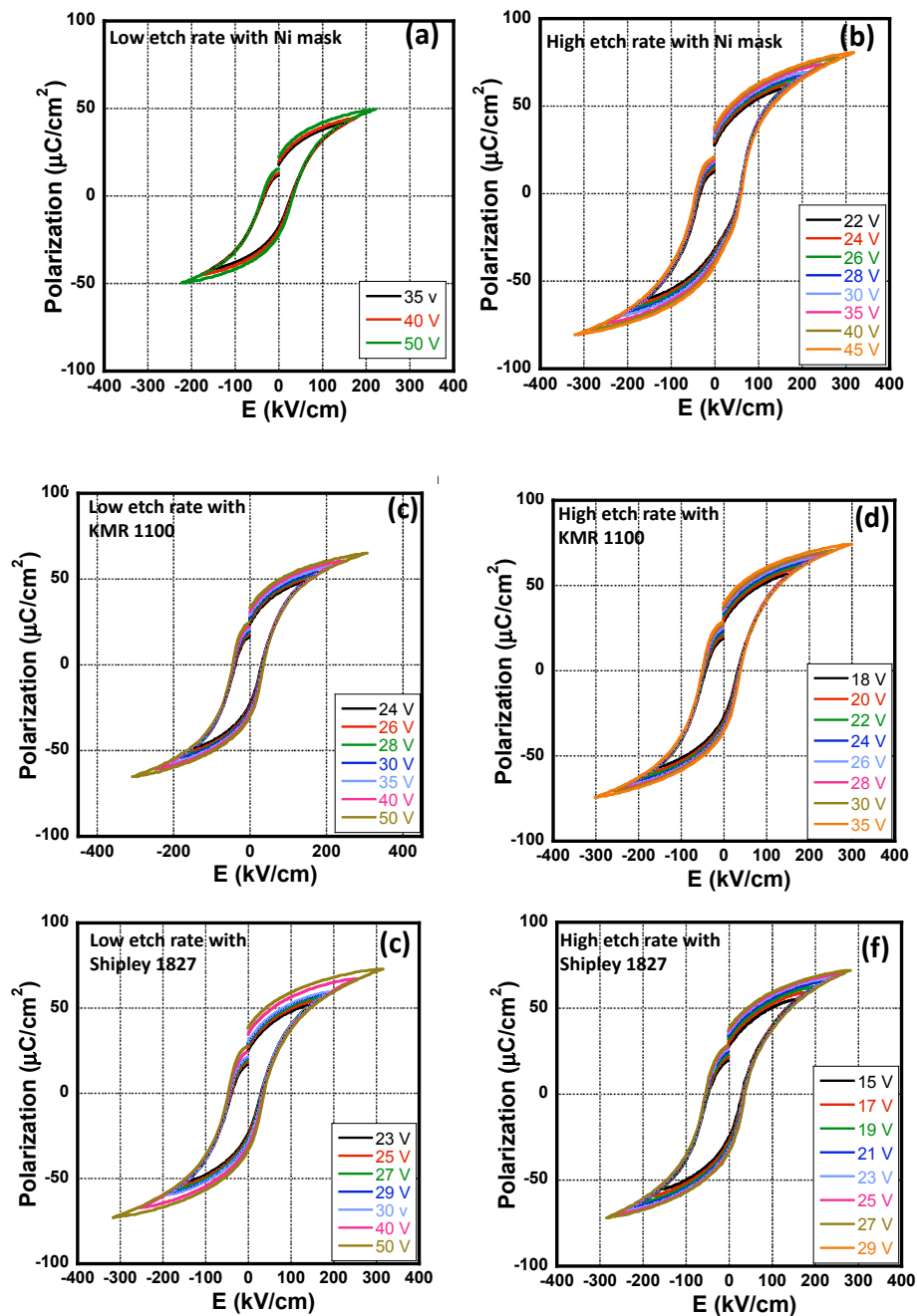


Figure 7- 15: Major hysteresis loops after dry etching PZT films with three different masks and two etch rates. Low etch rate refers to $0.188 \pm 0.001 \mu\text{m}/\text{min}$ and the high etch rate refers to $0.283 \pm 0.005 \mu\text{m}/\text{min}$ (a) Low etch rate with Ni mask, (b) High etch rate with Ni mask, (c) Low etch rate with negative resist KMR 1100, (d) High etch rate with negative resist KMR 1100, (e) Low etch rate with positive resist Shipley 1827, and (f) High etch rate with positive resist Shipley 1827

Figure 7- 16, Figure 7- 17, and Figure 7- 18 illustrated the minor P-E loops after dry etching using a Ni mask, negative photoresist KMR1100, and positive photoresist Shipley 1827, respectively. It can be seen that using an etch rate of $0.188 \pm 0.001 \mu\text{m}/\text{min}$, none of the mask types yielded strongly pinched loops. In contrast, the P-E loops after etching at a rate of $0.283 \pm 0.005 \mu\text{m}/\text{min}$ were all somewhat distorted. For both the Ni mask and positive photoresist 1827 mask, imprint of minor P-E loops was observed. Some degree of either imprint or pinching was apparent for the negative resist. All of these changes would be consistent with the development of local internal fields as a result of the etching process. As can be seen in Figure 7- 11 (a), higher substrate holder power shows a higher substrate holder voltage (self-bias), which increases the ion bombardment. It is possible that the additional damage apparent at high etch rates is associated with the additional bombardment. Therefore, the high etch rate revealed pinched and imprinted P-E loops.

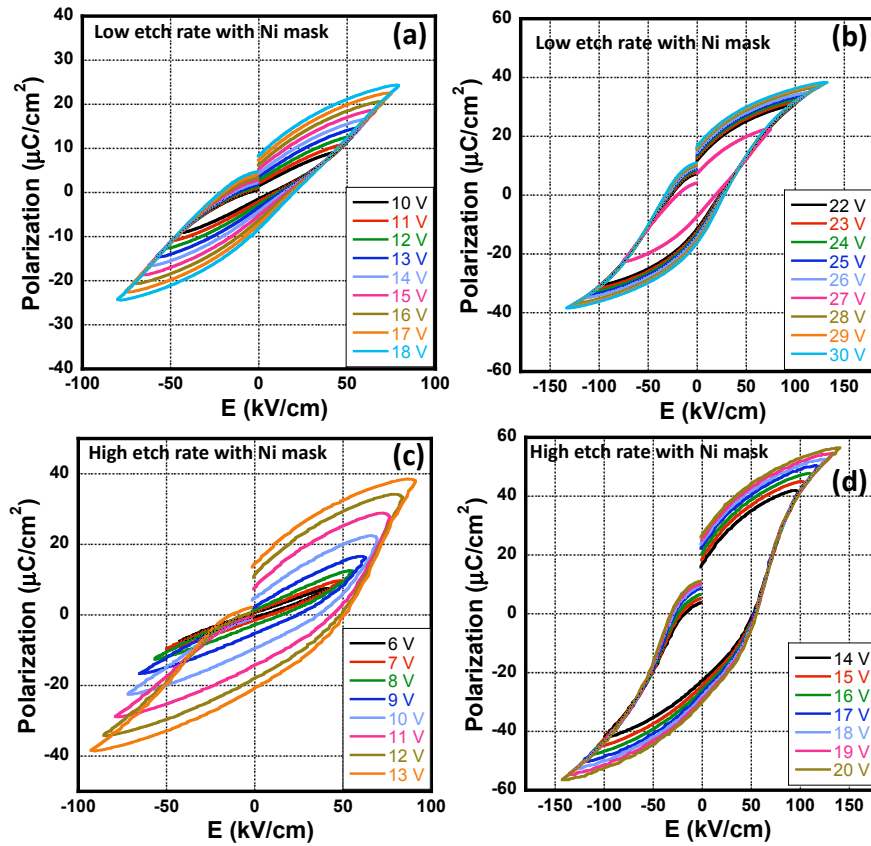


Figure 7- 16: Minor loops of PZT after etching with Ni mask (a) and (b) Minor loops measured after exposing to a low etch rate ($0.188 \pm 0.001 \mu\text{m}/\text{min}$) (c) and (d) Minor loops measured after using a high etch rate ($0.283 \pm 0.005 \mu\text{m}/\text{min}$)

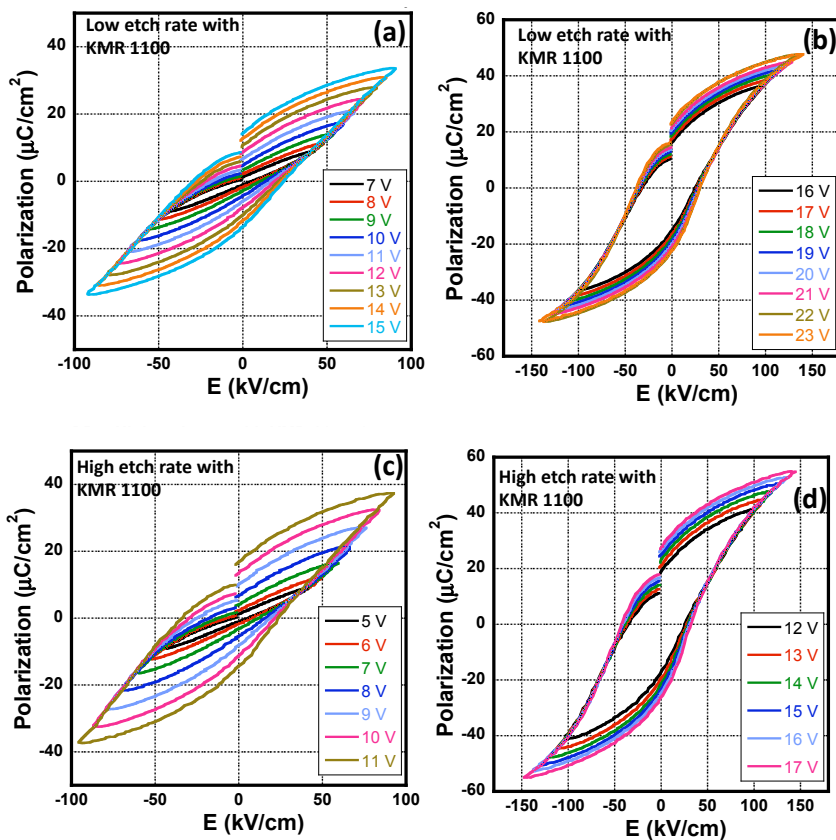


Figure 7- 17: Minor loops of PZT after etching using a negative photoresist KMR 1100 mask (a) and (b) low etch rate ($0.188 \pm 0.001 \mu\text{m}/\text{min}$) (c) and (d) high etch rate ($0.283 \pm 0.005 \mu\text{m}/\text{min}$)

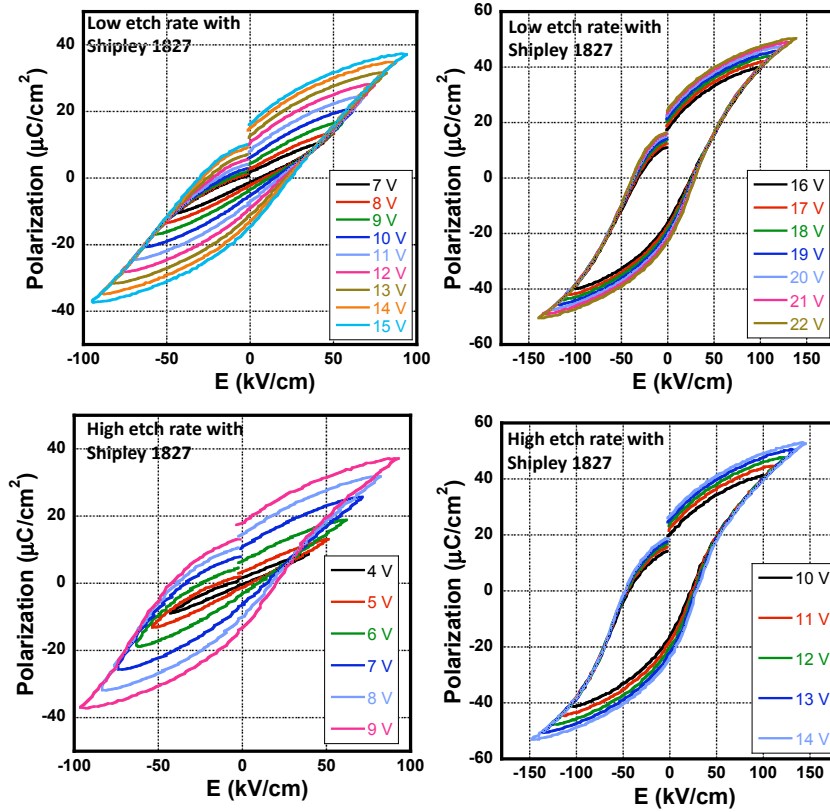


Figure 7- 18: Minor loops of PZT after etching with positive photoresist Shipley 1827 (a) and (b) Minor loops with low etch rate ($0.188 \pm 0.001 \mu\text{m}/\text{min}$) (c) and (d) Minor loops with high etch rate ($0.283 \pm 0.005 \mu\text{m}/\text{min}$)

The concentration of defects affects the mobility of the domain walls in the films. Defects result in deformation of the surrounding volume and modification of the local fields. Equation 7-11 showed the dipole moment associated with a defect.

$$\overline{\Delta\mu} = \Delta\mu_d + \sum_i q_i \Delta x_i$$

Equation 7- 11^[11]

where $\overline{\Delta\mu}$ = the change of dipole moment at the defect site, Δx_i = displacement of charge q_i in the surrounding lattice owing to the presence of defect. The macroscopic polarization change is shown in Equation 7-12 where N is defect concentration.

$$\Delta P = N \overline{\Delta\mu} \quad \text{Equation 7- 12}^{[11]}$$

Equations 7-13 to 7-15 show the internal energy of the ferroelectric.

$$U = f(D) = f(D_p + \Delta P) \quad \text{Equation 7- 13}^{[11]}$$

$$U = f(D_p) + \left(\frac{\partial U}{\partial D}\right)_{D_p} \Delta P \quad \text{Equation 7- 14}^{[11]}$$

$$\frac{\partial f(D_p)}{\partial D_p} = E - \frac{\Delta P}{\epsilon\epsilon_0} \quad \text{Equation 7- 15}^{[11]}$$

When the polarization is reversed by an electric field, the polarization (ΔP) due to the defects may or may not reverse. When the defects can be reoriented under the driving electric field, the coercive field will depend on the field required to switch the defects, as well as the sign and the magnitude of ΔP . When ΔP cannot be reversed in an external field, the defects will still affect the switching properties. Figure 7- 19 (a) shows imprint in a P-E loop which occurs when all the dipoles are aligned. Figure 7- 19 (b) illustrated the pinched P-E loop which results from randomly oriented dipole orientations.^[1, 11] It would be important in future work to assess the effect of these etching-included defects on the piezoelectric response, as well as its stability as a function of time.

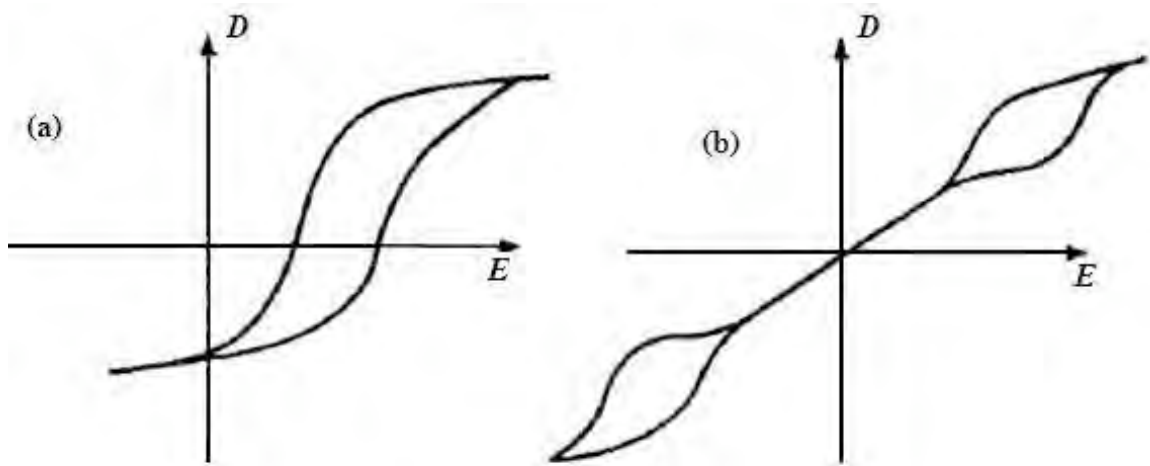


Figure 7- 19: Defects in a ferroelectric crystals (a) Imprinted P-E loop and (b) strongly pinched P-E loop

Chapter 8

Conclusions and Future Work

This chapter will briefly conclude the major findings in this thesis. Possible directions for future work will be recommended based on the experimental observations.

8.1 Conclusions

8.1.1 Processing Control and Characterization of Mixed {001} and {111} Orientation and {001}-Textured PZT films

PZT films are utilized as piezoelectric layers in MEMS systems. Dense and crack free thick films are important to achieve, in order to enhance the performance of devices. In this work, dense and crack free polycrystalline $\text{Pb}(\text{Zr}_{0.52}\text{Ti}_{0.48})\text{O}_3$ films up to 4.4 μm in thickness were obtained by chemical solution deposition method. X-Ray studies showed that the films were phase-pure perovskite. A modified chemical solution deposition process and {001} PbTiO_3 seed layer were employed to achieve {001}-textured PZT films. Using the Lotgering factor, estimates of the degree of {001}-orientation showed 83% and 75% for 0.92 μm and 0.27 μm thick films, respectively.

The dielectric permittivity of mixed {001} and {111} orientation 0.28 μm and 4.40 μm PZT films were 1100 with 3% loss and 1370 with 4.6% loss, respectively, at 1 kHz. Thicker films showed higher dielectric constant values. The coercive field dropped somewhat as a function of thickness. {001}-textured 0.92 μm and 0.27 μm PZT films showed dielectric permittivities of 1123 with 2.6% loss and 672 with 2.6% loss at 1 kHz, respectively. The

transverse piezoelectric coefficient of PZT films with mixed $\{111\}$ and $\{100\}$ texture ranged from about $-7.3 \pm 0.7 \text{ C/m}^2$ to $-8.6 \pm 0.8 \text{ C/m}^2$ and the highest transverse piezoelectric coefficient of $\{001\}$ -textured PZT films was $-14 \pm 1.4 \text{ C/m}^2$. In the case of thin $\{001\}$ -textured PZT films, the transverse piezoelectric coefficient was improved from $-5 \pm 0.5 \text{ C/m}^2$ to $-10 \pm 1.4 \text{ C/m}^2$ by modified processing.

The grain size of PZT films with mixed $\{001\}$ and $\{111\}$ orientation was 50 nm to 150 nm while $\{001\}$ -textured films showed larger grain sizes of 50 nm to 200 nm.

8.1.2 Dielectric Nonlinearity

The Rayleigh law was used to observe the dielectric nonlinearity of the mixed $\{001\}$ and $\{111\}$ orientation and $\{001\}$ -textured PZT films. It was found that dielectric nonlinearity is a strong function of thickness in both sets of PZT films but it is not a strong function of orientation. The irreversible parameter (α_e) increased with the film thickness up to about 2 μm and then saturated. This was attributed to either a higher mobility or a higher concentration of domain walls and phase boundaries. The dielectric nonlinearity under the application of external dc bias showed that the dielectric nonlinearity dropped under external dc bias as the domain configuration is stabilized.

8.1.3 Piezoelectric Nonlinearity and Switching Spectroscopy Piezoelectric Force Microscopy

In the longitudinal ($d_{33,f}$) measurement, Piezoelectric Force Microscopy was employed. Two main experiments were studied: piezoelectric nonlinearity and switching behavior of PZT films.

8.1.3.1 Piezoelectric Nonlinearity

Piezoelectric nonlinearity at sub-switching electric fields was studied locally. Conventional PFM with single frequency excitation was not quantitative enough to permit measurement of piezoelectric nonlinearity. Thus, band excitation PFM was utilized for piezoelectric nonlinearity, where the resonant enhancement was used to increase the signal to noise ratio. There were several significant findings. Firstly, the results of 100 measurements on the same point showed high reproducibility by BE-PFM. Secondly, piezoelectric nonlinearity was mapped for a series of polycrystalline PZT films. There was not a one to one correspondence of the measured nonlinearity to topology, suggesting that the piezoelectric measurements were probing the piezoelectric film, rather than nonlinearity of the tip - surface contact. Thirdly, it is also important to know that the volume of the sample probed at any pixel was a function of the film thickness. Thus, the spatial resolution of the measurement increased for thinner film. Fourthly, for the 4 micron thick sample, the spatial variation of irreversible to reversible ratio ($\alpha_d/d_{33,f}$) was small, on the order of the error of measurement. Thus, this sample is quite uniform in term of domain wall motion. As the film thickness was decreased, there was some clustering of the response. Although the error of the thinner film was larger, it is unlikely that the error could result in the clustering behavior. Thus, local variations in domain wall contributions to the properties were locally probed. Comparison of the global dielectric and piezoelectric nonlinearity at sub-switching field suggests that the same population of domain walls or phase boundaries contribute to both sets of properties.

8.1.3.2 Switching Spectroscopy PFM

The local switching behavior in 1.09 μm PZT films with mixed $\{001\}$ and $\{111\}$ orientation was studied using spatially resolved hysteresis loop measurements. The amount of switchable response increased as the excitation window bias increased. The switchable response was independent of the surface morphology. For measurements made using a top electrode, the spatial variability of SS-PFM maps indicated correlated switching across $\sim 1\text{-}2\ \mu\text{m}$ sized clusters comprised of $10^2 - 10^3$ grains. Without using top electrode, there was little correlation from pixel to pixel because the electric field was strongly confined under the PFM tip. The comparison of local switchable response from SS-PFM and global switchable from Preisach model calculation are comparable.

8.1.4 Nanoindentation of PZT films

The mechanical behavior of approximately PZT films with mixed $\{001\}$ and $\{111\}$ orientation was characterized by nanoindentation. There was little sensitivity in the measurements to strain rate. The results showed that the ferroelastic wall motion took place during loading, at least at stress levels on the order of GPa. In contrast, the reduced elastic modulus is much higher when measured using the unloading curve, presumably because there is no contribution from mechanical softening associated with ferroelasticity.

8.1.5 Dry Etching of PZT Films

A maximum PZT etch rate of $0.310 \pm 0.007\ \mu\text{m}/\text{min}$ was obtained with an Ar / overall gas flow rate of 68% and a substrate holder power of 400 W. The etch rates do not significantly change with the feature spacing for openings of at least 3 μm . The uniformity of the etching over

the middle 3.5” or 2” of a 4” diameter wafer are 5% and 15%, respectively. High etch rates do not yield substantial PZT film damage of major P-E loops. However, pinched minor loops were found with etch rates of $0.283 \pm 0.005 \mu\text{m}/\text{min}$. For lower etch rates ($0.188 \pm 0.001 \mu\text{m}/\text{min}$), the minor P-E loops are normal.

8.2 Future Work

This thesis compared global measurements of the nonlinearity based on the *dielectric* response, and local measurements of the *piezoelectric* nonlinearity. It would be very interesting to extend these studies by allowing direct comparisons of global and local measurements of the *same property*. The results should allow better prediction of the behavior of piezoelectric MEMs devices.

The local dielectric nonlinearity measurements would be approached by patterning the top electrodes with small features of $<1 \mu\text{m}$ in diameter. This would allow dielectric measurements to be made which sample fewer domain walls. The global piezoelectric nonlinearity could be characterized by double beam interferometer. This set of experiments would be intended to help discriminate whether there are small differences between the populations of domain walls that contribute to the dielectric and piezoelectric properties.

The AC displacements of the samples could be measured under the application of ac electric fields with and without external dc bias fields.^[6] It is suggested that local piezoelectric measurements be made as a function of the amplitude of the ac field dependence by BE-PFM under external dc bias field. The dc external bias field is important because the field stabilizes the domain structure and the ratio of irreversible to reversible should be decreased. Making this family of measurements may also help resolve some of the questions remaining on the

nonlinearity in {001}-textured PZT films. In particular, the local dielectric measurements would not be as susceptible to artifacts associated with topology.

Moreover, it is important that there be a proper statistical comparison between the topology and $d_{33,f, \text{init}}$, α_d , and $\alpha_d/d_{33, \text{init}}$. A proper correlation analysis is proposed for future work. The correlation will provide the radially averaged correlation and cross correlation function of $d_{33, f, \text{init}}$, α_d , and $\alpha_d/d_{33, f, \text{init}}$ with respect to surface roughness.

8.2.1 180° and non-180° Domain Wall Contribution

It would be useful to know the relative importance of 180° and non-180° domain wall contributions to the properties of PZT films as a function of grain size, film thickness, and orientation. Although some information on this is available in the literature, in most cases, it was not possible to unambiguously separate the relative importance of each of the factors. Thus, it would be useful to grow a set of model films for this purpose. A combination of dielectric and mechanical testing would then need to be employed to begin to separate the relative importance of 180° and non-180° domain wall motion. The mechanical measurements would only be sensitive to non-180° domain wall motion. Of particular use here might be to perform a series of measurements of the nonlinear behavior under applied biaxial stresses.^[6]

8.2.2 The Origin of the Domain Wall Pinning

Domain wall pinning is one of the factors that obstructs domain wall motion. Thus, the extrinsic properties are decreased. There are several possible sources of domain wall pinning, including stresses, dislocations, trapped charges, grain boundaries, defect dipoles, and a high concentration of domain walls.^[1]

In future work, it would be interesting to begin to separate the relative importance of these various factors using experiments on model systems. This should be possible now that a viable means of tracking non-linearity on a local level is available. As an example, it should be possible to observe the effect of domain wall pinning as a function of defect concentration. To control the defect concentration, additional annealing steps after the deposition process could be used. Using BaTiO_3 as a model system (to avoid problems associated with the volatility of Pb), the oxygen content could be reversibly changed by annealing the films in a reducing furnace. Films with different concentrations of donor or acceptor dopants could also be prepared. The nonlinearity could then be studied as a function of the changes either in oxygen vacancy content or defect dipole concentration.

Along the same lines, epitaxial PZT film could be prepared in order to eliminate grain boundaries, and the properties compared to PZT films with mixed $\{001\}$ and $\{111\}$ orientation. Likewise, using bicrystal substrates, single well-defined “grain boundaries” could be introduced into the films.

8.2.3 SS-PFM

The SS-PFM measurements on capacitor structures requires analysis of behaviors emerging on several independent length scales, including the signal generation region, the lateral size of the global structure bending and vibration modes. However, once these effects are taken into account, the coupling effects between the grains and mesoscopic switching mechanisms can be elucidated. It is expected that SS-PFM measurements for variable sample thickness, excitation bias window, and SS-PFM based first order reversal curve measurements would provide additional insight into the factors that influence switching locally.

The formation of complex patterns related to dynamic behavior is ubiquitous for systems with structural (glasses, polymers), magnetic (spin glasses) or polar (dipole glass) disorder. Polycrystalline ferroelectrics provide a convenient model system, in which the dipole reorientation does not change the underlying crystallographic lattice, and hence is potentially reversible. At the same time, the strong coupling between polarization and strain reversible lattice deformation allows the dynamics to be studied. The result of these studies can be extended to other disordered systems such as structural glasses, polymers in which the dynamics are irreversible and spin and cluster glasses in which mapping local magnetization is a challenge.

8.2.4 Study Effect on $\epsilon_{31,f}$ After Dry Etching in Term of Aging Effect

Typically, the aging rate of PZT films is about 6 – 12 % per decade due to depoling.^{[84,}
^{142]} Ion bombardment during etching is able to generate imprint due to the high energy of the incoming ions. When the films are exposed to plasma, point defects and defect dipoles may be generated. The aging of $\epsilon_{31,f}$ of PZT films can be strongly affected by the defect dipole concentration, as reported by Polcawich.^[84] To quantify this, aging rate of $\epsilon_{31, f}$ could be investigated before and after etching to investigate the imprint effect. Both pre-poled and unpoled films should be measured.^[84, 142]

References

- [1] S. Trolier-McKinstry and P. Muralt, "Thin film piezoelectrics for MEMS," *Journal of Electroceramics*, vol. 12, pp. 7-17, 2004.
- [2] L.-P. Wang, "Microelectromechanical systems (MEMS) sensors based on lead zirconate titanate (PZT) films," in *Ph.D., Engineering Science and Mechanics*. vol. Ph.D University Park: The Pennsylvania State University, 2001, p. 143.
- [3] N. Ledermann, P. Muralt, J. Baborowski, S. Gentil, K. Mukati, M. Cantoni, A. Seifert, and N. Setter, "{100}-textured, piezoelectric $\text{Pb}(\text{Zr}_x\text{Ti}_{1-x})\text{O}_3$ thin films for MEMS: integration, deposition and properties," *Sensors and Actuators A-Physical*, vol. 105, pp. 162-170, Jul 2003.
- [4] N. Setter, D. Damjanovic, L. Eng, G. Fox, S. Gevorgian, S. Hong, A. Kingon, H. Kohlstedt, N. Y. Park, G. B. Stephenson, I. Stolitchnov, A. K. Taganstev, D. V. Taylor, T. Yamada, and S. Streiffner, "Ferroelectric thin films: Review of materials, properties, and applications," *Journal of Applied Physics*, vol. 100, Sep 2006.
- [5] S. Jesse, A. P. Baddorf, and S. V. Kalinin, "Dynamic behaviour in piezoresponse force microscopy," *Nanotechnology*, vol. 17, pp. 1615-1628, Mar 2006.
- [6] N. Bassiri-Gharb, "Dielectric and piezoelectric nonlinearities in oriented $\text{Pb}(\text{Yb}_{1/2}\text{Nb}_{1/2})\text{O}_3$ - PbTiO_3 thin films," *Ph.D. in Materials Science and Engineering*. The Pennsylvania State University, 2005.
- [7] K. Uchino, *Ferroelectric Devices*. New York: Marcel Dekker, Inc., 2000.
- [8] A. L. Kholkin, I. K. Bdikin, D. A. Kiselev, V. V. Shvartsman, and S. H. Kim, "Nanoscale characterization of polycrystalline ferroelectric materials for piezoelectric applications," *Journal of Electroceramics*, vol. 19, pp. 81-94, 2007.
- [9] B. Jaffe, W. R. Cook, and H. Jaffe, *Piezoelectric Ceramics*. Marietta: Academi Press Ltd., 1971.
- [10] F. Jona and G. Shirane, *Ferroelectric Crystals*. New York: The Macmillan Company, 1962.
- [11] M. E. Lines and A. M. Glass, *Principles and Applications of Ferroelectrics and Related Materials*. New York: Oxford University Press, 1977.
- [12] J. Scott, *Ferroelectric Memories*. Berlin: Springer Verlag, 2000.
- [13] R. Waser, *Nanoelectronics and Information Technology*: Wiley-VCH, 2003.
- [14] H. Nagata, S. W. Ko, E. Hong, C. A. Randall, and S. Trolier-McKinstry, "Microcontact printed BaTiO_3 and LaNiO_3 thin films for capacitors," *Journal of the American Ceramic Society*, vol. 89, pp. 2816-2821, 2006.
- [15] D. I. Woodward, J. Knudsen, and I. M. Reaney, "Review of crystal and domain structures in the $\text{PbZr}_x\text{Ti}_{1-x}\text{O}_3$ solid solution," *Physical Review B*, vol. 72, Sep 2005.
- [16] A. J. Moulson and J. M. Herbert, *Electroceramics*, Second ed. Sussex: John Wiley & Sons Ltd., 2003.
- [17] F. Xu, S. Trolier-McKinstry, W. Ren, B. M. Xu, Z. L. Xie, and K. J. Hemker, "Domain wall motion and its contribution to the dielectric and piezoelectric properties of lead zirconate titanate films," *Journal of Applied Physics*, vol. 89, pp. 1336-1348, Jan 2001.

- [18] R. A. Wolf and S. Trolier-McKinstry, "Temperature dependence of the piezoelectric response in lead zirconate titanate films," *Journal of Applied Physics*, vol. 95, pp. 1397-1406, Feb 2004.
- [19] G. W. Scherer, "Sintering of sol-gel films," *Journal of Sol-Gel Science and Technology*, vol. 8, pp. 353-363, 1997.
- [20] R. G. Polcawich, J. S. Pulskamp, P. R. D. Judy, and a. M. D. S. Trolier-McKinstry, "Surface Micromachined RF MEMS Ohmic Series Switch Using Thin Film Piezoelectric Actuators," *IEEE T-MTT*, vol. 55, pp. 2642-2654, 2007.
- [21] M. Umeda, K. Nakamura, and S. Ueha, "Energy storage characteristics of a piezo-generator using impact induced vibration," *Japanese Journal of Applied Physics Part 1- Regular Papers Short Notes & Review Papers*, vol. 36, pp. 3146-3151, May 1997.
- [22] G. W. Taylor, J. R. Burns, S. M. Kammann, W. B. Powers, and T. R. Welsh, "The energy harvesting eel: A small subsurface ocean/river power generator," *IEEE Journal of Oceanic Engineering*, vol. 26, pp. 539-547, Oct 2001.
- [23] G. K. Ottman, H. F. Hofmann, and G. A. Lesieutre, "Optimized piezoelectric energy harvesting circuit using step-down converter in discontinuous conduction mode," *IEEE Transactions on Power Electronics*, vol. 18, pp. 696-703, Mar 2003.
- [24] P. Glynn-Jones, S. P. Beeby, and N. M. White, "Towards a piezoelectric vibration-powered microgenerator," *IEEE Proceedings-Science Measurement and Technology*, vol. 148, pp. 68-72, Mar 2001.
- [25] F. Calame and P. Muralt, "Growth and properties of gradient free sol-gel lead zirconate titanate thin films," *Applied Physics Letters*, vol. 90, Feb 2007.
- [26] S. Wada and T. Tsurumi, "Enhanced piezoelectric properties of perovskite single crystals with engineered domain configuration," *Piezoelectric Single Crystals and Their Applications*, pp. 190-206, 2004.
- [27] D. Damjanovic, M. Budimir, and N. Setter, "Phase transitions, piezoelectric shear effects and anisotropy of d_{33} in BaTiO_3 and PbTiO_3 monodomain single crystals," *Piezoelectric Single Crystals and Their Applications*, pp. 207-224, 2004.
- [28] S. E. Park and T. R. Shrout, "Ultrahigh strain and piezoelectric behavior in relaxor based ferroelectric single crystals," *Journal of Applied Physics*, vol. 82, pp. 1804-1811, Aug 1997.
- [29] S. Kalpat and K. Uchino, "Highly oriented lead zirconium titanate thin films: Growth, control of texture, and its effect on dielectric properties," *Journal of Applied Physics*, vol. 90, pp. 2703-2710, Sep 2001.
- [30] N. Bassiri-Gharb, I. Fujii, E. Hong, S. Trolier-McKinstry, D. V. Taylor, and D. Damjanovic, "Domain wall contributions to the properties of piezoelectric thin films," *Journal of Electroceramics*, vol. 19, pp. 47-65, Sep 2007.
- [31] C. D. E. Lakeman, Z. K. Xu, and D. A. Payne, "On the evolution of structure and composition in sol-gel-derived lead-zirconate-titanate thin-layers," *Journal of Materials Research*, vol. 10, pp. 2042-2051, Aug 1995.
- [32] I. M. Reaney, K. Brooks, R. Klissurska, C. Pawlaczyk, and N. Setter, "Use of transmission electron-microscopy for the characterization of rapid thermally annealed, solution-gel, lead-zirconate-titanate films," *Journal of the American Ceramic Society*, vol. 77, pp. 1209-1216, May 1994.
- [33] S. Y. Chen and I. W. Chen, "Texture development, microstructure evolution, and crystallization of chemically derived PZT thin films," *Journal of the American Ceramic Society*, vol. 81, pp. 97-105, Jan 1998.

- [34] K. Kushida, K. R. Udayakumar, S. B. Krupanidhi, and L. E. Cross, "Origin of orientation in sol-gel-derived lead titanate films," *Journal of the American Ceramic Society*, vol. 76, pp. 1345-1348, May 1993.
- [35] S. Trolrier-McKinstry, N. B. Gharb, and D. Damjanovic, "Piezoelectric nonlinearity due to motion of 180 degree domain walls in ferroelectric materials at subcoercive fields: A dynamic poling model," *Applied Physics Letters*, vol. 88, May 2006.
- [36] N. B. Gharb, S. Trolrier-McKinstry, and D. Damjanovic, "Piezoelectric nonlinearity in ferroelectric thin films," *Journal of Applied Physics*, vol. 100, 2006.
- [37] Q. M. Zhang, H. Wang, N. Kim, and L. E. Cross, "Direct evaluation of domain-wall and intrinsic contributions to the dielectric and piezoelectric response and their temperature-dependence on lead-zirconate-titanate ceramics," *Journal of Applied Physics*, vol. 75, pp. 454-459, Jan 1994.
- [38] F. Tyholdt, F. Calame, K. Prume, H. Raeder, and P. Muralt, "Chemically derived seeding layer for {100}-textured PZT thin films," *Journal of Electroceramics*, vol. 19, pp. 311-314, Dec 2007.
- [39] A. Kholkin, "Non-linear piezoelectric response in lead zirconate-titanate (PZT) films," *Ferroelectrics*, vol. 238, pp. 799-807, 2000.
- [40] D. Damjanovic, M. Budimir, M. Davis, and N. Setter, "Piezoelectric anisotropy: Enhanced piezoelectric response along nonpolar directions in perovskite crystals," *Journal of Materials Science*, vol. 41, pp. 65-76, Jan 2006.
- [41] S. Trolrier-McKinstry, "An introduction to piezoelectric single crystals," *Piezoelectric Single Crystals and Their Applications*, pp. 21-36, 2004.
- [42] A. Roelofs, N. A. Pertsev, R. Waser, F. Schlaphof, L. M. Eng, C. Ganpule, V. Nagarajan, and R. Ramesh, "Depolarizing-field-mediated 180 degrees switching in ferroelectric thin films with 90 degrees domains," *Applied Physics Letters*, vol. 80, pp. 1424-1426, 2002.
- [43] D. V. Taylor and D. Damjanovic, "Evidence of domain wall contribution to the dielectric permittivity in PZT thin films at sub-switching fields," *Journal of Applied Physics*, vol. 82, pp. 1973-1975, Aug 1997.
- [44] J. A. Christman, R. R. Woolcott, A. I. Kingon, and R. J. Nemanich, "Piezoelectric measurements with atomic force microscopy," *Applied Physics Letters*, vol. 73, pp. 3851-3853, Dec 1998.
- [45] A. Gruverman and A. Kholkin, "Nanoscale ferroelectrics: processing, characterization and future trends," *Reports on Progress in Physics*, vol. 69, pp. 2443-2474, 2006.
- [46] C. Dehoff, B. J. Rodriguez, A. I. Kingon, R. J. Nemanich, A. Gruverman, and J. S. Cross, "Atomic force microscopy-based experimental setup for studying domain switching dynamics in ferroelectric capacitors," *Review of Scientific Instruments*, vol. 76, pp. 023708-1-5, 2005.
- [47] D. J. Kim, J. Y. Jo, T. H. Kim, S. M. Yang, B. Chen, Y. S. Kim, and T. W. Noh, "Observation of inhomogeneous domain nucleation in epitaxial $\text{Pb}(\text{Zr},\text{Ti})\text{O}_3$ capacitors," *Applied Physics Letters*, vol. 91, pp. 132903-1-3, 2007.
- [48] I. Stolichnov, L. Malin, E. Colla, A. K. Tagantsev, and N. Setter, "Microscopic aspects of the region-by-region polarization reversal kinetics of polycrystalline ferroelectric $\text{Pb}(\text{Zr},\text{Ti})\text{O}_3$ films," *Applied Physics Letters*, vol. 86, 2005.
- [49] W. W. Cao and C. A. Randall, "Grain size and domain size relations in bulk ceramic ferroelectric materials," *Journal of Physics and Chemistry of Solids*, vol. 57, pp. 1499-1505, Oct 1996.
- [50] S. V. Kalinin, B. J. Rodriguez, S. H. Kim, S. K. Hong, A. Gruverman, and E. A. Eliseev, "Imaging mechanism of piezoresponse force microscopy in capacitor structures," *Applied Physics Letters*, vol. 92, 2008.

- [51] S. Jesse, H. N. Lee, and S. V. Kalinin, "Quantitative mapping of switching behavior in piezoresponse force microscopy," *Review of Scientific Instruments*, vol. 77, 2006.
- [52] S. Jesse, A. P. Baddorf, and S. V. Kalinin, "Switching spectroscopy piezoresponse force microscopy of ferroelectric materials," *Applied Physics Letters*, vol. 88, 2006.
- [53] H. Y. Guo, J. B. Xu, I. H. Wilson, Z. Xie, E. Z. Luo, S. B. Hong, and H. Yan, "Study of domain stability on $(\text{Pb}_{0.76}\text{Ca}_{0.24})\text{TiO}_3$ thin films using piezoresponse microscopy," *Applied Physics Letters*, vol. 81, pp. 715-717, 2002.
- [54] A. Roelofs, U. Bottger, R. Waser, F. Schlaphof, S. Trogisch, and L. M. Eng, "Differentiating 180 degrees and 90 degrees switching of ferroelectric domains with three-dimensional piezoresponse force microscopy," *Applied Physics Letters*, vol. 77, pp. 3444-3446, 2000.
- [55] P. Bintachitt, S. Trolier-McKinstry, K. Seal, S. Jesse, and S. V. Kalinin, "Switching spectroscopy piezoresponse force microscopy of polycrystalline capacitor structures," *Applied Physics Letters*, vol. 94, pp. 042906-1-3, 2009.
- [56] K. Seal, S. Jesse, S. V. Kalinin, I. Fujii, P. bintachitt, and S. Trolier-McKinstry, "Spatially resolved spectroscopic mapping of polarization reversal in polycrystalline ferroelectric films: crossing the resolution barrier ", *submitted to Physical Review Letters*, 2009.
- [57] I. D. Mayergoyz, "Mathematical-models of hysteresis," *IEEE Transactions on Magnetics*, vol. 22, pp. 603-608, 1986.
- [58] T. G. Sorop, C. Untiedt, F. Luis, L. J. de Jongh, M. Kroll, and M. Rasa, "Magnetization reversal of individual Fe nanowires in aluminates studied by magnetic force microscopy," *Journal of Applied Physics*, vol. 93, pp. 7044-7046, 2003.
- [59] M. S. Pierce, C. R. Buechler, L. B. Sorensen, S. D. Kevan, E. A. Jagla, J. M. Deutsch, T. Mai, O. Narayan, J. E. Davies, K. Liu, G. T. Zimanyi, H. G. Katzgraber, O. Hellwig, E. E. Fullerton, P. Fischer, and J. B. Kortright, "Disorder-induced magnetic memory: Experiments and theories," *Physical Review B*, vol. 75, pp. 144406-1-23, 2007.
- [60] A. P. Young and H. G. Katzgraber, "Absence of an Almeida-Thouless line in three-dimensional spin glasses," *Physical Review Letters*, vol. 93, pp. 207203-1-4, 2004.
- [61] G. Catalan, H. Bea, S. Fusil, M. Bibes, P. Paruch, A. Barthelemy, and J. F. Scott, "Fractal dimension and size scaling of domains in thin films of multiferroic BiFeO_3 ," *Physical Review Letters*, vol. 100, pp. 027602-1-4, 2008.
- [62] S. Jesse, B. J. Rodriguez, S. Choudhury, A. P. Baddorf, I. Vrejoiu, D. Hesse, M. Alexe, E. A. Eliseev, A. N. Morozovska, J. Zhang, L. Q. Chen, and S. V. Kalinin, "Direct imaging of the spatial and energy distribution of nucleation centres in ferroelectric materials," *Nature Materials*, vol. 7, pp. 209-215, 2008.
- [63] S. M. Yang, J. Y. Jo, D. J. Kim, H. Sung, T. W. Noh, H. N. Lee, J. G. Yoon, and T. K. Song, "Domain wall motion in epitaxial $\text{Pb}(\text{Zr},\text{Ti})\text{O}_3$ capacitors investigated by modified piezoresponse force microscopy," *Applied Physics Letters*, vol. 92, 2008.
- [64] A. Gruverman, D. Wu, and J. F. Scott, "Piezoresponse force microscopy studies of switching behavior of ferroelectric capacitors on a 100-ns time scale," *Physical Review Letters*, vol. 100, 2008.
- [65] S. Kalinin, "Local polarization switching and PFM Spectroscopy," in *PFM Workshop Oak Ridge National Laboratory*, 2007.
- [66] A. Gruverman, "Principals and applications of piezoresponse force microscopy," in *PFM Workshop Oak Ridge National Laboratory*, 2007.
- [67] P. Muralt, "Recent progress in materials issues for piezoelectric MEMS," *Journal of the American Ceramic Society*, vol. 91, pp. 1385-1396, 2008.

- [68] F. Xu, "Longitudinal piezoelectric characterization and domain wall contributions in lead zirconate titanate thin films," in *Ph. D. in Materials Science and Engineering*, The Pennsylvania State University, 1999
- [69] Y. C. Hsu, C. C. Wu, C. C. Lee, G. Z. Cao, and I. Y. Shen, "Demonstration and characterization of PZT thin-film sensors and actuators for meso- and micro-structures," *Sensors and Actuators A-Physical*, vol. 116, pp. 369-377, 2004.
- [70] R. A. Wolf, "Temperature dependence of the piezoelectric response of lead zirconate titanate films for MEMS applications," in *Materials Science and Engineering*. vol. MS. University Park: The Pennsylvania State University, 2001, p. 128.
- [71] K. H. Brosnan, "Processing, properties, and application of textured $0.72\text{Pb}(\text{Mg}_{1/3}\text{Nb}_{2/3})\text{O}_3\text{-}0.28\text{PbTiO}_3$ ceramics," in *Materials Science and Engineering*. vol. Ph.D. thesis: The Pennsylvania State University, 2007.
- [72] R. A. Vaia, M. S. Weathers, and W. A. Bassett, "Anomalous peaks in grazing incidence thin film X-ray diffraction," *Powder Diffraction*, vol. 9, pp. 44-49, 1994.
- [73] J. F. Shepard, P. J. Moses, and S. Trolrier-McKinstry, "The wafer flexure technique for the determination of the transverse piezoelectric coefficient (d_{31}) of PZT thin films," *Sensors and Actuators A-Physical*, vol. 71, pp. 133-138, Nov 1998.
- [74] S. Jesse, S. V. Kalinin, R. Proksch, A. P. Baddorf, and B. J. Rodriguez, "The band excitation method in scanning probe microscopy for rapid mapping of energy dissipation on the nanoscale," *Nanotechnology*, vol. 18, 2007.
- [75] L. Fang, C. L. Muhlstein, J. G. Collins, A. L. Romasco, and L. H. Friedman, "Continuous electrical in situ contact area measurement during instrumented indentation," *Materials Research Society*, vol. 23, pp. 2480-2485, 2008.
- [76] W. C. Oliver and G. M. Pharr, "Measurement of hardness and elastic modulus by instrumented indentation: Advances in understanding and refinements to methodology," *Journal of Materials Research*, vol. 19, pp. 3-20, 2004.
- [77] I. Ben-Yaacov and A. Berenstein, "Photolithography," Santa Barbara, 2005.
- [78] A. Goyal, V. Hood, and S. Tadigadapa, "High speed anisotropic etching of Pyrex((R)) for microsystems applications," *Journal of Non-Crystalline Solids*, vol. 352, pp. 657-663, May 2006.
- [79] Inostek, "Piezo and Pyroelectric Properties of PZT Films for Microsensors and Actuators," in <http://www.inostek.com> Gyeonggi: Inostek, 2008.
- [80] J. Cheng, W. Zhu, N. Li, and L. E. Cross, "High temperature dielectric properties of sol-gel derived thick PZT thin films with different Zr/Ti atom ratios," *Mat. Res. Soc. Symp. Proc.*, vol. 688, pp. C7.4.1-7.4.6, 2002.
- [81] R. W. Schwartz, "Chemical solution deposition of perovskite thin films," *Chemistry of Materials*, vol. 9, pp. 2325-2340, 1997.
- [82] S. Hong, *Nanoscale phenomena in ferroelectric thin films*: Kluwer Academic Publishers, 2004.
- [83] A. L. Kholkin, C. Wutchrich, D. V. Taylor, and N. Setter, "Interferometric measurements of electric field-induced displacements in piezoelectric thin films," *Review of Scientific Instruments*, vol. 67, pp. 1935-1941, 1996.
- [84] R. G. Polcawich, "Piezoelectric and dielectric reliability in lead zirconate titanate thin films," M. S. in *Materials Science and Engineering*, The Pennsylvania State University, 1999.
- [85] A. L. Kholkin, A. K. Tagantsev, E. L. Colla, D. V. Taylor, and N. Setter, "Piezoelectric and dielectric aging in $\text{Pb}(\text{Zr},\text{Ti})\text{O}_3$ thin films and bulk ceramics," *Integrated Ferroelectrics*, vol. 15, pp. 317-324, 1997.

- [86] D. Damjanovic and M. Demartin, "Contribution of the irreversible displacement of domain walls to the piezoelectric effect in barium titanate and lead zirconate titanate ceramics," *Journal of Physics-Condensed Matter*, vol. 9, pp. 4943-4953, Jun 1997.
- [87] D. J. Kim, J. P. Maria, A. I. Kingon, and S. K. Streiffer, "Evaluation of intrinsic and extrinsic contributions to the piezoelectric properties of $\text{Pb}(\text{Zr}_{1-x}\text{Ti}_x)\text{O}_3$ thin films as a function of composition," *Journal of Applied Physics*, vol. 93, pp. 5568-5575, May 2003.
- [88] V. V. Shvartsman, A. L. Kholkin, and N. A. Pertsev, "Piezoelectric nonlinearity of $\text{Pb}(\text{Zr}, \text{Ti})\text{O}_3$ thin films probed by scanning probe microscopy," *Applied Physics Letters*, vol. 81, pp. 3025-3027, 2002.
- [89] J. H. Li, L. Chen, V. Nagarajan, R. Ramesh, and A. L. Roytburd, "Finite element modeling of piezoresponse in nanostructured ferroelectric films," *Applied Physics Letters*, vol. 84, pp. 2626-2628, 2004.
- [90] J. Nosek, "Drive level dependence of the resonant frequency in BAW quartz resonators and his modeling," *IEEE Transactions on Ultrasonics Ferroelectrics and Frequency Control*, vol. 46, pp. 823-829, 1999.
- [91] N. B. Gharb and S. Trolier-McKinstry, "Dielectric nonlinearity of $\text{Pb}(\text{Yb}_{1/2}\text{Nb}_{1/2})\text{O}_3$ - PbTiO_3 thin films with $\{100\}$ and $\{111\}$ crystallographic orientation," *Journal of Applied Physics*, vol. 97, pp. 064106-1-7, 2005.
- [92] D. Damjanovic, "Stress and frequency dependence of the direct piezoelectric effect in ferroelectric ceramics," *Journal of Applied Physics*, vol. 82, pp. 1788-1797, Aug 1997.
- [93] D. Ricinschi, L. Mitoseriu, A. Stancu, P. Postolache, and M. Okuyama, "Analysis of the switching characteristics of PZT films by first order reversal curve diagrams," *Integrated Ferroelectrics*, vol. 67, pp. 103-115, 2004.
- [94] G. A. Rossetti and A. G. Khachaturyan, "Inherent nanoscale structural instabilities near morphotropic boundaries in ferroelectric solid solutions," *Applied Physics Letters*, vol. 91, pp. 072909-1-3, 2007.
- [95] B. J. Rodriguez, S. Jesse, A. P. Baddorf, T. Zhao, Y. H. Chu, R. Ramesh, E. A. Eliseev, A. N. Morozovska, and S. V. Kalinin, "Spatially resolved mapping of ferroelectric switching behavior in self-assembled multiferroic nanostructures: strain, size, and interface effects," *Nanotechnology*, vol. 18, p. 405701, 2007.
- [96] P. Paruch, T. Giamarchi, and J. M. Triscone, "Domain wall roughness in epitaxial ferroelectric $\text{PbZr}_{0.2}\text{Ti}_{0.8}\text{O}_3$ thin films," *Physical Review Letters*, vol. 94, 2005.
- [97] P. Delobelle, O. Guillon, E. Fribourg-Blanc, C. Soyer, E. Cattan, and D. Remiens, "True Young modulus of $\text{Pb}(\text{Zr}, \text{Ti})\text{O}_3$ films measured by nanoindentation," *Applied Physics Letters*, vol. 85, pp. 5185-5187, 2004.
- [98] P. Delobelle, E. Fribourg-Blanc, and D. Remiens, "Mechanical properties determined by nanoindentation tests of $[\text{Pb}(\text{ZrTi})\text{O}_3]$ and $[\text{Pb}(\text{Mg}_{1/3}\text{Nb}_{2/3})_{(1-x)}\text{Ti}_x\text{O}_3]$ sputtered thin films," *Thin Solid Films*, vol. 515, pp. 1385-1393, 2006.
- [99] J. A. Howell, J. R. Hellmann, and C. L. Muhlstein, "Correlations between free volume and pile-up behavior in nanoindentation reference glasses," *Materials Letters*, vol. 62, pp. 2144-2146, 2008.
- [100] A. L. Romasco, "Time dependent deformation of thin film platinum during nanoindentation testing," M. S. in *Materials Science and Engineering*, The Pennsylvania State University, 2009
- [101] A. B. Schaufele and K. H. Hardtl, "Ferroelastic properties of lead zirconate titanate ceramics," *Journal of the American Ceramic Society*, vol. 79, pp. 2637-2640, 1996.
- [102] J. A. Howell, J. R. Hellmann, and C. L. Muhlstein, "Nanomechanical properties of commercial float glass," *Journal of Non-Crystalline Solids*, vol. 354, pp. 1891-1899, 2008.

- [103] D. Tabor, *The Hardness of Metals*. New York: Oxford University Press, 1951.
- [104] E. M. Bourim, H. Tanaka, M. Gabbay, and G. Fantozzi, "Internal friction and dielectric measurements in lead zirconate titanate ferroelectric ceramics," *Japanese Journal of Applied Physics Part 1-Regular Papers Short Notes & Review Papers*, vol. 39, pp. 5542-5547, 2000.
- [105] A. Bouzid, E. M. Bourim, M. Gabbay, and G. Fantozzi, "PZT phase diagram determination by measurement of elastic moduli," *Journal of the European Ceramic Society*, vol. 25, pp. 3213-3221, 2005.
- [106] A. Zarycka, R. Zachariasz, J. Ilczuk, and A. Chrobak, "Internal friction related to the mobility of domain walls in sol-gel derived PZT ceramics," *Materials Science-Poland*, vol. 23, pp. 159-165, 2005.
- [107] T. H. Fang, S. R. Jian, and D. S. Chuu, "Nanomechanical properties of lead zirconate titanate thin films by nanoindentation," *Journal of Physics-Condensed Matter*, vol. 15, pp. 5253-5259, 2003.
- [108] H. P. Wu, L. Z. Wu, Q. Sun, W. D. Fei, and S. Y. Du, "Mechanical properties of sol-gel derived lead zirconate titanate thin films by nanoindentation," *Applied Surface Science*, vol. 254, pp. 5492-5496, 2008.
- [109] S. S. Subasinghe, A. Goyal, and S. A. Tadigadapa, "High aspect ratio plasma etching of bulk lead zirconate titanate," *Micromachining and Microfabrication Process Technology XI*, vol. 6109, pp. 6109D-1-6109D-9, 2006.
- [110] J. Baborowski, "Microfabrication of piezoelectric MEMS," *Journal of Electroceramics*, vol. 12, pp. 33-51, 2004.
- [111] M. J. Madou, *Fundamentals of microfabrication*, Second edition ed.: CRC Press, 2002.
- [112] S. Marks and J. P. Almerico, "Profile and etch characterization of high wafer temperature etched Y1/Pt stacks," *Integrated Ferroelectrics*, vol. 66, pp. 19-27, 2004.
- [113] Y. Kokaze, I. Kimura, M. Endo, M. Ueda, S. Kikuchi, Y. Nishioka, and K. Suu, "Dry etching process for Pb(Zr,Ti)O₃ thin-film actuators," *Japanese Journal of Applied Physics Part 1-Regular Papers Brief Communications & Review Papers*, vol. 46, pp. 280-282, Jan 2007.
- [114] G. McLane, R. Polcawich, J. Pulskamp, B. Piekarski, M. Dubey, E. Zakar, J. Conrad, R. Piekarz, M. Ervin, and M. Wood, "Reactive ion etching of sol-gel deposited lead zirconate titanate (PZT) thin films in SF₆ plasmas," *Integrated Ferroelectrics*, vol. 37, pp. 397-404, 2001.
- [115] M. G. Kang, K. T. Kim, and C. I. Kim, "Recovery of plasma-induced damage in PZT thin film with O₂ gas annealing," *Thin Solid Films*, vol. 398, pp. 448-453, Nov 2001.
- [116] W. Pan, C. L. Thio, and S. B. Desu, "Reactive ion etching damage to the electrical properties of ferroelectric thin films," *Journal of Materials Research*, vol. 13, pp. 362-367, Feb 1998.
- [117] S. Peng and Y. Xi, "Effect of microstructure on reactive ion etching of sol-gel-derived PZT thin film," *Ceramics International*, vol. 30, pp. 1215-1218, 2004.
- [118] E. Zakar, M. Dubey, B. Piekarski, J. Conrad, R. Piekarz, and R. Widuta, "Process and fabrication of a lead zirconate titanate thin film pressure sensor," *Journal of Vacuum Science & Technology a-Vacuum Surfaces and Films*, vol. 19, pp. 345-348, Jan-Feb 2001.
- [119] A. M. Efremov, D. P. Kim, K. T. Kim, and C. I. Kim, "Etching characteristics and mechanism of Pb(Zr,Ti)O₃ thin films in CF₄/Ar inductively coupled plasma," *Vacuum*, vol. 75, pp. 321-329, Aug 2004.

- [120] D. P. Vijay, S. B. Desu, and W. Pan, "Reactive ion etching of lead-zirconate-titanate (PZT) thin-film capacitors," *Journal of the Electrochemical Society*, vol. 140, pp. 2635-2639, Sep 1993.
- [121] M. Bale and R. E. Palmer, "Deep plasma etching of piezoelectric PZT with SF₆," *Journal of Vacuum Science & Technology B*, vol. 19, pp. 2020-2025, Nov-Dec 2001.
- [122] X. Jiang, J. R. Yuan, A. Cheng, G. Lavallee, P. Rhrig, K. Snook, S. Kwan, W. Hackenberger, J. Catchmark, J. McIntosh, and X. Geng, "Micromachined PMN-PT single crystal for advanced transducers," *Solid-State Sensors, Actuators, and Microsystems Workshop*, pp. 384-387, 2006.
- [123] C. W. Chung, Y. H. Byun, and H. I. Kim, "Inductively coupled plasma etching of a Pb(Zr_xTi_{1-x})O₃ thin film in a HBr/Ar plasma," *Microelectronic Engineering*, vol. 63, pp. 353-361, Sep 2002.
- [124] C. W. Chung, "Reactive ion etching of Pb(Zr_xTi_{1-x})O₃ thin films in an inductively coupled plasma," *Journal of Vacuum Science & Technology B*, vol. 16, pp. 1894-1900, Jul-Aug 1998.
- [125] M. Bale and R. E. Palmer, "Reactive ion etching of piezoelectric Pb(Zr_xTi_{1-x})O₃ in a SF₆ plasma," *Journal of Vacuum Science & Technology A*, vol. 17, pp. 2467-2469, Sep-Oct 1999.
- [126] S. A. Wang, X. H. Li, K. Wakabayashi, and M. Esashi, "Deep reactive ion etching of lead zirconate titanate using sulfur hexafluoride gas," *Journal of the American Ceramic Society*, vol. 82, pp. 1339-1341, May 1999.
- [127] A. M. Efremov, D. P. Kim, and C. I. Kim, "Etching characteristics of Pb(Zr,Ti)O₃ thin films in Cl₂/Ar and CF₄/Ar inductively coupled plasmas: effect of gas mixing ratios," *Thin Solid Films*, vol. 474, pp. 267-274, Mar 2005.
- [128] S. M. Koo, D. P. Kim, K. T. Kim, S. H. Song, and C. Kim, "Etching properties of lead-zirconate-titanate thin films in Cl₂/Ar and BCl₃/Ar gas chemistries," *Journal of Vacuum Science & Technology A*, vol. 22, pp. 1519-1523, Jul-Aug 2004.
- [129] K. T. Kim, M. G. Kang, and C. I. Kim, "Study on the etching damage characteristics of PZT thin films after etching in Cl-based plasma," *Microelectronic Engineering*, vol. 71, pp. 294-300, May 2004.
- [130] C. W. Chung and I. Chung, "Etch behavior of Pb(Zr_xTi_{1-x})O₃ films using a TiO₂ hard mask," *Journal of the Electrochemical Society*, vol. 148, pp. C353-C356, May 2001.
- [131] K. T. Lim, S. M. Koo, K. T. Kim, D. P. Kim, and C. I. Kim, "Improvement in ferroelectric properties of Pt/PZT/Pt capacitors etched as a function of Ar/O₂ gas mixing ratio into Cl(2)/CF₄ plasma," *Thin Solid Films*, vol. 459, pp. 71-75, Jul 2004.
- [132] T. H. An, J. Y. Park, G. Y. Yeom, E. G. Chang, and C. I. Kim, "Effects of BCl₃ addition on Ar/Cl₂ gas in inductively coupled plasmas for lead zirconate titanate etching," *Journal of Vacuum Science & Technology A*, vol. 18, pp. 1373-1376, Jul-Aug 2000.
- [133] J. W. Coburn, "Plasma etching and RIE short course note," The Pennsylvania State University, 2005.
- [134] R. A. Gottscho, C. W. Jurgensen, and D. J. Vitkavage, "Microscopic uniformity in plasma-etching," *Journal of Vacuum Science & Technology B*, vol. 10, pp. 2133-2147, Sep-Oct 1992.
- [135] T. Pandhumsoporn, L. Wang, M. Feldbaum, P. Gadgil, M. Puech, and P. Maquin, "High etch rate, deep anisotropic plasma etching of silicon for MEMS fabrication," *Vide-Science Technique Et Applications*, vol. 56, pp. 673-+, 2001.
- [136] M. Surendra, C. R. Guarnieri, G. S. Selwyn, and M. Dalvie, "Across wafer etch rate uniformity in a high-density plasma reactor-experiment and modeling," *Applied Physics Letters*, vol. 66, pp. 2415-2417, May 1995.

- [137] N. Launay, H. W. v. Zeijl, and P. M. Sarro, "Design and characterization of a novel ICP plasma tool for high speed and high accuracy DRIE processing," in *IEEE MEMS 2008*, pp. 311-314.
- [138] M. Ohring, *Materials Science of Thin Films*: Academic Press, 2002.
- [139] R. G. Polcawich, M. Scanlon, J. Pulskamp, J. Clarkson, J. Conrad, D. Washington, R. Piekarz, S. Trolier-McKinstry, and M. Dubey, "Design and fabrication of a lead zirconate titanate (PZT) thin film acoustic sensor," *Integrated Ferroelectrics*, vol. 54, pp. 595-606, 2003.
- [140] C. Soyer, E. Cattan, and D. Remiens, "Reactive ion beam etching effects on maskless PZT properties," *Integrated Ferroelectrics*, vol. 48, pp. 221-229, 2002.
- [141] B. Lo, C. C. Tai, J. Y. Chang, C. H. Wu, B. J. Chen, T. C. Kuo, P. J. Lian, and Y. C. Ling, "Supercritical carbon dioxide-assisted oxidative degradation and removal of polymer residue after reactive ion etching of photoresist," *Green Chemistry*, vol. 9, pp. 133-138, 2007.
- [142] R. G. Polcawich and S. Trolier-McKinstry, "Piezoelectric and dielectric reliability of lead zirconate titanate thin films," *Journal of Materials Research*, vol. 15, pp. 2505-2513, 2000.

Appendix A

Electrical Properties of PZT Films

This appendix contains additional data on some of the PZT films described elsewhere in the thesis.

A.1 Dielectric and Hysteresis Loops

This section shows the plots of dielectric constant as a function of frequency and Polarization-Electric field (P-E loops).

A.1.1 {001} Textured PZT Films

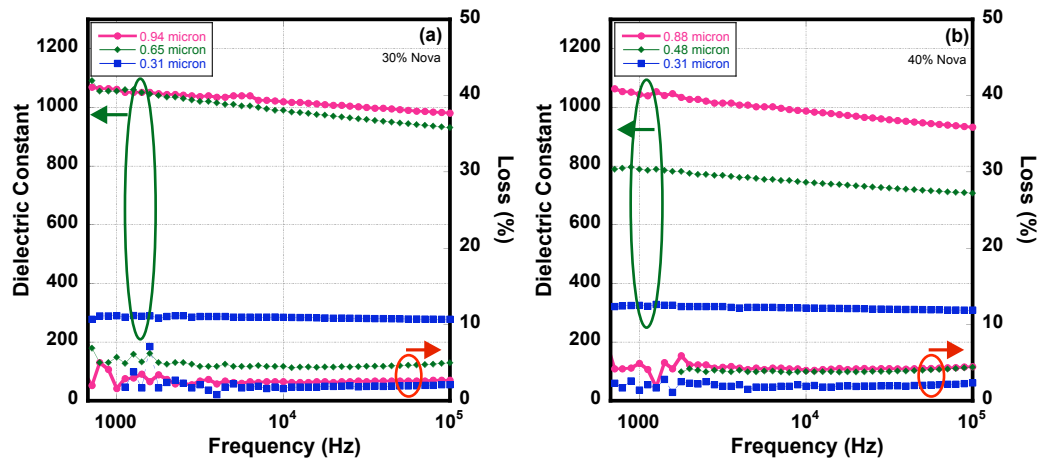


Figure A- 1: Dielectric constant and losses for PZT film on (a) 30% Pb-excess buffer layers, Nova substrates (b) 40% Pb-excess buffer layers, Nova substrates. The details of the process condition were described in Chapter 2 and Chapter 3.

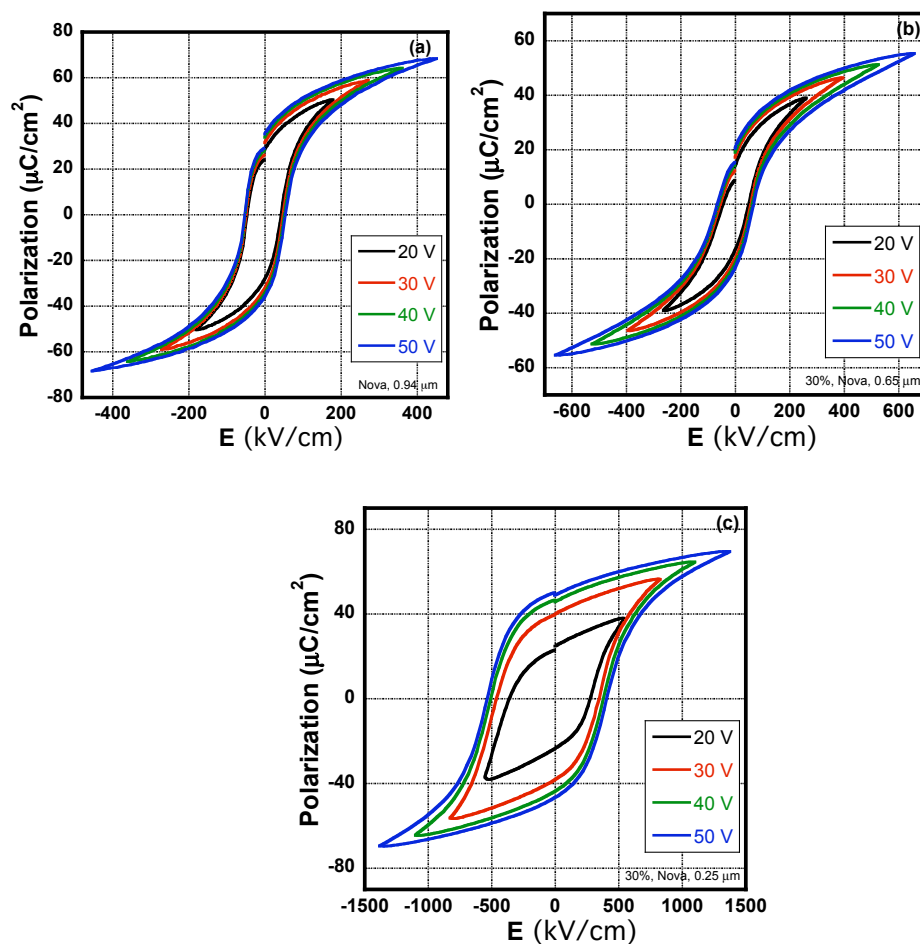


Figure A- 2: P-E loops for {100} textured PZT films of different thickness on 30% Pb-excess buffer layers (a) 0.94 μm , (b) 0.65 μm , (c) 0.25 μm , Nova substrates. The details of the process condition were described in Chapter 2 and Chapter 3.

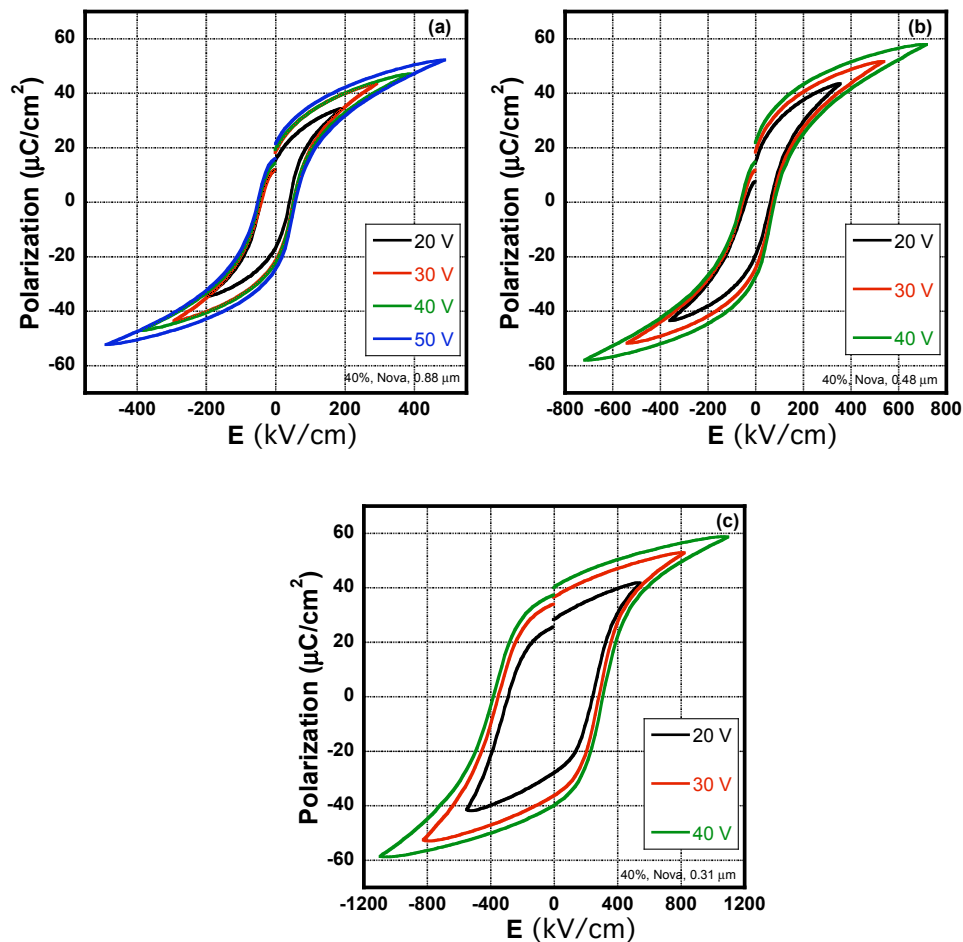


Figure A- 3: P-E loops for PZT films of different thickness on 40% Pb-excess buffer layers (a) 0.88 μm , (b) 0.48 μm , and (c) 0.31 μm , Nova substrates. The details of the process condition were described in Chapter 2 and Chapter 3.

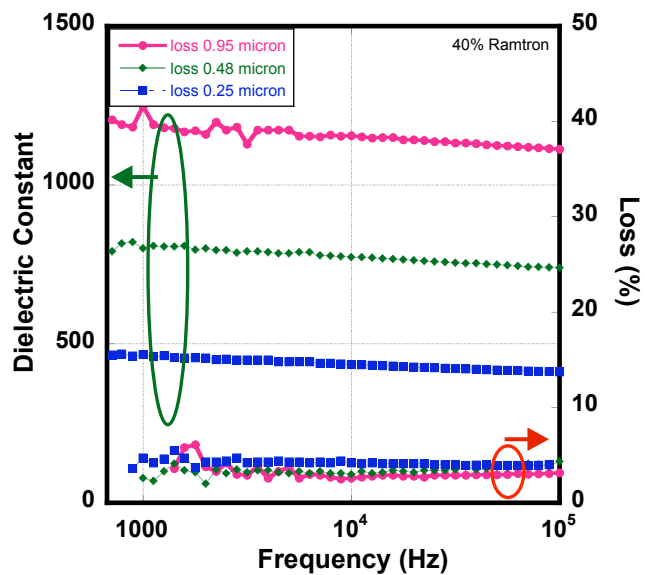


Figure A- 4: Dielectric constant and losses for {100} PZT films of different thickness on 40%excess buffer layers, Ramtron substrates. The details of the process condition were described in Chapter 2 and Chapter 3.

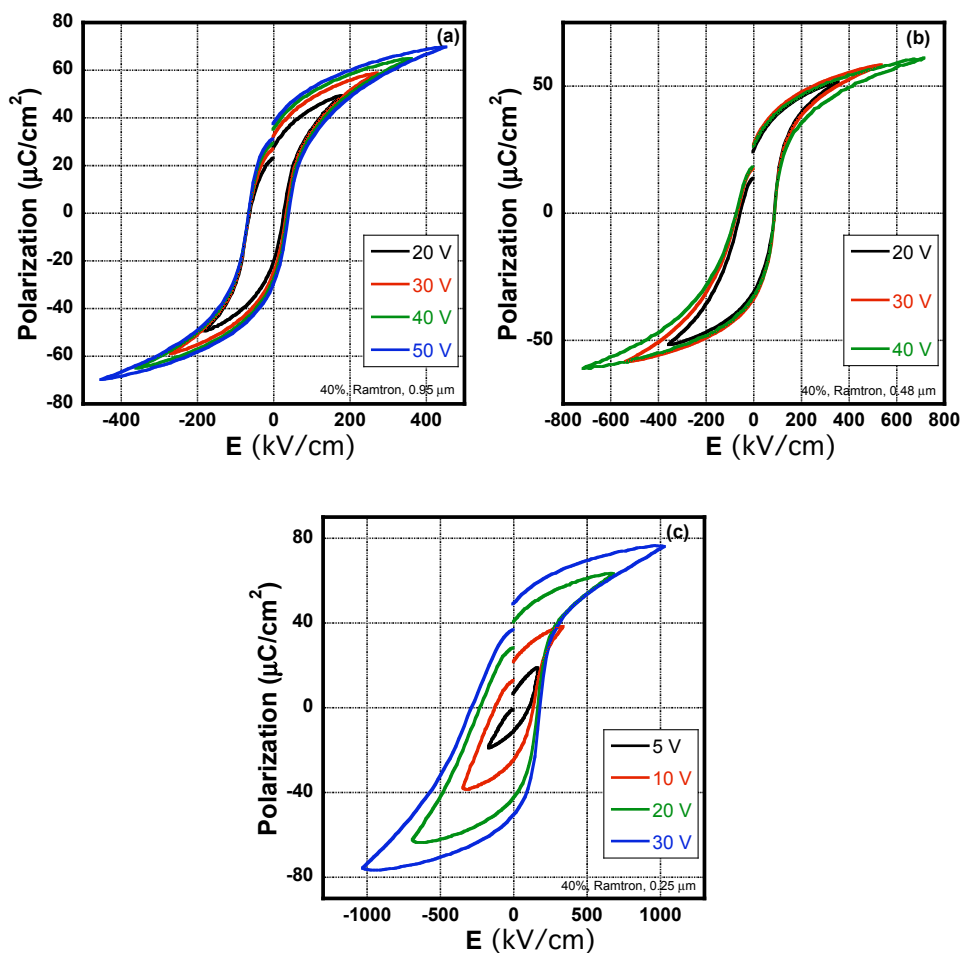


Figure A- 5: P-E loops for PZT films of different thickness on 40% Pb-excess buffer layers (a) 0.95 μm, (b) 0.48 μm, and (c) 0.25 μm, Ramtron substrates. The details of the process condition were described in Chapter 2 and Chapter 3.

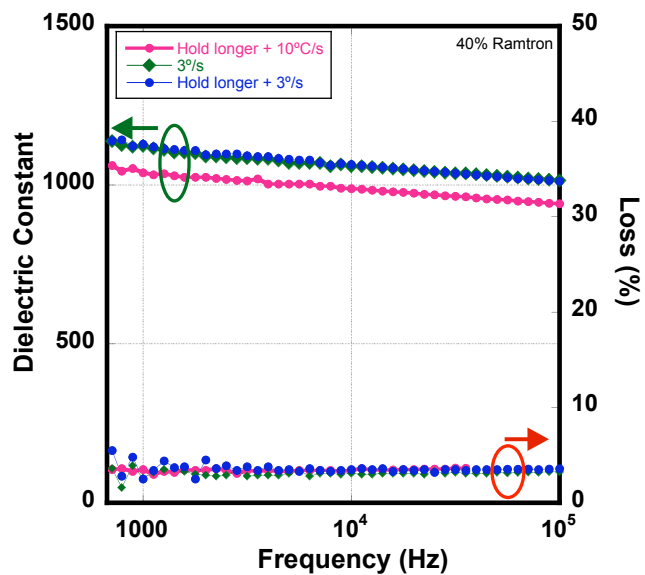


Figure A- 6: Dielectric constant and losses for PZT films on 40% Pb-excess PbTiO_3 buffer layers (a) $0.92 \mu\text{m}$, RTA with heating rate $3^\circ/\text{s}$ (hold 30 s), (b) $0.71 \mu\text{m}$, RTA with holding longer (hold 60 s) with heating rate $3^\circ\text{C}/\text{s}$, and (c) $0.72 \mu\text{m}$, RTA with holding longer (hold 60 s) with heating rate $10^\circ/\text{s}$

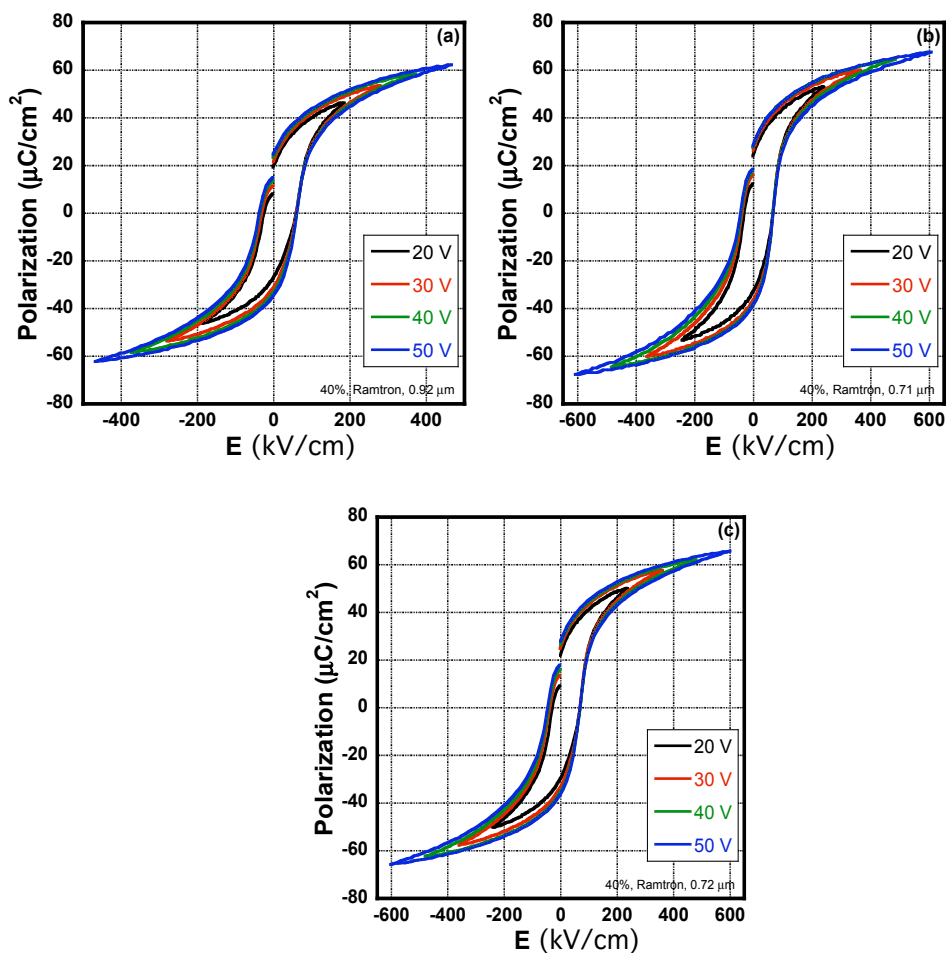


Figure A- 7: P-E loops for PZT films of different thickness on 40% Pb-excess buffer layers (a) 0.92 μm , RTA with heating rate 3°/s (hold 30 s), (b) 0.71 μm , RTA with holding longer (hold 60 s) with heating rate 3°/s, and (c) 0.72 μm , RTA with holding longer (hold 30 s) with heating rate 10°/s

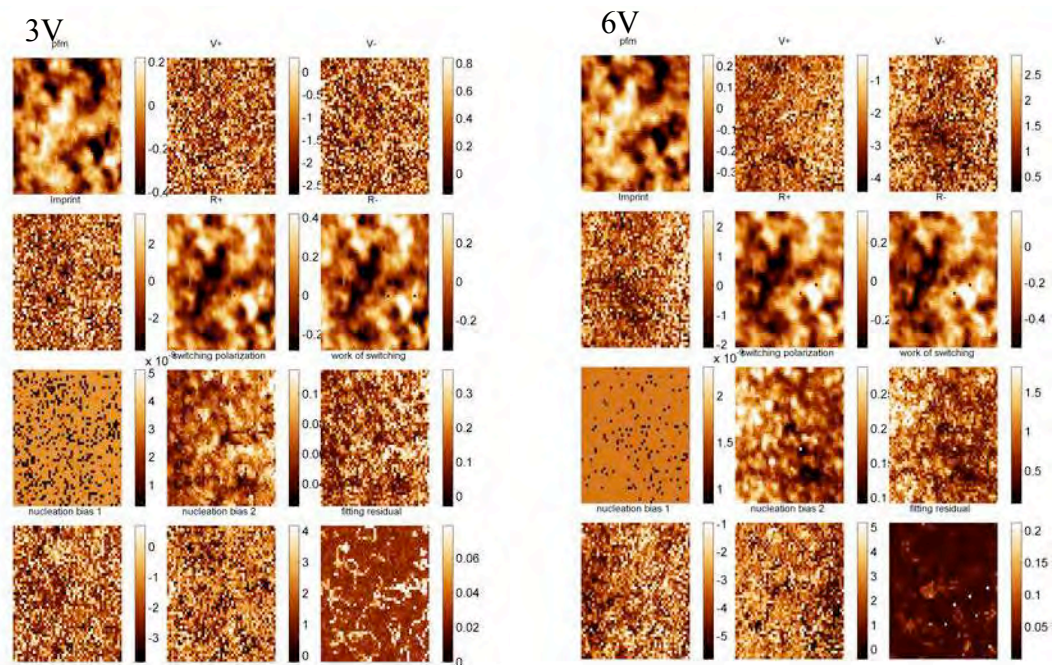
Appendix B

Piezoelectric Nonlinearity of PZT Films

This appendix contains additional data on SSPFM of the PZT films described elsewhere in the thesis.

B.1 Bias Evolution of Switchable Polarization and Piezoelectric Response

The full maps of SS-PFM are shown in **Error! Reference source not found.** and **Error! Reference source not found.** for 50 x 50 pixel and 144 x 144 pixel images, respectively.^[56]



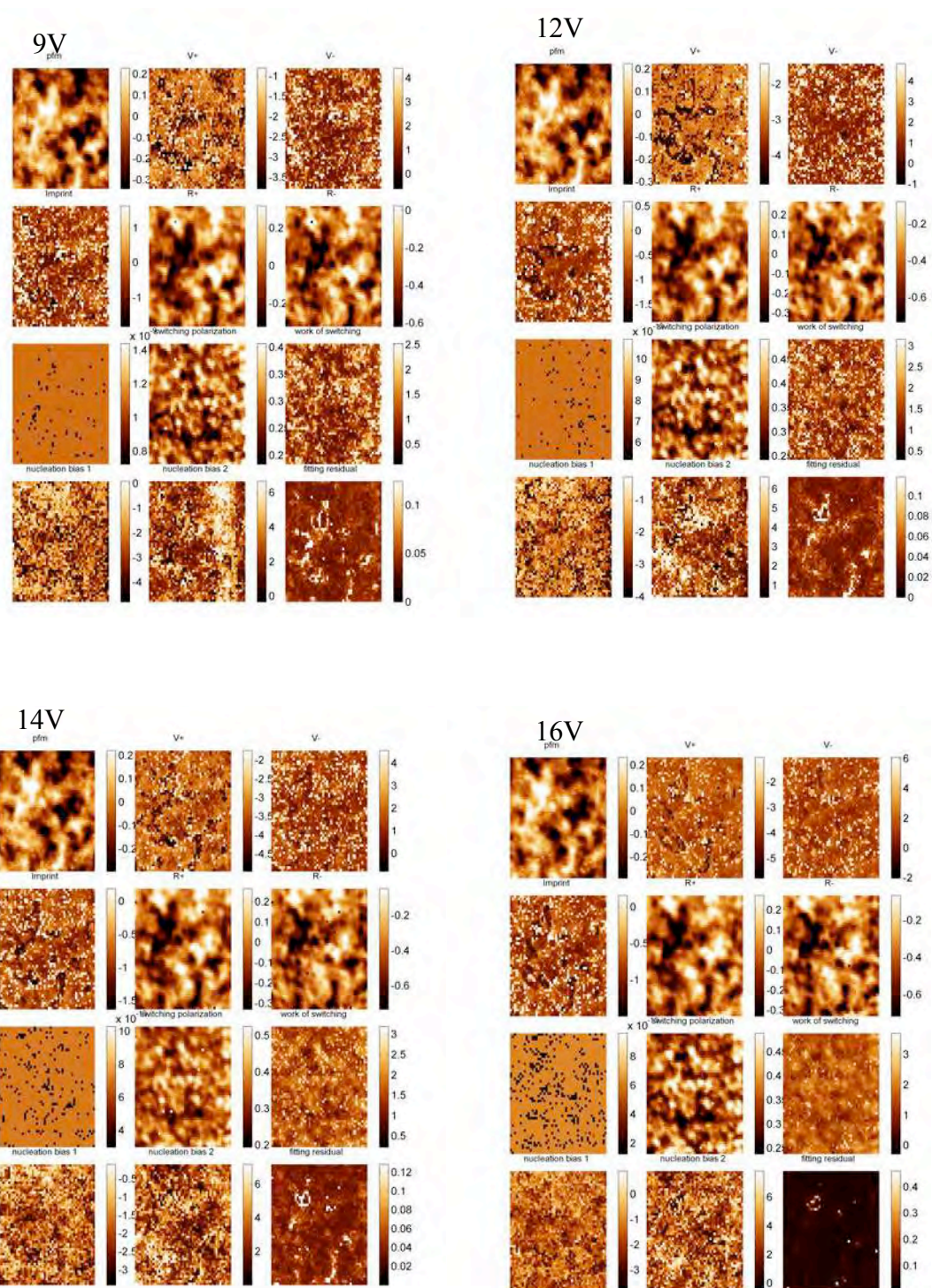
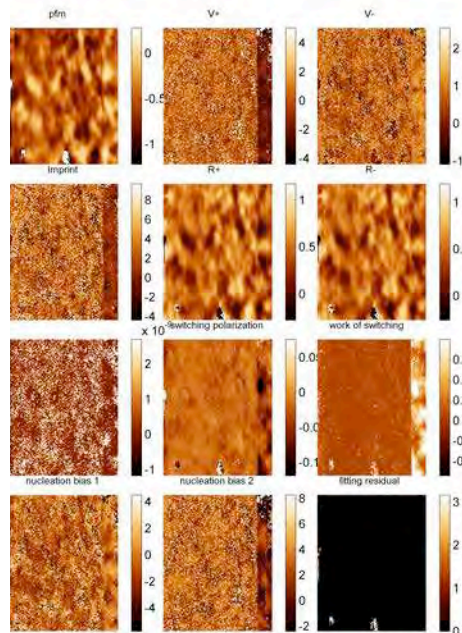
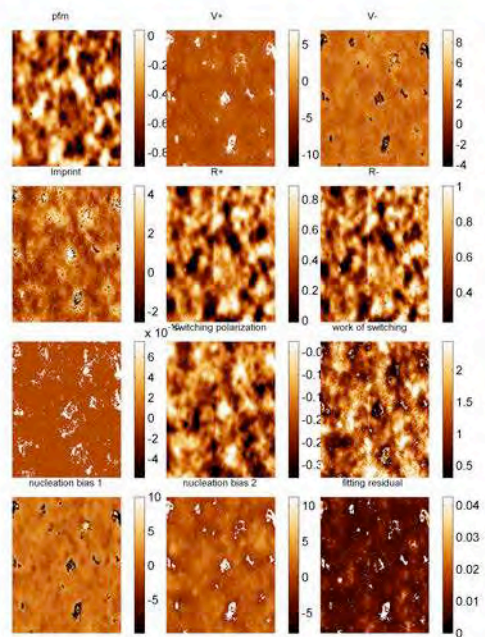


Figure B- 1: Maps of switching parameters at different bias windows from 3 to 16 V for 50 by 50 pixel images.

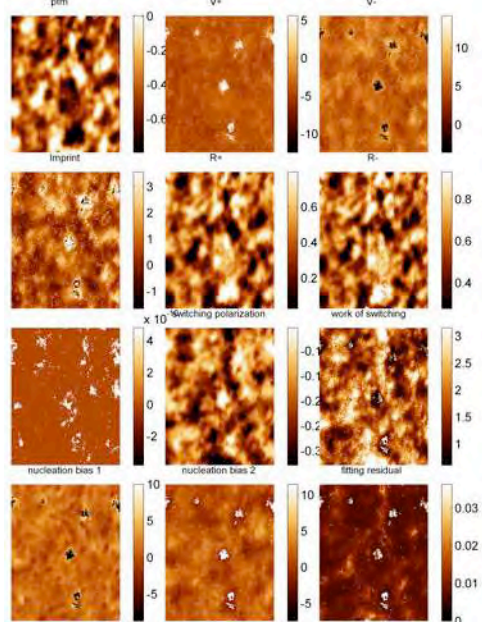
4V



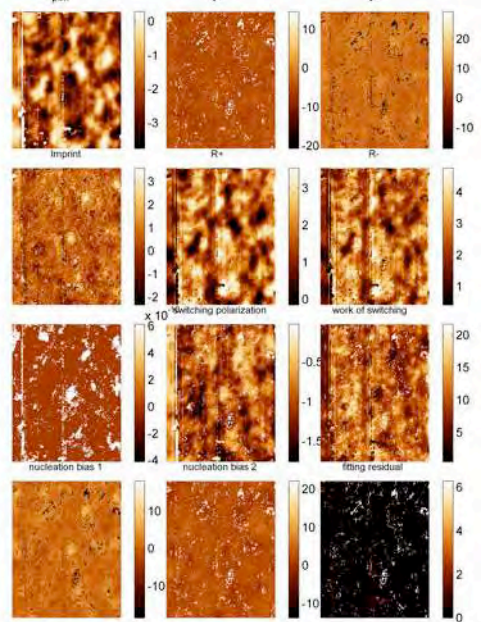
7V



10V



13V



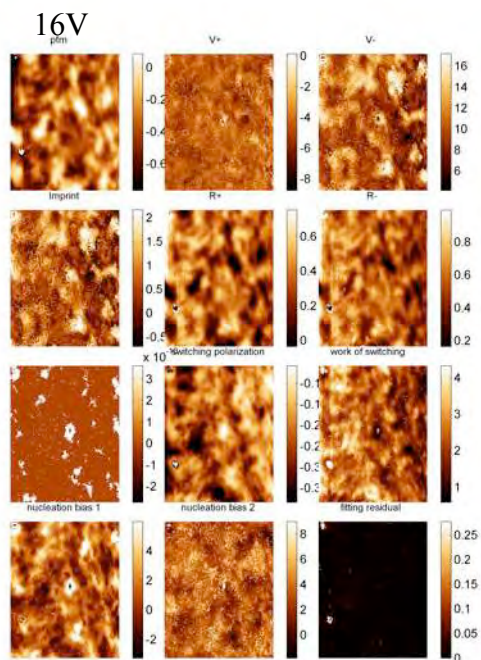


Figure B- 2: Maps of switching parameters at different excitation bias windows from 4 to 16 V for 144 by 144 pixel images.

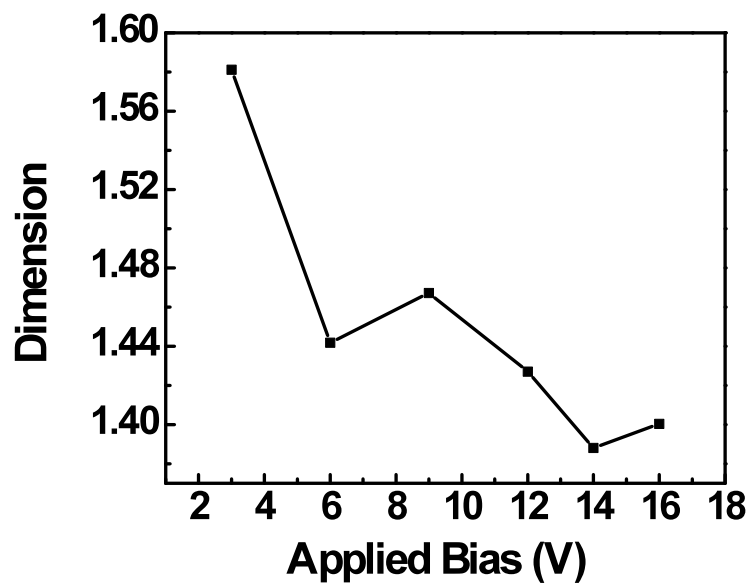


Figure B- 3: Fractal dimension vs. excitation window for 6 μm data set.

Appendix C

Nanoindentation of PZT Films with Mixed {001} and {111} Orientation

This appendix contains additional data on nanoindentation of the PZT films described elsewhere in the thesis.

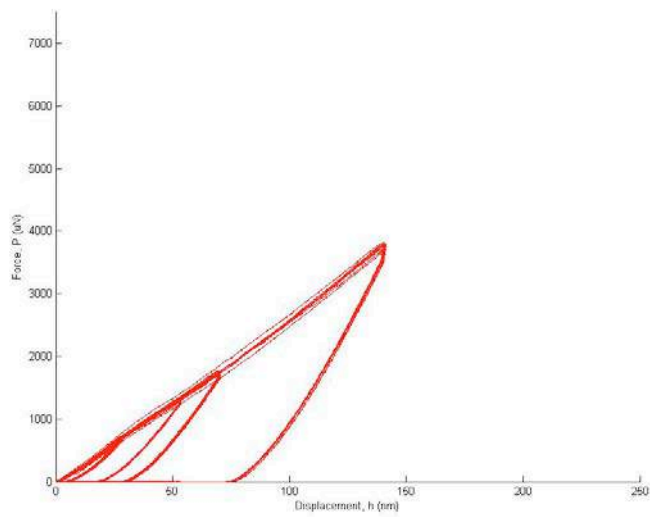


Figure C- 1: Loading and unloading curve of 0.28 µm PZT films

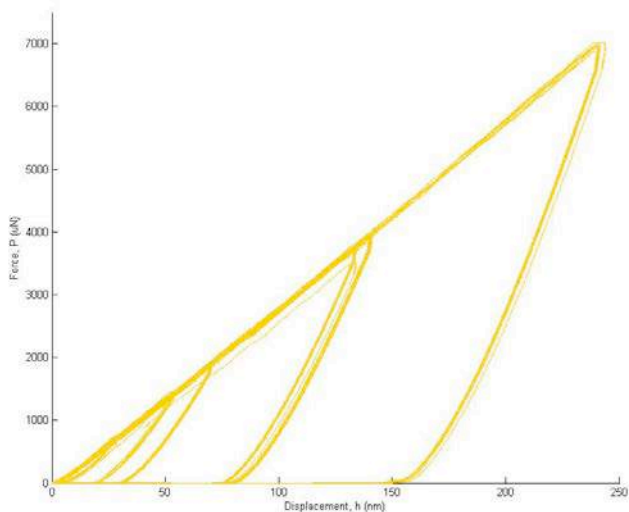


Figure C- 2: Loading and unloading curve of 0.53 μm mixed {001} and {111} orientation PZT film

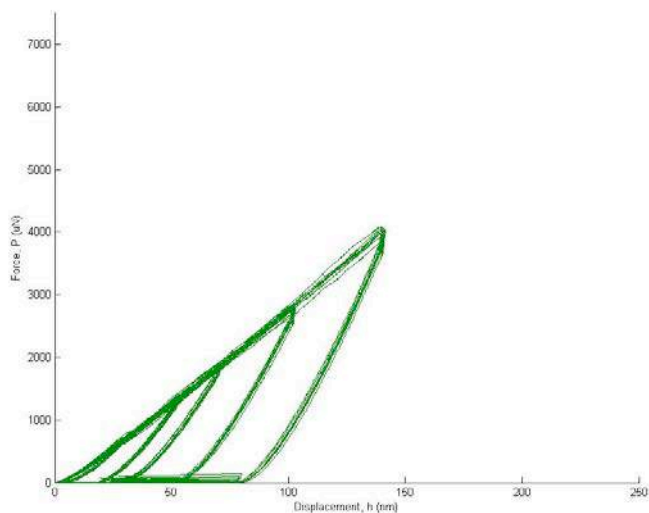


Figure C- 3: Loading and unloading curve of 1.09 μm mixed {001} and {111} orientation PZT film

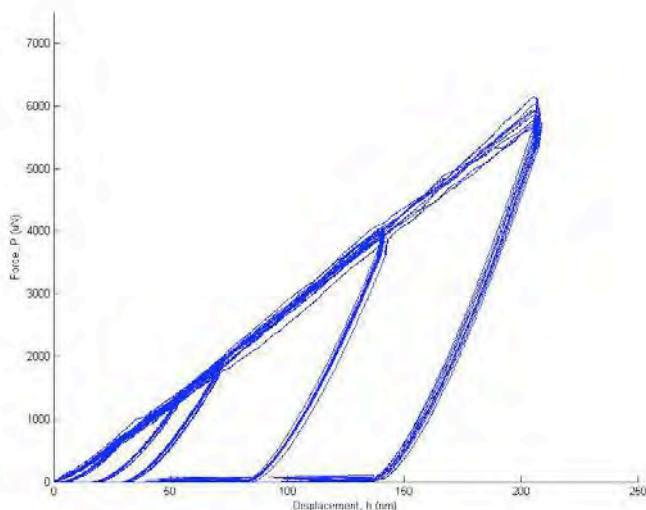


Figure C- 4: Loading and unloading curve of 2.06 mixed $\{001\}$ and $\{111\}$ orientation PZT film

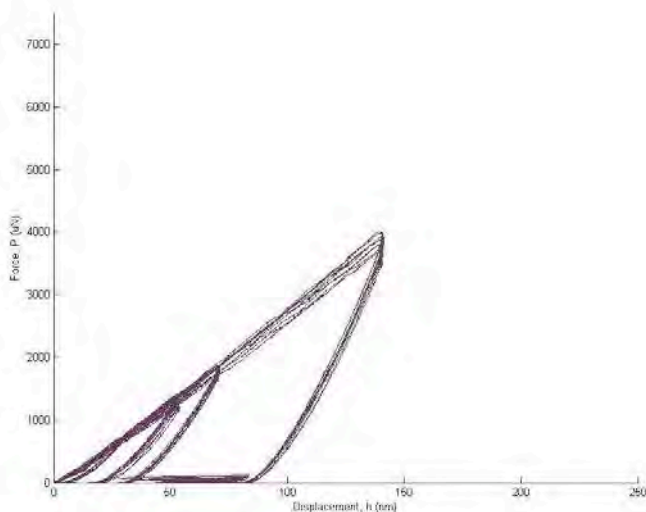


Figure C- 5: loading and unloading curve of 4.40 μm mixed $\{001\}$ and $\{111\}$ orientation PZT film

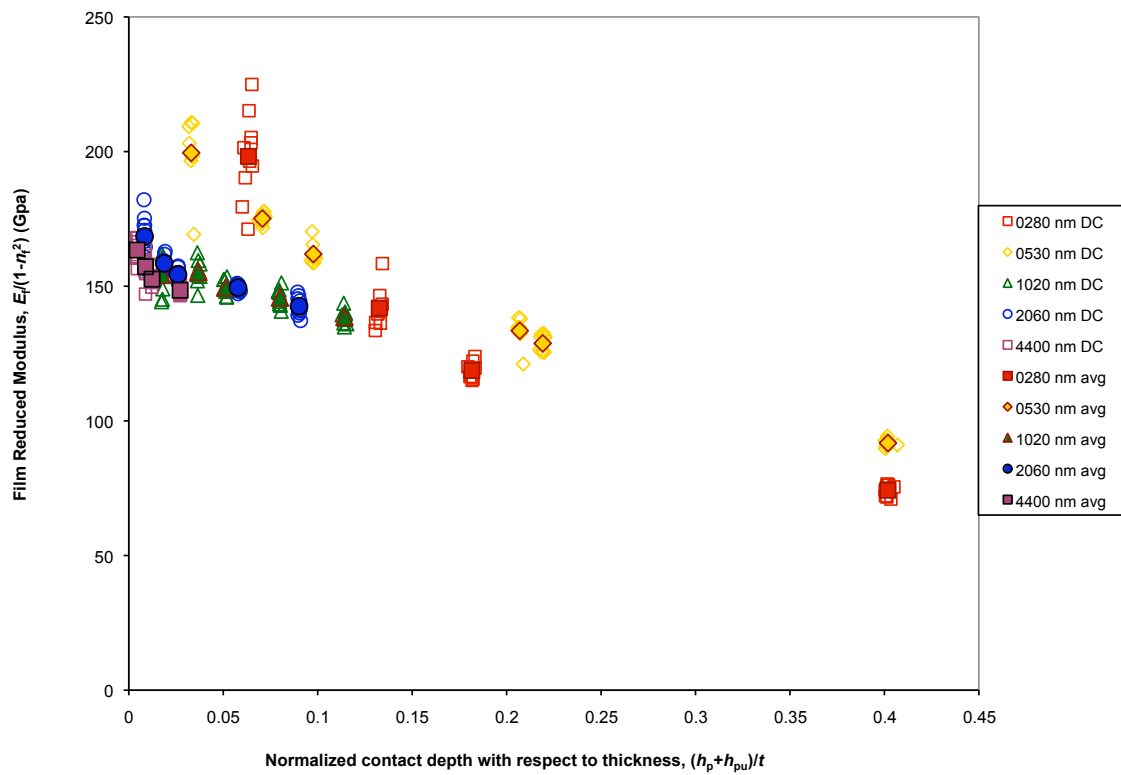


Figure C- 6: Elastic modulus of film with the correction of substrate modeling by King method

VITA

Patamas Bintachitt

Patamas Bintachitt was born in Bangkok, Thailand. She received a Bachelor's of Materials Science from Chiangmai University, Chiangmai, Thailand in 1995. In 1996, she joined Alphatec Electronic Semiconductors as a package development engineer. In 2001, she obtained a Master of Research (MPhil) in the Science and Engineering of Materials, the University of Birmingham, UK. In 2002, she joined National Metal and Materials Science, Thailand. She began to work toward her doctorate degree in Materials Science and Engineering at the Pennsylvania State University in August 2004.